An Experimental and Numerical Study on Complex Behaviour of Cement Paste under SAGD Operating Conditions

by

Ehab Ahmed Mahmoud Hamza

A thesis submitted in partial fulfillment of the requirements for the degree of

Doctor of Philosophy

in

Geotechnical Engineering

Department of Civil and Environmental Engineering

University of Alberta

ABSTRACT

During the exploration stage for oil sands mining or in situ thermal projects, many wells are drilled to recover core for resource assessment: these wells are referred to as stratigraphic wells. These stratigraphic wells are subsequently plugged with either thermal or non-thermal quality cement and permanently abandoned. The integrity of these cement plugs is a key factor for ensuring the long-term performance of these abandoned stratigraphic wells. While generally not an issue for mining projects since abandoned stratigraphic wells are simply mined as part of operations, the presence of abandoned stratigraphic wells within or adjacent to thermal in situ recovery projects poses potential integrity risks due to an increase in fluid pressure and temperature. These variations in both pressure and temperature may compromise the integrity of cement, especially in the case of non-thermal cement, and potentially result in leakage pathways into the shallow subsurface.

To attain and ensure a better understanding of well cement characterization for wellbore integrity, the performance of both thermal and non-thermal cements under SAGD operation conditions were studied and compared in terms of mechanical, thermal and shrinkage behavior.

The initial phase of this research encompassed examining the early-age shrinkage behavior of cement paste. To take into account the effect of curing conditions, a new approach was developed to enable us to measure the shrinkage of hardening samples at pressure and temperature encountered in the field. In the second phase, the alterations that may occur for the mechanical properties of cement paste due to high temperature were investigated by studying the impact of elevated temperature on the

compressive strength, tensile strength, and Young's modulus of cement. The behavior of cement paste under triaxial compression test conditions at several confining pressures was explored as well.

A critical stage of any modeling work is the selection of the simulation parameters. The accuracy of simulation results is mainly dependent on this choice. One of the most crucial properties, needed in simulation, is shear strength parameters of cement-shale interface because the interface between cement and formation is one of the potential leakage paths. Accordingly, both cement-shale interfacial shear behavior and the shear strength parameters of cement itself were investigated in detail through direct shear test. Cohesion and friction angle of cement were determined for different cement mixes with various water-to-cement ratio (w/c).

The knowledge of the behavior of cement slurry is essential to specify the appropriate mix design. The latter has to be determined to allow the cement paste to gain a certain level of early-age strength, which is required to achieve hydraulic isolation of the borehole. Accordingly, the variations in the development of early-age mechanical properties of cement, due to changing of curing conditions, were evaluated acoustically. Elastic moduli and compressive strength of cement were monitored continuously and investigated as a function of pressure and temperature. Correlations between curing conditions and the mechanical properties of cement paste were developed. These correlations will increase our ability to predict the performance of cement under different curing conditions.

Since both mechanical and transport properties of cement are highly affected by the cement matrix, a better understanding of the microstructure evolution of cementitious material during hydration would enable us to not only understand the reaction kinetics of this process, but also to obtain a complete and accurate prediction of the performance of cement paste. Consequently, one part of this thesis was focused on examining the solidification process of cementitious material with an emphasis on the influence of curing conditions on this process. The importance of exploring cement microstructure evolution during solidification process was evident. It was observed that there is a direct link between mechanical properties development and the hydration process.

In the last part of this research, the behavior of stratigraphic wells, abandoned with non-thermal cement and exposed to SAGD operation conditions, was further investigated numerically. To increase the efficiency and decrease the computational time, a shared boundary modeling approach was utilized. The dependence of stratigraphic well performance on its relative position to the steam chamber was also explored by inspecting several stratigraphic wells at different locations. Simulation results indicated that the performance of stratigraphic wells was very sensitive to the proximity of the steam chamber.

PREFACE

All research completed in this thesis is an original work of Ehab Hamza, who planned, designed, and conducted all experimental work and numerical simulations in addition to analysis of results, and interpretation of the data. The research described herein was performed under full supervision of Dr. Rick Chalaturnyk.

In addition to paper-based thesis, the traditional format for a doctoral dissertation is a common type of thesis layout, which is acceptable by the faculty of graduate studies and research. Along the journey of my PhD, I delivered my thesis in the traditional format even though, each individual chapter, with the exception of Chapters 2 and 8, serves as an individual paper addressing a unique topic and dealing with one of the objectives of the thesis. The relationship between the main idea of each chapter and how it is connected and associated to other chapters are summarized in Chapter 8. No part of this thesis has been previously published; however, a modified version of each chapter will be published as a separate paper.

DEDICATION

I gratefully dedicated this thesis to my parents and to my wife who supported me and provided me with the power and strength. You always helped me achieve my goals. I could have never crossed the finish line without your prayers and encouragement.

ACKNOWLEDGEMENTS

In the name of Allah, the most Gracious, the most Merciful. First, I would like to thank Allah Almighty for guiding me to my accomplishments.

First and foremost, I would like to express my deep and sincere gratitude to my supervisor, Dr. Rick Chalaturnyk, for his intellectual support and inspiring guidance. Dr. Chalaturnyk has been a continuous source of valuable knowledge, inspiration, and advice. Thank you for giving me the opportunity of being a part of your prestigious Reservoir Geomechanics Research Group "RGRG" and to be among this amazing team.

I also would like to thank my reading and examination committee members for their careful reading of my thesis, thoughtful comments, and insightful suggestions.

I am grateful to Mr. Wilf Day from MultiCrete for the gracious donation of the thermal and non-thermal cement formulations. It has been a huge privilege to have Abel Sanchez Juncal as my office mate. You were always helpful, offering me valuable feedback in terms of theory and codes.

Special thanks to Dr. Alireza Rangriz Shokri who made my time at RGRG a delight. I enjoyed all our coffee breaks and long chats. I appreciate his input and reviewing of my thesis. He always inspired me on my work. I express my gratitude to Mr. Keivan Khaleghi, his keen interest and support were a great help throughout my experimental work.

I would like to express my sincere thanks to Dr. Nathan Deisman for his support and his valuable feedback. I appreciate all his generous advice. All appreciation goes to Mr. Gilbert Wong, our lab manager for sharing his knowledge and technical know-how.

To my closest and best friends, Dr. Ahmed Moustafa, Dr. Mohamed Meshref, and Dr. Mohamed Ibrahim, thank you for your beautiful friendship; it has been such a huge support.

I would also like to express my gratitude to my office mates: Dr. Stephen Talman, Mr. Seungjoo Lee. Special thanks goes to Mr. Jacob Brandl, our smart mechanical engineer who designed many of the apparatus used in this research.

Thank you Hope Walls for your great effort to facilitate our meetings and organizing many social activities for our group. I really enjoyed those activities and I felt I was among my family. Also, I would like to extend my thanks to all of my friends and colleagues in RGRG and to anyone I may have missed here.

I would like to express my deepest and warmest gratitude to my beloved parents and amazing wife Dr. Sara Nouh for their patience and support.

Finally, I am very grateful for the financial support provided by Helmholtz-Alberta Initiative (HAI) and the Energi Simulation Industrial Research Consortia for Reservoir Geomechanics.

TABLE OF CONTENTS

LIST OF TABLES

LIST OF FIGURES

NOMENCLATURE

C_3S	Tricalcium Silicate (Alite)
C_2S	Dicalcium Silicate (Belite)
C_3A	Tricalcium Aluminate (Aluminate)
$C_4(A,F)$	Calcium Aluminoferrite (Ferrite)
CSH_2	Calcium Sulfate
API	American Petroleum Institute
bwoc	By weight of cement
AER	Alberta Energy Regulator
CSS	Cyclic Steam Stimulation
SAGD	Steam Assisted Gravity Drainage
CSS	Cyclic Steam Stimulation
LCTE	Linear coefficient of thermal expansion
LVDT	Linear variable differential transformer
RH	Relative humidity
C: CaO	Lime
S: SiO_2	Silica
H: H_2O	Water
A: Al_2O_3	Alumina
F: Fe_2O_3	Ferric Oxide
S: SO_3	Sulfate
C-S-H	Calcium Silicate Hydrate
CH	Calcium Hydroxide (Porlandite)
C_SH_2	Calcium Sulfate (Gypsum)
$CaCl_2$	Calcium chloride
OSR	Oil-steam ratio
CSOR	Cumulative steam-oil ratio
hr	Hour
min	Minute

Chapter 1 : Introduction, Research Objectives and Thesis Organization

1.1 Background

1.1.1 Portland cement: overview and classification

Portland cement is fabricated through the burning of limestone, clay, siliceous sand and iron oxide in a rotary kiln at 1450 °C forming clinker nodules upon cooling. As shown in Table 1.1, clinker is mainly composed of tricalcium silicate, dicalcium silicate, tricalcium aluminate, and tetracalcium aluminoferrite. After cooling, clinker is finely ground in continuous mills to produce cement. The rate of cooling controls the quality of the clinker and generally, a slow rate of cooling to about 1250 °C followed by rapid cooling usually (18-20 °C/min) is used.

Table 1.1 Contents of Portland cement

Compound	**Phase Name**	**Cement Chemistry Abbreviation**	**Formula**	**Typical Amount**
Tricalcium Silicate	Alite	C_3S	$3CaO \cdot SiO_2$	50-70%
Dicalcium Silicate	Belite	C_2S	$2CaO \cdot SiO_2$	10-30%
Tricalcium Aluminate	Aluminate	C_3A	$3CaO \cdot Al_2O_3$	5-10%
Calcium Aluminoferrite	Ferrite	$C_4(A,F)$	$4CaO \cdot Al_2O_3 \cdot Fe_2O_3$	5-15%
Calcium Sulfate	Gypsum	CSH_2	$CaSO_4 \cdot 2H_2O$	2-10%

The current study focuses on cement used in the oil and gas industry named "oilwell cement". As per API specification 10A (2010), oilwell cement is classified

into eight classes designated A through H (Table 1.2). This classification is based on depth, pressure, and temperature, which those types can be used at. Class A is used when no special properties are needed while Class B is used when sulfate resistance is required. Class C is developed to gain high early strength. In case of moderately elevated temperature and high pressure, Class D is recommended. Class E and Class F are designed to be used under the condition of elevated temperature and high pressure. Finally, both Classes G and H are utilized as a basic well cement.

Thermal cement is widely used in situations where cement is expected to experience high temperature, such as deep oil wells, geothermal wells, and thermal recovery wells. In these cases, non-thermal cement cannot be employed as elevated temperature strongly affects the physical and chemical properties of cement. Thermal cement is usually made by adding fine silica sand or silica flour to Portland cement. In order to avoid strength retrogression that may occur at temperatures higher than 230 ºC, 35% to 40% silica by weight of cement (bwoc) should be added to cement (Nelson and Guillot, 2006).

1.1.2 Oil sands and bitumen recovery technologies

Canada has over 170 billion barrels of oil reserves, which constitutes the third-largest oil reserves after Saudi Arabia and Venezuela (AER, 2019). About 168 billion barrels exist in three oil sands regions within Alberta: Athabasca, Cold Lake, and Peace River. The Athabasca oil sands region in northern Canada represents the second largest reserve worldwide (Barrow et al., 2010). The viscosity of oil sands remains as a big challenge to produce it. At in-situ conditions, the viscosity of the bitumen can exceed 1,000,000 cP. The two most common recovery methods are surface mining or in-situ thermal recovery. Surface mining technology can be used for shallow deposits. However, it has a high potential risk on the environment and has its own limitations as well. On the contrary, in-situ thermal recovery technologies are suitable for deeper deposits and primarily include cyclic steam stimulation (CSS) and steam assisted gravity drainage (SAGD).

SAGD is considered one of the most promising thermal recovery methods for the in-situ production of oil sand. It was developed by Roger Butler (Butler, 1980; Butler et al., 1981; Butler and Stephens, 1981) and first used in 1980 in Cold Lake. In a typical SAGD process, two parallel and horizontal wells are drilled with 5 m distance apart in vertical direction. High quality steam is injected into the upper well while the lower well acts as a producer.

Table 1.2 API well cement types

Well Class	**Depth**	**Sulfate resistance options** [a]	**Notes**
Class A	Surface to 6,000' (1828 m)	O	Used when special properties are not required
Class B	Surface to 6,000' (1828 m)	M, H	Used when conditions require moderate to high sulfate resistance
Class C	Surface to 6,000' (1828 m)	O, M, H	Used when high early strength is needed
Class D	6,000' (1828 m) to 10,000' (3048 m)	M, H	Used under moderately high pressure and temperature conditions
Class E	10,000' (3048 m) to 14,000' (4267 m)	M, H	Used under high pressure and temperature conditions
Class F	10,000' (3048 m) to 16,000' (4876 m)	M, H	Used under extremely high pressure and temperature
Class G	Surface to 8,000' (2438 m) (as manufactured)	M, H	Basic well cement. Can add accelerators or retarders to cover a wide range of well depths and temperatures
Class H	Surface to 8,000' (2438 m) (as manufactured)	M, H	Basic well cement. Can add accelerators or retarders to cover a wide range of well depths and temperatures

[a] O = ordinary, M = moderate, H = high. Source: American Petroleum Institute (2002).

As the injected steam has lower density than oil, it moves upward and laterally away from wellbore, producing a steam-saturated zone. This operation causes a reduction in oil viscosity. Thereafter, under the effect of gravity, oil and

condensate fall to the bottom and drain into the production well. The oil production mainly depends on the steam chamber growth. Some researchers discussed the mechanism of the heat propagation through the steam chamber. Butler mentioned that conduction controls the heat transfer process. Farouq-Ali (1997) challenged this assumption and pointed out the importance of convection. Similar conclusions were reached by Ito and Suzuki (1996).

In fact, SAGD process has several advantages over other recovery techniques. The injecting of steam facilitates the process of obtaining oil from the production well, as oil stays mobile due to elevated temperatures. On the contrary, in the conventional steam flooding method, some difficulties exist to extract oil as it is cools while moving towards a production well.

Normally, the rate of production of heavy oil in the SAGD process is approximately three times higher than utilizing cold oil gravity drainage (Joshi, 1986). In addition, the use of horizontal wells leads to enhancing the connection between vertical fractures, improving productivity from gravity drainage, and increasing injectivity (Moritis, 1990). In SAGD operations, gravity acts as the main force to collect the oil. Consequently, the heated oil is collected directly through the producer without affecting uncontacted oil. Moreover, the amount of sand, which migrates into the well, is minimal due to the low fluid velocity. Last but not least, SAGD involves a stable displacement, as the only driving force is the gravity (Chen, 2009).

SAGD reservoirs can be classified into three categories: shallow, mid-depth, and deep (Collins, 2005). This classification is mainly based on the relative magnitude of the vertical stress, the minimum horizontal stress, and the maximum horizontal stress.

1.1.3 Challenges in oilwell cementing for the oil and gas industry

The success of the primary cementing job is a key to achieving long-term well integrity. Failures that occur to a cement sheath may require costly remedial processes. Some of the oilwell cementing challenges are as follow:

i) Several factors influence the setting process of cement slurry inside wells such as pressure, temperature, chemical shrinkage, capillary pressure, properties of formation, and well history (Backe et al., 1999). It is important to understand the impact of these parameters on well integrity.

ii) Oilwell cements will encounter wide ranges of pressures and temperatures along the wellbore. Accordingly, the cement is exposed to variable stresses and the long-term integrity of the cement is extremely challenging to maintain under downhole conditions.

iii) The understanding of cement hydration mechanisms is not well developed. The mechanical properties of cement alter continuously during this process. In addition, the complexity of changes would increase with the use of additives such as accelerators, retarders, and fluid-loss control agents.

iv) Mechanical and transport properties are largely dependent on the hydration process. During early-age (first 24 hrs), it is hard to monitor the development of the mechanical properties of cement paste as it is still in a gel state. None of the static tests can be conducted to determine the mechanical properties of cement slurry. In general, characterization of the mechanical properties is required in order to predict the long-term performance of cement.

v) Traditional destructive tests cannot be used to determine the in-situ properties. While cement specimens may have been cured under in-situ stresses, in most cases they are tested at ambient temperature and atmospheric pressure, which does not reflect downhole conditions.

vi) The impact of elevated temperature on cement permeability is not well understood.

vii) In thermal recovery operations where steam is injected down the casing, a cement sheath can be subjected to extreme temperature cycles; this may cause fatigue to the cement and destroy the integrity of cement.

1.2 Research Problem Statements

1.2.1 Problem 1

In SAGD operations, stratigraphic wells are drilled to recover core for resource assessment as well as to plan SAGD well pair orientation and drilling trajectory. Afterwards, these wells are usually abandoned by filling with cement. The number of wells and their locations are mainly dependent on the variability of the reservoir base along the length of the horizontal wells. Given that these wells were abandoned with non-thermal cement and will encounter steam chambers, there is a significant uncertainty regarding the integrity of these wells. To date, the understanding of the performance of non-thermal cement under the impact of elevated temperatures is limited.

1.2.2 Problem 2

There are several significant issues related to the integrity of a cement sheath. First, oilwell cements encounter wide ranges of pressure and temperature along the wellbore during the life of the well, starting from drilling to the abandonment phase. These variations in temperature and pressure induce thermal stresses on the cement sheath and increase the degree of hydration that causes changes in microstructure (Kutchko et al., 2007). Most of the studies have aimed to report the performance of cement paste samples cured under downhole conditions, yet they were tested at room temperature. These measurements did not reflect the actual behavior of cement under the real oilwell conditions.

Second, gas migration may occur through several leakage pathways around the wellbore. One of these paths is the cement - formation interface where shear failure may occur in case of anisotropic in-situ stress condition (Bosma et al., 1999). Several studies investigated the cement – casing interface; however, the cement – formation interface did not receive adequate consideration.

Thirdly, the Mohr-Coulomb criterion is commonly used in the modeling of cement sheaths, employing the friction angle, φ', and cohesion, c', to determine the increase in strength gained due to an increase in the effective stress. These

parameters can be obtained from triaxial tests. Most research studies have focused on the impact of high pressure and elevated temperature on the unconfined compressive strength of cement paste; however, less work was found in literature on the behavior of cement paste under drained and undrained triaxial conditions, especially at an early-age, under downhole conditions.

1.3 Research Hypothesis

The hypothesis for this research is that the complex temperatures, pressures and deformations arising from the SAGD process, that are imposed on geological exploration boreholes (stratigraphic wells) abandoned with non-thermal cements, will negatively impact well integrity, and ultimately increase the risk for condensed water and other fluids to move out of the reservoir zone along these compromised wellbores.

1.4 Research Objectives

The overall objective of this research is to enhance our understanding of well cement characterization to better assess, experimentally and numerically, the performance of both thermal and non-thermal cements for wellbore integrity under SAGD operation conditions in terms of mechanical, thermal and shrinkage behavior with a focus on stratigraphic well behavior.

Several research objectives were defined in order to allow the research hypothesis to be tested and are structured around the two main problem statements provided in §1.2. These objectives are addressed through the following steps:

1. Determine the volume changes in cement paste due to chemical shrinkage and thermal expansion.
2. Characterize the thermo-mechanical properties of oilwell cement, cured and exposed to typical ranges of temperature and pressure during SAGD operations.
3. Evaluate shear strength parameters of cement-shale interface.
4. Assess the development of compressive strength of cement paste during early age.

5. Examine the impact of elevated temperature and high pressure on the mechanical properties of cement paste.
6. Model the evolution of microstructure of cement paste during hydration process.
7. Investigate numerically the performance of a stratigraphic well, abandoned with non-thermally compatible cements, when it encounters a steam chamber.

1.5 Thesis Organization

The thesis consists of eight chapters. Chapter 1 presents a brief background of the problem statement, a summary of the research objectives, hypotheses and approaches. Specifically, it encompasses a review of the oilwell cement classification, oil sands, and different recovery technologies, aiming to provide insight about challenges in oilwell cementing operation. The outline of the thesis is also introduced in this chapter. The methodologies and the detailed experimental procedures, modeling approaches, results, and conclusions are presented separately in each chapter (Chapters 2-7).

Chapter 2 discusses the shrinkage behavior of thermal and non-thermal cement cured under high pressure. A new method for measuring the chemical shrinkage of cement paste during the hydration process is presented. A good correlation between volumetric shrinkage and cement content is found and proposed. The second part of this chapter deals with the thermal characterization of oilwell cement. A detailed description of the different thermal properties of cement paste and the corresponding measurement techniques are provided along with the experimental results from the thermal expansion of cement paste.

Chapter 3 consists of a detailed description of the impact of high temperature on the mechanical properties of non-thermal cement. The variations of compressive and tensile strength of cement paste with temperature are experimentally evaluated.

Chapter 4 describes the experimental program undertaken to investigate the properties of cement-shale interface and shear strength parameters of the cement paste itself. The effect of water cement ratio on the shear strength properties of cement paste is also discussed.

Chapter 5 explores the application of ultrasonic techniques in monitoring mechanical properties and evolution of oilwell cement during setting and hardening. New correlations between curing conditions (pressure and temperature) and elastic moduli (Young's modulus and bulk modulus) are proposed in this chapter.

Chapter 6 introduces the concept of a vector approach and the application of μic platform to predict the microstructural evolution of cement paste at early age. Homogenization theory is employed to estimate the elastic properties based on the output of the proposed model.

Chapter 7 explains the numerical modeling approach developed to investigate the performance of stratigraphic wells, abandoned with non-thermal cement, when exposed to a steam chamber.

Chapter 8 provides a summary of the work performed in this research along with the conclusions and contributions of this study in addition to the recommendations for future work.

Finally, the appendices documents some of the experimental methodologies, with supplementary tables and figures, referred in the main chapters.

Chapter 2 : A New Approach to Assess the Shrinkage of Oilwell Cement Slurries

2.1 Introduction

Gas migration through well cement jobs is still considered one of the challenges in the oil and gas industry. Normally, it occurs shortly after the primary cementing job and it has a significant impact on wellbore integrity and in some cases, will require major remedial measures.

Numerous studies have discussed gas migration problems occurring through cement matrix in oilwells (Sabins et al., 1984; Cheung et al., 1985; Sykes et al., 1987). The impacts of other parameters such as composition of cement slurry, porosity, chemical shrinkage, and dissolved gas on this phenomenon have been previously investigated (Justnes et al., 1995; Backe et al., 1994; Tavares et al., 2013). Gas migration may occur through the cement annulus, the interface between cement and casing, and the interface between cement and formation (Stewart and Schouten, 1988). Gas leakage initiates in the cement before it reaches a solid state through microannuli or microfractures (Skalle et al., 1997).

After the primary cementing job, a cement slurry hardens under different temperatures and pressures based on the well conditions and during this hardening process, cement will experience volumetric changes, typically shrinkage. This shrinkage may lead to cracks in the cement matrix and/ or debonding between the cement and the casing. Additionally, chemical shrinkage of cement causes a reduction in the hydrostatic pressure of the cement column and usually occurs before the complete development of cement strength. The difference between the pressure of the formation gas and the hydrostatic pressure of the cement slurry may be high enough to break the matrix and allow the gas to migrate through the fracture (Backe et al., 1999). Thus, utilizing low shrinkage slurry is desirable to control the decreasing of hydrostatic pressure, and to minimize the possibility of gas migration to occur. In fact, it is essential to investigate the chemical shrinkage of cement to fully understand the mechanisms of initiating gas migration. Internal and external

shrinkage processes are the two components comprising chemical shrinkage of a cement slurry. Internal shrinkage results from the development of contraction pores while external shrinkage is the volumetric change of the slurry and it is the main reason for the potential formation of a microannulus between the cement and the wellbore (Backe et al., 1999).

An early attempt to determine the chemical shrinkage of Portland cement was made in 1900 by Le Chatelier. He reported a value of 4.6% for chemical shrinkage. Since then, many researchers have studied this topic from different angles. A very detailed description of the various stages of cement paste and mortar shrinkage is given by Hass (1975). In this study, volume shrinkage, pulse velocity, and heat evolution rate were monitored and measured during the hydration process. Tests were conducted on slurry with water cement ratios (w/c) of 0.20 and 0.50, respectively, at 20 °C. The authors deduced that the shrinkage behavior is closely related to the mechanism of the formation of ettringite along with its morphology. They mentioned that high water cement ratio slurry gives relatively low shrinkage. This is due to the nature of the ettringite formed. For the case of high w/c, the shapes of the ettringite crystals are longer and perpendicular to the grain. Thus, allowing more spaces between the grains causing more resistance to shrinkage. After some time, the rate of the dissolution of C_3A decreases and the formation of ettringite crystals increases resulting in a reduction of the shrinkage rate (Hass, 1975). This is because the difference in the volume between ettringite and clinkers is low and the ettringite formed compensates for most of the amount of the shrinkage occurring during this stage.

Parcevaux and Sault (1984) divided the chemical shrinkage into two phases. During the first phase, shrinkage occurs with a high rate due the chemical reaction between water and cement. Afterwards, the shrinkage continues with a lower rate due to the movement of water into solid cement paste.

Backe et al. (1999) employed the correlation between pressure, temperature, and volume of a gas to measure the total shrinkage of cement. The sensitivity of their method to the temperature change was the main disadvantage of this

technique. They performed the experiments on three different slurries. Additives were added to two of them to avoid gas migration. Tests were performed at 90 °C, 140 °C, and 180 °C. The reported values of the total shrinkage (Vol %) at 20 hours were in the range of 1.79 to 3.92%.

Thermal recovery methods of heavy oil, such as steam-assisted gravity drainage (SAGD) or cyclic steam stimulation (CSS) involve introducing heat into the reservoir by injecting steam to enhance oil production. During this process, the well and the surrounding formations experience a significant change in temperature resulting in the expansion of casing, cement sheath and formations. Any incongruity between the linear coefficient of thermal expansion (LCTE) of casing and cement sheath would probably lead to the development of microannulus and cracks within the cement due to the high stress which may act on the cement sheath. Therefore, the knowledge of the thermal properties of cement paste, especially thermal expansion, under field conditions is essential to determine the changes in the stress, and strain fields due to thermal volumetric deformation. This enables us to evaluate the long-term integrity.

The specific objectives of this chapter are to investigate the shrinkage behavior of cement paste during hydration, and to determine the coefficient of thermal expansion of hardened cement paste. We examine the impact of water cement ratio on both shrinkage and thermal behavior of cement and explore the difference in the shrinkage performance of thermal and non-thermal cement. The outcome of this research would help the oil and gas industry to better adopt a proper cement mix.

2.2 Types of shrinkage occurring in cementitious material system

2.2.1 Chemical shrinkage

Chemical shrinkage refers to the reduction in the internal volume of cement paste due to the hydration of the clinker. Normally, chemical shrinkage can be obtained directly by measuring the volumetric variations of the cement sample with time during hydration process, or indirectly by monitoring the quantity of water

adsorbed by cementitious material system. The latter can be determined as a function of specific volume and saturated density of the sample (Geiker & Knudsen, 1982).

2.2.2 Autogenous shrinkage

Chemical shrinkage and autogenous shrinkage are different terms and cannot be used interchangeably. Autogenous shrinkage represents the decrease in the length that takes place without any change in temperature and under constant moisture content. In other words, it is the bulk deformation of a closed, isothermal cement paste system without the impact of any external forces (Jensen & Hansen, 2001). In his paper, Holt (2005) summarized a few ways, which may lead to a reduction in the amount of autogenous shrinkage taking place at early age. These measures include, but are not limited to, utilizing clinker with high amount of C_2S and low C_3A content; increasing the rate of hydration and accelerating the formation of cement matrix to resist shrink stresses; and reducing the amount of silica fume to obtain cement paste with coarser pore structure, causing to minimize early-age capillary pressure

2.2.3 Carbonation shrinkage

This phenomenon happens due to the reaction between cement paste, water, and carbon dioxide resulting in a reduction in the volume and pH of the cement sample. This reaction can be defined according to Mehta and Monteiro (1993) as follows:

$$H_2CO_2 + Ca(OH)_s \rightarrow CaCO_3 + 2H_sO \quad (2.1)$$

Several factors may affect the magnitude of the carbonation shrinkage such as cement paste density, sample age, and the condition of the surrounding atmosphere. However, it does not extend more than 2 cm of the depth of the sample surface (Lura, 2003).

2.2.4 Drying shrinkage

The third type of volume change, which may occur to cement paste, is drying shrinkage. This phenomenon takes place when cement is cured without sealing to open air. As a result, water evaporates and causes a volume reduction. Drying shrinkage is considered a time-dependent deformation (Hansen, 1987).

Both the rate of evaporation and the quantity of water expelled from the cement paste control the magnitude of the drying shrinkage (Lura, 2003). For instance, no drying shrinkage would take place if the bleeding rate is higher than the evaporation rate because the internal water, filling the pores, will not be consumed during the evaporation process. On the other hand, if the bleeding rate is lower than the evaporation rate, water will be pulled out from the internal pores, after the surface water resulting from bleeding is being consumed by evaporation, causing volume reduction. A detailed description of drying shrinkage is found in Hansen (1987). Drying and carbonation shrinkage are outside the scope of this work and will not be discussed in detail.

2.3 Driving forces of shrinkage

2.3.1 Surface tension

The surface tension of a solid particle is strongly dependent on its state and the surrounding environment. The maximum surface tension can be reached when the sample is under vacuum. The magnitude of the surface tension decreases accordingly when the sample is placed in a media of fluid or gas (Powers, 1968).

Powers (1968) mentioned that the volume change of porous media is affected by the surface tension of the material due to the influence of the latter on the density. This volume change can be divided to the change in the inner and the outer part of the material. The author proposed an equation, which describes the volume change of the inner part of a spherical particle due to the change of relative surface tension as follows:

$$-\frac{dV_i}{V_i} = 2\alpha_c dP \tag{2.2}$$

where α_c is the coefficient of compressibility of the material; and P is the compressive stress due to the surface tension.

The impact of surface tension on cement shrinkage is affected by relative humidity (RH). It decreases as relative humidity (RH) increases. This influence becomes insignificant when the value of RH is higher than 75% (Jensen, 1993). This can be attributed to the fact that any adsorbed water by the solids after the third layer has a trivial effect on the change in the surface tension of these solids (Lura et al., 2003).

2.3.2 Disjoining pressure

Disjoining pressure occurs due the interaction between several mechanisms such as the overlapping double ionic layers, boundary electromagnetic fluctuation fields, and boundary layers of liquids, with a structure modified under the effect of surface forces. It can be calculated as the summation of van der Waals forces, double layer repulsion, and structural forces (Derjaguin & Churaev, 1974). In cementitious material, the influence of capillary forces should be considered because the degree of saturation of the sample is usually less than 100% (Ferraris & Wittmann, 1987). Any variation of disjoining pressure will lead to a volume change of the cement sample due to its effect on the porosity of the sample by changing the space between solid surfaces.

According to Powers (1968), the change in the volume due to the variation in disjoining pressure can be written as:

$$\left(\frac{\Delta V}{V}\right)_d = \beta' f(w) \frac{RT}{MV_a'} Inh \tag{2.3}$$

where ΔV_d denotes volume change due to disjoining pressure; β' is the coefficient of compressibility of the specimen under sustained stress; *f(w)* is the fraction of gross section area over which the disjoining pressure is effective and is a function of water content; V is the overall volume; V_a' is the partial specific volume of the adsorbed water; R is the universal gas constant that is 8.314 J/(mol·K); T is the absolute temperature; $h = p / p_s$; and p_s is the saturation pressure for the existing temperature and atmospheric pressure.

In equation 2.3, the term $(\frac{RT}{MV_a^{'}} Inh)$ represents the pressure in the adsorbed water.

Both Na^+ and K^+ content and the concentration of Ca^{2+} ions in the pore solution have a significant influence on the disjoining pressure (Beltzung et al., 2001; Beltzung et al., 2005). Also, Beltzung et al. (2001) mentioned that disjoining pressure increases with relative humidity (RH) due to the change of the thickness of fluid between particles. Therefore, the effect of disjoining pressure on the volume change of cement paste is very significant at high relative humidity. However, determining the variations in disjoining pressure with the change of relative humidity in cementitious material is not easy due to the complexity of the skeleton structure of this material.

2.3.3 Capillary tension

In general, capillary tension phenomenon describes the capability of a fluid to move within very small spaces without the influence of any external force. In partially saturated cement paste, capillary tension builds up due to the movement of pore fluid from the bigger capillary voids to the smaller voids. This stress varies according to the diameter of the largest fluid-filled capillary pore and the surface tension of pore fluid and can be obtained from the following equation:

$$P_c = \frac{4\gamma}{\varphi_{pore}} \tag{2.4}$$

where P_c is the capillary stress; γ is the surface tension of pore fluid; and φ_{pore} is the diameter of the largest water-filled capillary pore.

Capillary tension of pore fluid of cement paste can be determined directly from the measurement of internal RH (Jensen, 1993), or indirectly by employing the mercury intrusion porosimetry technique (MIP) (Hua et al., 1995). The significance of capillary tension on determining cement shrinkage increases when RH is higher than 45% (Soroka, 1979).

2.4 Factors affecting cement chemical shrinkage

Many factors may affect the shrinkage behavior of cement paste such as chemical compositions, the presence of additives, water cement ratio, the thickness of cement sample, curing temperature and pressure.

2.4.1 Cement composition

The dependency of chemical shrinkage on the cement mineralogy has been observed by several researchers. Of interest, Yodsudjai and Wang (2013) measured the chemical shrinkage of cement pastes made of several types of cement. Their mix had water to cement ratio of 0.40. They concluded that the chemical shrinkage of cement paste is sensitive to the C_3A + C_4AF content and equivalent alkali content. The higher the C_3A + C_4AF content and the equivalent alkali content, the greater the chemical shrinkage.

2.4.2 Curing conditions

Both curing pressure and temperature have an impact on cement paste shrinkage. Geiker and Knudsen (1982) mentioned that the rate of the development of chemical shrinkage increases with temperature, however the chemical shrinkage at infinite time will decrease. Sabins and Sutton (1991) explored plastic-state shrinkage, which refers to the change in overall volume. This change occurs during the low-strength plastic state of cement and before the initial set. They measured plastic-state shrinkage under downhole conditions and recognized that plastic-state volume change mainly occurs due to fluid loss, and not due to hydration. They concluded that the amount of plastic shrinkage increased from 0.02 % at 0.02 MPa to 0.12 % at 0.6 MPa.

Xueyu Pang et al. (2015) employed a new apparatus to estimate the chemical shrinkage of cement at in-situ conditions. The fluctuations of ambient temperature during the test were the main drawback of this technique. The impact of ambient temperature variations was obvious especially in long time span tests. The authors performed their tests on hollow and solid cylinders. The impact of specimen thickness on the cement shrinkage was observed to be minimal. This can

be explained by the ability of water to penetrate the cement specimen due to the application of water pressure during the test. The same conclusion has been drawn by Costoya (2008) based on his experimental work performed on tricalcium silicate. The impact of curing temperature on chemical shrinkage was found to be sensitive to temperature range. The higher the curing temperature, the greater the chemical shrinkage especially at early age. On the other hand, the dependency of chemical shrinkage on curing pressure was observed to be insignificant as chemical shrinkage increased marginally with pressure. However, it has to be mentioned that the tests have been conducted at a small pressure range.

Other studies investigated the total and external chemical shrinkage of oilwell cement under different temperature ranges from room temperature up to 224 °C and at pressures up to 121 MPa (Sabins et al., 1991; Justnes et al., 1995; Parcevaux et al., 1984). The reported values for total shrinkage at 24 hours varied from 0.6 to 6 by volume percentage.

2.4.3 Utilization of additives

It is common practice to use different additives in order to improve the performance of the cement paste or to change its behavior by controlling setting time. These additives affect the shrinkage behavior of cement paste due to their impact on cement dispersion and hydration kinetics.

Chenevert and Shrestha (1991) investigated the impact of bentonite, sodium silicate, salt levels, silica sand, and silica flour on the chemical shrinkage of Class H cement at different pressures and temperatures. Curing temperature ranged from 38 °C to 224 °C and applied pressure varied from 8.3 MPa to 121.3 MPa. They noted that the use of bentonite and sodium silicate decreased chemical shrinkage. The reduction in chemical shrinkage increased with higher temperature. In addition, the presence of silica flour decreased chemical shrinkage more effectively than silica sand. Chemical shrinkage was found to be related directly to slurry yield. Justnes et al. (1995) measured both external and total chemical shrinkage of Class G cement. The total chemical shrinkage reported at 20 °C after 48 hours was 2.6 %.

No significant impact was observed on chemical shrinkage due to the addition of precipitated calcium carbonate (≤ 15%) or polyvinyl-alcohol (≤ 3%).

2.4.4 Composition and amount of ponding solution

The composition of the fluids surrounding cement during the hydration process, the "ponding" solution, may alter the chemical shrinkage behavior of cement paste. Sant et al. (2006) investigated the influence of the composition of the fluid used on the measured chemical shrinkage and focused their study on two types of fluid; deionized water (pH 7.65), and lime (0.15 KOH + 0.05 NaOH solution, pH 13.27). They found that utilizing lime slightly reduced the chemical shrinkage and exhibited a slow retardation. On the other hand, increasing the amount of ponding fluid from 10 g of deionized water to 40 g led to a rapid initial increase of chemical shrinkage and accelerated the reaction rate as well. They concluded that some alterations would occur to composition of the ponding solution to become similar to the internal pore solution.

2.5 Approaches for chemical shrinkage determination

Measuring chemical shrinkage of cement paste is not an easy task due to the complex nature of the hydration process. The three widely known methods, which can be used to measure chemical shrinkage of cement, are dilatometry, pyconometry, and gravimetry (Justnes et al., 2000). Dilatometry was firstly introduced by Le Chatelier and then has been used by many researchers to identify the different factors which may affect the chemical shrinkage such as cement composition, w/c, and utilizing of additives (Justnes et al., 1994; Beltzung et al., 2000; Charron et al, 2002). This method involves monitoring the change of the sample length or volume by measuring the variations of water level with time using a pipette, which is fixed through a rubber stopper in the top of the bottle. To obtain an accurate result from this method, the sample has to be completely saturated and pore spaces fully filled with water. One disadvantage of this method is that it requires manual readings (Holt, 2001).

The pyconometry method was introduced based on Archimedes law. In this technique, the sample is kept immersed in water and the change in the volume of cement is calculated by monitoring the change of the weight of the sample during solidification while maintaining the total volume of the system constant by adding water to replace the consumed water during hydration. This method has been used to study the effect of temperature on chemical shrinkage of cement paste (Geiker & Knudsen, 1982). The concept of gravimetry method is similar to pyconometry, however an enhancement has been made to record the results automatically. Figure 2.1 summarizes the concept of these techniques.

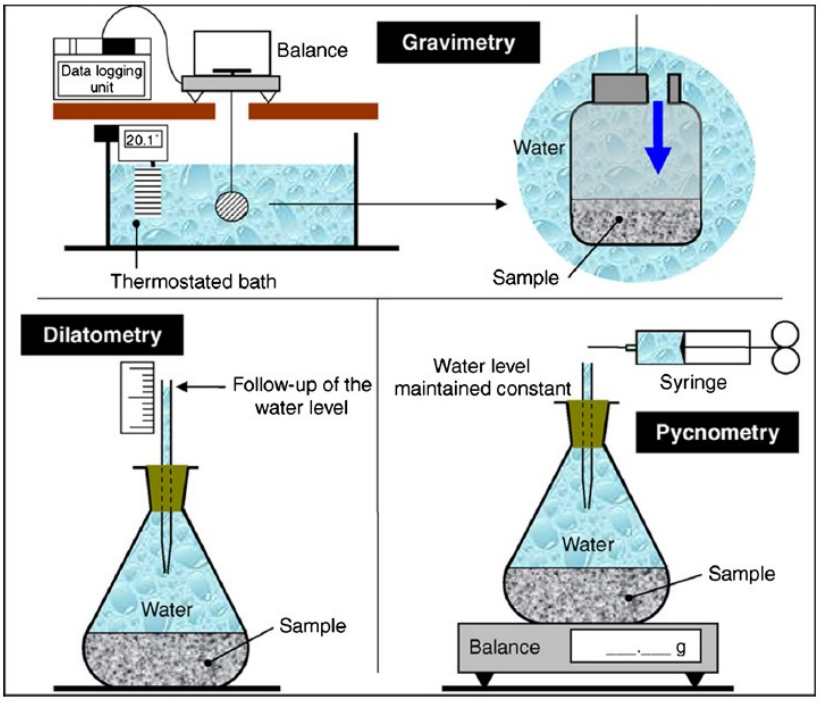

Figure 2.1 Principal measurement methods for chemical shrinkage of cement based-materials (Bouasker et al., 2008)

2.5.1 Determination of chemical shrinkage in accordance with ASTM C1608

According to ASTM C 1608, the chemical shrinkage of cement paste can be determined at atmospheric pressure by measuring the change in the water volume, which covers a thin layer of cement paste. This method is characterized by its simplicity, but it has some drawbacks. The accuracy of the results obtained by this method is affected by different factors resulting in low precision and poor repeatability. The following sections discuss these factors briefly.

2.5.1.1 Amount and composition of water added during the test

During the test, water is added to keep the sample saturated. This water should be added in a way that does not cause any disturbance to the cement specimen. In addition, the composition of this water strongly affects the results. Especially, if there is a significant difference in the chemistry between the fluid added on the surface of the sample and the water filling the pore spaces, which leads to leaching.

2.5.1.2 Water to cement ratio (w/c)

Selecting a proper value for w/c is essential to get reliable results. Using cement paste with low w/c might affect the quality of the sample due to difficulties in obtaining uniform and homogeneous paste. On the other hand, testing a sample with a high w/c will increase the possibility of having a bleeding resulting in obtaining inaccurate results (Zhang et al., 2013). According to ASTM C 1608, the recommended value of w/c is 0.40.

2.5.1.3 Thickness of the sample

The thickness of sample should be small enough to allow the water to move quickly to fill up the pore spaces created by chemical shrinkage and to have sufficient water for both hydration and full infiltration of water to the specimen to avoid self-desiccation. According to ASTM C 1608, the recommended range for the sample thickness is 5-10 mm. Holt (2001) reported a reduction in the chemical shrinkage when bigger samples were used. The same conclusions were obtained by Zhang et al. (2013). They noticed that the impact of sample thickness on the results

is insignificant during the first 3 days. Afterwards, samples with small thicknesses experienced higher rates of change in chemical shrinkage than those samples with larger thicknesses. The impact of sample thickness on cement shrinkage can be attributed to the higher degree of hydration that can be achieved at later ages when a thinner sample is used due to ease of hydrating most of the sample by water. In addition, thicker samples have a lower permeability resulting in increasing the difficulty of pore fluid to reach to all pore spaces (Xueyu Pang et al., 2015).

To improve the results obtained by ASTM C 1608, Zhang et al. (2013) develop a new technique, in which they placed a magnetic stirring bar into the Erlenmeyer flasks, to eliminate the formation of skeleton structure in the paste during solidification and to reduce the effect of the shape of glass vial on the specimens.

2.5.2 Determination of chemical shrinkage mathematically

The amount of chemical shrinkage can be estimated by calculating the difference in volumes between unhydrated cement and the hydration product. To do so, hydration reaction along with molecular weights and densities of all cement phases should be defined first (Tazawa et al., 1995; and Mounanga et al., 2004).

According to Zhang et al. (2013) and based on the values of densities and molar volume for unhydrated cement and the hydration product shown in Table 2.1, the chemical shrinkage of cement paste can be obtained from Paulini equation:

$$Vcs = 0.0775*(C_3S) + 0.0742*(C_2S) + 0.171*(C_3A) + 0.171*(C_4AF) \quad (2.5)$$

where (C_3S), (C_2S), (C_3A), (C_4AF) are the mass percent of Tricalcium silicate, Dicalcium silicate, Tricalcium aluminate, Tetracalcium aluminoferrite, respectively, which exist in the clinker.

In Equation 2.5, the numbers multiplied by the mass percent of the clinker phases represent the coefficients of the chemical shrinkage of these individual phases. The coefficients of chemical shrinkage for Tricalcium aluminate may vary from 0.1745 to 0.1122 depending on whether all the aluminate phases will convert to ettringite or to monosulfate. It can be noticed that the accuracy of the obtained

chemical shrinkage mainly depends on molecular weights and densities of cementitious compound; any error in the estimation of these values may result in unreliable results. Typically, the amount of the chemical shrinkage of Portland cement is about 6-9 ml/100 g (Powers & Brownyard 1948; Bentz et al., 2005).

Table 2.1 Summary of densities and molar volumes for unhydrated cement and the hydration products (Bentz , 1997; Balonis, 2009)

Clinker Phases			**hydration product**		
Compound	**Density (g/cm^3)**	**Molar volume (cm^3/mole)**	**Compound**	**Density (g/cm^3)**	**Molar volume (cm^3/mole)**
C_3S	3.21	71.0	**$C_{1.7}SH_4$**	2.12	108.0
C_2S	3.28	52.0	**CH**	2.24	33.1
C_3A	3.03	89.1	**$C_6AS_3H_{32}$**	1.70	735.0
C_4AF	3.73	128.0	**C_4ASH_{12}**	1.99	313.0
CSH_2	2.32	74.2	**C_3AH_6**	2.52	150.0
H	1.0	18.0	**FH_3**	3.0	69.8

2.6 Approaches for Autogenous shrinkage determination

Two methods have been described in literature to measure autogenous shrinkage. The first method is based on measuring the volume change of cement slurry placed in a rubber balloon and completely submerged in water (volumetric measurement). This can be done by calculating the difference in the weights due to immersing the specimen in water.

The second approach deals with vertical displacement (linear measurement). In this case, autogenous shrinkage can be obtained by measuring the variation of the length of cement paste sample cast in a mold with low friction

(Figure 2.2). To compare the reliability and the accuracy of these methods, both the advantages and disadvantages of each method have to be discussed first. Using volumetric measurement gives the ability of carrying out the test shorty after pouring the cement sample. However, bleeding water and entrapped air may undesirably affect the results as they reduce the contact between the rubber balloon and the specimen; this results in an error when estimating the change of the volume. In addition, there is a high possibility of damaging the sample during early age due to pressure resulting from a tight rubber balloon (Buil, 1979).

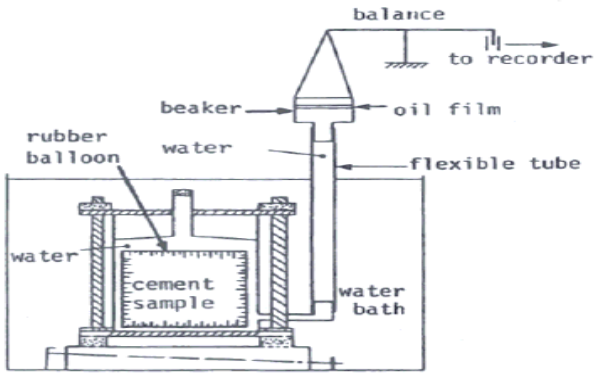

Figure 2.2 Principal measurement method for autogenous shrinkage for cement based materials (Buil 1979)

On the other hand, the main disadvantage of the linear technique is that the measurement has to be conducted after the setting time of cement paste to be able to record the vertical deformation of the sample. The inability of the specimen to deform freely, due to the friction between a cement surface and a rigid tube, is considered to be another issue (Barcelo et al., 1999). To minimize the effect of friction, lubricant should be applied on the surface of the tube. As with volumetric measurement, the results obtained from linear measurement are also affected by bleeding.

Barcelo et al. (1999) mentioned that the volumetric approach gives 3-5 times higher autogenous shrinkage than the linear method. This difference in the results can be attributed to the fact that at early age the vertical deformation is higher than horizontal deformation due to settlement of cement paste. The discrepancy in the results between the two techniques is affected by cement composition and experimental setup.

To obtain more accurate results by avoiding the disadvantages of both volumetric and linear measurement techniques, Jensen and Hansen (1995) developed a new technique to measure autogenous shrinkage. They used a dilatometer submerged in a glycol bath to control the temperature during the test. The dilatometer frame was made of invar to decrease the thermal deformation of the frame. They used a corrugated mold to allow the sample to deform freely in the vertical direction. This method enabled them to start their test 1 hour after adding water to the clinker.

2.7 Thermal properties of cementitious materials

Heat propagation through cementitious materials is a complex process as these materials are non-homogenous and multiphase system. Numerous mechanisms contribute to heat transfer through cement paste such as conduction and convection through the liquid phase, conduction through the solid matrix and the contact region between solid particles, and evaporation-condensation mechanisms. The principal properties required to describe the thermal behavior of cement paste are thermal conductivity, thermal diffusivity, heat capacity, and the linear coefficient of thermal expansion. The following sections describe these parameters

2.7.1 Thermal conductivity

Thermal conductivity is a material property, which describes the ability of the material to transfer heat by conduction. It can be defined as the rate at which heat is transmitted by conduction through a unit cross section area of the material

due to a unit temperature gradient under steady state condition. Thermal conductivity can be obtained from the following equation:

$$k = \frac{\mathrm{Q}*\mathrm{L}}{A(T_2 - T_1)} \tag{2.6}$$

where Q is the heat flow (W); L is the length of the sample (m^2); and T_2—T_1 is the temperature gradient through the sample (K).

Experimental methods generally utilized to determine thermal properties of solid materials can be divided into two categories, steady state and transient techniques. Steady state approach has been widely used to obtain thermal conductivity of different materials such as Athabasca oil sand, soils, and concrete (Morabito, 2001). This approach is based on one-dimensional linear heat conduction and is governed by the following Laplace's equation:

$$\frac{\partial^2 \mathrm{T}}{\partial \mathrm{Z}^2} = 0 \tag{2.7}$$

where T is the temperature at any point; and Z *(m)* is the distance from the origin.

The steady state technique includes Guarded Hot Plate (GHP), The Radial Heat Flow (RHF), and Guarded Heat Flow Meter (GHFM).

Transient approach is mainly based on measuring the temperature changes, as a function of time, due to the heat transfer from a controlled heating source to the material. One-dimensional radial heat flow in an infinite homogenous medium is governed by the following equation:

$$\frac{1}{\alpha}\ \frac{\partial \mathrm{T}}{\partial \mathrm{t}} = \frac{\partial^2 \mathrm{T}}{\partial \mathrm{r}^2} + \frac{1}{\mathrm{r}}\ \frac{\partial \mathrm{T}}{\partial \mathrm{r}} \tag{2.8}$$

Different techniques are available now to determine the thermal conductivity of a material based on transient method such as hot strip, hot wire, hot bridge, and plane source.

The steady state methods often give higher values of thermal conductivity of moist materials compared to transient methods (Combs et al., 1977; Andrew Chin-Keung, 1985). Andrew Chin-Keung (1985) reported a 15% reduction in the thermal conductivity of water-saturated sand when a transient state method was used, due to the impact of moisture redistribution.

A significant contribution to understand the factors influencing the thermal conductivity of cementitious materials was made by Kim et al. (2003). Their study was conducted with the main emphasis on the effect of seven testing parameters on the thermal conductivity of concrete, mortar, and cement paste. Experimental results revealed the independency of thermal conductivity on the age of concrete except at early age. Meanwhile, the impact of the aggregate volume fraction and moisture content of the sample on the thermal conductivity of concrete was significant. The thermal conductivity increases with the increase of aggregate volume ratio and degree of saturation as well. Water cement ratio and admixture were found to be the most effective factors on thermal conductivity in case of cement paste. The higher the water cement ratio, the lower the thermal conductivity. A reduction of free moisture content from 1 to 0 led to a decrease of the thermal conductivity of cement by 35%. A reduction in thermal conductivity with temperature was noted as well. Moreover, thermal conductivity was found to be largely dependent on the curing conditions. The thermal conductivity of cement paste samples cured in ambient air was observed to be higher than the specimens cured in water (Brown et al., 1970; Schutter et al., 1995).

2.7.2 Thermal diffusivity

Thermal diffusivity measures the ability of the heat to propagate through a material. Therefore, it describes the change in the thermal profile during the unsteady, transient period when the sample is subjected to a variation in temperatures (Yoon et al., 2014). The magnitude of thermal diffusivity of cement paste during hardening is not constant and varies with the degree of hydration. A reduction in thermal diffusivity during hydration was reported by De Schutter & Taerwe (1995). They proposed a new relationship between degree of hydration and thermal diffusivity in which the latter decreases linearly with the degree of hydration.

2.7.3 Specific heat

Specific heat is a thermodynamic property of the material, which measures the ability of the material to preserve the heat and can be defined as the amount of heat per unit mass required to increase the temperature of the material by one degree Celsius. Specific heat can be calculated by knowing thermal conductivity and thermal diffusivity from the following equation:

$$C_p = \frac{k}{\rho \alpha_d} \quad [\frac{kJ}{kg^oC}] \tag{2.9}$$

where k is the thermal conductivity (W/m ºC); α_d is thermal diffusivity (m^2/s); and ρ is density of the material.

Specific heat of cement paste can be improved by admixture surface treatment. Using silica fume and silane-treated carbon fibers causes 12% increase in the specific heat for the cement paste (Xu & Chung, 1999).

2.7.4 Thermal expansion

The coefficient of linear thermal expansion CTE, denoted by α_T, is a material property that defines the change in the unit length per unit rise in temperature. Normally, CTE is determined by measuring the thermal deformation when the sample is exposed to temperature difference under a stress-free condition. It is expressed in terms of millionths per degree centigrade (x 10^{-6} /°C).

Many researchers have tried to investigate the deformation of cement based materials due to temperature. Verbeck and Helmuth (1968) proposed three types of coefficient of thermal expansion for cement paste as following:

(1) X_i represents the instantaneous coefficient utilized to measure a process too quickly to allow significant redistribution of moisture within the specimen.
(2) X_w employed to evaluate the process, which is slow enough to permit a continuous redistribution of moisture to happen without any change in total moisture content.
(3) X_{sat} is the coefficient most likely to be applied in practical situations and is used in case of fully saturated samples and the equilibrium state is maintained in the specimen.

On the other side, Mitchell (1966) and Neville (1987) divided the thermal expansion into two parts: true thermal expansion and apparent thermal expansion. True thermal expansion mainly occurs due to the kinetic molecular movements. This movement is caused by the force of intermolecular attraction and repulsion and increases due to temperature; however, the apparent thermal expansion takes place due to the development of adsorptive and capillary force resulting from temperature changes.

In fact, the determination of the CTE of cement paste materials at early age is more complicated. This is because at this stage, cement paste is considered as a heterogeneous material and porous medium. Some precautions should be considered during the test such as keeping the specimen fully saturated, estimating the relationship between the autogenous shrinking and thermal deformation, and maintaining the gradient of temperature inside the sample homogenous (Boulay, 2002).

2.8 Thermal deformation of hardened cement paste

The deformation of hardened cement paste that occurs due to temperature change includes an immediate and a delayed part (Wittman & Lukas, 1976; and Day, 1974). The immediate component takes place because of thermal changes and continues until thermal equilibrium is achieved; however, the delayed component happens after the thermal equilibrium is reached (Sabri & Illston, 1982). The moisture contents affect the history of the delayed component and its value as well. The sign of the delayed component may be positive (+ve) or negative (-ve). This is based on whether the sample expands or contracts. It was observed that any increase in temperature leads to an increase in delayed expansion.

The delayed thermal dilatation in partially saturated cementitious materials has been shown by Bažant (1970) to have three components as follows:

(1) pure thermal dilatation,
(2) thermal shrinkage or swelling,
(3) hydrothermic dilatation.

Volumetric changes of cement paste at early age consist of two components of thermal, and autogenous deformations. These deformations are caused by moisture and temperature variations. Maturity methods can be used as a decoupling technique to determine autogenous deformation and thermal deformation separately by employing the degree of reaction indices (Viviani et al., 2007).

2.9 Available techniques to measure coefficient of thermal expansion

Dilatometry and X-ray diffraction are the most common techniques used to measure the coefficient of thermal expansion (CTE) of bulk samples. The dilatometry approach involves measuring the height change of the sample due to temperature variations. Then CTE is given by:

$$\alpha = \frac{\mathrm{L}}{\Delta \mathrm{L}} \Delta \mathrm{t} \tag{2.10}$$

where α is the coefficient of linear thermal expansion; L is the sample height; ΔL is the change in height; and Δt is the change in temperature.

The deformation, occurring due to temperature changes, can be measured by the electrical dial gauges, linear variable differential transformer (LVDT) (Emborg, 1989; Sabri & Illston, 1982), oscillating mirrors, or mechanical dial gauges (Meyers, 1940; Fulton, 1963). The main advantage of an LVDT is that temperature has minor impact on it. In addition, it has no influence on the strain field in contrary to a strain gauge, which requires a thermal correction to eliminate the temperature effects on the signals (Boulay, 2002).

The coefficient of volumetric thermal expansion can be defined as the ratio of the change of volume per unit volume per degree of temperature change. Volume change is expressed as:

$$\mathrm{V}_t = \mathrm{V}_o\,(1 + \beta \mathrm{t}) \tag{2.11}$$

where V_t is the final volume at temperature change; V_o is the initial volume; and β is the coefficient of volumetric thermal expansion.

In general, the coefficient of volumetric thermal expansion for an isotropic material is equal to three times the coefficient of linear thermal expansion where:

$$B = 3\alpha \quad (2.12)$$

Loser et al. (2010) proposed a new method to measure the thermal expansion of cement paste and mortar. Their technique was based on volume measurement in which cement slurry was poured into an elastic membrane then immersed in temperature-controlled buoyancy liquid. A high precision balance was used to monitor the change in the sample weight with the variation of the temperature. Then, CTE could be calculated using Archimedes' principle.

2.10 Factors affecting thermal expansion of cement-based materials

Several factors may affect the coefficient of linear thermal expansion of cementitious materials such as moisture content, cement content, mineralogy, additives, and age. These parameters are briefly discussed in the following sections.

2.10.1 Cement composition

Meyers (1940) observed the impact of the amount of tricalcium silicate (C_3S) on CTE of cement. He pointed out that the greater the quantity of tricalcium silicate, the higher the coefficient of thermal expansion.

In his study, Mitchell (1953) focused on the rule of fineness and its impact on CTE. He found that the CTE of cement paste is sensitive to fineness. The author reported 25% increase in CTE due to the change of cement fineness from 1200 cm^2/g to 2700 cm^2/g. Work conducted by Emanuel and Hulsey (1977) confirmed this concept of increasing CTE with the fineness of cement.

2.10.2 Size of sample

Selecting a proper size of the specimen is very important to precisely determine the coefficient of thermal expansion. For instance, when a small specimen is used, a dimensional change occurs as a result of drying or wetting due to moisture exchange with the surrounding atmosphere. Oppositely, a large

specimen requires enough time to achieve thermal stability, which might cause a significant change in its properties especially at early age.

2.10.3 Age of sample

Loser et al. (2010) investigated the development of the CTE of cement paste at early age by placing the sample in an elastic membrane and submerging it in a silicon oil bath. The temperature was then increased and the variation of the mass was observed. The CTE was obtained from the measured strain due to temperature changes. Test results revealed that the CTE increased in the beginning of the hydration process. When cement paste achieved the final setting, the CTE declined rapidly. After 30 hours, the CTE continued to increase again as a consequence of self-desiccation of cement paste.

2.10.4 Moisture content

The moisture content of the sample controls its coefficient of thermal expansion. The maximum CTE can be achieved at intermediate humidities (60-70%) and decreases when samples are dry or saturated (Meyers, 1951). The same values of CTE have been reported for fully saturated and completely dry samples (Sabri & Illston, 1982).

2.10.5 Additives

Various additives have different influences on the CTE of cement based materials. For example, polymer addition was found to increase the CTE of concrete (Rebeiz et al., 1992). On the contrary, utilizing mineral addition such as fly ash, silica fume, and blast furnace slag led to a reduction in the CTE of cement paste due to the significant influence of these mineral on both porosity and amount of portlandite (CH) formed during hydration (Shui et al., 2010).

2.10.6 Test temperature and heating rate

The range of temperatures used during a thermal expansion test has a minor impact on the CTE of cement paste as long as the test is performed at ambient pressure. However, the temperature has to be above 0 °C to avoid any volume

increases that may occur due to freezing of free water existing inside pore spaces (Dettling, 1964).

2.10.7 Variation of coefficient of thermal expansion with test temperature path: heating up and cooling down

The coefficient of thermal expansion (CTE) obtained during heating up (expansion) is generally lower than CTE reported during contraction due to temperature decrease. This phenomenon is valid only in the absence of plastic deformation (Dettling, 1964). The same conclusion has been drawn by Yamakawa et al. (1979).

2.10.8 Storage conditions

In his paper, entitled thermal coefficient of expansion of Portland cement long-time test, Meyers (1940) confirmed the dependency of thermal expansion on the storage conditions of the specimens. Lower coefficients of thermal expansion were reported for samples stored in water than those specimens stored in kerosene or glycerol. He explained that by the fact that kerosene does not react with cement gel, but water becomes a part of the cement gel structure. Therefore, samples stored in water may be exposed to expansion or contraction even at constant temperatures.

2.11 Materials and methods

2.11.1 Materials specifications

2.11.1.1 Combined X-Ray diffraction analysis

API Class G oilwell cement provided by Multicrete, Edmonton, Canada was used in this study. It was provided in two batches designated as thermal Class G cement and non-thermal Class G cement. Both types were analyzed for bulk and clay XRD mineralogy. The samples were examined using XRD techniques to determine mineralogical composition.

In order to separate the particles less than 3μm in size (clay fraction) from the bulk fraction, the samples were treated in an ultrasonic bath using sodium

metaphosphate as a deflocculating agent. The materials were then centrifuged at different speeds which separated the clay fraction from the bulk materials. The weight fraction was measured for both bulk and clay portions of the samples.

The combined bulk and clay XRD results of Glass G thermal cement shown in Table 2.2 indicate that the sample consists mainly of quartz (47%) [silicon dioxide, SiO_2], with lesser amounts of hatrurite (29%) [calcium silicate, Ca_3SiO_5] and potassium feldspar (13%) [potassium aluminum silicate, $K(SiAl_3O_8)$]. Minor amounts of plagioclase feldspar (7%) [sodium aluminum silicate, $Na(AlSi_3O_8)$], brown millerite (2%) [calcium iron aluminum oxide, $Ca_2(Fe,Al)_2O_5$] and gypsum (2%) [calcium sulfate hydrate, $CaSO_4\ 2H_2O$] are also present. The clay fraction (<3μm) weight is 1.13% of the total rock volume. The clay fraction XRD results (Table 2.2) indicate that the sample consists mainly of quartz (54%), with lesser amounts of hatrurite (34%). Minor amounts of brown millerite (6%), plagioclase feldspar (4%) and potassium feldspar (2%) are also present. No clay minerals were found in the clay fraction of the sample. The analyses indicate that this sample consists mainly of silicon dioxide (quartz) and silicates (hatrurite, plagioclase/potassium feldspars), with minor amounts of calcium iron aluminum oxide (brown millerite). No clay minerals were detected in the sample.

According to data presented in Table 2.2, non-thermal cement consists mainly of hatrurite (83%) [calcium silicate, Ca_3SiO_5], with lesser amounts of brown millerite (12%) [calcium iron aluminum oxide, $Ca_2(Fe,Al)_2O_5$] and minor gypsum (5%) [calcium sulfate hydrate, $CaSO_4\ 2H_2O$]. The clay fraction (<3μm) weight is 0.95% of the total rock volume. The clay fraction XRD results indicate that the sample consists mainly of hatrurite (61%), with lesser amounts of brown millerite (24%) and gypsum (15%). No clay minerals were found in the clay fraction of the sample. The analyses indicate that this sample consists mainly of calcium silicate (hatrurite), with minor amounts of calcium iron aluminum oxide (brown millerite) and calcium sulfate hydrate (gypsum). No clay minerals were detected in the sample.

2.11.1.2 Particle size analysis

Two solid samples (one for non-thermal cement and one for thermal cement) have been analyzed for particle size distribution. The samples were analyzed using a “Coulter LS” Laser Diffraction particle size analyzer. The results of the particle size analysis are summarized in

Table **2.3** and illustrated graphically in Figure 2.3.

2.11.2 Specimen Preparation

The cement paste specimens used in this research were made of distilled water and cement and no additives were used. The dry cement was weighed and blended uniformly then mixed with distilled water in a mechanical mixer at 4000 rpm/min ±200 rpm/min for 15 ± 1 second followed by a motor speed of 12,000 rpm/min ± 500 rpm/min for 35 ± 1 second. Cement slurries were poured into brass cylindrical molds then compacted at 3 layers using a pudding rod. Molds were placed in pressurized curing chambers (model No. 1910, Chandler Engineering) to cure the samples under 9 °C and 3 MPa for different intervals. Shortly before the end of curing time, pressure and temperature were decreased to ambient conditions. Then, cylindrical samples were removed from curing chamber and ground to make parallel ends. The above steps were applied for preparation of all specimens tested in the current research. Detailed procedure for sample preparation can be found in Appendix A.

Table 2.2 Summary of XRD Analysis

Sample ID	Type of Analysis	Weight %	QTZ[a]	Plag[b]	K-Feld[c]	Clay[d]	Hatrurite[e]	Brown[f]	Gyps[g]	Total Clay
1 Thermal Class G Cement	Bulk Fraction:	98.87	47	7	13	0	29	2	2	0
	Clay Fraction:	1.13	54	4	2	0	34	6	0	0
	Bulk & Clay:	100	47	7	13	0	29	2	2	0
2 Non-Thermal Class G Cement	Bulk Fraction:	99.05	0	0	0	0	83	12	5	0
	Clay Fraction:	0.95	0	0	0	0	61	24	15	0
	Bulk & Clay:	100	0	0	0	0	83	12	5	0

a. Quartz; b. Plagioclase feldspar; c. Potassium feldspar; d. Clay e. Hatrurite f. Brown millerite; g. gypsum.

Table 2.3 Summary of particle size analysis results

Sample Description	D_{50} [%]	Range [µm]
Thermal Cement	21.51	0.393 – 203.5
Non-Thermal Cement	22.35	0.393 – 140.1

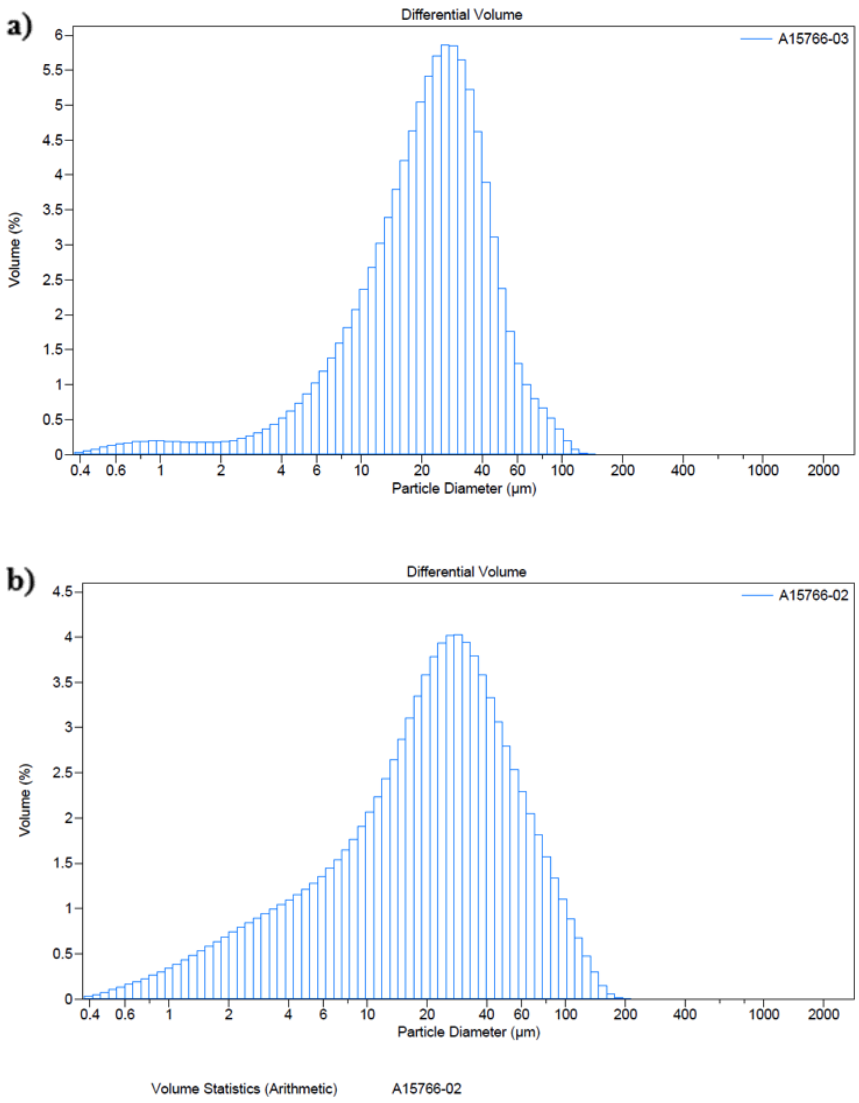

Figure 2.3 Particle size distribution: a) non-thermal cement; b) thermal cement

2.11.3 Chemical shrinkage test procedure

A triaxial cell was used to evaluate the range of volumetric shrinkage that could occur to cement slurry with different water cement ratios (w/c) under the placement conditions in SAGD operation. Firstly, cement slurries were poured and compacted in three equal layers into a Viton membrane that was fastened to the bottom endcap of the triaxial cell. Subsequently, the cell was filled with water and placed inside an oven, where temperature was 9 °C and the temperature fluctuations were kept within 1 °C. Cell pressure pump has been used to apply a confining stress of 3 MPa which is equivalent to in-situ stress. During the test, pump volumes,

temperature, and time were precisely monitored and recorded. Then, the chemical shrinkage was calculated from the volume changes of the cell pressure pump. After the tests were terminated, the specimens were taken from the cell and visually inspected. Additionally, Scanning Electron Microscope test (SEM) was performed on some samples for more details about microstructure evolution.

2.11.4 Thermal expansion test procedure

After curing cement paste for 28 days, the sample was inserted inside a high temperature oedometer cell (Figure 2.4). This cell is made of stainless steel and consists of two parts connected together with six steel tie-bolts. A linear voltage displacement transducer (LVDT) was vertically attached to a loading piston to capture the vertical deformation of the specimen. A hydraulic ram was utilized to push this loading piston down to apply vertical load on the sample. The cell has two ports to apply backpressure. The top pore pressure was applied through the upper port while the lower port was used for bottom pore pressure. An ISCO pump was used for the application of backpressure. Two porous stones were used at the top and the bottom of the sample to develop a uniform distribution of backpressure at both faces of the specimen.

Four heaters were inserted symmetrically inside the wall of the lower part of the cell to heat the system. The temperatures of the system (the oedometer cell and the sample) were monitored by two J-type thermocouples. The first thermocouple was inserted in a hole that exists in the bottom porous plate and is used mainly to capture the temperature of the specimens. The second thermocouple was placed in the oedometer cell wall to monitor the cell temperature and was connected to the temperature controller. The latter responds to the feedback received from the thermocouple. Accordingly, it turns the heating system on and off to maintain the temperature of the system at its set-point temperature. After placing the sample inside the cell and before starting the heater, the cell was wrapped with insulation to eliminate the variation of temperature during the test. Confining stress and backpressure were increased simultaneously to 3000 kPa and 2000 kPa respectively in 200 kPa increments. Then, the sample was kept under

these pressures for 24 hours for saturation. Afterwards, the heater was turned on to reach the target temperature. It is well known that the CTE of water is higher than that of cement paste; this means that fluid inside pore spaces will expand more than cement particles once the temperature is increased, resulting in inaccurate measurements. Therefore, the specimens were heated up very slowly with a rate of 10 °C per hour to allow the excess pore pressure to dissipate and to provide a uniform temperature distribution throughout the specimen. Thereafter, the samples were maintained at the target temperature for sufficient time to reach a steady-state condition before moving to the next heating cycle. The coefficients of thermal expansion of two samples were measured for each w/c and the average value was calculated.

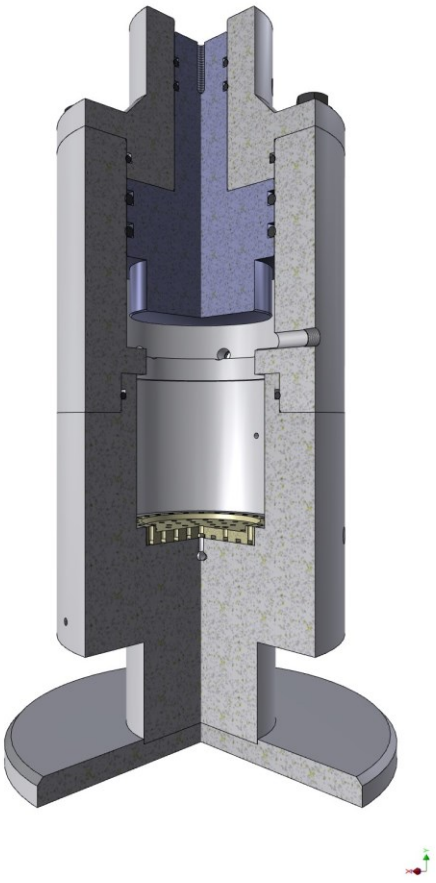

Figure 2.4 Cross section through the oedometer cell

2.11.5 Calibration test

A dummy sample made of Aluminum was used to calibrate the oedometer cell and to obtain the linear coefficient of thermal expansion for the entire setup. This was performed by using the Aluminum sample in the same setup over the same temperature range, as used in the real test. The theoretical CTE of the Aluminum and the one obtained from the experiment were compared to estimate the expansion of the system.

2.12 Results and discussion

2.12.1 Chemical shrinkage test results

In this study, a series of chemical shrinkage tests were conducted on samples made of Class G non-thermal cement with water cement ratio of 0.4, 0.5, and 0.6, respectively. These values were selected to cover the uncertainty occurring in the field. Therefore, the impacts of cement type and water cement ratio on the chemical shrinkage were examined. To avoid any impact of changing the total volume of water in cement slurry, cement pastes with different w/c were prepared by keeping the amount of water constant while the cement content were modified to achieve a certain w/c. The tests were run for about 80 hours. Each test was performed twice using the same type of cement with the same w/c to ensure the repeatability of the tests. The final values and the curves shown in this study represent the average result obtained from the two test results. The experimental program plan of chemical shrinkage test can be found in Appendix C.

Figure 2.5 depicts the rate of chemical shrinkage as a function of time. As shown in these curves, chemical shrinkage development can be divided into different stages. At the beginning, chemical shrinkage initially increased due to the rapid dissolution of cement particles, accompanied with the reaction between the aluminate phase and the water. In the second stage, a continuous chemical shrinkage was observed with lower rate due to the reduction of the rate of hydration during the induction period. Therefore, limited amounts of reaction products were formed. After 8 hours, chemical shrinkage started to pick up again and increased

rapidly as the reaction rate increased until it reached the peak. Then the curve decreased again until the rate of chemical shrinkage started to plateau.

Also, it was noticed that the rate of chemical shrinkage had the tendency to decrease earlier in case of low w/c pastes due to the rapid formation of cement matrix. The transition state, from liquid viscoelastic to the solid elastic stage, is more gradual and requires less time for pastes having lower w/c than those with higher w/c. These results support the close relationship between chemical shrinkage and hydration kinetic.

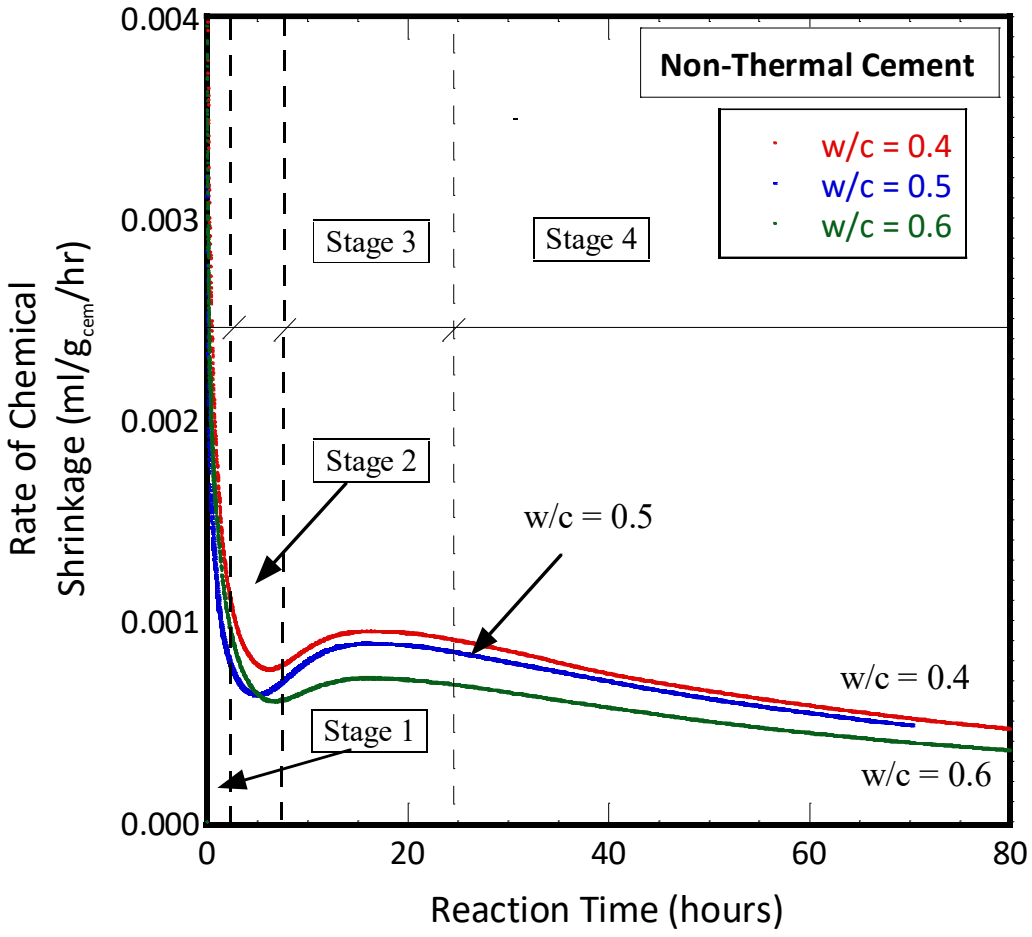

Figure 2.5 Rate of chemical shrinkage

Figure 2.6 presents the chemical shrinkage curves for cement paste made of non-thermal cement with different w/c during the observation time. These figures reveal that regardless of the w/c of the paste, all curves show the same trend.

However, the curve of cement paste with lower w/c started to flatten out earlier. This can be explained by the earlier development of connectivity of solid phases, which leads to an increase in the cement matrix formation. Looking closely at chemical shrinkage curves, one can notice the link between chemical shrinkage and hydration kinetics. This concept has been used by several authors to investigate the hardening process through monitoring the chemical shrinkage of the sample (Knudsen & Geiker, 1982; Geiker, 1983).

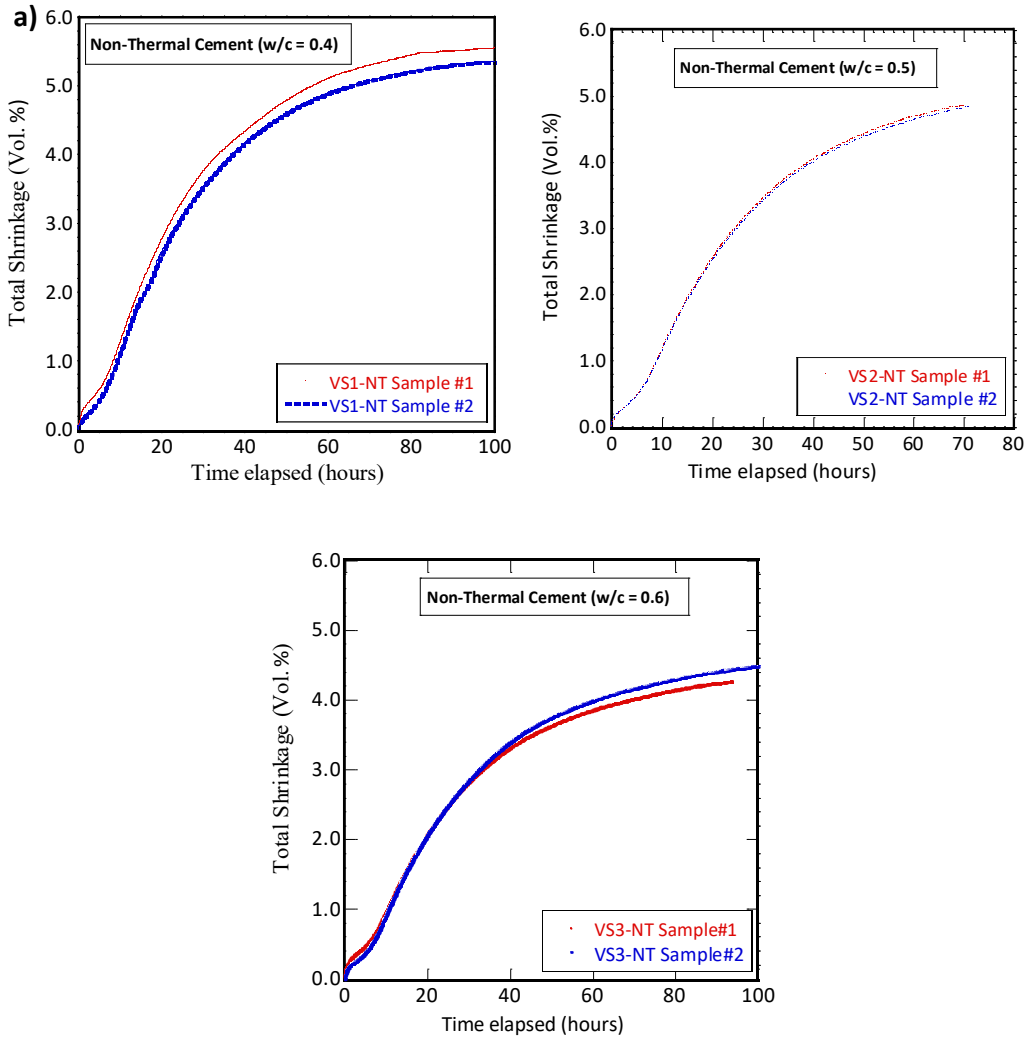

Figure 2.6 Total chemical shrinkage (vol%) versus time for non-thermal cement paste: a) w/c = 0.4; b) w/c = 0.5; c) w/c = 0.6

To grasp more insight on the relationship between cement paste chemical shrinkage and cement content, a comparison between the measured chemical shrinkage of specimens with different w/c at different times is presented in Figure 2.7. The dependency of volumetric shrinkage on cement content is clearly demonstrated in Figure 2.7. It can be observed that there are noticeable differences between the chemical shrinkage of cement paste made with different w/c. As shown in Figure 2.7, the higher the water cement ratio, w/c, the lower the amount of the shrinkage. This can be attributed to the existence of finer pores in cement matrix of samples with lower w/c. In addition, it can be seen that during the first few hours, the chemical shrinkage for all mixtures are quite similar regardless of w/c. Then, the discrepancy between the three curves started to be evident at the later age where the impact of w/c ratio on chemical shrinkage is much higher than the early stage.

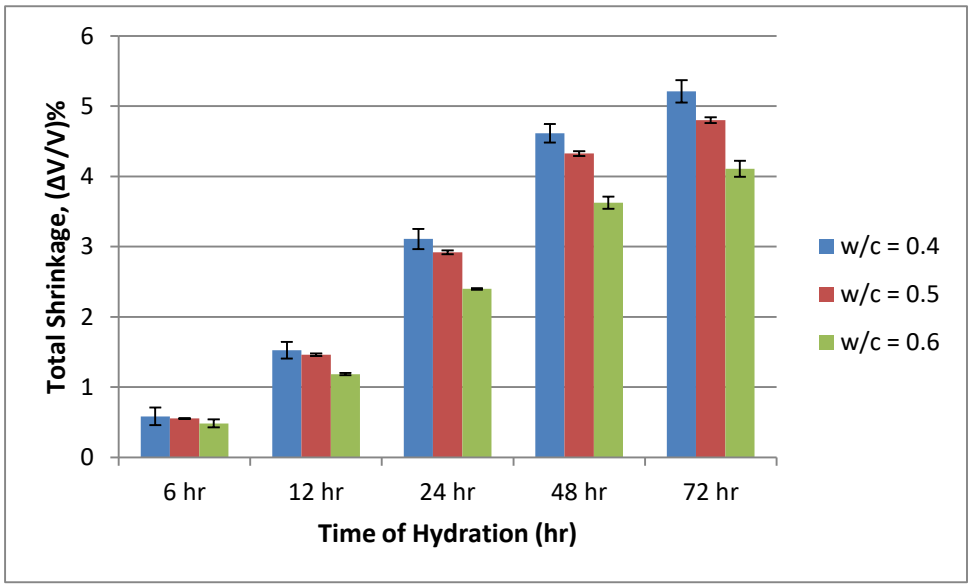

Figure 2.7 Comparison between chemical shrinkage (vol%) of cement pastes with different w/c ratio at several ages.

As shown in Figure 2.8, a good correlation between volumetric shrinkage and cement content was found. The fitting line is forced to pass through zero because at the zero-cement content, no volumetric change would occur. Other authors have reported similar correlations.

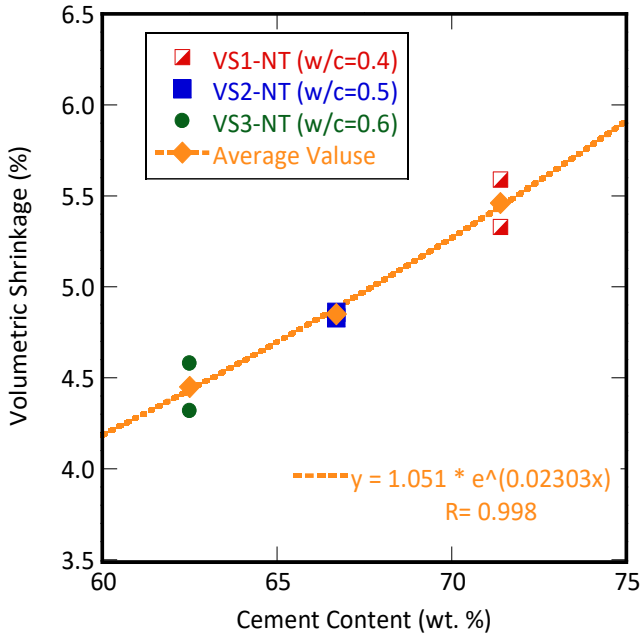

Figure 2.8 The correlation between volumetric shrinkage and cement content

In general, different authors had different opinions about the relationship between w/c and shrinkage behavior. Charron et al. (2002) mentioned that the impact of water cement ratio on cement paste deformation is highly dependent on the experimental procedures. On the other hand, Justnes et al. (1996) stated that there is no direct link between water cement ratio and chemical shrinkage.

To clarify the impact of cement type on its chemical shrinkage behavior, the chemical shrinkage for non-thermal cement and thermal cement pastes with w/c of 0.5 are compared in Figure 2.9. As shown in Figure 2.9, there is a significant difference between chemical shrinkage obtained for these two types of cement. The shrinkage of non-thermal cement was found to be higher than thermal cement. The difference may be attributed to the relatively finer particles existing in thermal cement compared to non-thermal cement, as is evident from their particle size distribution curve given in Figure 2.3, resulting in a slightly different hydration kinetic mechanism of both types of cement pastes. In addition, this is evidence on the significant impact of silica flour on the volume change behavior of cement paste during the hydration process. This influence could be due to the fact that thermal

cement needs more water during the solidification process to hydrate the silica flour particles which have larger surface area than cement particles.

Finally, it is worth mentioning that chemical shrinkage of cement paste is sensitive to pore structure. Sabins and Sutton (1991) stated that the presence of empty contraction pores is responsible for the occurrence of 97.5-99% of the total chemical shrinkage.

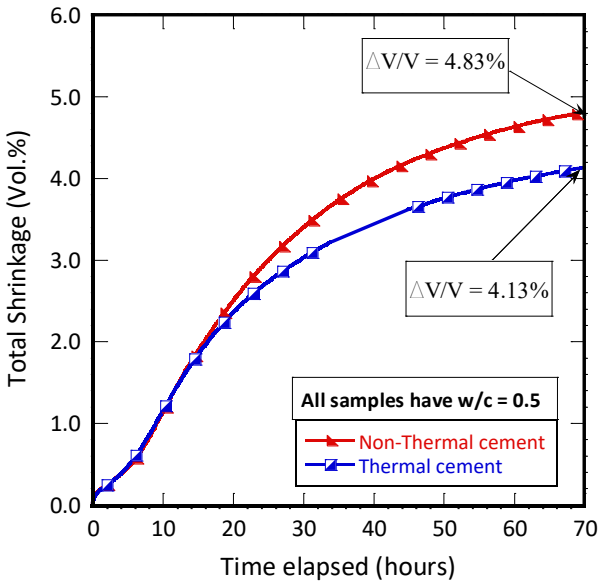

Figure 2.9 Comparison between chemical shrinkage of thermal and non-thermal cement

2.12.2 Thermal expansion test results

The thermal expansion coefficients (CTEs) of class G thermal and non-thermal cement paste were measured under vertical effective confining stress and backpressure of 3 MPa and 2.5 MPa respectively. Linear strain was monitored over the range 20 °C to 180 °C where no lateral strains were allowed. Sample temperature was increased slowly to avoid the expansion of the fluid inside pores and to allow water to flow out of the sample. Then, thermal deformation was

measured after the system achieved a steady state condition. The experimental program plan of thermal expansion test can be found in Appendix C.

The measured thermal deformations as a function of temperature are shown in Figure 2.10. These figures reveal that the relationship between thermal strain and the temperature variation shows some non-linearity. This can be attributed to the changes happening to C-S-H crystallites due to temperature.

Test results showed that the coefficient of thermal expansion of cement paste varies with w/c. This variation can be explained by the effect of the amount of water, available for reaction with clinker, on the porosity and on the quantities of portlandite (CH) and C-S-H crystallites formed during hydration. According to the theory of thermo-elasticity, porosity does not affect the CTE of a porous medium as long as the material has a homogenous matrix (Mushkelishvili, 1963). However, recent studies proved the relationship between the CTE of cement paste and the porosity of the sample. The CTEs of cement increased with porosity for undrained condition (Ghabezloo et al., 2009). Also, the change in permeability with w/c could be another explanation for this variation in the CTE of cement paste. The latter is dependent on the permeability. The higher the permeability, the lower the thermal expansion due to the rapid flow of the pore fluid outside of the sample. In general, when cement paste is exposed to temperatures of 110 °C and above, the permeability increases due to the formation of alpha di-calcium silicate hydrate phase, which has a higher density (Nelson & Guillot, 2006).

Moreover, test results reveal that the sample made of thermal cement expanded more than the non-thermal cement specimen. The average CTE of the hardened thermal cement increased to be 10.3 $x10^{-6}$ $ºC^{-1}$. This probably results from the impact of temperature on the cement matrix. Generally, high temperature causes deterioration of non-thermal cement paste grains resulting in a volume reduction. Also, the presence of silica flour in the thermal cement powder might affect its permeability, causing a change in CTE. In brief, the knowledge of CTE of cement paste is essential to evaluate the cement sheath integrity, especially in operations where a sudden change in temperature is expected such as SAGD and CSS. To

accurately determine CTE of cement paste, some measures have to be taken into consideration. For example, cement slurry must be cured at field conditions due to the impact of curing temperature on the CTE.

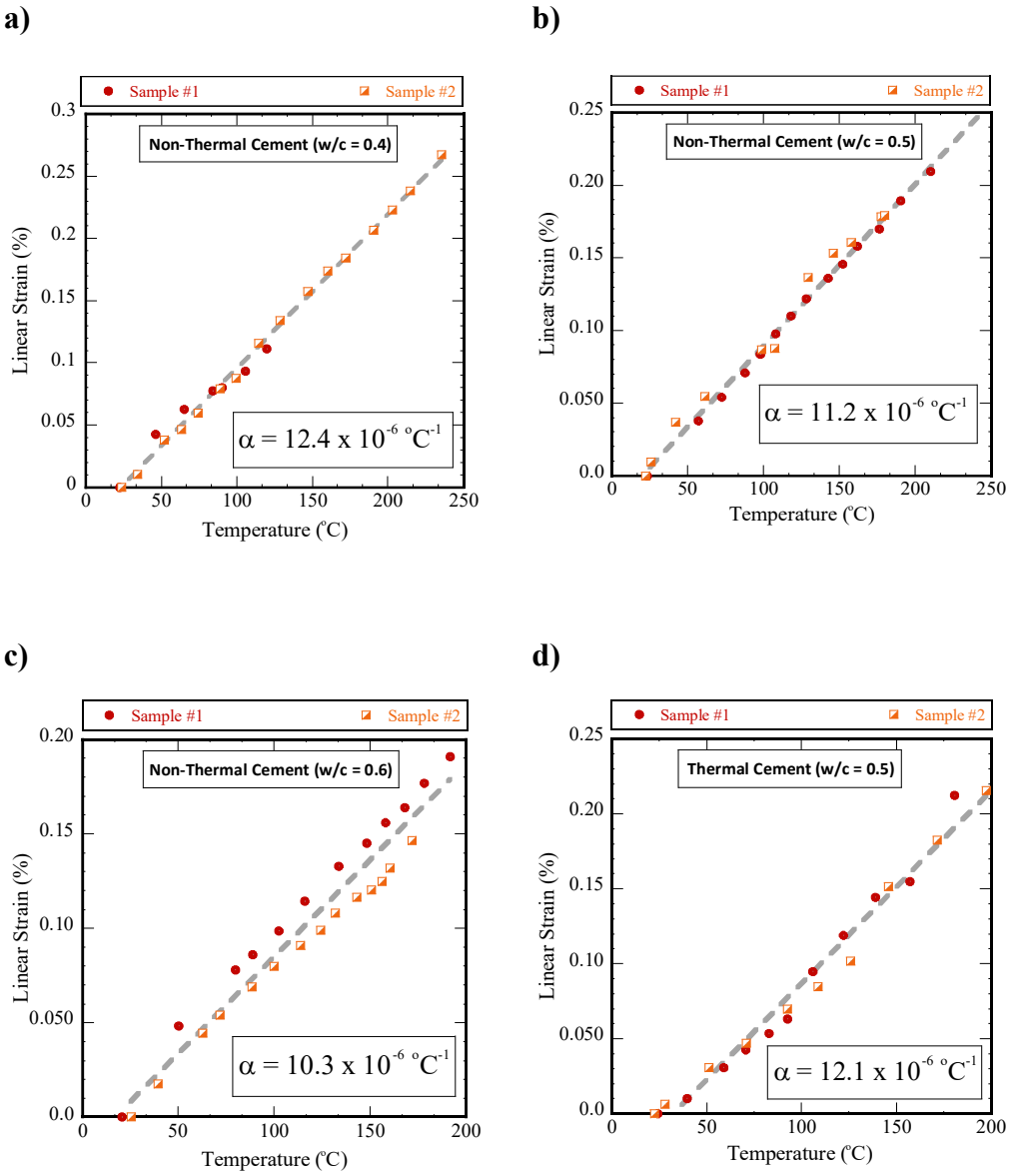

Figure 2.10 Linear strain vs. temperature a) non-thermal cement w/c = 0.4 b) non-thermal cement w/c = 0.5 c) non-thermal cement w/c = 0.6 d) thermal cement w/c = 0.5

2.12.3 Microstructure observation

An environmental scanning electron microscope (ESEM) was used to investigate the microstructure of both thermal and non-thermal cement pastes obtained from thermal shrinkage test. In this technique, an image of the sample surface can be obtained by a fine probe of electrons, which is focused on the sample. This technique was firstly used by Scrivener and Pratt (1984) to study cement paste and concrete.

ESEM includes two detectors. The first one is a detector of the secondary electron (SE) that has energies of tens of eV. A three-dimensional topographical image can be obtained by SE where steep and flat surfaces can be distinguished by its brightness. The second one is a detector of backscattered electrons (BSE) which is mainly used to investigate the variation of chemical compositions through the sample as the degree of brightness is related directly to the atomic number.

Figure 2.11 provides an illustration of backscatter SEM image of thermal and non-thermal cement paste with w/c of 0.5. These images were taken at relatively high magnification (approximately 5000x). The dimensions of the images are about 44 μm in height and 62.5 μm in width with an average area of 2750 μm^2. As mentioned by Diamond (2004), the bright zones represent unhydrated cement particles, which consist of Alite and Belite. On the other hand, hydrated cement grains can be distinguished with dark areas that have a uniform gray color. As we can see, these hydrated grains grow over unhydrated grains. Two types of reaction products can be observed, namely the inner and outer products. The outer products can be seen as finer particles formed in the pore space between the inner products. It is remarkable that the size of unhydrated grains is bigger than the size of hydrated grains. In addition, the existence of fibrous particles, connected together to form a cross-linked network, can be noticed.

a) b)

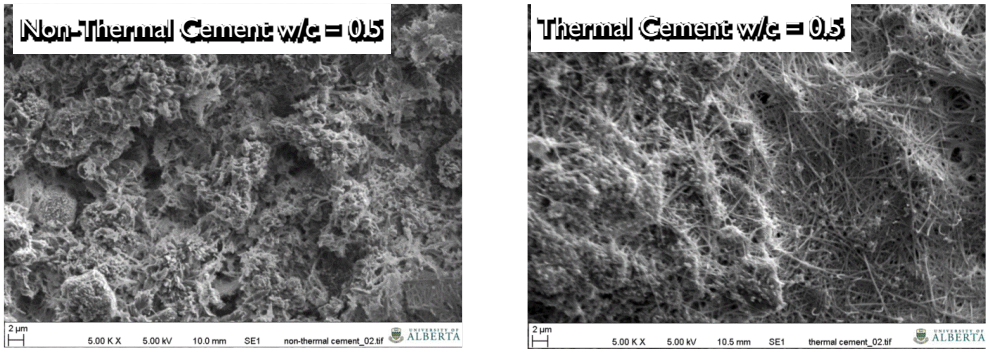

Figure 2.11 SEM image (5000X) for Class G cement of w/c = 0.5: a) Non-thermal cement; b) Thermal cement

2.13 Summary and conclusion

The phenomenon of chemical shrinkage is a concern in oilwell cement pastes. It may lead to uncontrolled leakage due to the reduction of the hydrostatic pressure of the cement slurry column resulting from cement volume changes. Accordingly, a new approach based on utilizing the conventional triaxial cell was developed to evaluate the range of volumetric shrinkage that could be happening for API Class G cement during the solidification stage with different water cement ratio (w/c) under the placement conditions in SAGD operation.

A series of tests was performed on thermal and non-thermal cement. Cement specimens were cured at temperature of 9 °C and pressure of 3 MPa. It was found that the new method can be used to represent accurately the real behavior of cement shrinkage during hydration under applying pressure. The proposed technique proves to have a good repeatability. It was noted that thermal cement experiences less shrinkage than non-thermal cement. The volumetric shrinkage was found to be related to water cement ratio and cement content in the slurry. The amount of shrinkage increases as w/c decreases. A new correlation between shrinkage and cement content was proposed. The amount of shrinkage recorded for cement samples was close to values reported in the literature.

It can be concluded that better understating of the factors affecting the cement shrinkage behavior leads to obtain the suitable slurry design required to minimize gas migration through the cement annulus.

In the second part of this chapter, a series of tests were conducted inside the oedometer cell. The testing program was designed mainly to study the coefficient of the thermal expansion of cement paste with different w/c. During the test, the back pressure was maintained at 2500 kPa while confining pressure was kept at 3000 kPa. Temperature was increased in 10 °C to 25 °C increments. The thermal expansion behavior was examined over a temperature range of 20 °C to 180 °C. Two types of cement and three levels of cement content were examined. Test results revealed that w/c has some influence on the thermal behavior of cement paste. The coefficients of thermal expansion of samples made with different w/c are slightly different from each other. The lower CTE was recorded for samples having a higher w/c.

Moreover, the thermal properties of hardened cement paste were observed to be significantly affected by cement formulation. Samples made of thermal cement had higher thermal expansion than non-thermal cement specimen did. The reported values of the coefficient of thermal expansion (α) for thermal and non-thermal cement paste with w/c of 0.5 were 1.12 x 10^{-5} $°C^{-1}$ and 1.28 x 10-5 $°C^{-1}$, respectively. In short, heating rates should be chosen carefully to avoid any influence from the water expansion on test results. It is highly recommended to determine the CTE during several cycles of heating and cooling, to completely understand the impact of test temperature path on the results. Furthermore, the test should be performed over a wide range of temperatures to cover the operation conditions in SAGD process.

Chapter 3 : Effect of High Temperature on the Mechanical Behavior of Cement Paste

3.1 Introduction

Cement paste gains its compressive strength due to the growth of hydrated calcium silicate crystalline structures. Any increase in water cement ratio decreases the bond strength of these crystals, and as a result, cement compressive strength decreases (Lea, 1971). Cement compressive failure occurs when the cement rupture stress exceeds uniaxial compressive strength. This typically happens when a cement sheath is subjected to high radial stresses or when cement encounters major changes in wellbore temperature where the formation has a relatively high Young's modulus (Al-Suwaidi et al., 2008). The development of compressive strength mainly relies on curing temperature and pressure. Elevated temperatures can have an undesirable impact on the long-term durability of cement.

In fact, the impact of high pressure and elevated temperature on the behavior of cement has been area of sustained interest. The performance of cement under these conditions was investigated experimentally (Handin, 1965; Thiercelin et al., 1998), analytically (Thiercelin et al., 1997), and numerically (Di Lullo et al., 2000). Many studies investigated the behavior of different classes of oilwell cements at diverse temperature and pressure conditions.

John Handin (1965) was one of the first researchers who raised the fact of the dependency of cement behavior on curing schedules. The author used the results of triaxial compression tests to study the impact of temperature, confining, and pore pressure on the ultimate strength of cement. He mentioned that the ductility of cement decreased due to heating. In addition, a linear relationship between cement strength and confining pressure was reported.

Noik and Rivereau (1999) examined the behavior of four types of Class G cement with different silica contents. They found that the compressive strength of cement samples increased as silica increased in cement slurry at 180 °C. To assess the impact of silica sand, another set of experiments was performed at 120 °C, 140

°C and 180 °C on cement slurry with silica sand. The initial compressive strength decreased with the increase of temperature. Sample compressive strength was stable for 6 months and then a reduction of strength was observed, accompanied with an increase in permeability. Jennings (2005) compared three cement systems: bentonite extended, Class G, and a cement blend containing hollow ceramic spheres (HCS). All samples were cured at 103 °C and 20.7 MPa. HCS showed severe compressive strength retrogression. The value of compressive strength declined from 19.7 MPa after seven days to 3.7 MPa after one year. Young's Modulus decreased for all three cements during the first 6 months followed by an increase in Young's Modulus for bentonite extended cement for another 6 months. Both HCS and bentonite extended showed an increase in permeability with time.

Le Roy-Delage et al. (2000) obtained compressive strength, modulus of rupture, elastic parameters of cement from three-point bending tests and compression tests. Young's modulus was estimated based on the linear part of the stress-strain curve. All the samples were cured under 20.7 MPa and at 77 °C or 114 °C for three days. Then samples were cooled down and kept saturated until the day of the test.

James and Boukhelifa (2006) experimentally determined compressive strength, tensile strength, Young's modulus, and Poisson's ratio of cement by conducting UCS and Brazilian tests. Cement samples were cured at 200 °C; however, the tests were performed at ambient temperature. The authors mentioned that in most cases an elastic constitutive model can be used to describe the cement behavior under downhole conditions.

Al-Yami et al. (2008) examined low-density cement (LDC) at both shallow and deep conditions. The first set of specimens was cured at 65 °C and 12.4 MPa and the curing condition for the second set was 127 °C and 20.7 MPa for 3 months. The average density of these slurries after 24 hours was 1.44 g/cm^3. The compressive strength after three months for shallow and deep conditions were 15.1 MPa and 9.9 MPa, respectively, which are higher than the recommended value of 3.45 MPa required to support the casing (Stiles, 1997).

As discussed above, it is clear that, recent and past efforts related to the impact of pressure and temperature on cement performance have focused on curing cement specimens at high pressure and elevated temperature and then conducting the tests at room temperature. No research has been performed on mechanical behavior of non-thermal cement cured at in-situ conditions and tested at elevated temperatures. In addition, no study gave a complete set of the cement mechanical properties under the effect of pressure and temperature variations as most research studies defined cement using a linear elastic mechanical behavior. Moreover, no study has discussed the failure mechanism of non-thermal cement paste when it encounters SAGD operation conditions. This lack of a reasonable failure criterion increases the difficulty of predicting the real behavior of non-thermal cement under field conditions. Consequently, the research reported in this chapter is aimed at studying the variations of the mechanical behavior that may occur when cement paste is subjected to elevated temperatures. This has been achieved by determining the impact of temperature on the key cement properties, including compressive strength, tensile strength, Young's modulus, cohesion, and friction angle. In this chapter, results of an investigation of compressive strength of cement paste are firstly presented, then the experimental results from Brazilian tests are presented. The shear behavior of cement is also analyzed and discussed in detail based on the triaxial test results. Furthermore, a comparison between the behavior of thermal and non-thermal cements is provided. Finally, a set of empirical relations, describing the influence of temperature on mechanical behavior of non-thermal cement, were derived. In the first series of the tests, experiments were conducted at 5 °C and the results were used as a benchmark to evaluate the effect of temperature on the behavior of cement. Afterwards, experiments were performed at elevated temperatures of 60 °C, 120 °C, and 180 °C.

3.2 Factors affecting cement paste strength

In general, the strength of a material refers to its ability to resist the applied force without a failure in plastic strain. In particular, cement paste strength is commonly characterized by its compressive, tensile, flexural, and shear strength.

Multiple researches have been performed to study the mechanical properties of cement paste, and to investigate the different factors which may affect its strength. Among these parameters are chemical composition, particle size distribution, fineness, and age. The next sections highlight these factors.

3.2.1 Chemical composition

As mentioned before, clinker is mainly composed of four compounds; namely tricalcium silicate (C_3S), dicalcium silicate (C_2S), tricalcium aluminate (C_3A), and tetracalcium aluminoferrite (C_4AF). Each phase has its own influence on early-age and later-age strength of cement paste. Generally, both tricalcium silicate (C_3S) and dicalcium silicate (C_2S) play an important role in the development of compressive strength in cement paste. However, the impact of C_3S is greater than C_2S. Utilizing cement with a higher amount of C_3S causes cement paste to gain more strength in a short time, leading to a reduction in the later strength. On the other side, C_3A affects the evolution of strength at early-ages while C_4AF has insignificant influence on cement strength (Taylor, 1977; Neville & Brooks, 1987).

Troxell et al. (1968) mentioned that the impact of chemical composition is not absolute. However, it is relative and depends on the fineness of the cement. They observed that using finer cement particles results in higher strength specimens and the effects of chemical composition influence the rate of strength development.

Zhang et al. (1995) proposed a new term called chemical compounds characteristic (FCH) which can be used to predict the cement paste strength at 3, 7, and 28 days based on chemical composition and particle size. The correlation between FCH and chemical composition can be written as:

$$FCH = C_3S + C_2S + C_3A - C_4AF \quad (3.1)$$

Then cement strength at different time can be obtained from the following equations:

$$3D = 0.3659\ FCF + 0.5577\ S8 - 26.87 \quad (3.2)$$

$$7D = 0.6476\ FCFI + 0.4868\ S8 - 36.01 \quad (3.3)$$

$$28D = 0.5564\ FCH + 0.3049\ S32 - 28.05 \quad (3.4)$$

where *3D*, *7D*, and *28D* are the compressive strength (MPa) of concrete at 3, 7, and 28 days respectively; *S8* is the cumulative passing size of 8 μm in cement product (%); and *S32* is the cumulative passing size of 32 μm in cement product (%).

3.2.2 Particle size distribution

Particle size distribution has classically been determined by sieve analyses and the sedimentation process. Increasingly, laser diffraction has became a more popular technique in this area due to its simplicity. In addition, this method gives a full picture of all particle sizes existing in cement powder. There are two approaches to measure particle size using laser diffraction either as a dry powder dispersed in air, or as suspension dispersed in a solvent such as methanol. In all cases, the particle size distribution is determined based on the diffraction pattern caused by the scattering of the laser light off of the particles.

Cement powder contains a wide range of particle sizes, which varies from a few microns up to hundreds of microns in size. This disparity in sizes greatly affects the rate of early hydration. Generally, fine particles react with water faster than coarse particles. For instance, a small particle hydrates completely in a few hours while large particles may not become fully hydrated even if there is still water available for reaction. A study conducted by Zhang and Napier-Munn (1995) on the effect of particle size distribution on cement paste strength, showed that the development of cement paste strength at early age (3 to 7 days) is largely dependent on the proportion of particles having size of 8 μm. If obtaining a higher 28 day strength is required, cement powder with a greater amount of 32 μm particles should be used.

3.2.3 Fineness

Usually, the term specific surface area is used to describe the fineness of cement particles. Specific surface area can be defined as the total surface area in square metres of cement particles in a unit weight of cement. The greater the

specific surface, the finer the cement particles. The surface area can be determined experimentally by the Blaine air permeability test. In this test, a certain amount of cement powder is placed in a special permeability cell of known area and volume to fill it. Then a predetermined volume of air is allowed to pass through the cement powder under a specific pressure gradient. The surface area can be obtained by measuring the rate at which air passes through the powder using the following equation:

$$S = \frac{k}{\rho} \chi \frac{\sqrt{e^3}}{(1-e)} \chi \frac{\sqrt{t}}{\sqrt{0.1\eta}} \quad (cm^2.g^{-1}) \tag{3.5}$$

where k is the apparatus constant; e is the porosity of cement; t is the measurement time (sec); ρ is the density of cement (g.cm^{-3}); and η is the viscosity of air at the test temperature.

The Blaine fineness of Portland cement varies from 300 – 500 m^2/g. Several formulae, used to estimate the surface area of cement, can be found in literature, for instance, an equation proposed by Kuhlmann et al. (1985) to describe the relationship between surface area and particle size distribution.

$$S_m = 807 + 1.2\ O_m \tag{3.6}$$

where O_m is the measured surface area (cm^2/g); and S_m is the surface area calculated from one of the following equations (cm^2/g):

$$S_m = \frac{6}{\rho} \sum_{i=1}^{n} \frac{1}{x_m} \Delta Q\,(x_i, x_{i+1}) \tag{3.7}$$

where ρ is the cement density (g/cm^3); X_m is the geometric mean size of x_i and x_{i+1} (cm); $\Delta Q\ (x_i\ ,\ x_{i+1})$ is the difference of the cumulative mass distribution of the i^{th} and $i+1^{th}$ particle size (%); and n is the number of size fractions.

Sumner et al. (1989) suggested the following equation to obtain cement surface area:

$$SSA = \sum_{i=1}^{n} \frac{6}{d_i \rho}\left(\frac{w_i F}{100}\right) \left(\frac{m^2}{kg}\right) \tag{3.8}$$

where w_i is the weight percentage in size fraction; F is the surface shape factor (between 1.1 and 1.15); d_i is the geometric mean size of particle size fraction i (cm); ρ is the apparent particle density (kg/m^3); and n is the number of size fractions.

Zhang and Napier-Munn (1995) used the linear regression to develop a relationship between the surface area and the particle size distribution. This correlation was derived from 144 data sets and can be written as:

$$O_s = 0.874 S_s - 42.74 \tag{3.9}$$

$$S_s = \frac{6}{\rho}\sum_{i=1}^{n}\left(\frac{w_i}{x_i}\right) \tag{3.10}$$

$$x_i = \left(\frac{\left(x_h^2 + x_j^2\right) + (x_h + x_j)}{4}\right)^{1/3} \tag{3.11}$$

where O_s is the observed surface area (m^2/kg); S_s is the surface area (m^2/kg) calculated by a formula given by Herdan (1953) in terms of a harmonic mean size x_i (Eq. (3.12)); x_h, and x_j are the upper and lower size of a size interval (cm); ρ is the density of the material (kg/m^3); and w_i is the weight fraction of size i.

Actually, fineness is one of the factors that affect early and later strength of cement-based materials. However, the impact of fineness is more significant at early age and decreases with time. It was reported that the concrete strength increased by 2% after 7 days and by 1% after 28 days due to an increase of 1% in surface area (Troxell et al., 1968). This can be attributed to the influence of the amount of the available surface area for reaction on the rate of formation of hydration products.

3.2.4 Age

The strength of cement paste is related to its age. Generally, cement paste gains more strength with time due to continued hydration. However, the rate of the change in strength is faster at the beginning and decreases with time. Most research studies conducted on this topic have focused mainly on concrete. Some authors tried to find a correlation between early and later concrete strengths. One of these equations, which describes the strength as a function of age, is the one proposed by Shetty (2006) and can be written as follows:

$$f_{c28} = k_2(f_{c7})^{k_1} \tag{3.12}$$

where f_{c7} and f_{c28} are the strength at 7 and 28 days respectively; k_1 is a coefficient which varies from 0.3 to 0.8 depending on cement type and curing condition; and k_2 is a coefficient which varies from 3 to 6 depending on cement type and curing condition.

As can be seen in Figure 3.1, each phase of cement clinker has a different rate of strength increase with time. C_3S achieved a high value of early strength, which increased gradually with time. Although the initial strength of C_2S was much lower than those of C_3S, both of them had almost the same strength after one year. This is because the strength development of C_2S increased more rapidly than C_3S. On the other hand, both C_3A and C_4AF showed a low strength even after one year.

In general, the relationship between cement paste strength and its age or the relationship between early age and later strength is dependent on many factors such as chemical composition, w/c, temperature and fineness.

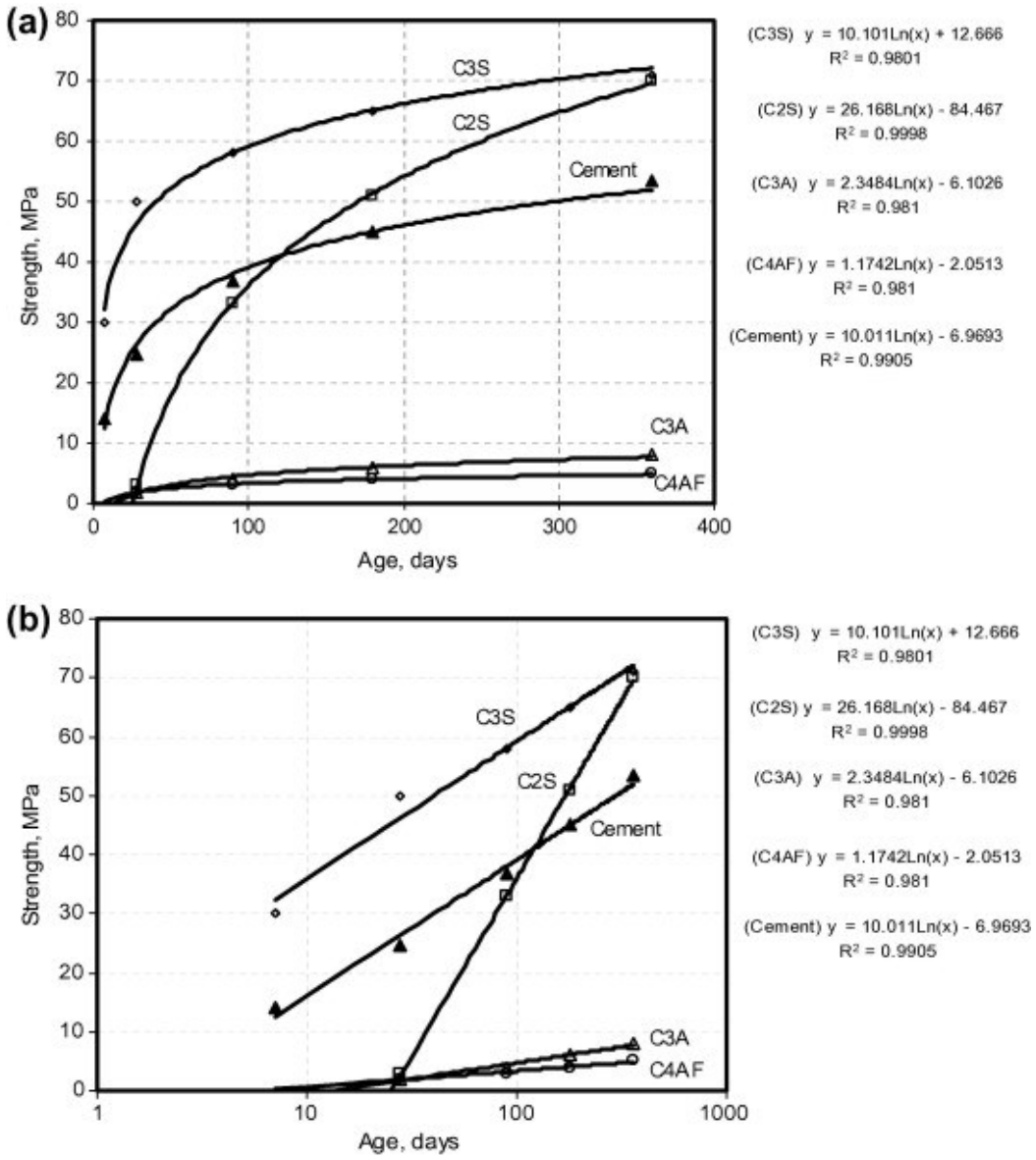

Figure 3.1 Relationship between compressive strength and age for clinker minerals and cement: a) linear scale; b) log scale (Hewlett, 2005)

3.3 Compressive strength measurements

Compressive strength of cementitious materials is usually obtained from uniaxial compression strength test (UCS). Normally, UCS tests are performed on either a cube specimen (ASTM C 109M-05) or a cylinder sample of height to diameter ratio of 2 (ASTM D7012-04). Generally, cube specimens give a higher

compressive strength compared with cylinder specimens due to the following reasons (Vutukuri et al., 1974; Garnier et al., 2007):

1- The compressive strength of cement is highly affected by the rate of loading. The larger the rate of applying the load, the greater the strength of the sample. In the case of using cylinder specimens, the load is applied uniaxially at constant strain rate. The rate of loading declines during the test due to deformability. As a result, the strength of the sample drops. Oppositely, crushing a cube sample is performed as constant strain test.
2- A non-uniform stress distribution occurs throughout the sample due to the friction at the specimen- machine platens interface. This means the sample is in a state of triaxial stress. Several authors have tried to estimate the stress distribution within a cylindrical sample subjected to a uniaxial loading (Peng, 1971; Brady, 1971 and Chalabi et al., 1974). Chalabi et al. (1974) pointed out that, compressive and tensile strengths tend to develop in the radial and tangential directions unless there is no friction between the sample surfaces and the machine platens.
3- Unlike cylindrical samples, uniaxial load is accompanied with buckling in the case of a cube specimen as no surface grinding is performed to obtain planar and parallel surfaces.

The main advantage of using cube samples is that it does not require any extra preparation before the test to obtain a parallel and flat end surfaces. However, cylinder samples do need this additional preparation process, which can be achieved either by capping or grinding. Although the recommended aspect ratio for cylinder sample is 2, the test results vary with the actual diameter of the sample. Samples with larger diameters will give lower compressive strength (Kim & Yi, 2002). The concept of decreasing concrete strength with any increase in the sample size was discovered experimentally earlier by Gonnerman (1925). This phenomenon is called “reduction phenomenon” and can be explained by the impact of specimen size on the pattern of crack propagation. As well, the aspect ratio itself controls the compressive strength of the sample. The compressive stress at failure decreases as the aspect ratio increases (Al-Sahawneh, 2013).

Regardless of whether a cube or cylinder specimen is used, the test is performed by applying a vertical force on the sample. This force increases gradually until failure. Both Young's modulus and Poisson's ratio can be calculated from UCS test results if strains are measured. However, additional parameters are needed to define cement behavior using a Mohr-Coulomb criteria, namely, friction angle (φ') and cohesion (c') of the material. These parameters mainly describe the impact of confining pressure on the strength of the material.

3.4 Tensile strength measurements

Backe et al. (1994) suggested a new mechanism for gas migration based on the tensile strength of the cement matrix. As the compressive strength of the cement matrix is much higher than its tensile strength, it is not expected that the gas can break the cement matrix from outside. However, when the gas enters the cement and fills the pores, it may overcome the tensile strength and can then break the matrix, initiating gas migration. It has been proven that when cement with a high Young's modulus is used, cement paste mainly fails due to the initiation of tensile cracks, which start to propagate radially (Thiercelin et al., 1997). In addition, improving the tensile strength of the cement sheath helps to provide adequate structural support to the tubulars (Mack & Dillenbeck, 2002).

In general, little attention has been paid to the importance of the tensile strength of cement paste. Most researchers have focused on using the compressive strength to criticize the quality of cement. For instance, Mack and Dillenbeck (2002) mentioned that a cement mix with a compressive strength of 100 psi can hold most oilwell casing strings in place. On the other hand, Stiles (1997) pointed out that a compressive strength of 500 psi was needed to support the casing.

Both direct and indirect methods are commonly used to measure the tensile strength of cement-based materials. In direct tension tests, a dog-bone specimen is used to overcome the difficulty of gripping the sample, to avoid eccentricity, and to maintain a uniform distribution of the tensile stress in the specimen at the same time. Tensile strength can be obtained by determining the applied tensile force at the failure, which occurs in the middle of the sample. When a direct tension method

is employed to test a brittle material, the sample may be subjected to local stress concentration, and both bending and torsion stresses are developed (Chen et al., 1993).

Unlike the direct technique, indirect methods involve loading such that tensile stresses develop indirectly and the results, to some extent, are inaccurate. However, it is common practice to utilize indirect methods to obtain the tensile strength of materials, due to their simplicity. Indirect methods include beam flexural test and splitting tensile test (Brazilian test).

3.4.1 Beam flexural test

In this method, a simply supported prismatic beam is loaded by a central point load or by two point loads placed at third points along the span. This load is increased gradually until flexural failure occurs (Figure 3.2) According to ASTM C78/C78M–16, the modulus of rupture can be calculated based on the maximum applied load and the location of fracture, as in the following cases:

Case 1: if the fracture initiates in the tension zone within the middle third of the beam's span length, then:

$$R = \frac{\mathrm{PL}}{\mathrm{b}d^2} \tag{3.13}$$

where R is the modulus of rupture (MPa); P is the maximum applied axial load (N), L is the span length (mm); b is the average width of the specimen (mm); and d is the average depth of the specimen (mm).

Case 2: if the fracture initiates in the tension zone outside the middle third of the beam's span length, but is not more than 5% of the span length, then:

$$R = \frac{3Pa}{bd^2} \tag{3.14}$$

where a is the average distance between the line of the fracture and the nearest support measured on the tension surface of the beam.

Case 3: if the fracture initiates in the tension zone outside of the middle third of the beam's span length by more than 5% of the span length, then the results should be discarded, and the test should be repeated.

In all cases, the ratio of the horizontal distance between the applied load and the nearest reaction to the depth of the beam should be 1.0 ± 0.03.

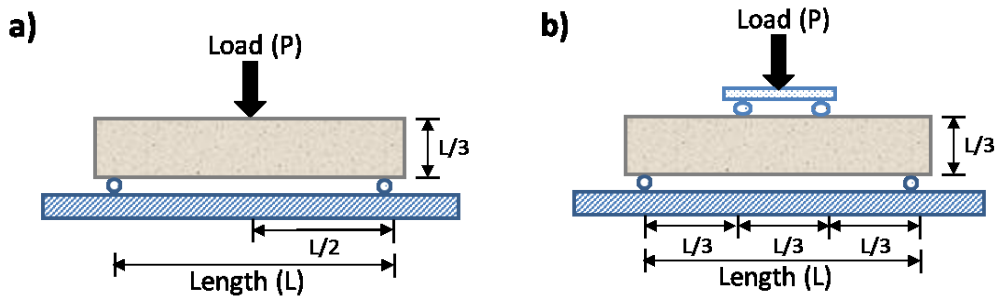

Figure 3.2 Schematic diagram for beam flexural test: a) central point load; b) two point loads

In their study, Wright and Garwood (1952) investigated several factors that may affect the modulus of rupture, such as depth, method, rate of loading, and size of the specimen. The impact of the loading method on the modulus of rupture was quite significant. The results, obtained from central loading, were 20% to 25% higher than third-point loading. In addition, the results were less uniform, which can be attributed to the stress concentrations that occur around the points where the load is applied under third-point loading. The modulus of rupture was found to be more sensitive to the variation of sample depth under central loading than under third-point loading. Increasing the depth of the specimen from 3 inches to 8 inches caused a 33% reduction in the modulus of rupture under central loading and a 28% reduction in the case of third-point loading. Moreover, increasing the depth of the specimen led to improved reproducibility of the results. On the other hand, the span-depth ratio was found to have a minor impact on the modulus of rupture. A small reduction in the modulus of rupture was reported to occur when increasing the span-depth ratio.

The modulus of rupture, as obtained from the beam flexural test, was found to be 30% higher than the tensile strength, as obtained from direct tension test (Neville, 1996). This is because concrete exhibits a nonlinear stress-strain behaviour in the tension zone. In general, beam flexural test results are greatly

affected by specimen preparation, handling, and the curing procedure. Therefore, the specimens must be prepared and cured in a standard manner.

3.4.2 Brazilian test

The Brazilian splitting test was initially introduced in 1953 by Carneiro and Barcellos. In this test, a disc-shaped specimen is loaded vertically by applying a diametral compression force along the top and bottom sides of the sample, until failure occurs. In this case, the stress distributions along the loading diameter vary from uniform tension at two mid thirds mid-sections to transverse compression at the top and bottom. Therefore, splitting tensile strength can be calculated using the following equation:

$$\sigma_t = \frac{2P}{\pi LD} \tag{3.15}$$

where P is the maximum applied axial load; L is the thickness of the specimen; and D is the diameter of the specimen.

Generally, the difference between Brazilian tensile test results and direct tension test results is in the range of 2% to 12%. This discrepancy between the two techniques is due to several reasons. For instance, the sample may be exposed to twisting/bending in the direct tensile strength test, resulting from how the specimen is gripped. As a result, the tensile strength of the sample declines. In addition, the results obtained from Brazilian test are affected by how the force is radially distributed within the sample. The slenderness ratio controls the stress distribution. Any increase in the specimen thickness will reduce the apparent tensile strength (Wijk, 1978). Moreover, samples are subjected to uniaxial stress in direct tensile and three-point bending tests. However, biaxial stress is developed throughout the specimen in the case of the Brazilian test. Finally, the preexisting fissures and defects in the sample enhance crack initiation. The larger the volume of the sample subjected to stress during the test, the higher the probability that these defaults will be encountered and result in cracking. This may explain the fact that the three-point bending test yields higher values of tensile strength than the other two tests.

In their study, Heinold et al. (2003) tried to find the relationship between cement tensile strengths derived from different tests. They found that the difference between cement tensile strengths obtained from Brazilian test and direct tension method was greatly influenced by sample size. Using a smaller specimen in the Brazilian test yielded a higher difference between the results. On the other hand, the curing temperature of the sample had a trivial impact on the ratio between the results of Brazilian and direct uniaxial tensile tests. Based on their experimental results, the authors proposed the following correlation between the two tests' results:

$$T_{Uniaxial} = T_{Splitting} * \left(0.021\, V_{Cylinder} + C_{Neat}\right) \tag{3.16}$$

where $T_{Splitting}$ is the uniaxial tensile strength (psi); $V_{Cylinder}$ is the cylinder volume (in^3); and C_{Neat} is the constant for neat cement, with a value of 0.39.

Rocco et al. (1999) performed 110 Brazilian tests on granite and mortars to explore the different factors affecting Brazilian test results. He concluded that the results of splitting test rely on the size of the specimen and the width of the load-bearing strip. The difference in results due to these two factors may reach up to 30%. The size effect decreases as the relative width of the bearing strip decreases. The researchers recommended using a bearing strip that is 8% less wide than the specimen diameter to obtain results close to direct tension test results. Figure 3.3 presents the relationship between the values of tensile strength obtained by direct and indirect techniques. The data shown in Figure 3.3 indicates that the direct method yields a higher tensile strength than indirect methods. However, the variation in results depends on the test itself. For example, the tensile strength measured using the Brazilian test is lower than that obtained from the beam flexural test.

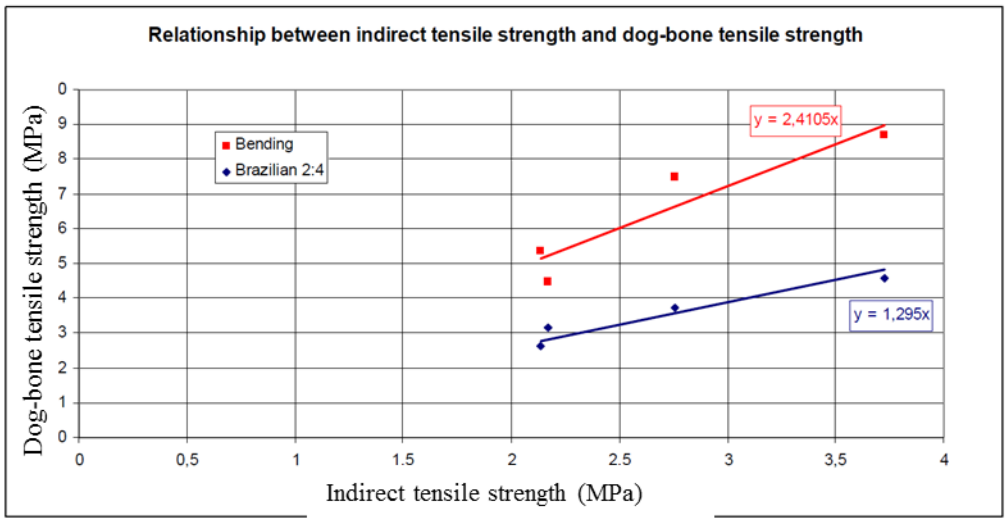

Figure 3.3 Correlation between direct tensile strength (dog-bone method) and indirect tensile strength (Brazilian and three-point bending) (from ASTM C 190-85)

The concept of bimodular materials was introduced early in 1864 by Saint-Venant. Material bimodularity denotes the properties of a material that has moduli of deformation which depend on the test type and whether it is in tension or compression. Chen and Stimpson (1993) numerically investigated the dependency of Brazilian test results on the moduli ratio, *k*. They used the finite–element software SIMEX, to build and analyze one quarter of the Brazilian test. They determined that the corrected tensile stress can be written as follows:

$$\sigma_x = -1.023k^{0.252}\frac{\mathrm{P}}{\pi \mathrm{tR}} \tag{3.17}$$

where σ_x is the corrected tensile stress; P is the applied force; t is the thickness of the disk; and R is the radius of the disk. 4298.23

3.4.3 Tensile strength measurement of irregular samples

Irregular samples could be used to quickly calculate the tensile strength of the specimens by imposing a pair of line loads (Wijk, 1978). However, this method is not accurate because stress distribution that develops within the sample is non-uniform. Wijk (1978) stated that the tensile strength of an irregular sample under

compression can be calculated as 90% of the maximum load at failure divided by the square of the distance between the loading points.

3.5 Triaxial test

The Triaxial compression test is one of the most widely used tests to determine the shear strength properties of materials. Many parameters can be measured in this test, such as friction angle (φ'), cohesion (c'), permeability (k), and undrained shear strength (C_u). Triaxial testing provides several advantages in comparison to direct shear testing, such as the ability to perform the test under different drainage conditions, having limited stress concentrations, and the failure plane can occur anywhere. Also, failure in the direct shear test occurs throughout a designated plane, which is not necessarily the weakest one. In addition, pore water pressure can be measured during triaxial test. This allows the effective shear strength parameter (i.e. φ', and c') to be determined under a reasonable shearing rate to reduce testing time. A triaxial test can be classified as either a drained or undrained test. Drainage is allowed during shearing in a drained test to maintain the pore pressure at a predefined value. To achieve this condition, the strain rate has to be low enough to prevent pressure from building up during the shearing stage. In general, triaxial test results and the behavior of the sample during the test depend very much on the drainage conditions.

3.6 Elastic moduli of cement

The elastic moduli of cement can be defined by Young's modulus (E) and Poisson's ratio (ν). In general, cement with a low Young's modulus is preferable in a wellbore. This is because, with a low Young's modulus, the tangential stress developed in the cement tends to be compressive stress. In contrast, increasing the Young's modulus of cement relative to the Young's modulus of rock leads to an increase in the cement's tensile strength requirement due to the reduced ability of the rock to support the cement (Thiercelin et al., 1997). Obviously, a minimum value for tensile strength is needed because the tensile strength of cement paste is much lower than its compressive strength.

Normally, methods used to determine the Young's modulus of a material can be divided into two categories: dynamic and static techniques. The dynamic approach is mainly based on measuring ultrasonic velocity. This technique usually yields a higher Young's modulus due to the effects of strain magnitude and frequency.

In the static technique, the UCS test is used to measure Young's modulus. According to ASTM D7012-10, Young's modulus can be calculated from the UCS test results using one of the following:

i. Tangent modulus, defined as the slope of a line drawn tangent to the stress-strain curve at some fixed percentage (usually 50%) of the maximum strength.
ii. Secant modulus, defined as the slope of a line drawn from the origin to some fixed percentage of maximum strength.
iii. Young's modulus is defined as an average slope of the straight-line portion of the stress-strain curve.

3.7 Mode of failure

Terzaghi (1945) categorized failure according to the direction of the failure planes, into three modes: splitting, shear, and pseudo-shear. Splitting occurs when tension force breaks the bonds between grains. In this case, the cracks tend to be parallel to the direction of the applied load. Shear failure mainly happens because of a relative displacement between the grains along a specific plane. On the other hand, a situation in which the sample experiences both shear and tension cracks describes pseudo-shear failure. The same conclusion was drawn by Griggs (1936), who conducted a series of triaxial tests on limestone, marble, and quartz. Both tension and shear failures were observed. Shear cracks tended to occur along an inclined plane. Griggs (1936) pointed out that increasing confining pressure would reduce the possibility of the occurrence of splitting failure.

Any failure criterion is usually well described by a surface in the principal stress space of σ_1, σ_2, and σ_3, and can be verified experimentally. In the case of

isotropic materials, the failure criterion becomes independent of the direction and can be expressed as follows:

$$f(\sigma_1, \sigma_2, \sigma_3) = 0 \quad (3.18)$$

3.8 Experimental program

The experimental program conducted in this study was divided into three parts. The first and second parts were dedicated to performing UCS and Brazilian tests on cement paste to study the impact of temperature on the compressive and tensile strengths of cement paste. The third part of this experimental program focused on examining the combined effects of both confining stress and temperature on the behaviour of cement paste during a triaxial compression test. The following sections describe the cement testing procedures used in this investigation.

3.8.1 Materials and sample preparation

The cementitious materials used in the current study are thermal and non-thermal Class G oilwell cement provided by Multicrete, Edmonton, Canada. The chemical compositions and the particle size distributions of this cement have been previously discussed in Chapter 2.

Four mixes were designed for the present study with different water-to-cement ratios (w/c). All slurries were prepared in accordance with API specifications. Immediately after mixing, the fresh slurries were cast into cylindrical brass molds, 101.6 mm in height and 38.1 mm in inner diameter, then compacted at three steps using a pudding rod to remove entrapped air. The molds were promptly placed into a pressurized curing chamber (Model No. 1910, Chandler Engineering), where a nearly constant pressure of 3 MPa and a temperature of 9 °C were maintained. The pressure and temperature were chosen to mimic field conditions. A temperature bath was attached to the curing chamber to achieve the low temperature condition. After three days of curing inside the curing chamber, the pressure was decreased gradually to ambient conditions. Then, the specimens were demolded and taken to the moisture room, where samples were

kept inside water at 7±2 °C and with a relative humidity higher than 90% until the testing date. Right before the test, the samples were cut at the ends using a rotating saw and then ground to achieve smooth and parallel surfaces, while the ends were kept perpendicular to the axis of the sample. During the cutting process, the specimens were kept saturated to prevent any cracks that may occur as a result of drying.

3.8.2 Factors investigated

A test plan was designed in order to study the impact of the following factors on the mechanical performance of cement:

1- Type of cement: Two types of cement were examined, Class G thermal and non-thermal cement.
2- Water-to-cement ratio (w/c): specimens with a w/c of 0.4, 0.5, and 0.6 were used in the experimental program.
3- Test temperature: Tests were conducted at four different temperatures, specifically 5 °C, 60 °C, 120 °C, and 180 °C.

3.8.3 Test apparatus

The Instron Series 3384 Load Frame was employed to apply an axial load on the specimen. The Instron 3384 is a computer servo-controlled universal testing machine with a maximum load capacity of 150 kN and an accuracy of 0.01%. To measure axial elongation, a linear variable differential transformer (LVDT) was used. While the load was measured by the load cell, a spherical seating was utilized to adjust the alignment between the machine platens and the specimen surface.

3.8.4 UCS test procedure

In this test, samples were loaded axially in compression to produce a constant rate of axial deformation of 0.05 mm/min. Applied load and axial deformation were monitored and recorded during the test. A spherical seat was placed on the upper surface of the sample. The specimen, the spherical seat, and the loading frame were exactly centred with respect to one another. For the samples tested at elevated temperatures (120 ºC and 180 ºC), the experiments were

conducted inside the triaxial cell to keep the sample saturated during the entire test and to eliminate any effect of dryness on the results. A pore pressure of 2 MPa was applied to raise the boiling point of water to more than 180 ºC. The confining pressure was chosen to be at the same value as the pore pressure to produce unconfined conditions. Detailed procedure for UCS test can be found in Appendix B.

3.8.5 Brazilian test procedure

In this study, Brazilian tensile strength test was used to investigate the behavior of cement under tension. The experiments were conducted on non-thermal cement with w/c of 0.4, 0.5, and 0.6. On the other hand, a w/c of 0.5 was selected for thermal cement samples.

The specimens' dimensions were selected to have a length to diameter ratio (L/D) of 2, according to ASTM D3967-08. The Instron Series 3384 Load Frame was used to apply axial load on the specimen. A constant axial deformation of 0.02 mm/min was applied for this test to ensure that the failure takes place within 1 to 10 min of initial loading. A sample holder was used between the specimen and the loading machine platens to apply a confinement and to reduce the effect of creating non-uniform stress distribution inside the sample. Detailed procedure for the Brazilian test can be found in Appendix B.

All samples were tested after 28 days. Experiments were performed at different temperatures: 5 °C, 60 °C, 120 °C, and 180 °C. Immediately before the test, the temperature of the sample was gradually increased to the target temperature using a slow heating rate (5 °C/hour) to prevent any cracks due to drying. A schematic diagram for the Brazilian test is shown in Figure 3.4.

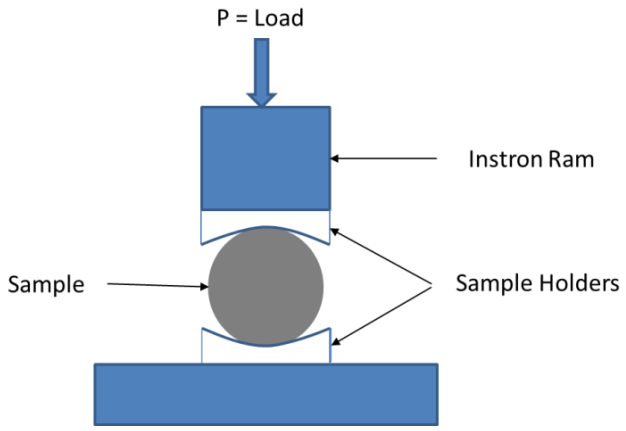

Figure 3.4 Schematic diagram of Brazilian test

3.8.6 Triaxial test procedures

A cross section of the triaxial cell used in this study is shown in Figure 3.5. The cell is made of high-strength steel. The base of the cell contains three ports. The confining fluid was injected from one port. The other two ports were used to apply both top and bottom pore pressures. Air was permitted to escape through a valve that exists in the top cap, while the cell was filled by injecting the confining fluid through the entry port in the base. Viton-O-rings were used to seal the connections between the base and the cylinder.

A 76.2 mm long by 38.1 mm diameter specimen was inserted inside a Viton membrane to seal the sample and to prevent any contact between the sample and the confining fluid. Furthermore, this enabled modifying the confining and pore pressure individually. Two stainless steel porous stones, both saturated and sintered, were placed at the top and bottom of the specimen. The sample was placed on a base pedestal inside a triaxial cell, and then the top platen was covered with the Viton membrane using a hose clamp. Three pumps were employed to develop and maintain the confining and pore pressures at the desired values. Both the confining and bottom pore pressures were manipulated by an ISCO pump. However, a Quizix pump was used to apply the top pore pressure. White oil with a high flash point was used to apply confining pressure, and brine (3% NaCl) was

utilized for pore pressure. Detailed procedure for the triaxial test can be found in Appendix B.

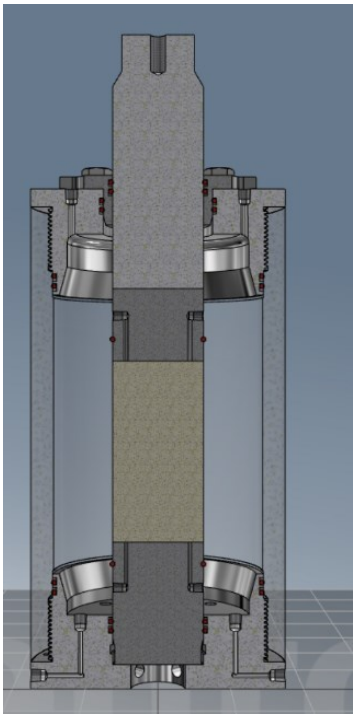

Figure 3.5 Cross section of the triaxial cell

The cell was placed inside an environmental chamber and under a loading frame. A seating load was applied to the sample, and then both the confining and pore pressures were increased gradually, with a rate of 0.5 MPa/ min, until reaching the desired effective confining stress and pore pressure. The system was held to achieve back saturation for the specimen and to ensure all drainage lines were completely de-aired. During this period, the volume of fluid pumped into the system was monitored. Afterwards, the cell was heated at a rate of 10 °C/hr to the test temperature. The heat was kept constant for one day before starting the shearing. The test was stopped after achieving a constant residual stress. The confining and pore pressures were monitored by pressure transducers. A J-type thermocouple was inserted inside the triaxial cell close to the specimen to measure the test

temperature. The pore fluid expelled from the sample during the shearing stage was determined from the change in volume of the backpressure pump. Figure 3.6 shows a schematic diagram of the triaxial test setup.

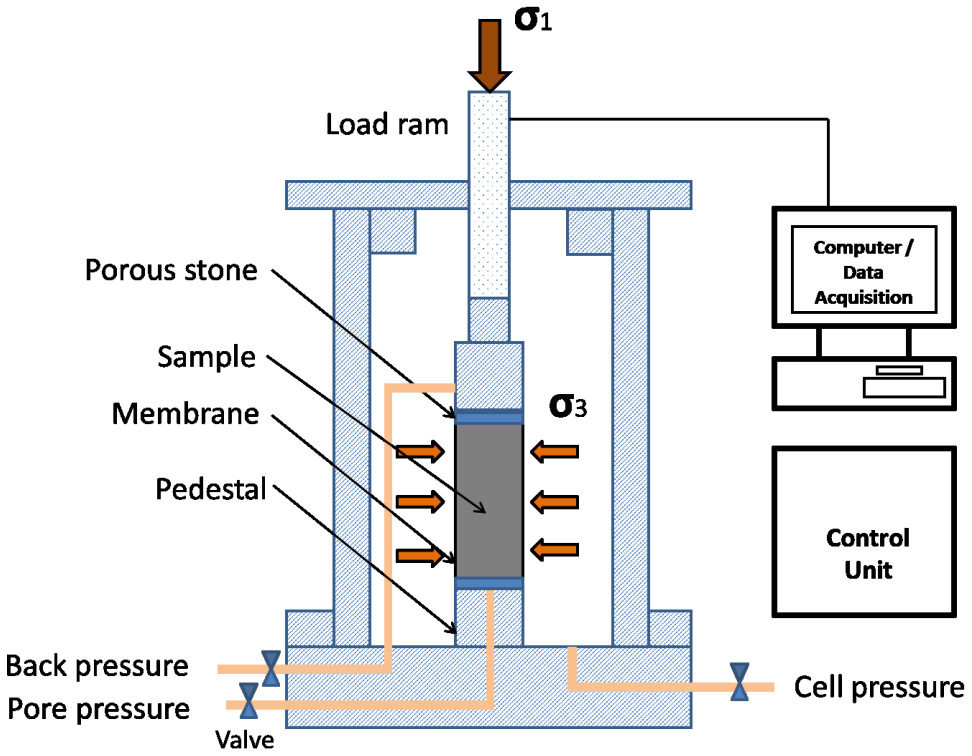

Figure 3.6 Schematic diagram of the triaxial test setup

3.9 Results and discussion

3.9.1 Unconfined compressive strength test results

3.9.1.1 Bulk density results

The bulk densities (ρ) of the samples were determined by measuring their volumes (V) and their masses (m) independently, and then the effective density was calculated from the following relationship:

$$\rho = \frac{\mathrm{m}}{\mathrm{V}} \tag{3.19}$$

Table 3.1 summarizes the effective density results. All measurements were performed after 28 days. The variation of bulk density in relation to the w/c is

presented in Figure 3.7. Data shown in Figure 3.7 indicated that there is a strong relationship between the two properties. The bulk density of the samples decreases linearly as the w/c increases. This can be attributed to the fact that the aqueous phase has a lower density than hydration products. Bulk density can be expressed as a function of the w/c, according to the following equation:

$$\rho = 2.358 - 0.75(w/c) \tag{3.20}$$

where ρ is the bulk density of the sample (g/cm^3), and w/c is the water-to-cement ratio (bwoc).

Table 3.1 Bulk density of cement paste with different w/c.

Cement Type	W/C [bwoc]	Bulk Density, ρ [g/cm^3]
Class G Non-Thermal Cement	0.4	2.06
	0.5	1.98
	0.6	1.91
Glass G Thermal cement	0.5	1.84

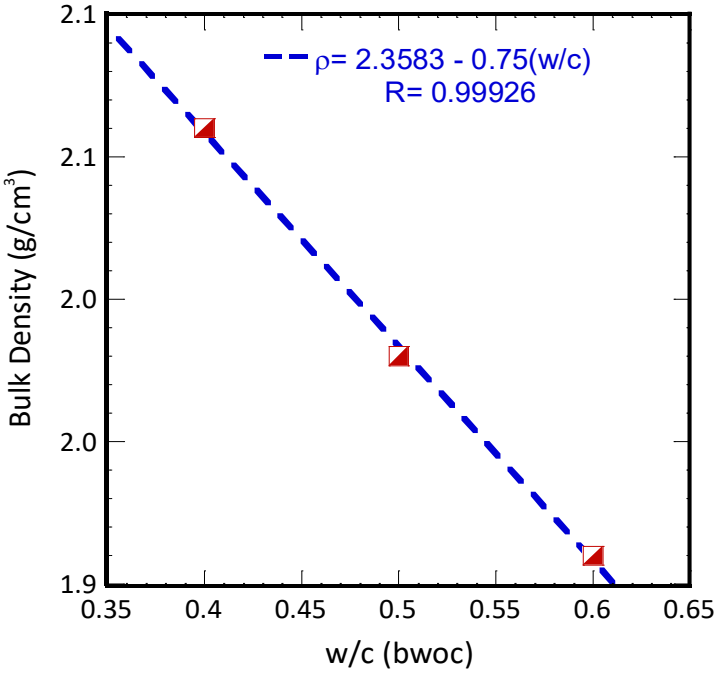

Figure 3.7 Variations of bulk density of cement paste with w/c

3.9.1.2 Repeatability of the test

In order to examine the reproducibility of the tests, a set of three samples from each mix were tested at the same temperature. The result, presented here for each curing condition, is the average value of the three tests.

The experiments were performed on specimens with different w/c and at several temperatures ranging from 5 ºC to 180 ºC. Samples were named in a way that indicates the test name, cement type, test temperature, and w/c. For example, UCS5-NT-0.5 denotes that the UCS test run on a cement sample with a w/c of 0.5 at 5 ºC. A set of three samples from each mix was tested at the same temperature. The experimental program plan of UCS test can be found in Appendix C.

3.9.1.3 Stress-strain behaviour

Figure 3.8 presents a series of stress-strain curves obtained from UCS tests performed on specimens with various w/c at different temperatures. It can be seen that all curves showed some nonlinearity upon initial loading. The applied stress increased gradually with the strain, then dropped dramatically almost immediately after the peak stress was reached where the rupture occurred. This behavior indicates that the specimens failed. However, samples with a w/c of 0.6 tested at 180 ºC showed some ductility.

Data in Figure 3.8 demonstrates that the compressive strength of non-thermal cement is significantly affected by temperature. A decrease in peak stress was observed with an increase in temperature. The decline of cement strength with heating can be attributed to the effect of temperature on the bond strength of hydrated calcium silicate crystalline structures.

The amount of strain at failure is observed to be dependent on the test temperature. Samples tested at high temperatures were subjected to more deformation before rupture. However, the apparent area under the stress-strain curve remained higher at a low temperature, which means that more energy is required to break the cement paste specimens at a low temperature. Detailed results of the unconfined compressive strength tests can be found in Appendix D.

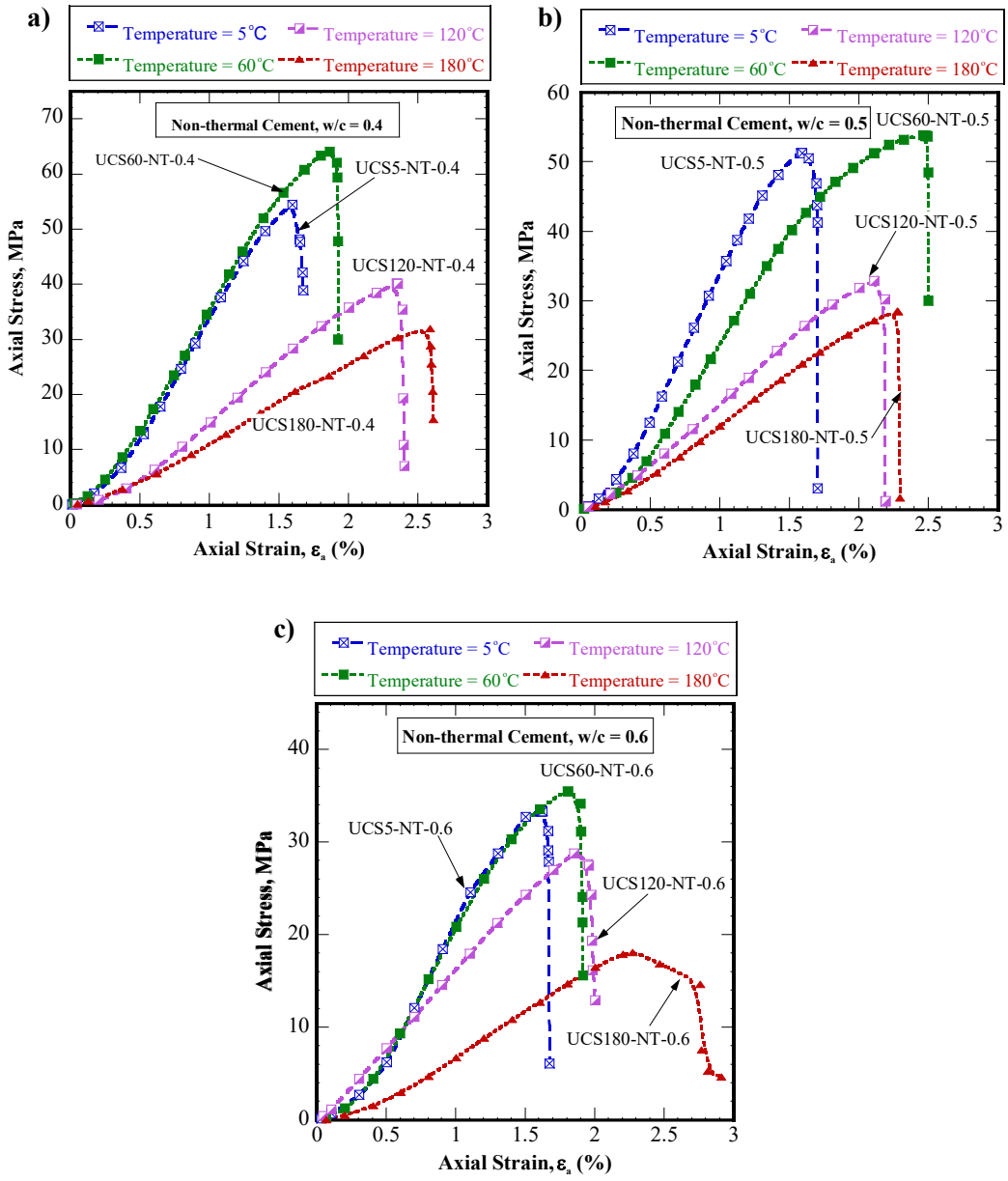

Figure 3.8 Unconfined compressive strength results for non-thermal cement: a) w/c = 0.4; b) w/c = 0.5; c) w/c = 0.6

On the other hand, the relationship between the w/c and strain at failure was observed to change its trend according to cement content. The lowest strains were recorded for samples with a w/c of 0.4. While at a w/c of 0.5, specimens experienced the largest strain. In other words, the strain at failure increased as the w/c increased from 0.4 to 0.5; afterwards, any increase in w/c would reduce deformation that occurs before rupture.

3.9.1.4 Effect of water-to-cement ratio on compressive strength of cement paste

Figure 3.9 illustrates the combined effects of w/c and temperature by plotting unconfined compressive strength values, obtained at different temperatures, as a function of the w/c. The average value of the three tests obtained for each w/c at each temperature was used to draw Figure 3.9. It can be seen that there is a considerable difference in the compressive strength of cement paste made of different cement content. The strength of the sample decreased as the w/c of the slurries increased. Such a trend is typical for cement paste. This is because clinker grains become closer in slurries with low w/c, which improves the ability of hydration products to fill the pore spaces between cement grains, resulting in increasing the connectivity of cement matrix. In addition, the increase in the growth of calcium silicate hydrate (C-S-H), which is mainly responsible for the interlock between particles, can be another reason behind this phenomenon.

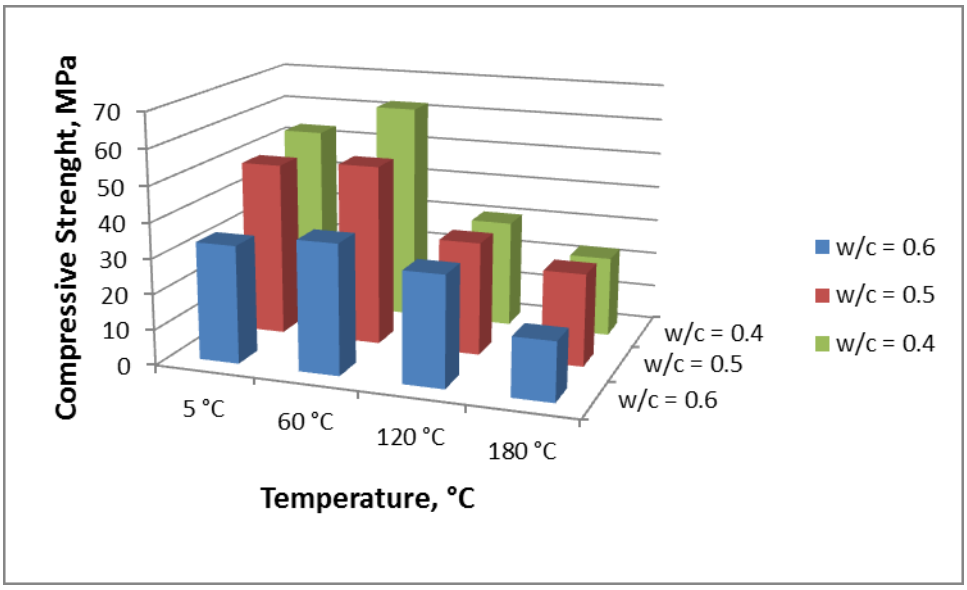

Figure 3.9 Variations of compressive strength with respect to w/c and temperature

It is important to note that the amount of reduction in compressive strength due to the variation of the w/c is largely dependent on the temperature. Figure 3.9 reveals that the variations in compressive strength due to temperature effects are less marked for the sample with a higher w/c. The strength of samples with a w/c

of 0.6 dropped from 33.3 MPa to 16.6 MPa when the test temperature increased from 5 ºC to 180 ºC; whereas, the compressive strength changed by 57.4% for cement paste with a w/c of 0.4 for the same variations in temperature.

According to data shown in Figure 3.10, compressive strength can be written in terms of the w/c as follows:

$$f_{cu,5} = 100/3^{1.5(\frac{w}{c})} \tag{3.21}$$

$$f_{cu,60} = 100/3^{1.5(\frac{w}{c})} \tag{3.22}$$

where $f_{cu,5}$ and $f_{cu,60}$ are cement compressive strength obtained for tests preformed at 5 ºC and 60 ºC respectively.

It should be mentioned that UCS tests performed at 60 ºC were conducted outside the triaxial cell where samples were heated immediately before the test. This means samples were exposed to dryness to some extent; this might explain the higher strength obtained at 60 ºC.

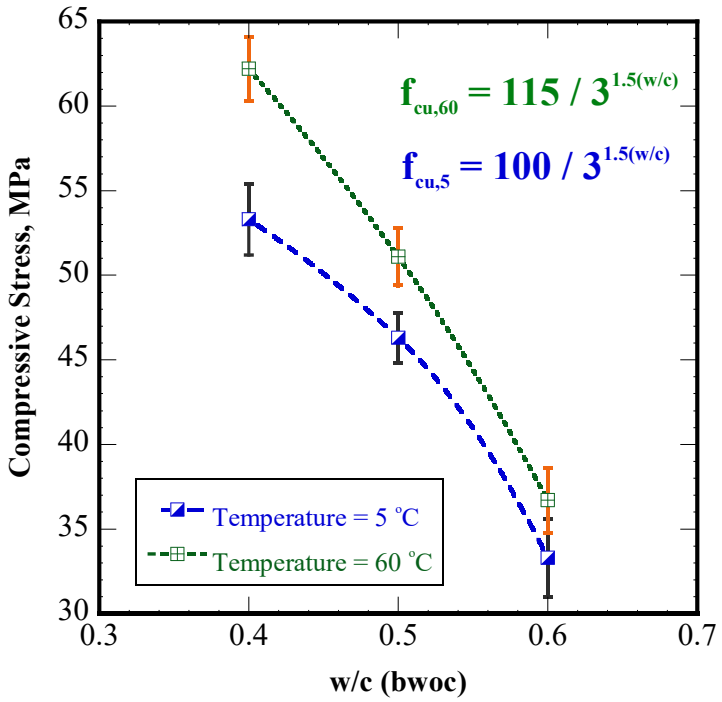

Figure 3.10 Relationship between compressive strength and w/c

3.9.1.5 Comparison of thermal and non-thermal cement behavior in UCS

To compare the performance of thermal and non-thermal cement pastes, the stress-strain curves for both types are plotted in the same graph (Figure 3.11).

It can be seen that samples made of non-thermal cement always have higher strength even at high temperatures. However, the difference in strength between the two types of cement is observed to be reliant on test temperature. This difference dropped drastically from approximately 73.4% at 5 ºC to approximately 25% at 180 ºC.

As expected, the compressive strength of thermal cement increases as the temperature increases. Still, the dependence of sample deformation on temperature can be observed. The increase in test temperature corresponded to an increase in axial strain at failure. Thereby, more energy is required to break thermal cement paste at elevated temperatures. In general, the strain at failure was found to be lower for the thermal cement specimen than the non-thermal cement specimen, regardless of temperature.

When analyzing the data in Figure 3.11 closely, it can be seen that the effect of temperature on the strain at failure is less noticeable for specimens made of thermal cement. In addition, even at low temperatures, thermal cement exhibited some kind of ductile behavior.

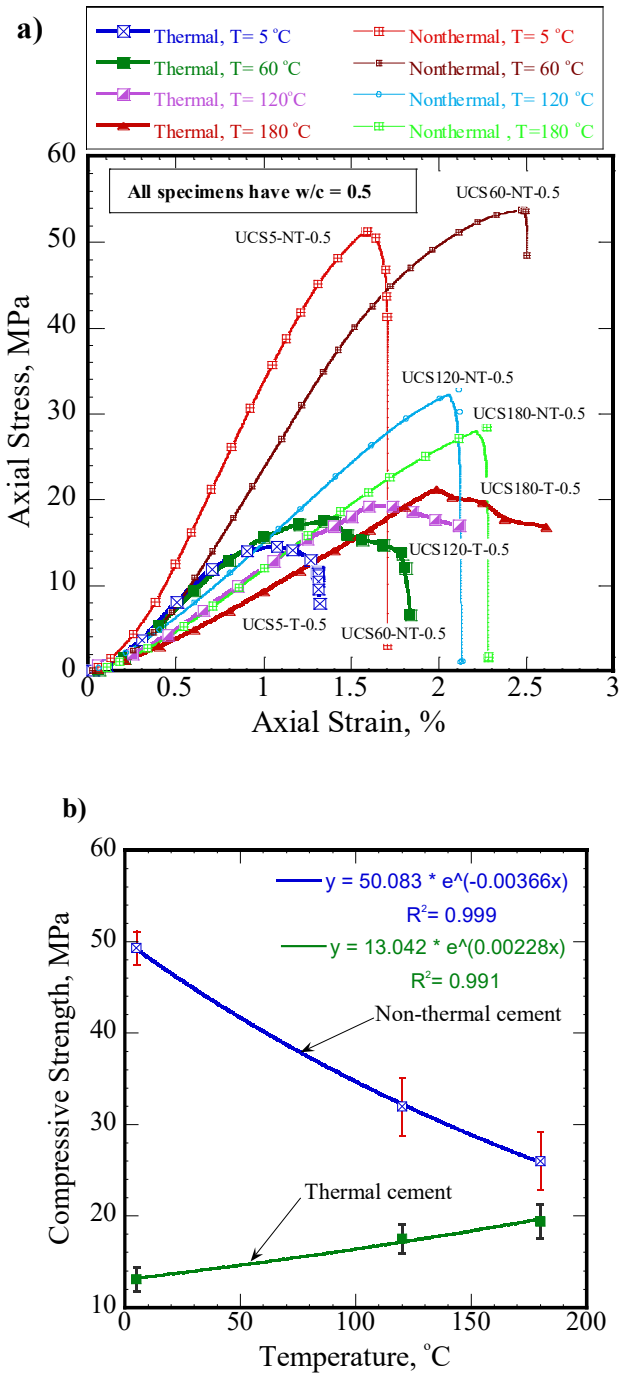

Figure 3.11 Comparison between the behavior of thermal and non-thermal cement under uniaxial compression test: a) stress-strain curves; b) variation of compressive strength with temperature

3.9.1.6 Effect of temperature on failure mode of cement paste

To fully understand the influence of elevated temperature on cement paste, it was important to study the impact of temperature on crack propagation during the loading stage. Figure 3.12 illustrates the influence of temperature on the macroscopic failure mode. It has been noted that increasing the test temperature leads to an increase in the ductility of cement. At room temperature, failure tended to occur along a single inclined shear plane. However, at a high temperature, cracks extended to a large portion of the sample, and the grains themselves failed.

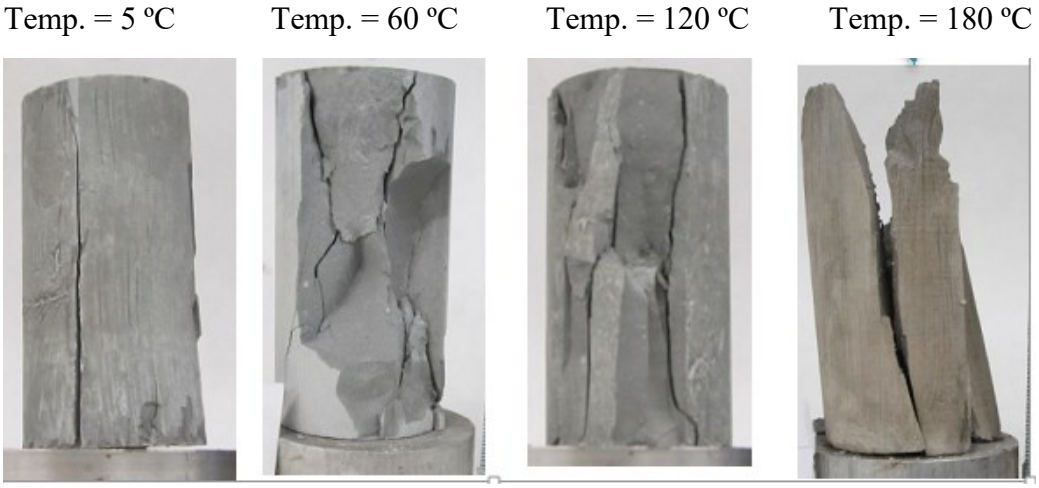

Figure 3.12 Photos illustrate mode of fracture of cement paste specimens after UCS conducted at various temperatures

3.9.2 Brazilian test results

During the course of this study, Brazilian tests were performed on four cement mixes. The effect of temperature on the tensile strength of cement paste was evaluated by testing cement pastes made with different w/c at various temperatures. Any individual Brazilian test with a result that deviated from the average value by more than 20% was discarded.

The digital photo in Figure 3.13 shows the failure mechanism of cement paste in the Brazilian test Cracks initiated at the disc's centre and then propagated

along the vertical diameter. It can be seen that, at failure, the specimen split into two separate parts close to the diametral plane.

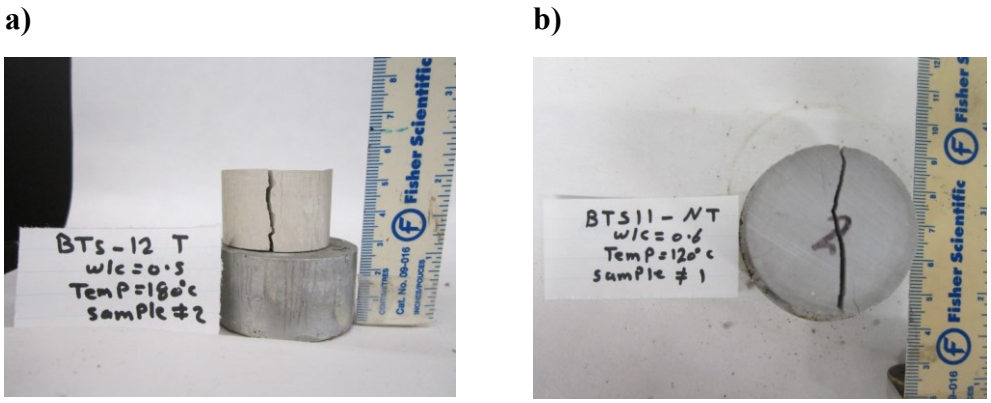

Figure 3.13 Failure pattern in Brazilian test: a) side view; b) top view

Stress-strain curves obtained from Brazilian tests at various temperatures are shown in Figure 3.14 As expected, the applied stress increased with the deformation until it reached the peak value, then dropped instantly. In general, all samples exhibited brittle behaviour, regardless of the w/c or temperature; however, some samples showed strain-softening characteristics. The stress-strain curve showed some nonlinearity. The slopes of the initial region of the curve at various temperatures were different, indicating that temperature considerably affects Young's modulus measured under tension. In addition, it can be seen that for a certain w/c and at the same temperature, the strain at the failure increased when utilizing non-thermal cement instead of thermal cement. In general, samples were subjected to more strain before reaching the peak load at a low temperature.

Test results indicate that there is a small improvement in the tensile strength of cement paste at a low temperature, due to decreasing the w/c. The results revealed that, at 5 °C, the tensile strength of specimens with a w/c of 0.4 was the highest, while the lowest tensile strength was recorded for samples with a w/c of 0.6. However, the effects of cement content were less marked at high temperatures. The data indicated that tensile strength is not highly affected by variations in the w/c of the samples at elevated temperatures. Theoretically, the cement paste performance would improve with any increase in cement content. In other words,

samples with a lower w/c will have higher tensile strength. However, in our case, there is another factor that may affect the tensile strength. This factor is dryness due to temperature, which may lead to the development of micro cracks within the cement matrix.

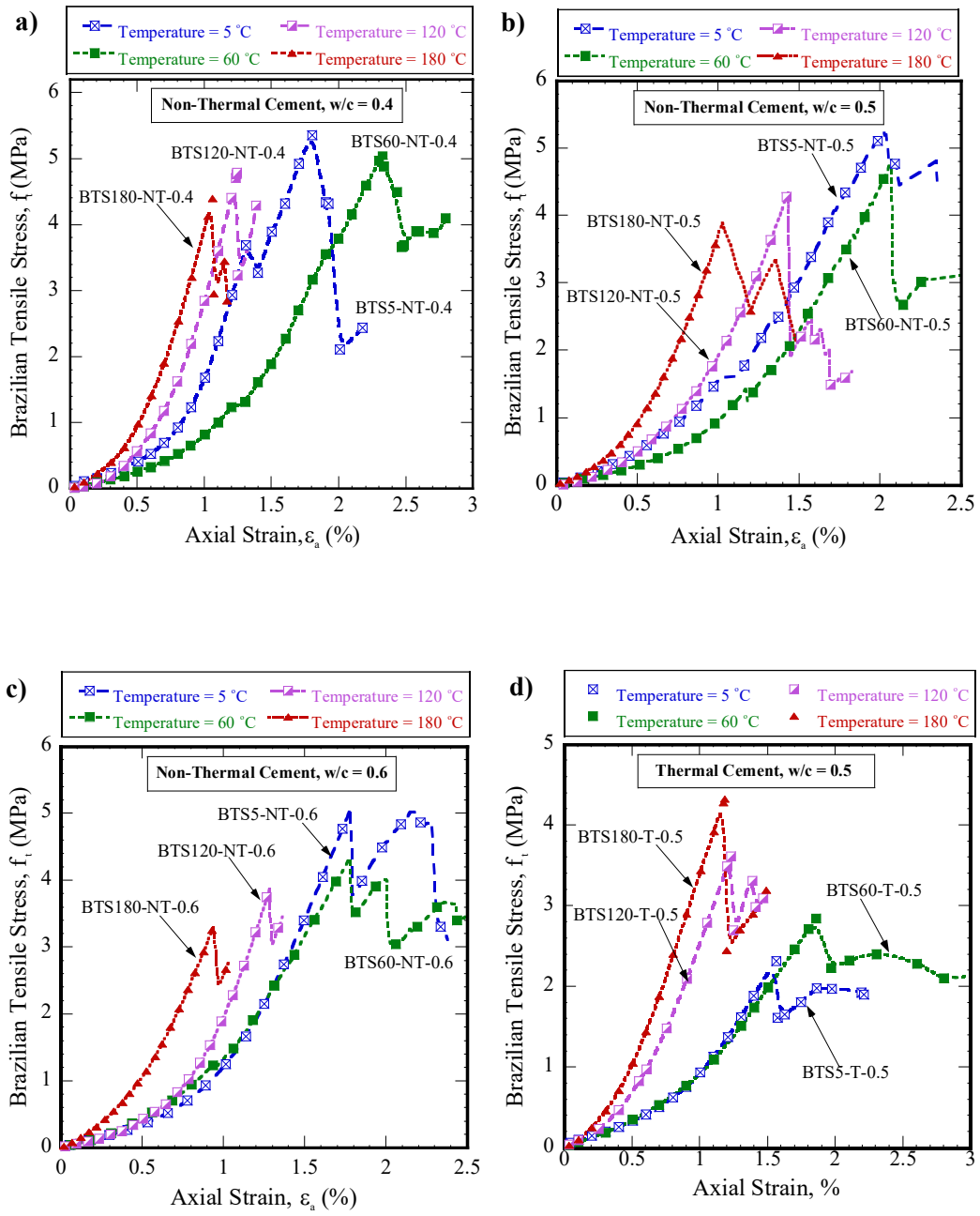

Figure 3.14 Brazilian indirect tensile strength test results: a) Non-thermal cement with w/c = 0.4; b) Non-thermal cement with w/c = 0.5; c) Non-thermal cement with w/c = 0.6; d) Thermal cement with w/c = 0.5

The influence of increasing temperature on the behaviour of thermal cement is provided in Figure 3.15, where the tensile strength of cement is shown as a function of the test temperature. In addition, the best fitted curves are presented in the same figure. As expected, the tensile strength of thermal cement paste increased with temperature. The tensile strength of thermal cement paste tested at 5 °C was about 54% of that of specimens tested at 180 °C. In general, type of cement has a substantial influence on tensile strength. Using thermal cement decreases the tensile strength of the sample at room temperature by approximately 35%.

According to Figure 3.15, the correlation between the tensile strength of thermal cement paste and temperature, as obtained from experimental data, can be written as follows:

$$\sigma_{t-thermal}(MPa) = 2.59 + 0.00825 * T(℃) \quad (3.23)$$

where $\sigma_{t-non\ thermal}$ and $\sigma_{t-thermal}$ are the tensile strength (MPa) of non-thermal and thermal cements, respectively, and T is the test temperature (℃) .

From the previous equations, it is clear that temperature has a similar impact on the tensile strength of both thermal cement and non-thermal cement.

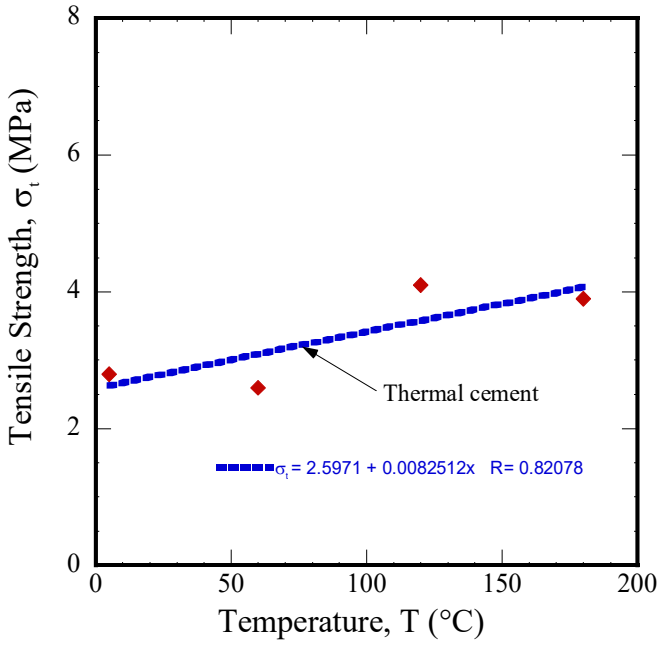

Figure 3.15 Variation of tensile strength of thermal cement with temperature

3.9.2.1 Relationship between tensile and compressive strengths of cement paste

The relationship between the tensile and compressive strengths of cement-based materials is complicated and may depend on several factors, such as age, curing conditions, and porosity. In our study, the experimental results, obtained from UCS and Brazilian tests, were compared to analyze this relationship. Figure 3.16 shows the variation of the ratio between tensile and compressive strengths with respect to the compressive strength of cement paste. It can be observed that the tensile strength of the specimens follows an ascending trend with the increase of compressive strength. The lower tensile to compressive strength ratios were recorded for samples with higher compressive strength. The variability in the ratio between both strengths is mainly due to the effect of dryness, which may affect the failure mechanisms.

Data shown in Figure 3.16 indicates that the w/c has a trivial effect on the ratio between tensile and compressive strengths. In contrast, the latter ratio was observed to vary according to the type of cement. Thermal cement had a higher tensile to compressive strength ratio.

According to data shown in Figure 3.16, the relationship between tensile and compressive strengths for non-thermal cement can be written as follows:

$$f_t = 4.85 * (f_{cu})^{-1.02} \tag{3.24}$$

In general, the tensile strengths of cement specimens obtained in this study were consistent with results that have been reported in the literature. In their studies, Mirza et al. (1979) found that the tensile strength of concrete usually falls between 8% to 15% of the compressive strength. The results reported by James and Boukhelifa (2006) revealed that tensile strength values obtained from the Brazilian test were about 15% to 17.5% of the compressive strength. To conclude, although the values of tensile strength obtained from the Brazilian test are distinct from those of the direct tensile strength test, the Brazilian test is a fast and easy way to investigate the tensile strength of cement paste. However, at elevated temperatures,

the results of the tests should be evaluated carefully and take into account the effect of dryness, which may reduce the accuracy of these results.

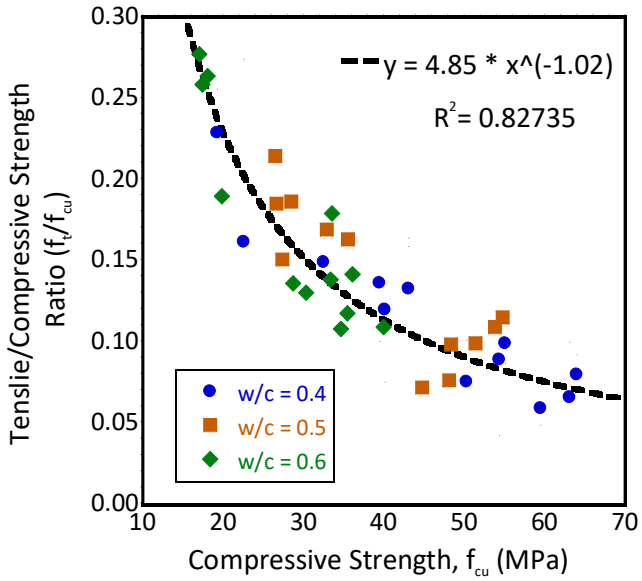

Figure 3.16 Relationship between tensile strength and compressive strength for non-thermal cement

3.9.3 Triaxial test results

3.9.3.1 Test plan

To explore the combined effects of cement type, cement content, and temperature on the performance of cement paste under confining pressure, forty-eight triaxial compression tests were performed on both thermal and non-thermal cements at different confining pressures. The temperature was kept constant during the tests at 20 °C, 60 °C, 120 °C, and 180 °C, respectively for each experiment. The tests were conducted at a constant pore pressure of 2 MPa. To achieve a drained condition during the test, the loading rate was selected to be slow enough to prevent excess pore pressure from building up during the shearing stage. This rate is very much dependent on the permeability and length of the sample. The experimental program plan of triaxial test can be found in Appendix C.

3.9.3.2 Stress-strain behavior

A series of stress-strain curves of cement specimens, with different w/c under various confining pressures, are shown in Figures 3.17 to 3.20. In general, deviator stress increased gradually with axial strain until peak stress was reached, where rupture occurred. After failure, the shape of the curve was observed to be dependent on the type of specimen and test conditions. At low temperatures, the stress-strain curves showed well-defined yield stresses at axial strains of 2% to 5%. In contrast, the stress-strain curves of specimens tested at elevated temperatures continuously increased with time due to the strain-hardening behavior of the sample. The nonlinear response of cement samples was evident. The strain measured at failure for non-thermal cement was observed to be higher than the strain obtained for thermal cement. Not only was the cement type found to govern the value of the strain at failure, but also other parameters, such as the w/c, test temperature, and confining pressure, could have a substantial impact on the axial deformation. The test results of non-thermal cement showed that increasing the test temperature led to an increase in the strain achieved at peak load, which means that samples tested at a low temperature reached their ultimate strengths earlier. This was the opposite in the case of thermal cement, as at low temperatures, samples experienced less deformation before failure. In general, non-thermal cement paste samples experienced a higher strain at failure than thermal cement specimens.

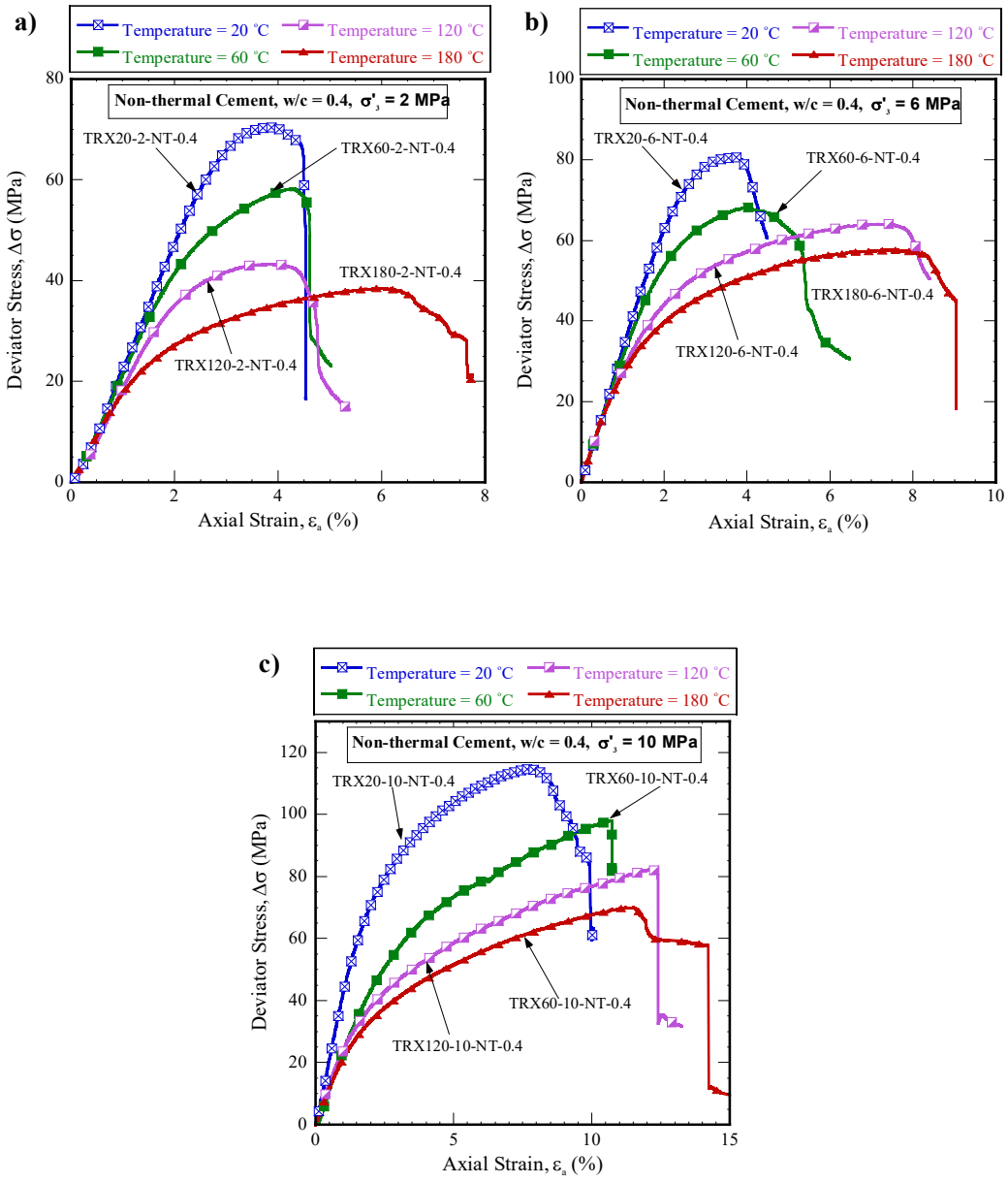

Figure 3.17 Plot of deviator stress vs. axial strain under triaxial compression for non-thermal cement with w/c = 0.4: a) confining stress σ_3'= 2 MPa; b) confining stress σ_3'= 6 MPa; c) confining stress σ_3'= 10 MPa

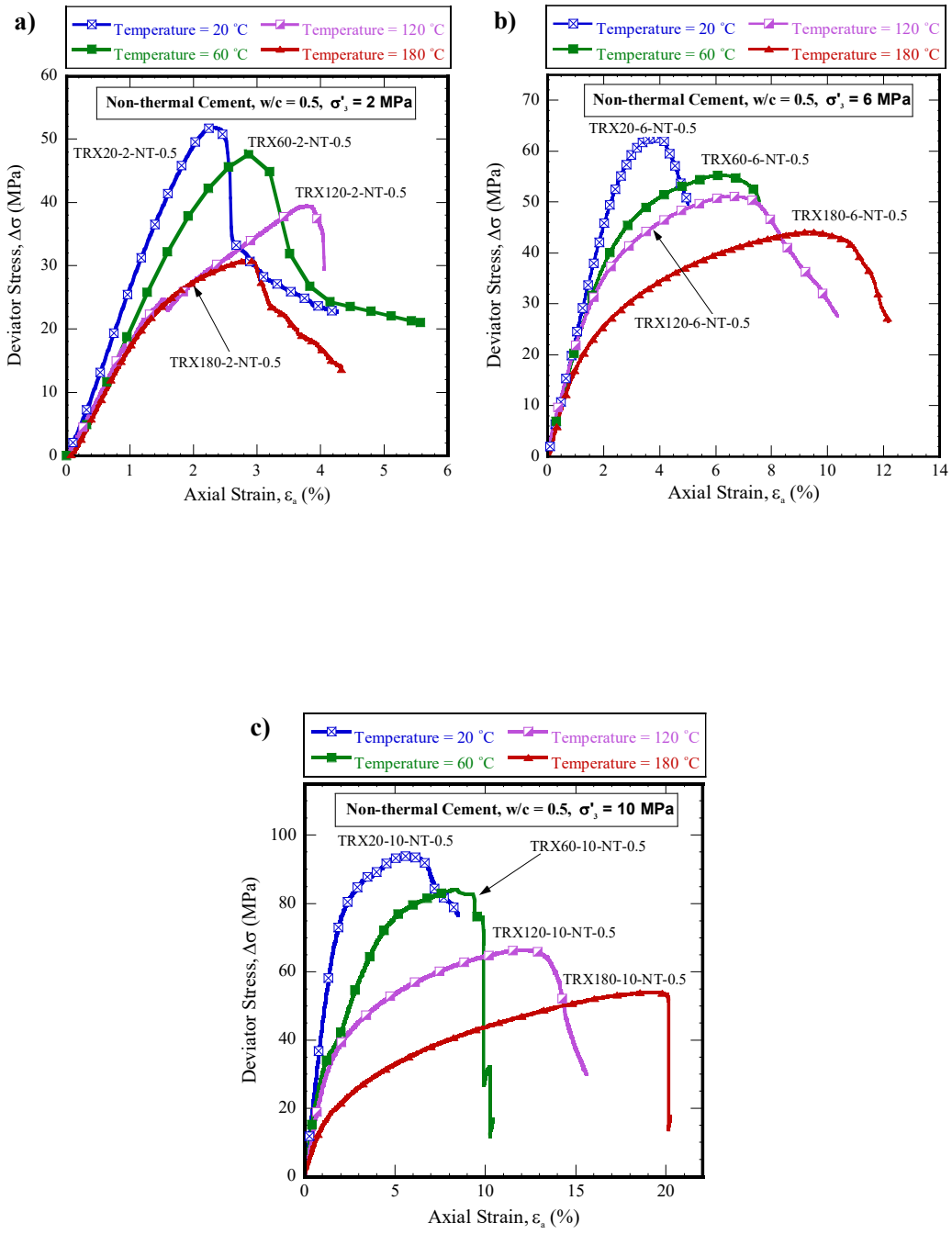

Figure 3.18 Plot of deviator stress vs. axial strain under triaxial compression test for non-thermal cement with w/c = 0.5: a) confining stress; σ_3'= 2 MPa; b) confining stress; σ_3'= 6 MPa; c) confining stress, σ_3'= 10 MPa

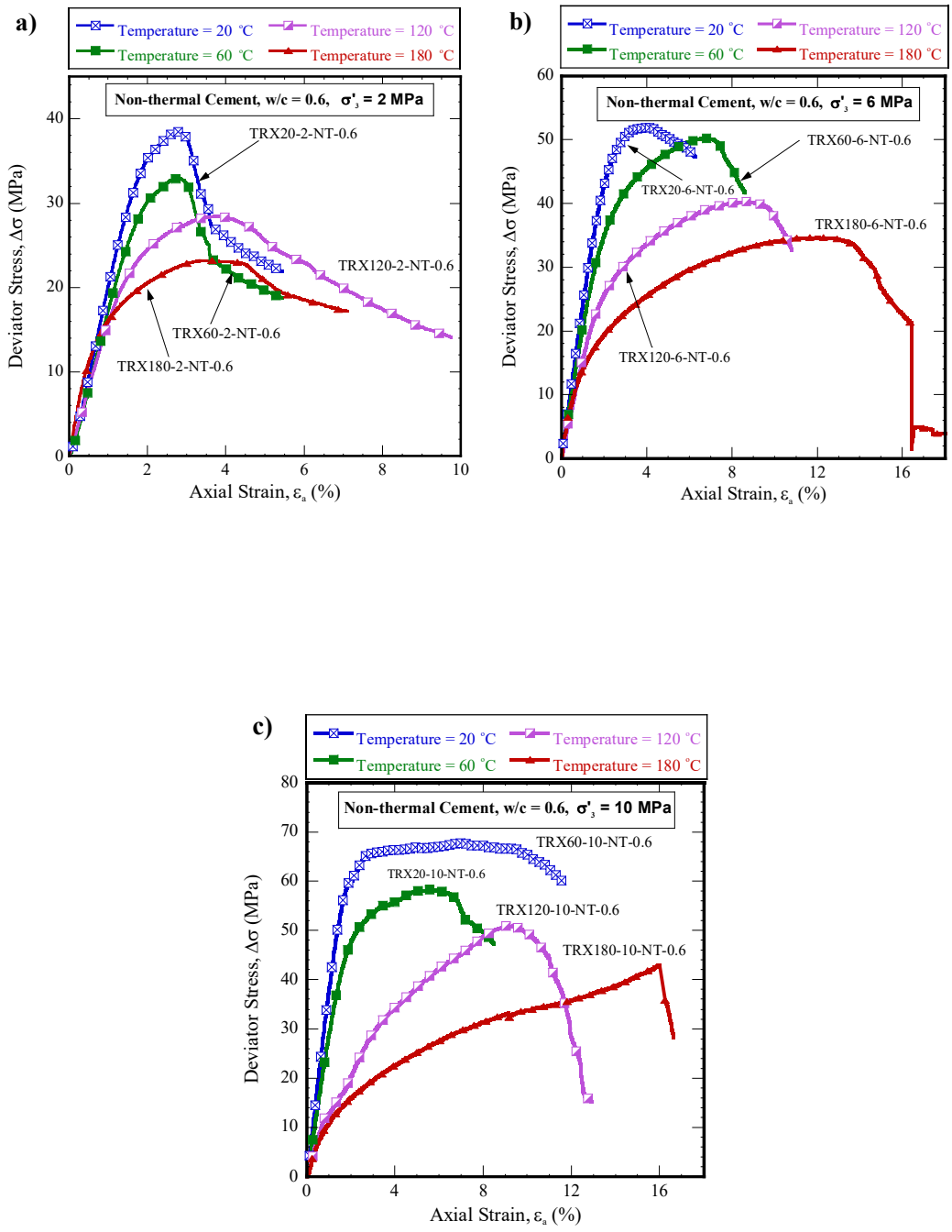

Figure 3.19 Plot of deviator stress vs. axial strain under triaxial compression test for non-thermal cement with w/c = 0.6: a) confining stress, σ_3'= 2 MPa; b) confining stress, σ_3'= 6 MPa; c) confining stress, σ_3'= 10 MPa

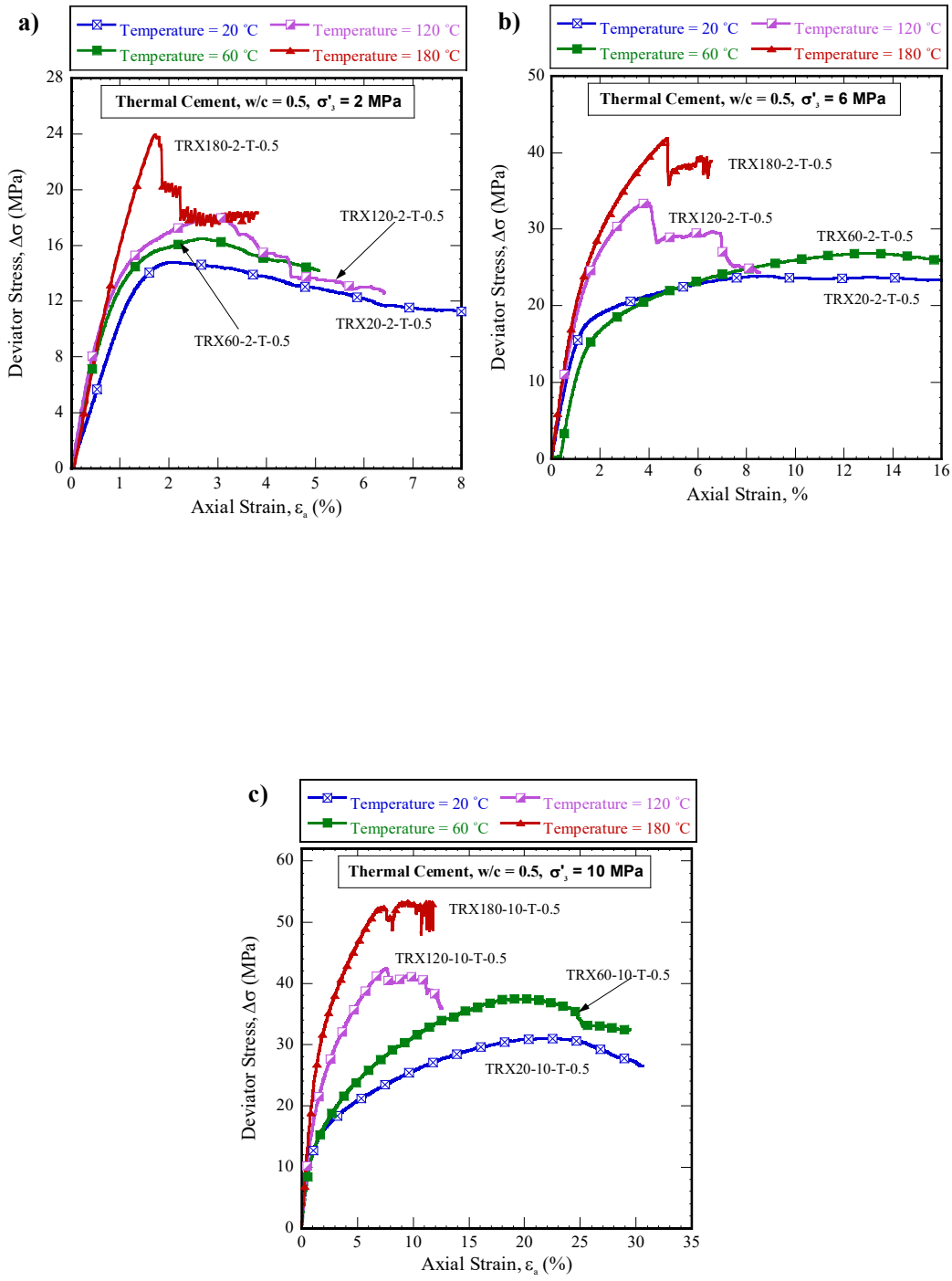

Figure 3.20 Plot of deviator stress vs. axial strain under triaxial compression test for thermal cement with w/c = 0.5: a) confining stress; σ_3'= 2 MPa; b) confining stress, σ_3'= 6 MPa; c) confining stress, σ_3'= 10 MPa

3.9.3.3 Stress path and failure envelope

Several methods can be used to determine the failure envelope under triaxial conditions. The most widely used technique is to plot a Mohr–Coulomb circle from the triaxial test data. This circle has a radius of $(\sigma_1' - \sigma_2')/2$ and its centre is located at $(\sigma_1' + \sigma_2')/2$. This approach can be used to calculate the principal stresses and to estimate the shear stress acting on any inclined plane. In the second method, a t-s plot can be drawn similarly by using the centre and the radius of a Mohr–Coulomb circle.

In this study, a p'-q' plot was employed to analyze the triaxial test results and to obtain shear strength parameters (cohesion, c', and friction angle, φ'). Figure 3.21 and Figure 3.22 show the effective stress path, which describes the relationship between deviator stress (q') and mean effective stress (p') at different stress regimes. Each point on this plot represents a successive stress state experienced by a cement sample during the test. Shear strength parameters can be determined based on the slope of the failure envelope as follows:

$$\tan \eta = 6 \sin \varphi' / (3 - \sin \varphi') \quad (3.25)$$

$$q' = 6 \cos \varphi' c' / (3 - \sin \varphi') \quad (3.26)$$

where *q'* is the intercept of the failure envelope with the y-axis, and *tan η* is the slope of the failure envelope.

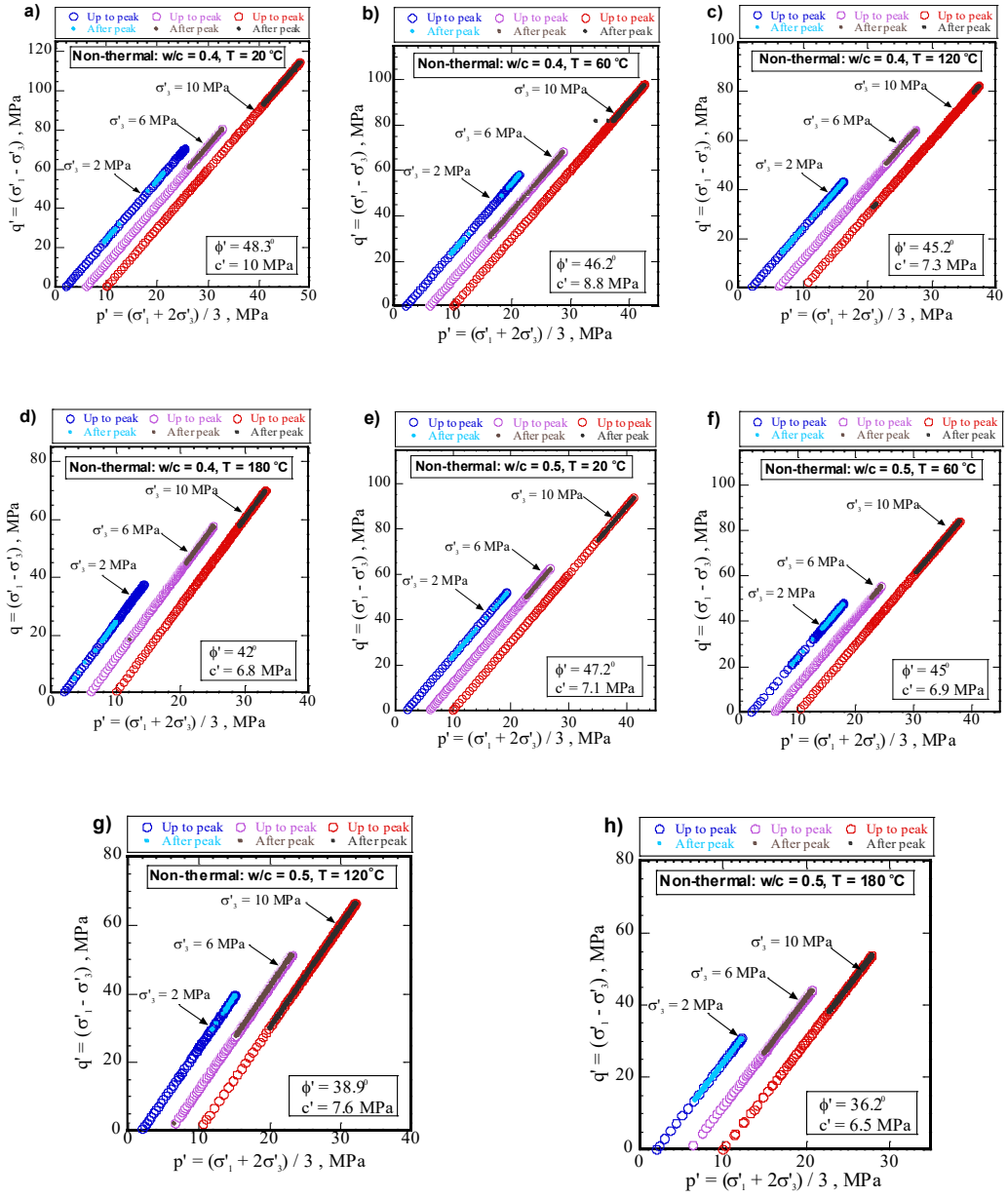

Figure 3.21 Plot of stress path (p'-q') under triaxial compression test for non-thermal cement paste: a) w/c = 0.4 and T = 20 ºC; b) w/c = 0.4 and T = 60 ºC; c) w/c = 0.4 and T = 120 ºC; d) w/c = 0.4 and T = 180 ºC; e) w/c = 0.5 and T = 20 ºC; f) w/c = 0.5 and T = 60 ºC; g) w/c = 0.5 and T = 120 ºC; h) w/c = 0.5 and T = 180 ºC

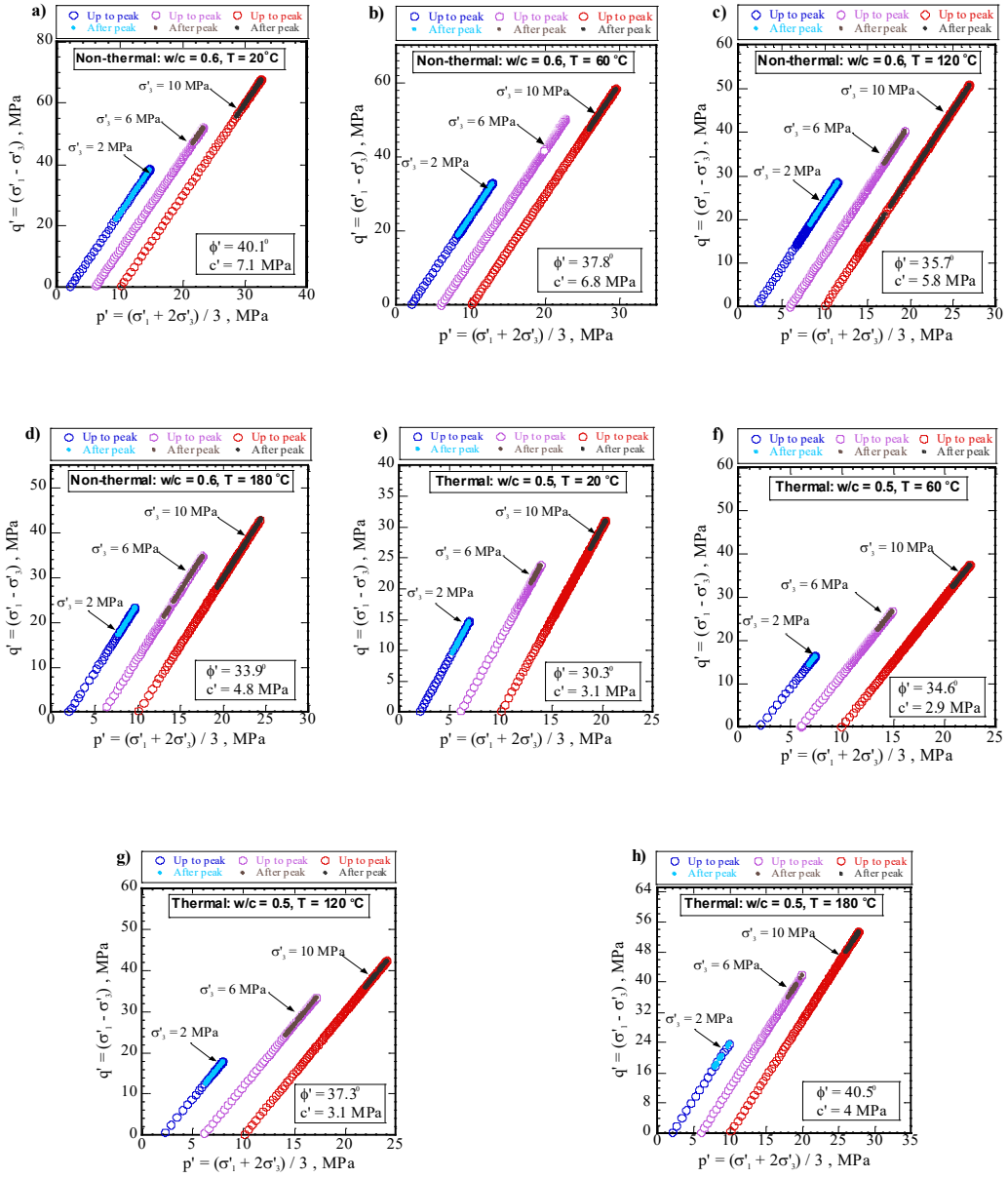

Figure 3.22 Plot of stress path (p'-q') under triaxial compression test for cement paste: a) non-thermal with w/c =0.6 and T = 20 ºC; b) non-thermal with w/c=0.6 and T = 60 ºC; c) non-thermal with w/c= 0.6 and T = 120 ºC; d) non-thermal with w/c=0.6 and T = 180 ºC; e) thermal with w/c=0.5 and T = 20 ºC; f) thermal with w/c=0.5 and T = 60 ºC; g) thermal with w/c=0.5 and T = 120 ºC; h) thermal with w/c=0.5 and T = 180 ºC

3.9.3.4 Variation of deviator stress with cement content and test temperature

To further illustrate the dependence of cement paste behavior on the cement content, Figure 3.23 depicts the combined test results and summarizes the influence of the w/c on the deviator stress at different temperatures. It can be seen that, regardless of temperature and confining pressure, the specimens with higher w/c tended to have a lower maximum deviator stress. However, the ductility was noticeably increased in these samples.

The effect of temperature is evident. In the case of non-thermal cement and for the same confining pressure and w/c, the maximum deviator stress considerably decreased with temperature. In contrast, thermal cement was capable of sustaining more deviator stress at higher temperatures.

3.9.3.5 Variation of deviator stress with confining pressure

Figure 3.24 shows the maximum deviator stress versus the confining pressure at different temperatures for thermal and non-thermal cement. In all cases, the deviator stress at failure rose significantly with an increase in the confining pressure because applying a higher confining pressure increases the stiffness of the sample. However, the impact of confining pressure on the strength of cement was noted to be related to the range of confining pressure. As the confining pressure rises, the corresponding increase in cement strength diminishes. For non-thermal cement, the maximum deviator stress obtained at room temperature was two times higher than the one obtained for thermal cement. However, this difference decreases with temperature.

The impact of confining pressure on the strength was much greater for non-thermal cement than for thermal cement. The results revealed that the deviator stress, obtained for samples made of non-thermal cement with a w/c of 0.5, increased by about 55% when the confining pressure went up from 2 MPa to 10 MPa. On the other hand, the strength of thermal cement rose only about 30% due to the same confining pressure changes. It is worth mentioning that, in the case of

thermal cement, the change in deviator stress due to increasing temperature was less remarkable at a low confining pressure.

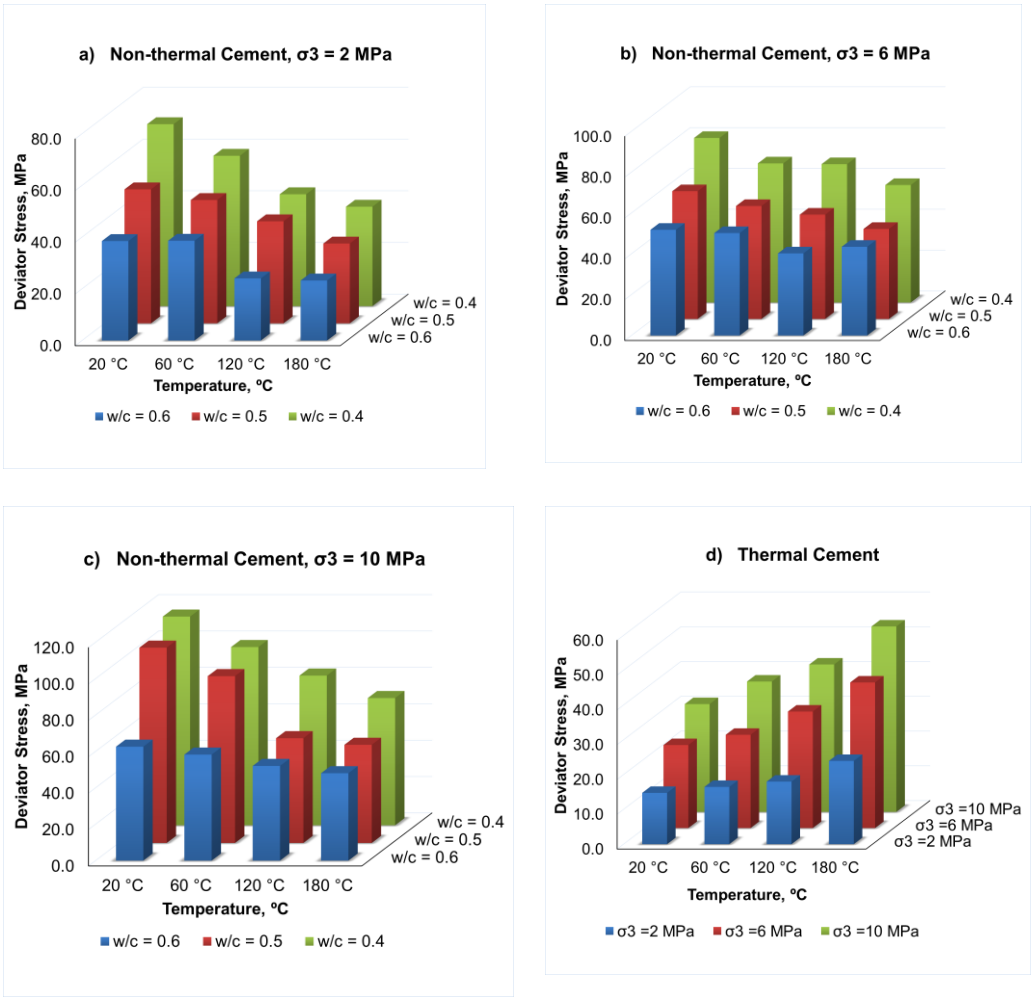

Figure 3.23 Variation of deviator stress with respect to cement content and temperature: a) non-thermal cement at σ'_3 = 2MPa ; b) non-thermal cement at σ'_3 = 6MPa; c) non-thermal cement at σ'_3 = 10MPa; d) thermal cement

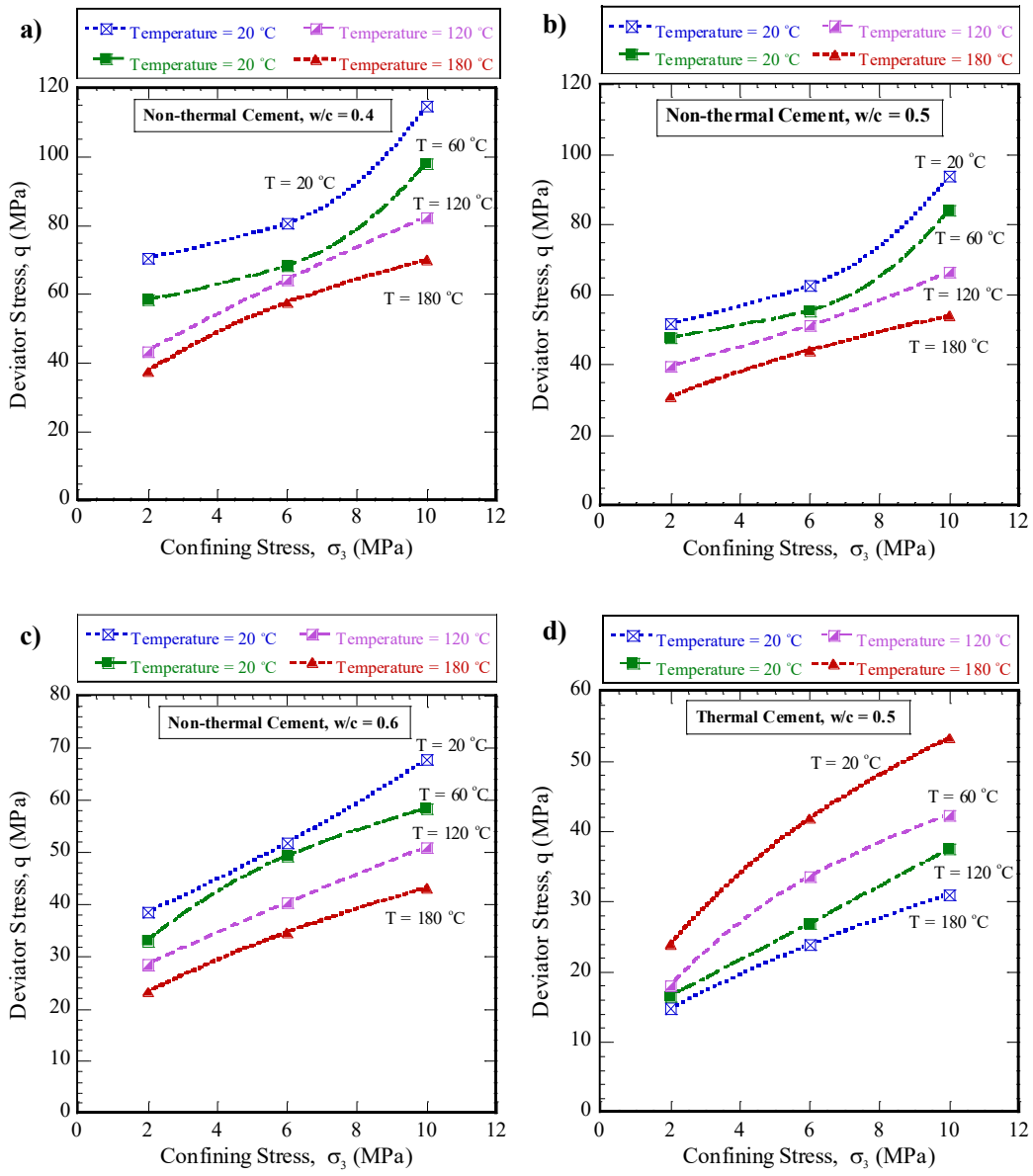

Figure 3.24 Variation of deviator stress with respect to confining pressure: a) non-thermal cement with w/c = 0.4; b) non-thermal cement with w/c = 0.5; c) non-thermal cement with w/c = 0.6; d) thermal cement with w/c = 0.5

3.9.3.6 Effect of temperature on shear strength parameters

As mentioned previously, friction angle and cohesion were estimated from a p'-q' plot. Figure 3.25 shows the variation in the shear strength parameters of cement paste with respect to temperature. It can be seen that the influence of the test temperature on the friction angle is obvious, especially at high temperatures.

The variation of the friction angle with temperature was observed to be dependent on the temperature range. The higher the temperature, the greater the reduction in the friction angle of non-thermal cement paste.

Unlike non-thermal cement, the friction angle values of thermal cement paste follow an ascending trend as the temperature increases. In general, the friction angles of non-thermal cement paste at room temperature were significantly greater than those of thermal cement. However, the difference between the friction angles of the two cement types tends to decrease with temperature, until the friction angle of thermal cement becomes the greatest at 180 °C.

Figure 3.26 presents the variation of friction angle values with the w/c. Data in Figure 3.26 indicates that the friction angle highly relies on cement content. As expected, the friction angle increased with the reduction of the w/c. Specimens with a w/c of 0.6 had the smallest friction angle, measuring 33.8º when tested at 180 ºC. On the other hand, the greatest friction angle, measuring 48º, was obtained at room temperature for samples with a w/c of 0.4.

The impact of temperature on cohesion was less significant than its influence on friction angle. However, it had a similar tendency. The cohesion of the non-thermal cement specimens followed a descending trend as temperature increased. The lowest values of cohesion were recorded for samples tested at elevated temperatures.

Thermal cement experienced the opposite trend. The cohesion of thermal cement first decreased then ultimately increased as the temperature rose.

Generally, the cohesion of thermal cement at room temperature was lower than that of non-thermal cement, but the difference between the two decreased with an increase in temperature. At 180 °C, the cohesion of thermal cement was 25% higher than for non-thermal.

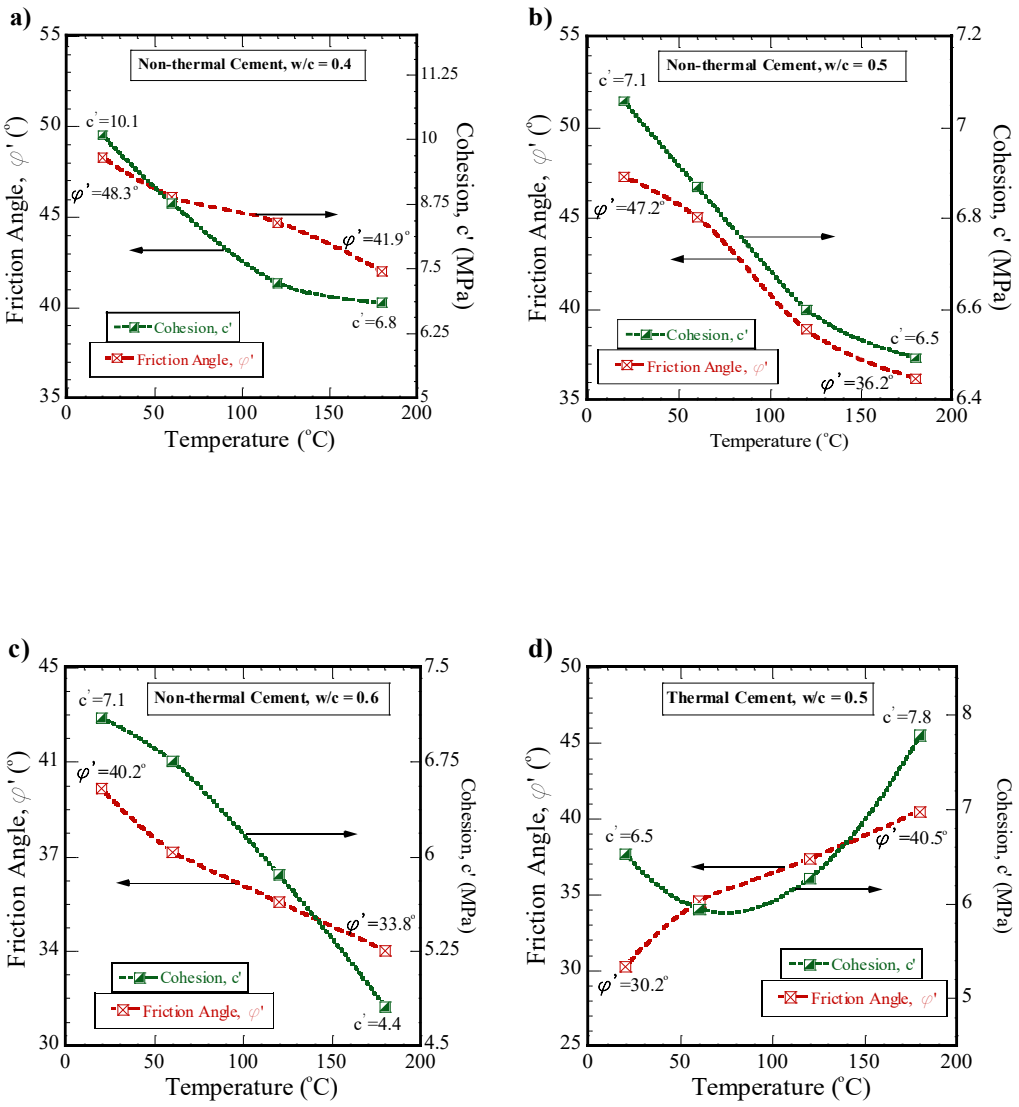

Figure 3.25 Variation of shear strength parameters with respect to temperature: a) non-thermal cement with w/c = 0.4; b) non-thermal cement with w/c = 0.5; c) non-thermal cement with w/c = 0.6; d) thermal cement with w/c = 0.5

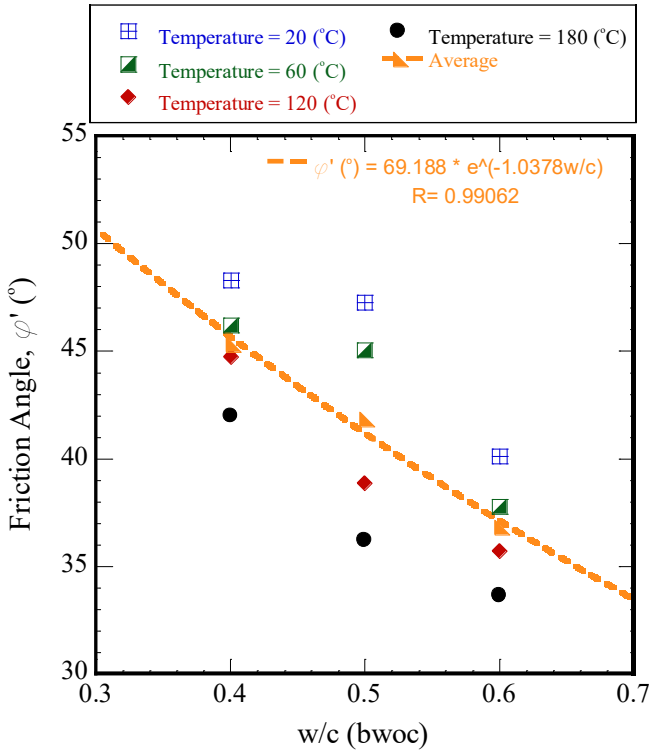

Figure 3.26 Variation of shear strength parameters of non-thermal cement with respect to w/c

3.9.3.7 Variation of Young's modulus with confining pressure and temperature

The test results revealed that Young's modulus of non-thermal cement is generally higher than that of thermal cement. As expected, for a given confining pressure, Young's modulus increases with the w/c. In general, the value of Young's modulus obtained from triaxial test is not constant and mainly depends on the drainage condition and the confining pressure. Drained conditions tend to yield a lower value of Young's modulus. On the other hand, Young's modulus increases when applying high confining pressures. This can be attributed to the impact of the confining stress on the stiffness of the sample. Cement becomes stiffer under high confining pressures.

3.9.3.8 Effect of temperature on failure behavior

The mechanism of cement failure during the triaxial compression test was observed to be primarily dependent on the w/c, confining pressure, and temperature. At a high temperature and low confining pressure, cracks occurred more quickly and vertically. Thereafter, inclined tensile cracks propagated along the sample. On the other hand, cement specimens with a low w/c, tested at a high confining pressure and moderate temperature, were observed to break suddenly in an unsymmetrical manner into only two or three pieces. In addition, a unique failure plane was noted. In contrast, non-thermal cement contained several slip planes. In general, the shape and the angle of the failure plane were found to be highly dependent on whether the cement behaved as brittle or ductile material.

As we can see, the effect of temperature on the mechanical behavior of non-thermal cement is very complex, due to the fact that cement paste includes different phases, such as unhydrated grains, inner and outer calcium silicate hydrate particles, and calcium hydroxide crystals. There could also be voids, which might be filled with air or water based on the saturation state of the sample. The response of each phase to temperature increase is different from other phases. Therefore, each phase experiences deformation differently, which leads to cracking at the surface between different phases. As a result, more degradation of the cement occurs.

3.10 Summary and conclusions

In addition to the impact of elevated temperatures on the compressive strength of non-thermal cement samples, this study investigated the shear behavior and tensile strength of cement specimens at different temperatures. The dependence of the mechanical behavior of cement on the w/c was also studied using specimens with varying w/c. To achieve the study objective, a series of UCS tests, and Brazilian tests was conducted at different temperatures (5 °C, 60 °C, 120 °C, and 180 °C). Test results obtained at 5 °C were used as a benchmark to evaluate the deteriorations occurring in non-thermal cement when exposed to high temperatures. In addition, a series of drained triaxial tests was performed at 20 °C, 60 °C, 120 °C, and 180 °C.

The following conclusions can be drawn from the test results presented in this chapter:

- In order to evaluate the accurate compressive strength of cement paste, when subjected to SAGD operating conditions, it is highly recommended to keep the samples saturated by conducting high temperature tests inside a triaxial cell. Using a dry sample yields a misleading result due to the impact of dryness on the measured compressive strength.
- Water-to-cement ratio (w/c) is a prime factor that controls the performance of cement. Cement strength varies largely with the w/c, especially at high temperatures.
- The compressive strength of non-thermal cement paste is very sensitive to temperature; a high temperature test would produce cement paste with a low compressive strength.
- The temperature effects on the compressive strength differ considerably with the w/c, especially for non-thermal cement.
- The dependency of shear strength parameters on the test temperature was evident. In general, the friction angle and cohesion of non-thermal cement decreased with temperature.
- The temperature effects on the elastic moduli of non-thermal cement were found to be significant. Young's modulus decreased by 30% when the temperature increased from 5 °C to 180 °C.
- The failure mode changed correspondingly with confining pressure and temperature.
- Unlike non-thermal cement, the temperature has a positive impact on the performance of thermal cement. The compressive strength of thermal cement increases with temperature. In general, utilizing thermal cement is known to enhance the performance of cement when subjected to high temperatures.
- Currently, the techniques available to measure tensile strength at high temperatures may induce cracks, due to dryness, which could affect the

accuracy of the results. Therefore, the values of tensile strength obtained from Brazilian test should be used with caution.

- Thermal cement paste had a lower tensile strength compared to non-thermal cement. The difference in strength between the two types of cement was not greatly affected by temperature.
- The test results showed that the maximum deviator stress at failure considerably increases with the cement content. The variation of deviator stress with the w/c is strongly dependent on the applied confining pressure.
- Both the confining pressure and temperature impacted the behaviour of cement at failure. At a high confining pressure and elevated temperature, the cement sample tended to behave as a ductile material. At the same time, the ultimate strength of cement depends very much on these two parameters. The ultimate strength of non-thermal cement decreased with an increase in temperature and a decrease in confining pressure.
- Finally, it should be noted that the experimental results presented in this research were obtained by utilizing Class G thermal and non-thermal cement, which have a certain formulation and cure at specific conditions. When using these results, this information should be taken into account.

Chapter 4 : Determination of Shear Strength Parameters of Cement Paste and Cement-Shale Interface

4.1 Introduction

The primary cementing job is still considered a challenging task in the oil and gas industry. During this operation, cement slurry is pumped into the annulus between the casing and formation. The main functions of this cement are to support the casing and to offer protection against corrosion and drilling shock. Another critical function of the cement sheath is to provide zonal isolation by preventing fluid communication between different formations during the various stages of well life, starting from drilling to abandonment.

In fact, the cement-shale interface behavior usually governs the long-term integrity of oil wells. Failure is often observed to take place at the interface; however, the failure of the rock or cement matrix itself was also noted to occur in some circumstances, especially in the case of soft rock (Ladva et al., 2005).

On the other hand, as shown in Figure 4.1, leakage around a wellbore may occur between the casing and cement, between the cement plug and casing, through the cement pore space, through the casing, through fractures in the cement, and between the cement and rock. It is apparent that uncontrolled leakage not only depends on the quality of the cement, but also on the performance of the cement-shale interface. Accordingly, knowledge of the shear strength parameters of cement paste and the interfacial shear behavior between cement and shale is crucial to assess long-term well integrity, as these parameters are considered key factors to accurately predict the performance of cement paste.

In general, using an accurate representation of cement-shale interface behavior in numerical simulation is essential to obtaining the actual response of the cement sheath when it is subjected to different stresses in the wellbore. Although much work has been conducted on the characterization of the cement-casing interface, studies on the cement-shale interface were limited in the literature. Consequently, a comprehensive testing program was conducted to estimate the

shear strength parameters of the cement-shale interface experimentally. This chapter describes this experimental program in depth. The shear behavior of cement is also analyzed and discussed in detail based on the direct shear test results. However, it was important to first review the characterization of cement-rock interface and highlight factors that may affect direct shear results. The findings of this research improve our prediction of the behavior of the cement-shale interface under SAGD placement conditions.

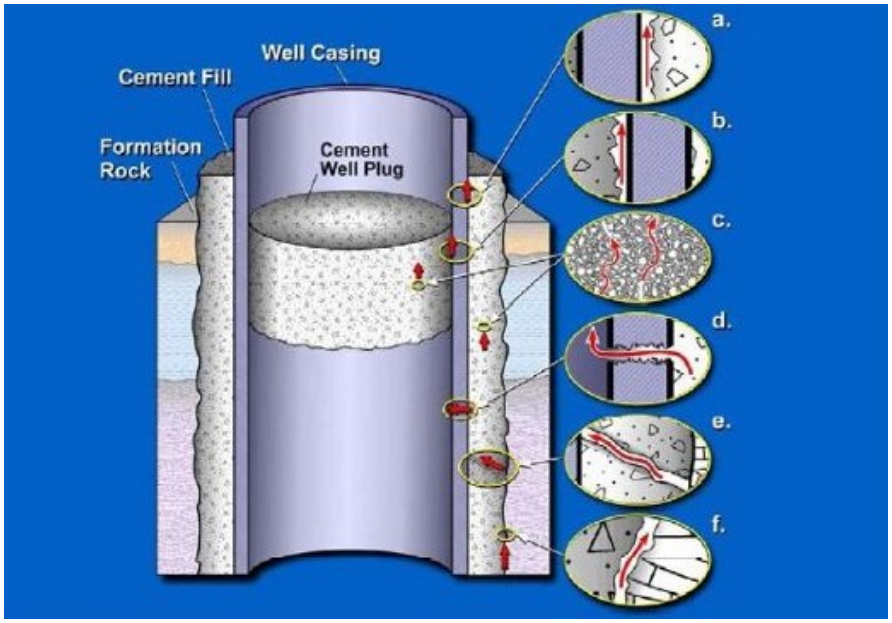

Figure 4.1 Possible leakage paths around a wellbore Gasda (2008)

4.2 Characterization of cement-rock interface

Generally, adhesive force at the interface between the cement and formation is the main factor which dominates the bonding between the two materials (Peterson, 1963). The bonding conditions at the interface between the cement and formation are usually characterized by two measurements, namely the shear bond and hydraulic bond. The shear bond refers to the load required to start the relative displacement between the cement and the surrounding formation, while the hydraulic bond reflects the ability to provide a good seal and prevent fluid migration. Debonding or insufficient bonding can lead to destroying the sealing of the borehole.

In their novel study, Liu et al. (2015) investigated both the shear and tensile bond strengths between cement and shale. Samples were prepared to have an inclined surface of 60° at the interface between cement and shale. The specimens were loaded vertically with a loading rate of 0.03 inch/min until failure occurred. Then the shear bond strength was calculated by dividing the applied shear force at failure by the area of the interface. It was observed that the shear bond strength increased slightly as the temperature increased from 21.1 °C to 65.6 °C. The ratio between the cement-shale shear bond strength and the compressive strength of cement paste was found to be 10% to 20%. The concept of Brazilian splitting test was adopted to estimate the tensile bond strength of the cement-shale interface. The tensile bond strength was found to be much lower than the compressive strength of the cement paste.

In general, the strength of the soil interface usually decreases with displacement due to dilatancy behavior that occurs at the shear plane and causes a reduction in the soil density. Another factor that may lead to further reduction in the interfacial strength is the realignment of soil particles, which occurs at the interface. The impact of this phenomenon on the interfacial shear behavior is largely dependent on soil content and mineralogy (Dixon, 2010).

4.3 Factors affecting cement-rock interface

The cement-rock interface behavior is highly affected by rock formations, the presence of drilling fluid, and the drilling fluid type. In general, the presence of drilling fluid at the interface between the cement and rock weakens the bond between the two materials because the contact area between the cement and rock is reduced. In this case, interface bonding can be improved by utilizing water-based fluid instead of oil-based fluid (Opedal et al., 2014). The impact of the drilling fluid on the bond is fairly related to the rock's porosity. The higher the rock's porosity, the greater the impact of the drilling fluid on the bonding strength (Opedal et al., 2014).

The interfacial bond strength can be enhanced by utilizing surfactants (Cowan & Eoff, 1993; Liu et al., 2015). The impact of surfactants was noted to be

temperature dependent, as utilizing Cocoamidopropyl betaine (surfactants B) increased the shear bond strength by 35% and 27% at 21 °C and 65 °C, respectively.

The effect of temperature on the bonding of cement to formation depends mainly on the temperature range. Raising the temperature up to 120 °C increases the sliding resistance, and then it declines with any further increase in temperature. This undesirable effect of high temperatures can be reduced by adding silica flour, which improves the bond strength at elevated temperatures up to 160 °C (Becker & Peterson, 1963).

4.4 Determining shear strength of cement paste by direct shear test

Besides the compressive and tensile strengths of cement paste, shear strength plays a vital role in cement sheathing integrity. Shear strength properties are regularly utilized as input parameters to define the constitutive model of the cement paste. The shear strength of cement paste is affected by various factors, such as the cement mineralogy, confining pressure, cement content, rate of shearing, and temperature.

Mohr–Coulomb failure criterion is one of the most commonly used criteria in defining the shear behavior of cement-based materials. In order to fully describe any material using Mohr–Coulomb constitutive model, both the cohesion and friction angle must be determined. There is a variety of testing methods to obtain the shear strength parameters of any material, such as triaxial test, ring shear device, and direct shear test. Direct shear test is considered one of the most widely used tests for characterizing the shear strength behavior of the materials due to its simplicity. In addition, this test is relatively cheap and faster to conduct than the triaxial test. However, as with any test, direct shear test has some disadvantages and limitations. For instance, the failure plane is predefined to be horizontal and is not along the weakest plane due to the horizontal direction of the applied shear force (Holtz & Kovacs, 1981; Das, 1985). The non-uniformity of stress and strain distributions along the shear surface is considered another drawback (Wood, 1990).

Moreover, the test should be carried out very slowly to maintain the drained condition because there is no feasible way to measure pore pressure changes during the test. Usually, direct shear test yields higher values than expected for shear strength parameters when the sample dilates during the test, and provides lower values when contraction occurs (Zhang & Thornton, 2007; Cerato & Lutenegger, 2006).

4.5 Factors influencing direct shear test results

The reliability and validity of shear strength parameters obtained from the direct shear box are mainly dependent on the precision of the test results. Therefore, it is important to first understand the different factors that may affect the test in order to be able to minimize their impacts on the accuracy of the results.

4.5.1 Stress distribution in the sample

Several factors may influence the stress distribution in the specimen during the direct shear test, leading to variance in the test results. Among these factors are the configuration and the stiffness of the loading plate, the location of the movable part of the shear box, the horizontal displacement of the movable part of the shear box, and how the vertical load is transferred to the sample (Amsiejus, 2000). Generally, the applied vertical load is transmitted partially to the specimen. The literature showed that only about 65% to 85% of applied normal stress is transferred to the shear plane (Amšiejus et al., 2014).

4.5.2 Size of shear box

The results of the direct shear test are strongly dependent on the size of the shearing device. The effects of the boundary and device friction are greater for smaller machines. It has been reported that the larger the dimensions of the shear box, the greater the cohesion obtained (Hsieh 2003). However, the peak value of the friction angle was found to be independent of the scale effect (Palmeira, 1988).

4.5.3 Configuration of shearing device

Shear strength parameters, obtained by direct shear box, vary with the type of direct shear apparatus. This occurs mainly because the configuration of the shearing device affects the actual value of the vertical force transferred to the sample. Accordingly, it controls the normal stress distribution on the shear plane of the specimen. Amšiejus et al. (2014) compared the results obtained by two different types of shear box, namely SPF-2, and ASD 1/3. The authors conducted a modification on apparatus SPF-2 to allow the user to monitor the normal stress acting on the shear plane. This modification included placing a load transducer onto the lower box.

In their experiments conducted using SPF-2, the vertical loads transmitted to the sample were measured at the top and bottom of the specimens. Meanwhile, two different sets of experiments were completed inside apparatus ASD 1/3. In the first set, the soil volume was kept constant; whereas, during the second set, the applied vertical load was kept constant. In both scenarios, the normal load was measured at the top of the specimen. The authors observed that the shear strength parameters obtained from the SPF-2 apparatus varied significantly compared with those calculated from tests performed using ASD 1/3. The lowest values for the angle of internal friction were recorded for the samples tested inside apparatus SPF-2 under constant vertical load, while apparatus ASD 1/3 gave a higher value of cohesion.

4.6 Experimental program

The experimental program included two stages. The first stage involved estimating the shear strength parameters of cement paste using direct shear tests. In addition, the influence of the w/c on shear strength was examined. The second part of this experimental program focused on characterizing the cement-shale interface. The following sections describe the cement testing plan and procedures that have been used in this chapter.

4.6.1 Factors investigated

The test plan was designed to study the impact of the following factors on both the cement-shale interface properties and the shear strength of cement:

1- Type of cement: two types of cement were examined, Class G thermal and non-thermal cement.
2- Water-to-cement ratio (w/c): three sets of direct shear tests were performed on non-thermal cement samples with different w/c.
3- Curing conditions: samples were cured at 9 °C and 3 MPa.
4- Applied normal stress: direct shear tests on cement paste were performed at normal stresses of 1 MPa, 2 MPa, 4 MPa, and 8 MPa, while vertical stresses of 50 kPa, 250 kPa, and 1000 kPa were used in the cement-shale interface tests.

4.6.2 Materials and sample preparation

In the experimental program herein presented, the study was undertaken on two types of Class G cement, namely thermal cement and non-thermal cement. The physical and chemical properties of these types were discussed earlier in Chapter 2. Cement slurries were prepared in accordance with API specifications. A pressurized curing chamber was used to cure cement specimens at 9 °C and 3 MPa.

4.6.3 Experimental setup for direct shear test

The RDS-100 Digital Rock Direct Shear System from Geotechnical Consulting & Testing Systems (GCTS) was used to conduct direct shear tests on the cement samples. The system basically consists of a lower box that is fixed horizontally and a movable upper box. The system was attached to two ISCO pumps to set and maintain the normal load and shear displacement rate.

An electric motor was used to generate the horizontal movement of the upper half of the shear box. Shear stress is developed as a result of the relative movement between the two halves of the shear boxes. The system is equipped with electronic sensors and a digital display to monitor normal and shear forces as well as vertical and horizontal displacements.

4.6.4 Direct shear test procedure

After curing the cement specimen for 28 days under curing conditions of 9 °C and 3 MPa, the specimen was placed in the lower part of the direct shear box, and the upper part was positioned on top of it. Then, the specimen was subjected to the selected normal stress. Thereafter, the specimen was sheared by applying horizontal force at rate of 0.1 mm/min on the upper box. This rate of deformation has been selected in accordance with ASTM D5607-16 and to maintain the drained condition during the entire test. Before starting the shearing phase, the upper half of the shear box was lifted to keep a distance of 1 mm between the upper and the lower boxes. This was necessary to prevent particles from being trapped and to eliminate friction between the two boxes; otherwise, the occurrence of these factors could lead to inaccurate results. The shear load was applied after the equilibrium state of the vertical displacement was achieved.

Normal stresses of 1.0 MPa, 2.5 MPa, 4.0 MPa, and 8.0 MPa were chosen to examine the shear strength parameters of cement paste specimens. These stresses were selected to represent a reasonable range of in-situ effective stress levels for cement columns, which would typically be utilized in SAGD operation. Normal stress, shear stress, vertical displacements, and horizontal displacements were monitored and recorded during the test. The variation of normal stress throughout the test was less than 2%, which conforms to ASTM D5321. The test was terminated when a shear displacement of 4 mm was reached, which corresponds to about 10% of the shear strain. The experimental program plan of direct shear test can be found in Appendix C.

The mean shear and normal stresses were calculated as follows:

$$\tau = \frac{P_s}{A_c} \tag{4.1}$$

$$\sigma = \frac{P_n}{A_c} \tag{4.2}$$

where P_s is the shear load; P_n is the normal load; and A_c is the cross-section area of the specimen corrected by the change of shear displacement.

$$A_c = \frac{D^2}{2}(\theta - \frac{\Delta x}{D} sin\theta) \tag{4.3}$$

where Δx is the shear displacement; D is the internal diameter of the cylindrical box; and θ is given by:

$$\theta = cos^{-1}(\frac{\Delta x}{D}) \tag{4.4}$$

4.6.5 Experimental setup of cement-shale interface testing

A conventional direct shear test apparatus was used to investigate the interfacial shear strength between clay shale and cement. The test apparatus consists mainly of an upper and lower half boxes. An electric motor is used to generate the horizontal movement of the lower half of the shear box. Normal stress is applied by air pressure. A pressure regulator is used to keep normal stress constant, by avoiding the occurrence of pressure fluctuations throughout the test, even with the presence of significant volumetric strain during the test. A rigid plate is used as a loading plate to distribute applied vertical force evenly on the sample. The shear force is produced by the horizontal movement of the upper shear box.

Two LVDTs are used to measure the vertical and horizontal displacements while applying the shearing force. The applied vertical force and horizontal shear force are recorded throughout the tests using two load cells. The entire system is connected to computer-aided data acquisition software to display and store the results.

4.6.6 Cement-shale interface test procedure

Grease was applied to the inside surface of the shear box to reduce side friction. Saturated sintered stainless steel porous stone was placed in the lower part of the direct shear box, and a Clearwater shale specimen with a diameter of 63 mm was placed on top of it then cement was placed in the upper part on top of the Clearwater sample as shown in Figure 4.2. Then the other porous stone was placed

above the shale sample. The main purpose of these porous stones is to allow free drainage. A seating load of 50 kPa was applied vertically on the clay shale specimen. The shear box was filled with fluid that has a salinity of 3000 ppm. After saturation, the vertical load was increased gradually up to the target stress. After each load increment, the sample was left to consolidate under this load. Before the shearing stage, the locking screws were removed, and the upper box was slightly lifted in order to provide a tiny gap between the upper and lower boxes. The sample was sheared by pushing the lower shear box horizontally. During the test, the shear and normal forces were measured. Two gauges were used to monitor the horizontal and vertical displacements. A displacement rate of 0.002mm/min and 0.01mm/min were used for forward and reverse motions, respectively. These shearing rates were chosen to ensure that draining will occur. The experimental program plan of cement-shale interface test can be found in Appendix C.

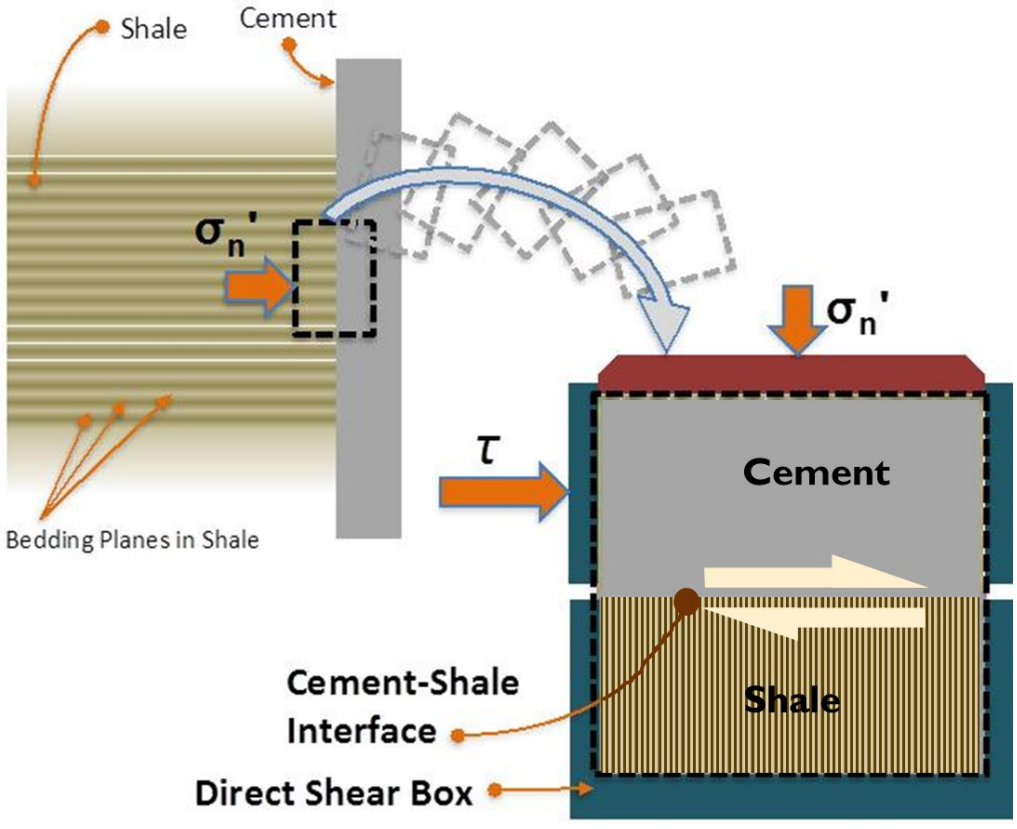

Figure 4.2 Schematic showing cement-shale interface direct shear test setup

4.7 Results and discussion

4.7.1 Direct shear tests on thermal and non-thermal cement

4.7.1.1 Shear behavior of non-thermal cement under direct shear test

Figure 4.3 presents shear stress-shear displacement curves obtained from direct shear box tests conducted on non-thermal cement under different w/c and thermal cement at w/c of 0.5. The applied normal stresses were 1.0 MPa, 2.5 MPa, 4.0 MPa, and 8.0 MPa, respectively. As shown in Figure 4.3, shear stress increased as horizontal displacement increased until peak shear stress was achieved. Generally, the ultimate shear stress was reached with relatively small shear strain. All tested specimens showed a well-defined peak shear strength, regardless of the cement content or normal stress. Shear stress suddenly dropped to its residual value after reaching the peak strength with further increase in the strain. In most cases, increasing the normal stress caused a delay in achieving peak shear stress. Thus, specimens tested under high confining pressure experienced more deformation than samples tested at low confining stress. This can be explained by the friction mobilization, which occurred at the maximum shear strength.

In addition, the value of strain at failure was observed to be somehow dependent on the w/c. The test results of non-thermal cement showed that increasing the w/c led to a reduction in the strain achieved at peak load, which means that samples with low cement content reached their ultimate strengths earlier. Generally, failures occurred at about 0.9% to 2.8% strain. The upper value was recorded for the cement paste sample with a w/c of 0.4 tested at a normal stress of 8 MPa.

The test results illustrated the independency of shear stiffness of cement samples with a w/c of 0.4 on the applied normal stress because of the rigidity of the specimens. As shown in Figure 4.3, all the samples have the same stress-strain curve slope regardless of normal stress. However, the impact of normal stress on the sample stiffness started to slightly appear for samples with a w/c of 0.5 and 0.6.

Figure 4.3(d) depicts the direct shear test results for thermal cement. As shown in Figure 4.3, the shear stress-strain curve shows a pattern similar to that of non-thermal cement. However, the values of the peak and residual shear stresses were considerably lower than those obtained for non-thermal cement. The shear stress of thermal cement continued to increase until it reached its peak value, then it suddenly dropped to the residual stress. It should be noted that the shear strain at peak stress for thermal cement was lower than the shear strain at peak strength for non-thermal cement. Unlike non-thermal cement, thermal cement samples tested at low temperatures experienced less deformation before failure. In general, non-thermal cement paste samples experienced a higher strain at failure than thermal cement specimens did. It should be mentioned that the results of the direct shear tests on non-thermal cement with a w/c of 0.5 were used as benchmark for further comparison with thermal cement.

Figure 4.4 shows the vertical displacement versus the horizontal shear displacement curves obtained from the direct shear tests conducted on non-thermal cement. Initially, the sample contracted a small amount. Subsequently, the specimens exhibited dilatancy behavior. Shear dilation started at a horizontal displacement of about 0.75 mm to 2.1 mm. The rate of dilation increased with the progress of shear displacement until ultimate strength was reached. The amount of dilation that affected the sample increased significantly right after reaching the peak strength due to crack propagation. Thereafter, the dilation rate declined dramatically until the curve started to reach a plateau. Two factors were observed to affect the contraction-dilation behavior of cement paste. Firstly, decreasing the w/c delayed the occurrence of dilation. Secondly, samples tested at a relatively low normal stress experienced greater vertical displacement.

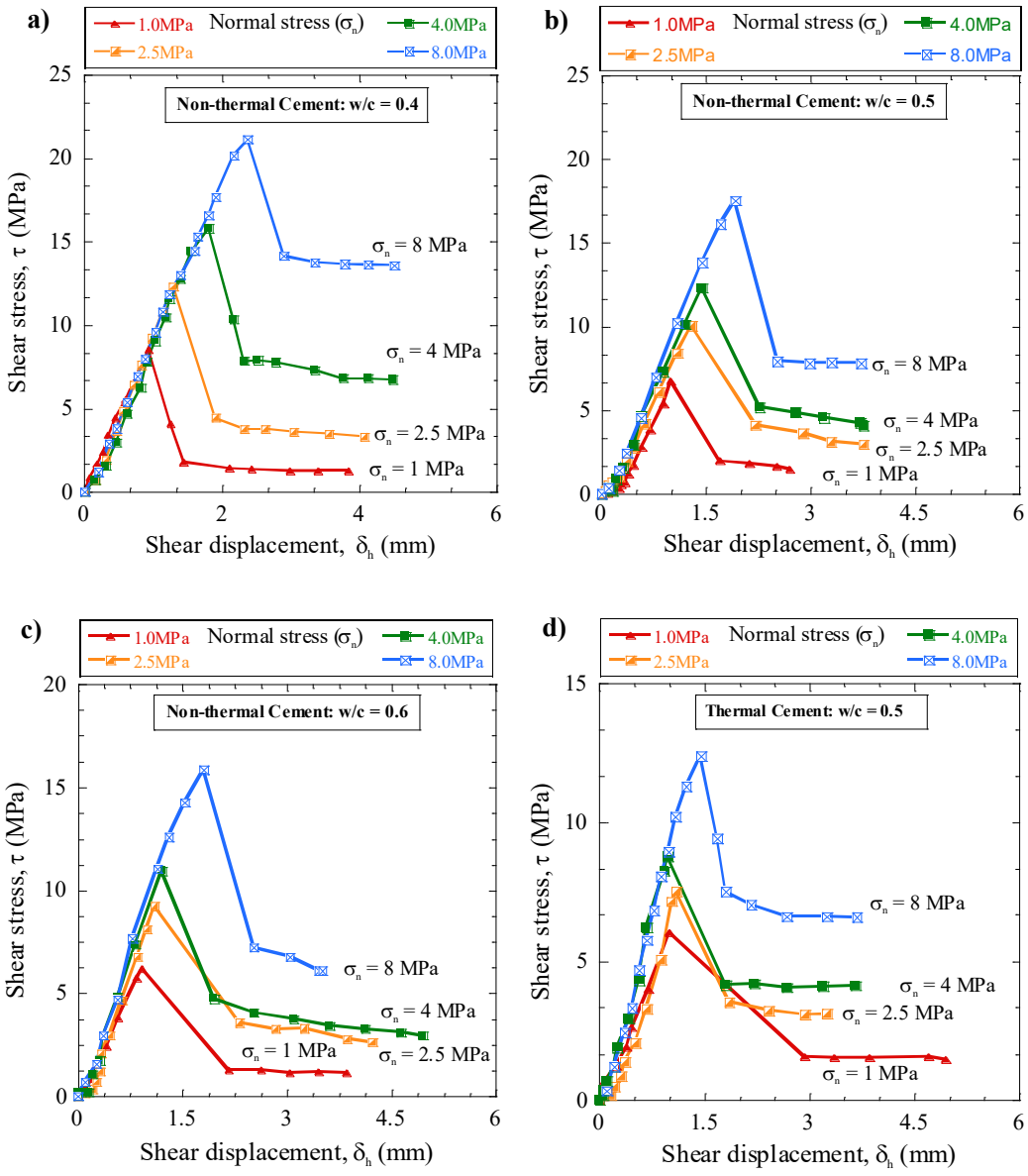

Figure 4.3 Shear stress-shear displacement curves for: a) non-thermal cement samples with w/c of 0.4; b) non-thermal cement samples with w/c of 0.5; c) non-thermal cement samples with w/c of 0.6; d) thermal cement samples with w/c of 0.5

As shown in Figure 4.4(d), thermal cement has the same general trend as the contraction-dilation behavior. However, the thermal samples initially contracted more than the non-thermal cement specimens. In addition, shear dilation started earlier with a lower value achieved at the end of the test. Moreover, the

effect of normal stress on dilation was found to be smaller, which means fewer changes in vertical displacement occurred due to any increase in the normal stress.

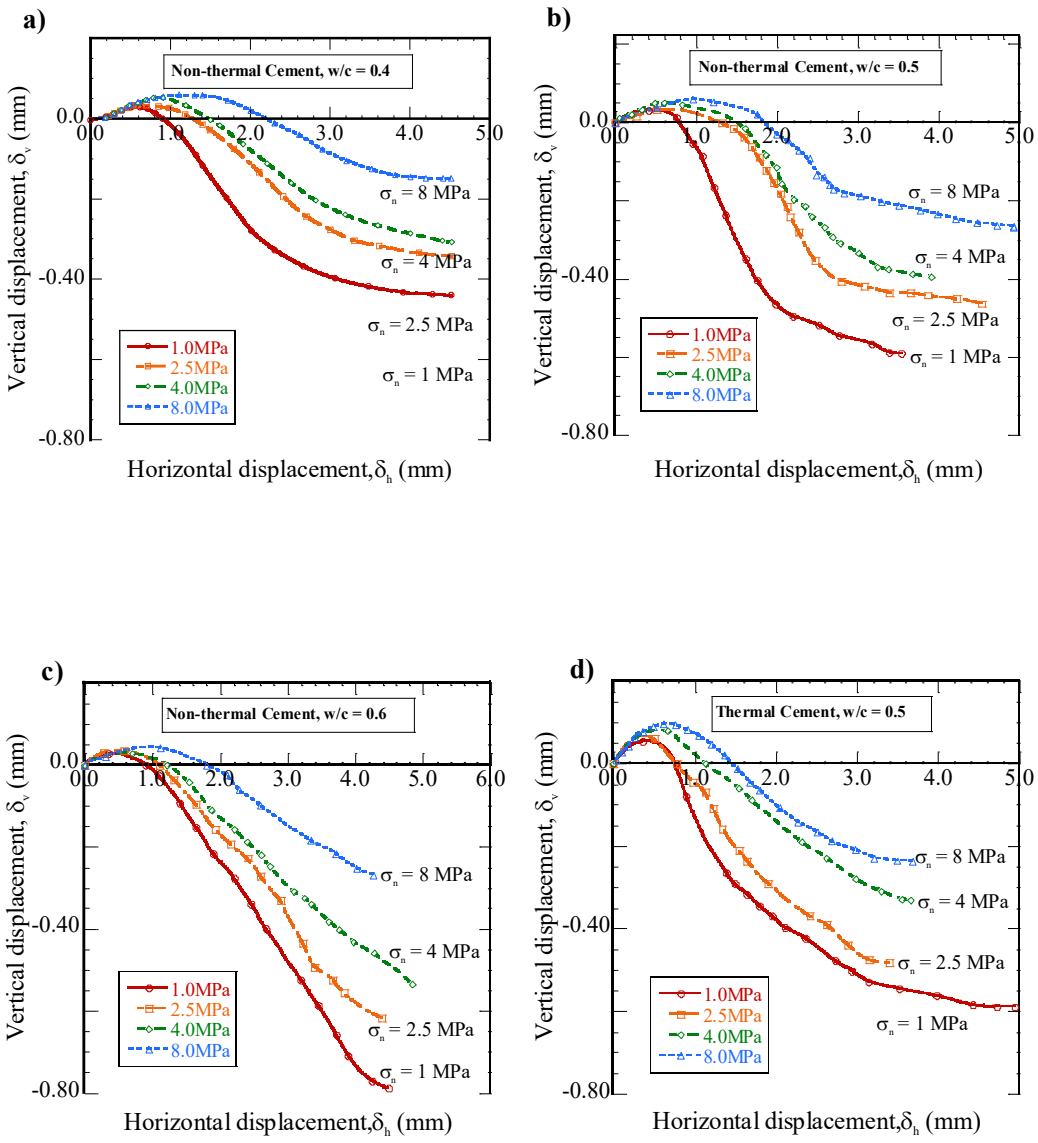

Figure 4.4 Vertical displacement across the shear plane of the specimens: a) non-thermal cement with w/c = 0.4; b) non-thermal cement with w/c = 0.5; c) non-thermal cement with w/c = 0.6; d) thermal cement with w/c = 0.5

4.7.1.2 Impact of w/c on shear behavior of non-thermal cement under direct shear test

To illustrate the impact of w/c on the stress-strain behavior of cement paste, the relationship between the maximum shear strength and the w/c for non-thermal cement is plotted in Figure 4.5. The figure shows that samples with the lowest w/c reached a higher shear stress than other samples before failure. The difference in peak shear stresses, between samples with different w/c, was not significantly affected by increasing the applied normal stress. It can be seen that the maximum shear stress curves of samples with different w/c are nearly parallel to each other. The maximum shear strength declined by about 24% when the w/c increased from 0.4 to 0.5, while the shear stress at failure for samples with a w/c of 0.5 was found to be 10 % higher than for samples with a w/c of 0.6.

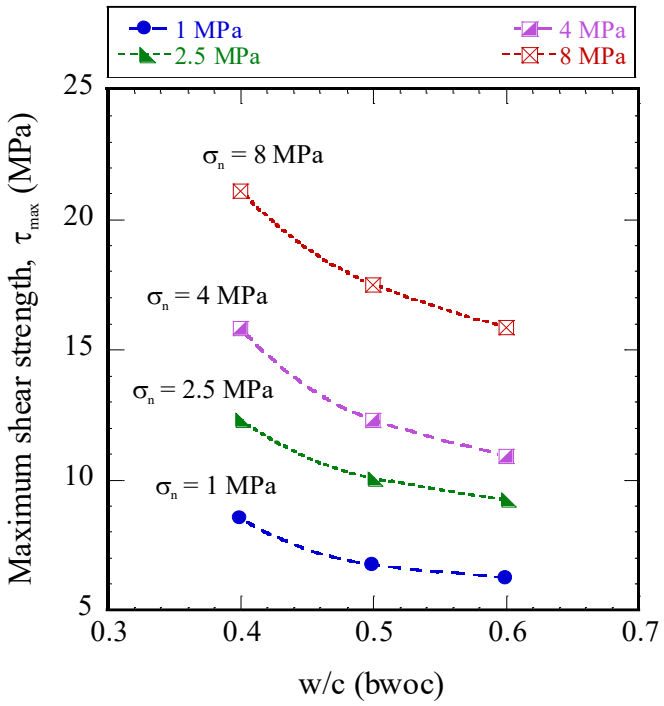

Figure 4.5 Relationship between maximum shear strength and w/c for non-thermal cement

4.7.1.3 Effect of w/c on mode of failure

All specimens with a different w/c were visually inspected after removing the samples from the apparatus. The impact of cement content on the mode of failure was trivial. The shearing planes were observed to have the same shape for all specimens, regardless of w/c or normal stress. As shown in Figure 4.6, the shear failure plane is not totally even due to the presence of a tiny space between the upper and lower shear boxes. Therefore, cracks started to propagate at this zone first before they extended to the specimen.

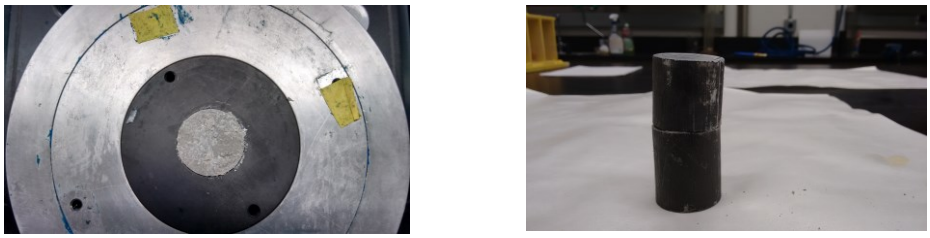

a) **b)**

Figure 4.6 Mode of failure of cement paste under direct shear test: a) top view; b) side view

4.7.1.4 Failure envelope and shear strength parameters of cement paste

Figure 4.7 depicts the relationship between peak/residual shear stress and applied normal stress. It can be observed that shear stress increases almost linearly as normal stress increases. Therefore, cement paste has a linear failure envelop which can be described by the Mohr-Coulomb criterion; whereas, the relationship between the shear stress (τ), friction angle (φ'), and cohesion (c') can be written as:

$$\tau = c + \sigma_n' \, tan\varphi \tag{4.5}$$

The difference between peak and residual friction angles varied from 37% to 43%. This difference was observed to be dependent on cement content; the higher the w/c, the smaller the residual friction angle. In general, non-thermal cement had a smaller ratio between its peak and residual values as peak friction angle was 20% higher than the residual value.

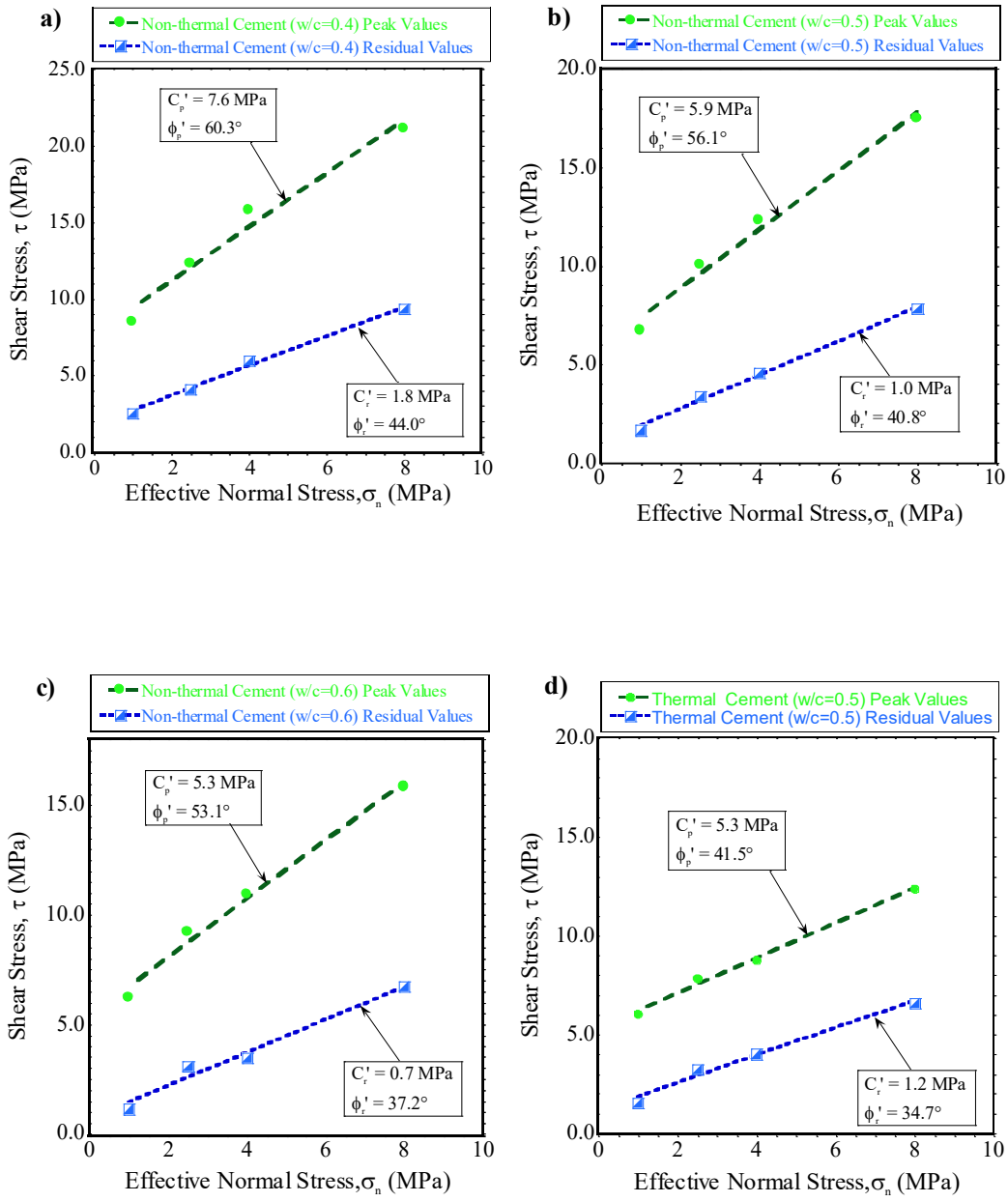

Figure 4.7 Linear Mohr-Coulomb envelope failure for peak and residual shear strength of: a) non-thermal cement with w/c of 0.4; b) non-thermal cement with w/c of 0.5; c) non-thermal cement with w/c of 0.6; d) thermal cement with w/c of 0.5

Figure 4.8 shows the influence of the water cement ratio (w/c) on the friction angle (φ'). As the w/c increased, the friction angle was observed to decrease. The peak value of the friction angle (φ'_p) dropped by about 14% when the w/c changed from 0.4 to 0.6. The impacts of the variations in w/c on both the peak and residual values of the friction angle were nearly the same. It is apparent that the two curves are almost parallel to each other. The empirical relationships between the friction angle of cement paste and the w/c can be derived from Figure 4.8 and are given by:

$$\varphi'_p = 74.5 - 36(w/c) \quad (4.6)$$

$$\varphi'_r = 57.66 - 34(w/c) \quad (4.7)$$

where φ'_p and φ'_r are the peak and residual values of the friction angles, respectively, and w/c is the water-to-cement ratio (bwoc).

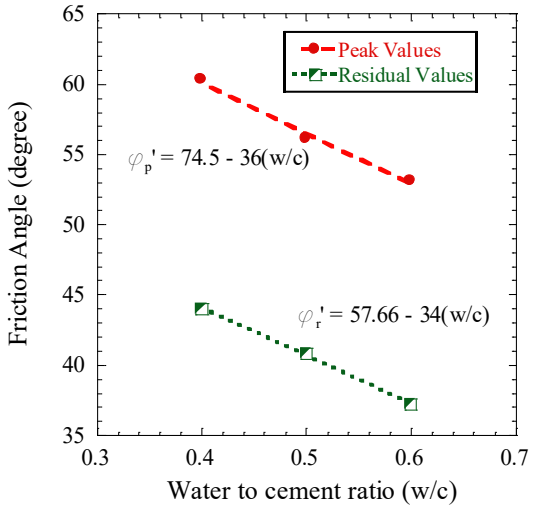

Figure 4.8 Relationship between friction angle and water-to-cement ratio for non-thermal cement

4.7.1.5 Comparison between thermal and non-thermal cement

To distinguish between the behavior of thermal and non-thermal cement pastes, a comparison between data in Figure 4.7(c) and (d) was done. It was concluded that changing the type of cement does not considerably affect the general shear behavior of cement paste. A linear relationship between the cement shear strength and applied normal stress was found in both cases. Using non-thermal

cement markedly enhances the shear strength due to the significant increases in the shear strength parameters. Comparing the friction angle of thermal and non-thermal cements, the latter's friction angle increased by 26%. However, cohesion did not increase significantly, as cohesion changed only from 5.9 MPa to 5.3 MPa as a result of using thermal cement as opposed to non-thermal cement. As expected, the shear strength of non-thermal cement was found to be higher than the shear strength of thermal cement. The ratios between the peak strength of the two cement types fall between 11% and 41%. This ratio was noted to be highly affected by normal stress. In general, the difference in the ultimate strength between thermal and non-thermal cements increased with the initial normal stress. This variability in thermal cement shear behavior is evidence of the significant impact that silica flour exerts on the shear performance of cement paste.

4.7.2 Cement-shale interface test results.

4.7.2.1 Shear behavior of cement-shale interface

In this study, the shear strength of the interface between the cement paste and shale was characterized using a series of direct shear tests. Stress-strain curves obtained from these experiments are plotted in Figure 4.9. It can be seen that shear stress increased with shear displacement until it reached its ultimate value. Thereafter, it dropped gradually to its residual strength. The maximum values of the ultimate and residual strengths were 578 kPa and 368 kPa, respectively. These numbers were recorded during experiments conducted on non-thermal cement specimens with a w/c of 0.4 and tested under normal stress of 1000 kPa. In general, samples of non-thermal cement with a w/c of 0.4 had the highest peak stress. However, increasing w/c from 0.5 to 0.6 had a trivial effect on the sample strength, as ultimate shear stress was very similar in both cases.

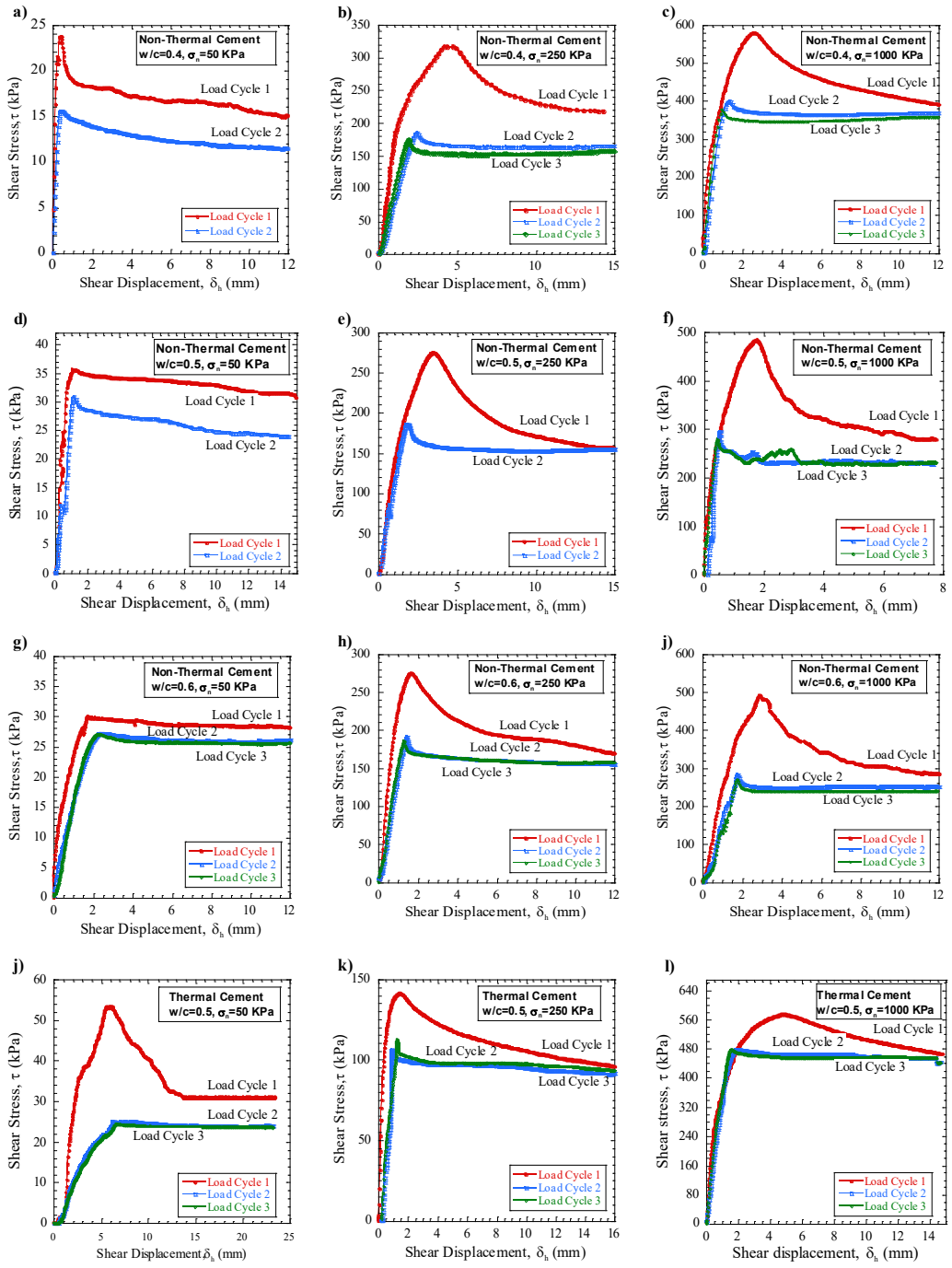

Figure 4.9 Shear stress-shear displacement curves obtained from cement-shale interface tests

The initial part of the stress-strain curve was noted to be fairly linear; however, samples exhibited a nonlinear behavior before failure. During the second load cycle, the stress-strain curve showed a slightly different pattern. The ultimate

strength dropped significantly by more than 30% in most cases. In addition, the peak stress was reached earlier. Thermal cement exhibited ductile behavior that has no clear peak value during the second load cycle. On the third load cycle, the interfacial behavior remained fairly unchanged with an almost similar value for the peak strength.

Comparing the behaviors of the different cement paste types with the same w/c showed that not only was the ultimate strength of the thermal cement-shale interface greater than that of the non-thermal cement, but it also was reached at a higher value of shear displacement. From the results, it is obvious that the interfacial shear behavior is greatly dependent on the applied normal stress. The higher the initial normal stress, the greater the ultimate strength. The interfacial strength increased by about 45% when changing the normal stress from 250 kPa to 1000 kPa. It is worth mentioning that the smaller the applied normal load, the greater the effect that increasing the normal stress has on the strength of the interface. Moreover, the normal stress has some impacts on the interfacial shear stiffness. The slope of the stress-strain curve was observed to increase with the normal stress. Therefore, it is crucial to conduct tests under ranges of normal stress that resemble real field conditions, in order to obtain reliable and representable results. Finally, the impact of normal stress on the maximum strain achieved at failure was inconsistent to some extent.

Figure 4.10 shows the shear strength versus the applied normal stress obtained from cement-shale interface tests. Although the relationship between shear and normal stress shows some non-linearity, especially at low normal loads, data analysis showed that this relationship can be represented by a line with a coefficient of determination (R^2) of 0.88 and 0.99 for thermal and non-thermal cements, respectively. Therefore, the Mohr–Coulomb theory can be adopted to construct the failure envelope and to predict shear strength parameters.

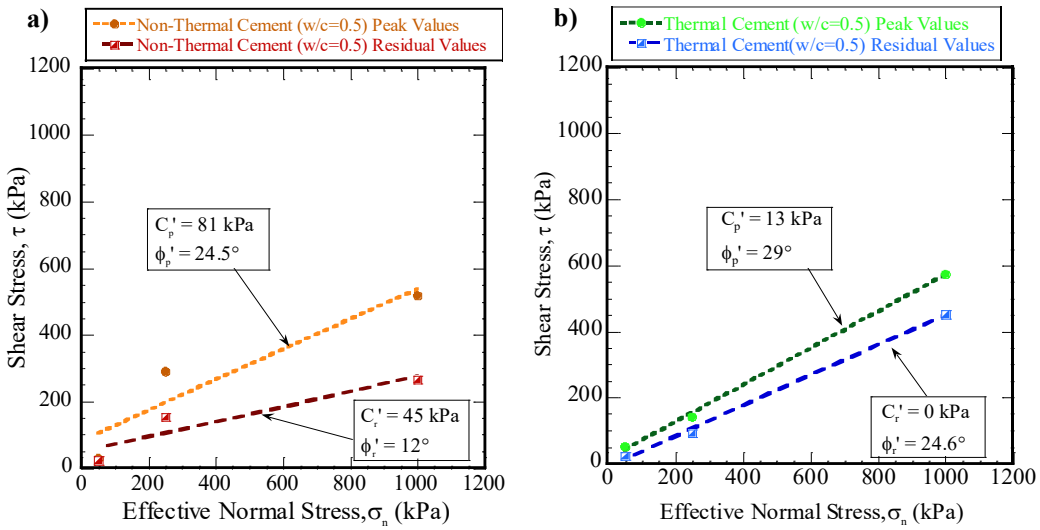

Figure 4.10 Mohr-Coulomb failure envelope for cement-shale interface: a) non-thermal cement with w/c of 0.5; b) thermal cement with w/c of 0.5

Table 4.1 summarizes the peak and residual values of cohesion, c', and the friction angle, φ', of the Mohr–Coulomb failure envelope for both thermal and non-thermal cement-shale interfaces. It was found that the friction angle tends to be higher in the case of thermal cement. However, the greatest value of cohesion was recorded in the case of non-thermal cement. The interfacial friction angle of thermal cement-shale was 29º. This value dropped to 24.5º for non-thermal cement. The difference between the peak and residual friction angles for the thermal cement-shale interface was observed to be lower than for non-thermal cement. These differences were 17% and 48% for thermal and non-thermal cements, respectively.

In general, the shear strength parameters of the interface were observed to be lower than the internal shear strength of the shale itself. This can be attributed to the sliding behavior that occurs at the interface.

Both the shale and cement surfaces were visually examined immediately after removing the sample from the direct shear box. It was observed that shearing took place locally at the interface between the cement and shale. The cement type and w/c were observed to have insignificant effects on the mode of failure.

Table 4.1 Comparison of the shear strength parameters obtained for cement-shale interface

Formulation	Friction Angle (º)		Cohesion (KPa)	
	Peak	Residual	Peak	Residual
Non-Thermal Cement	24.5	12	81	45
Thermal Cement	29	24	13	0

All samples have w/c of 0.5

In general, the shear resistance at the cement-shale interface can be attributed to the shear resistance between the two surfaces of shale and cement in addition to the internal shear resistance of shale particles, which are trapped in the grooves of the cement. Several phenomena may affect interfacial shear strength, such as rolling, sliding, and the interlocking of shale grains at the cement surface. In summary, the development of shear resistance along the cement-shale interface could be due to the interaction between different mechanisms. For instance, the shale could penetrate the cement's surface, during and even after hydration, due to the application of a normal load and a capillary force generated at the interface because of the existence of water. In addition, the roughness of the hardened cement surface develops more friction between the cement and shale.

4.8 Summary and conclusions

This chapter presents insights about the shear behavior of the cement-formation interface along with the shear strength parameters of cement paste. It specifically deals with characterizations of cement-shale interface. The similarities, as well as the differences, between the performance of thermal and non-thermal-cement are highlighted to clarify the impact of cement's chemical composition on its performance.

A set of direct shear tests was performed on cement paste made of Class G non-thermal cement with w/c of 0.4, 0.5, and 0.6. Thermal cement specimens with a w/c of 0.5 were also investigated. All specimens were cured at 9 °C and 3 MPa. The effect of the w/c on the shear behavior of cement paste was studied in terms of the friction angle and cohesion. Tests were conducted under a wide range of normal stresses. These levels of normal stress were chosen to be close to the in-situ stress

and to be smaller than the compressive strength of cement paste. The maximum shear resistance of cement paste was observed to be highly dependent on the normal stress, regardless of the cement type or w/c of the sample. The impact of normal stress on the peak shear strength was observed to be more significant at a lower w/c. The general behavior of the shear stress-displacement curve of thermal cement was similar to that of non-thermal cement. However, the maximum shear strength of non-thermal cement was more sensitive to normal stress than thermal cement.

In general, all samples showed a well-defined peak shear strength. This peak shear strength and its corresponding horizontal displacement increased with the normal stress. A linear relationship between the shear strength of cement paste and the normal stress was noted in all cases. As expected, higher values of the maximum shear strength were recorded for samples of non-thermal cement rather than thermal cement. The angle of shearing resistance was found to be dependent on the cement content. Increasing the w/c led to a reduction in the shear strength of the sample. The values of the peak friction angle, obtained from direct shear tests conducted on non-thermal cement paste with different w/c, varied from 60.3º to 53.1º. This value increased as the w/c decreased. On the other hand, the residual friction angle fell in the range between 44º and 37.2º. It is worth mentioning that, in most cases, the volume contraction induced by the direct shear increased with a decrease in normal stress.

In the second part of this chapter, the interaction mechanism between cement and shale at the interface was investigated through a conventional direct shear test apparatus. The direct shear test has proven to be a valuable tool to investigate the characterization of the cement-shale interface by obtaining interface shear strength parameters.

Overall, the interfacial cement-shale shear strength is largely dependent upon the combined effects of the index properties of the shale and the cement paste surface conditions. The test results demonstrated the presence of an apparent cohesion at the interface between the cement and shale. Moreover, the friction angle was found to be stress dependent. A linear relationship between the shear stress and

normal stress was established. The greatest angle of shearing resistance at the interface was observed for thermal cement. Using thermal cement increased the friction angle from 24.5º to 29º. However, a higher value of cohesion at the cement-shale interface was obtained for non-thermal cement. The effect of the w/c on the interface behavior was slightly significant. It was noted that the friction angles were very similar for all w/c values, declining from 26.4º to 24.5º when the w/c changed from 0.4 to 0.5.

Chapter 5 : Experimental Study on the Mechanical Properties Evolution of Oilwell Cement during Setting and Hardening

5.1 Introduction

Assessing the early-age behavior of oilwell cement is essential to planning drilling and completion operations, and to evaluating the performance and the integrity of the well during the later stages. Overestimating the strength of the cement sheathing could lead to serious problems. In fact, determining the early-age properties of cement paste is not an easy task. During this stage, the sample transitions gradually from a liquid state to a solid state. These changes in the cement phases are accompanied with a volume reduction, and any external factor, such as pressure or temperature, would greatly affect the hydration process. In the last decade, several techniques, based on acoustics, have been developed to investigate cement-based materials at early age, such as ultrasonic pulse velocity method, ultrasonic wave reflection method, resonant frequency method, and acoustic emissions. Generally, the ability of the shear modulus technique to monitor the development of the microstructure during the first two hours was found to be much better than ultrasonic wave measurements. However, after the initial setting, ultrasonic wave measurement is considered a valuable tool to investigate the evolution of the cement matrix structure (Keating et al., 1989).

In this study, a Mechanical Properties Analyzer was employed to continuously monitor the setting process of oilwell cement under high pressure and at an elevated temperature. The elastic properties and the compressive strength of cement samples were measured and recorded during the first 24 hours of the hydration process. In this chapter, the impact of the curing conditions on the performance of the cement paste is discussed. It is essential to first explain the characteristics of different types of ultrasonic waves and to briefly discuss the available acoustic techniques along with their advantages and limitations. These topics are covered in the next sections of this chapter.

5.2 Theoretical background

The compression or primary (P) wave, shear or secondary (S) wave, and surface or Rayleigh (R) wave are the three principal types of acoustic waves. The compression wave travels through all kinds of materials, including solids, liquids, and gases, while the shear wave passes only through solids. The Rayleigh wave propagates along the surface of the materials. The main difference between these waves is the particle movement caused by the wave. Particles move perpendicular to the direction of shear wave propagation and parallel to the direction of the compression wave. In the case of the Rayleigh wave, particle deformations take the shape of an elliptical path. Another difference between these waves is their velocities. The compression wave moves with the fastest speed, while the Rayleigh wave is the slowest wave.

In the solid phases, the relationships among compression wave velocity (v_p), shear wave velocity (v_s), Young's modulus (E), and Poisson's ratio (μ) can be written as follows:

$$v_p = \sqrt{\frac{E(1-\mu)}{\rho(1+\mu)(1-2\mu)}} \tag{5.1}$$

$$v_s = \sqrt{\frac{E}{2\rho(1+\mu)}} \tag{5.2}$$

On the other hand, the velocity of the wave in aqueous media is governed by the following equation:

$$v = \sqrt{\frac{K}{\rho}} \tag{5.3}$$

where K is the bulk modulus of a compressible fluid; and ρ is the density.

The theory of velocity and the attenuation of ultrasound in suspensions has been investigated by several authors (Urick, 1947; Ament, 1953; Biot, 1956; Kuster et al., 1974; Schwartz & Plona, 1985). The following sections describe the most widely used models for ultrasonic propagation.

5.2.1 Urick's model

Urick (1947) derived an equation for the acoustic velocity within a suspension based on the effective density (ρ_{eff}) and compressibility (β_{eff}). Those effective properties are controlled by the relative amount of liquid and solid in the suspension. Taking into consideration that the suspension acts as an ideal solution and consists of liquid and solid phases, then the velocity is given by:

$$v_s = (\rho_{eff} * \beta_{eff}) - \frac{1}{2} \quad (5.4)$$

$$\rho_{eff} = \rho(1 - \emptyset) + \rho'\emptyset \quad (5.5)$$

$$\beta_{eff} = \beta_c(1 - \emptyset) + \beta'_c\emptyset \quad (5.6)$$

where $\emptyset$ is the solid volume fraction; ρ is the density; and β'_c is the compressibility.

5.2.2 Biot's theory

In his theory, Biot (1956) investigated the elastic wave propagation in a porous elastic solid saturated by a viscous fluid. This theory can be used to describe wave propagation in a cement slurry. During hydration, cement can be treated as a dense suspension that contains a large volume fraction of solid particles rather than as a suspension in water. Biot divided his theory, based on the level of frequency range, into two parts. The first part dealt with a low frequency range where Poiseuille flow regime can be considered. The second part of the theory covered high frequency ranges, except for those with a wavelength of the same order as the pore size. In general, the kinematic viscosity of the fluid and pore size primarily determine the classification of frequency to be low or high. He concluded that two dilatational waves and one rotational wave can be used to describe materials that contain both fluid and solid phases. Sayer and Dahlin (1993) pointed out that high-frequency Biot's theory is suitable to describe cement slurry behavior at the beginning when the slurry has low viscosity and contains large pores. On the other hand, low-frequency Biot's theory should be used at advanced stages.

5.2.3 Harker and Temple model

Harker and Temple (1988) established their model based on the hydrodynamic approach, taking into account the influence of parameters

that control the dispersion of fine particles, such as density, viscosity, and particle concentration. Among the assumptions they made was the absence of a gravitational field and the thermal conduction or mass transfer between phases. They also assumed that the fluid is considered an infinite continuum. Based on their model, the velocity, $V_s(\omega)$, and attenuation, $\alpha_s(\omega)$, are given by:

$$V_s(\omega) = \frac{\omega}{R_e[k]} \tag{5.7}$$

$$\alpha_s(\omega) = \text{In[k]} \tag{5.8}$$

where:

$$k^2 = \beta_{eff}\omega^2 \left[\frac{\rho\{\rho' + (\emptyset\rho' + (1-\emptyset)\rho)M(\omega)\}}{(\rho + \big((1-\emptyset)\rho'\big)M(\omega)}\right] \tag{5.9}$$

where $M(\omega)$ is the strength of the coupling confident and can be written as:

$$M(\omega) = \frac{1+2\emptyset}{2(1-\emptyset)^2} + \frac{1}{1-\emptyset}\,\frac{9\varepsilon_v}{4}\left[1 + \left(1 + \frac{\varepsilon_v}{R}\right)i\right] \tag{5.10}$$

where ε_v is the viscous skin depth.

5.3 Review of acoustic techniques

Various non-destructive methods, based on the acoustic techniques, are commonly used to examine the behaviour of cement-based materials at early age, such as the ultrasonic pulse velocity measurement (Sayers & Dahlin, 1993; Trtnik & Gams, 2014), shear wave reflection measurements (Stepisnik et al., 1981; Feylessoufi et al., 2001), the resonance frequency method, acoustic emission (AE) (Ye et al., 2004; Lura et al., 2009), and the impact-echo method (Grosse et al., 2004). A brief review of these methods is presented in the next section.

5.3.1 Ultrasonic pulse velocity method

The first attempt at employing ultrasonic wave measurements to study the behavior of cement-based materials was made in 1949 (Jones, 1949). Jones observed a similarity between P-wave velocity measurements and the compressive strength curve of the concrete samples during the first 7 days. The author noticed a

quick increase in P-wave velocity in concrete mixtures at the beginning. The rate of increase declined after one day. The compression wave velocity measurement was found to be dependent on the cement-to-coarse-aggregate ratio.

Keating et al. (1989a) mentioned that the fluid phase controls the P-wave propagation at the beginning of the hydration process. They recommended utilizing the shear modulus obtained from oscillatory shear measurements during the early age to investigate the development of cement paste structure. However, the ultrasonic techniques were more suitable after hardening to study the impact of the different mix formulations on the build-up of the structure. In their continuation of the previous work, Keating et al. (1989b) compared the ultrasonic wave velocity with the cube strength of cement paste during the first 24 hours. They observed that the rate of developing compressive strength is lower than the change in the acoustic velocity.

Grosse and Reinhardt (1994) developed a device to monitor ultrasonic wave velocity in cementitious materials along with the frequency content and relative energy. They investigated the effects of accelerator, air entrainer, and retarder on the wave velocity. Retarder was found to have a more significant impact on velocity than other parameters. They mentioned the applicability of this method to different materials, such as gypsum, lime, and starch. It was concluded that velocity measurement is a good tool to monitor the setting at early age using a mathematical approach. Meanwhile, the final setting is based on empirical experience.

Boumiz et al. (1996) used the measurements of ultrasonic velocity, heat flow, and electrical conductivity to investigate the hydration behavior of cement paste and mortar during the setting and hardening process. They found that unlike Poisson's ratio, Young's modulus increases as the w/c decreases. They concluded that the evolution of compressive strength is controlled by filling the capillary pores in the hydration process, while the interconnection between cement particles dominates the development of elastic moduli.

Guang et al. (2001) used ultrasonic pulse velocity measurements to investigate the evolution of the microstructure of fresh concrete. They concluded

that both the w/c and the degree of hydration influence the evolution of the ultrasonic pulse. The increase in temperature and the decrease in w/c lead to an increase in pulse velocity.

Ye et al. (2003) used ultrasonic measurement to monitor the microstructure evolution of cement paste. They conducted their tests on cement pastes with w/c of 0.40, 0.45, and 0.55, and cured at 20 °C, 30 °C, and 40 °C. A parameter called bridge volume, which describes the connectivity of solid phases, was compared with P-wave velocity. No impact of the w/c or curing temperature was observed on the correlation between the growth of bridge volume and ultrasonic velocity. They concluded that the bridge volume can be used to foresee P-wave velocity and to investigate the development of the microstructure of cementitious materials.

Lee et al. (2004) utilized the same technique employed by Grosse and Reinhardt (1994) to study the relationship between P-wave velocity and the setting process on mortar and concrete. The effect of the w/c and the presence of fly ash were taken into consideration during the study. It was reported that certain values of P-wave velocity can be used to indicate the occurrence of initial setting. These values are strongly dependent on the existence of fly ash in the mixture.

5.3.2 Resonance frequency method

The resonance frequency method is widely used to determine the dynamic elastic moduli of isotropic materials (Pickett, 1945; Spinner & Tefft, 1961). In general, Young's modulus, shear modulus, and Poisson's ratio can be determined from the density, the dimensions of the sample, and the natural frequency measurements during vibration. According to ASTM C215-14, the elastic properties of the materials can be calculated from the natural frequency of the specimen using the following equations:

$$E = B * W * (n')^2 \quad (5.11)$$

$$G = D * W * (n")^2 \quad (5.12)$$

where E is a dynamic Young's modulus; G is a dynamic shear modulus; B and D are shape and dimension factors; W is the weight of the specimen; n' is the longitudinal resonance frequency; and $n"$ is the torsional resonance frequency.

Swamy and Rigby (1971) used the resonant frequency method to obtain the dynamic properties of cement paste. The tests have been performed on cement paste with different w/c (0.3, 0.4, 0.5, and 0.6). Their results demonstrated the significant impact of the w/c and age on the dynamic elastic moduli, which were observed to increase with age and with a decrease in the w/c as well. The reported value of the shear modulus was about 40% of Young's modulus. The same conclusion was drawn by Sun et al. (2005).

Sayers and Dahlin (1993) combined the ultrasonic compression wave velocity measurement and the theory of elastic wave propagation through fluid-saturated porous media to investigate the behavior of oilwell cement. Class G cement was used to prepare the samples. The wave propagation after mixing was found to be affected by fluid movement and extremely dominated by the existence of air bubbles, which leads to resonant scattering. Early on, the wave velocity decreased as a consequence of the increase in tortuosity, due to filling the pore space with hydration products. A rapid increase in wave velocity was noticed after a few hours of mixing due to the increase in connectivity. This stage included the movement of the solid frame. The authors mentioned that starting from the time where cement paste shows connectivity between particles, the material should be treated as a fluid-saturated porous elastic solid.

In 2004, Ye et al. investigated the evolution of cement paste properties throughout resonance frequency and ultrasonic pulse velocity measurements. The tests were conducted on specimens with a w/c of 0.5 and 0.6. The test results showed that the evolutions of cement paste properties are highly dependent on the w/c of the sample. A rapid evolution of the stiffness was observed for samples with a lower w/c.

Using the frequency spectrum of ultrasonic P-waves to estimate the compressive strength of the cementitious materials at an early-age was reported by Trtnik and Gams (2014). The evolution of the TG parameter, which defines the ratio between maximum amplitudes of low and high frequency ranges, was compared to the compressive strength. Both the TG parameter and compressive

strength were noted to have a similar trend. A good relationship between these two parameters was defined, regardless of the cement composition or w/c of the samples. The authors concluded that TG can be used to distinguish between two types of material behavior, namely plastic, highly deformable and solid, which occur during the transition stage from fluid to solid.

5.3.3 Shear wave reflection measurement

The shear wave reflection measurement can be employed to investigate the various properties of cementitious materials, such as the compressive strength, setting time, and elastic moduli of cement paste during the phase change from liquid (viscoelastic) to hardened (elastic stage). In addition, the density of the material controls the P-wave reflection coefficient. Therefore, the P-wave reflection is an effective way to determine the w/c, as the density of a cement slurry is affected by the amount of water in the mix. Moreover, changes in ultrasonic wave reflection during the solidification process were noted to be related to the setting of cement. Thus, this technique can be used to investigate the stiffening behavior of cement paste.

Stepisnik et al. (1981) determined the shear modulus and dynamic viscosity of cement paste by measuring the reflections of transverse waves at the interface between the cement paste sample and quartz bar. The impacts of the w/c, curing temperature, and different additives on the development of the reflection coefficient were obvious. Lasiˇc and Stepiˇsnik (1984) reported the same observation.

Valiˇc et al. (1999) proved the ability to use wave reflection measurements to estimate the initial and final settings of cement paste by comparing the Vicat test with the shear wave reflection coefficient. It was concluded that a specific range of reflection coefficient can be used as an indicator for initial and final settings. A linear relationship between calcium hydroxide (CH) content and the reflection coefficient at early age was reported (Valiˇc & Vuk, 2000).

Feylessoufi et al. (2001) divided the hydration process into five stages based on the results of the compression and shear wave reflection coefficient

measurements, chemical shrinkage, and calorimetric measurement. The first stage is the settling period, which was found to be monitored only by the P-wave reflection coefficient. An appreciable amount of chemical shrinkage was observed, and no changes in the shear wave reflection coefficient were recorded during this stage. In the second stage, an aggregation period, the shear wave reflection coefficient decreased marginally. On the other hand, the heat of hydration increased. The chemical shrinkage was observed to be stable at this stage. During the third stage, a post percolation bond development phase, the compression and shear wave reflection coefficients decreased dramatically. The bulk modulus and Young's modulus were noted to be equal in the fourth stage. The fifth stage described a hyperstatic phase, where the connectivity between particles was completely established. The bulk modulus remained almost constant while Young's modulus increased slightly.

5.3.4 Acoustic emission (AE)

When cracks and fractures happen, a change in the microstructure occurs, accompanied by a release of energy in a state of elastic waves. Based on this fact, acoustic emission (AE) has been widely used to evaluate concrete conditions. Piezoelectric sensors are usually used to monitor the propagation of the acoustic waves on the surface of the sample due to crack event. The number of active sources is directly related to the number of acquired signals (Grosse & Ohtsu., 2008; Carpinteri et al., 2009). AE is considered a passive technique, as this method is based on monitoring the ultrasonic waves generated by the material (Gabrijel et al., 2010).

Lura et al. (2009) monitored the acoustic activity of cement paste at early age. The tests were conducted on cement paste specimens with a w/c of 0.30, 0.35, and 0.40. For samples with a low w/c (0.30), no AE events were recorded during the first 2 hours of hydration. After that, minor events were observed, followed by a silent period (3-7 hours). The events were recorded again at seven hours as a result of final setting, and ceased at nine hours. Unlike specimens with a w/c of 0.4, a clear peak was noted for samples with a w/c of 0.3. In general, fewer events were

monitored for specimens with a high w/c. The authors claimed that these events were attributed to gas-filled bubbles in the pores. These bubbles are formed due to the formation of a cement matrix. Lura et al. (2009) concluded that the AE technique could be used to investigate the transition stages that occur during hydration.

5.3.5 Impact-Echo method

Impact-echo method was presented by the researchers of the National Institute of Standards and Technology (NIST). In this technique, the compression waves are generated at the surface of the material by mechanical impact, and the reflected waves, due to internal flaws, are monitored. This method has been used widely in the field as a non-destructive test to monitor cracks and other defects in the concrete structures. In 1988, the ability of utilizing this technique to investigate the behavior of concrete at an early age was highlighted (Pessiki & Carino, 1988). Since 1988, much research has been conducted to estimate the in-place compressive strength of early-age concrete (Pessiki & Jonson, 1994), and to evaluate early-age concrete properties (Grosse et al. 2004)

In 2004, Han and Kim investigated the factors that may affect the compressive strength of concrete and the relationship between dynamic and static moduli by means of impact-echo measurements. Three parameters, namely cement type, curing temperature, and age were studied. The ratio between dynamic and static moduli decreased as the temperature increased. However, the impacts of age and cement type were found to be trivial. These observations were found to be applicable to the relationship between the dynamic modulus and compressive strength as well.

5.4 Factors affecting the evolution of ultrasonic velocity in cement-based materials

The propagation of ultrasonic wave in cementitious materials relies on several factors, which not only affects the amplitude of the acoustic waves, but also has a significant impact on its period and rise time. The next sections discuss these parameters and the impact on the evolution of wave velocity.

5.4.1 Microstructure evolution and setting time

The microstructure formation during hydration strongly affects the propagation of ultrasonic waves through cement paste. Before the final setting and while the cement is in a liquid state, the ultrasonic velocity is controlled by the water/air phase more than the cement matrix (Sayers & Dahlin, 1993). Once the solid phase starts, the pulse velocity increases rapidly due to the development of the connectivity of the cement matrix. In addition, the signal duration increases sharply at the final setting time (Gabrijel et al., 2010).

5.4.2 Water-to-cement ratio (w/c)

The alterations in the amplitude, duration, and rise time that occur as the cement paste changes from a liquid state to a solid state, start early in the case of cement paste with a low w/c. The velocity of ultrasonic propagation increases as the w/c decreases. The magnitude of the relative signal strength was found to be largely dependent on cement content as well. Samples with a higher w/c showed lower relative values of signal strength (Gabrijel et al., 2010). According to Trtnik et al. (2008), this phenomenon occurs due to the higher volume fraction of the total and connected solid phases in the cement matrix with a lower w/c.

5.4.3 Air voids

Among the various parameters that have a great impact on ultrasonic wave propagation in cementitious materials at early age, is the existence of air bubbles inside the cement matrix. This can be attributed to resonant scattering, caused by air bubble, due to the variation in the compressibilities between air and pore fluid

(Gaunaurd & Uberall, 1981). Generally, air bubbles form inside the cement paste due to the presence of air in the mixing fluid or because air is trapped into voids during mixing (Ye, 2003).

Kmack (2008) performed ultrasonic wave measurements on cement pastes with various amounts of air-entraining agent (AEA). He found that both the wave velocity and signal amplitude decreased when air-entraining agent was utilized. To grasp more insight into the influence of air voids on ultrasonic wave propagation, Zhu et al. (2011) used Biot's theory for pyroclastic materials to conduct compressional and shear wave velocity measurements on cement pastes with different air void content (0.1% to 5.3% by volume of cement). They found that the presence of air voids within the cement paste reduces the compressional wave velocity; however, it has an insignificant impact on the shear wave velocity. They recommended utilizing shear waves to investigate the solidification process of cement.

5.4.4 Influence of chemical composition and fineness

The ultrasonic P-wave velocity is strongly affected by both the chemical composition and fineness. Using cement with a high amount of tri-calcium aluminate (C_3A) will increase the P-wave velocity. On the other hand, the impact of fineness was observed to be significant at early age due to its effect on the hydration rate. The higher the fineness, the more rapid the reaction rate, and accordingly, the faster the evolution of the P-wave (Trtnik et al., 2008).

5.5 Static and dynamic moduli

Elastic moduli can be determined either from stress-strain measurements obtained from uniaxial compression test (static moduli), or estimated from the propagation of acoustic velocity through the specimen (dynamic moduli). In the last few decades, ultrasonic velocity measurements have been utilized to determine the dynamic mechanical properties of concrete and rock samples, and have been used as a non-destructive test to investigate the quality of concrete (Leslie et al.,

1949). In addition, they have been extensively employed to characterize the performance of cementitious material, especially at early age.

Numerous studies have investigated the relationship between static and dynamic moduli. Ideally, the dynamic moduli of a perfectly elastic material without pores are equal to its static moduli. However, the static values of Young's modulus have been reported to be considerably smaller than the dynamic values. The difference between the two moduli was found to be mainly dependent upon the type of rock and the value of confining stress during the test (Ide, 1936; Brace, 1965; Walsh, 1965).

Zisman (1933) reported a 20% difference between static and dynamic Young's moduli measured using a resonance frequency method for granite. He explained this discrepancy with the assumption that most of the wave energy scattered around the cavities while entering the cracks or pores resulted in a loss of energy. However, there was no impact on the pulse passing through the rock, due to the random distribution of the cavities in the rock matrix.

Cheng and Johnston (1981) have performed an extensive study on sandstone, granite, a tuff, limestone, and oil shale. They measured the static and dynamic bulk moduli as a function of applied pressure. They found that the ratio between the static and dynamic moduli (K_s/K_d) depended mainly on the pressure and increased from 0.4 at atmospheric pressure to 0.9 at high pressure for sandstone samples. On the other hand, a decrease in the K_s/K_d ratio was observed after the onset of pore collapse in limestone. However, in the case of oil shale with a few micro cracks, a constant value of 0.7 was obtained for K_s/K_d regardless of the applied confining pressure. They deduced through their investigations that the correlation between static and dynamic moduli depends on the cracks that exist in the matrix. At low pressure, these cracks remain open. As a consequence, a difference between the dynamic and static moduli was observed. As the pressure increases, the majority of cracks start to close, resulting in the values of the two moduli becoming relatively similar. Comparable results have been experientially reported by various authors (Simmons & Brace, 1965; King, 1969).

In their study, Han & Kim (2004) used the impact-echo method to investigate the relationship between static and dynamic moduli of concrete and to quantify the impact of cement type, temperature, and age on this relationship. They performed their tests at 1, 3, 7, and 28 days on two different types of cement (types I and V). Specimens had a w/c of 0.40 and 0.50, and were cured at 10 °C, 23 °C, and 50 °C. The authors mentioned that the dependency of the relationship between dynamic and static moduli on the cement type and age is trivial, but the curing temperature clearly affects this relationship. The ratio between the two moduli increases with the curing temperature. They proposed the following equation to describe the relationship between the two moduli:

$$E_c = E_d(1 - ae^{-bE_d}) \tag{5.13}$$

where E_c is the static elastic modulus (GPa); E_d is the dynamic elastic modulus (GPa); and a and b are constants shown in Figure 5.1.

The relationship between dynamic and static moduli was observed to be similar to the relationship between the elastic modulus and compressive strength, regardless of the cement type and temperature. In general, the difference between the initial chord elastic modulus and the dynamic modulus is minor. This can be attributed to the insignificant influence of deformation on the initial chord elastic modulus as it is measured at a lower strain level (Han & Kim, 2004).

To compare between results derived from dynamic and static tests, Pedam (2007) conducted unconfined compression test and ultrasonic measurement on the same sample. He found that there is a significant difference in the results between the two approaches. The results from the Mechanical Properties Analyzer apparatus were found to be greater than the results obtained from static tests by a factor of three in the case of Young's modulus and by a factor of two for compressive strength.

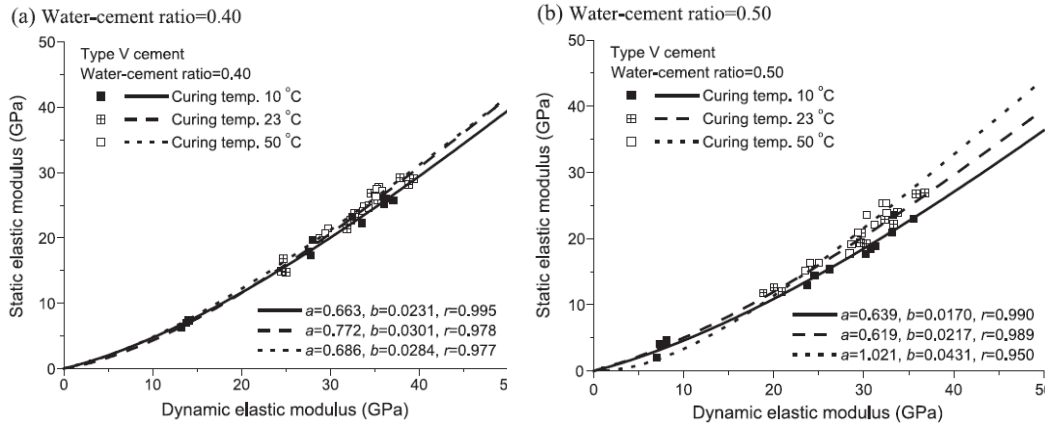

Figure 5.1 Relationships between dynamic and static elastic moduli for different curing temperatures: a) w/c = 0.40; b) w/c = 0.50 (Han & Kim ,2004)

5.6 Mechanical characterization of oilwell cement

Among the various parameters, which has a great impact on the development of mechanical properties of cement paste, especially at an early age, is curing conditions. In general, curing cementitious materials at elevated temperatures tends to increase early-age compressive strength while the later-age strength becomes lower. On the other hand, within a temperature range of 10 ºC to 50 ºC, the relationship between the compressive strength and elastic modulus is independent of the curing temperature (Han & Kim, 2004).

Labibzadeh et al. (2010) investigated the development of early-age compressive strength for Class G cement under different pressures and temperatures. They used a cement slurry with a w/c of 0.5. Class G cement was used to prepare all slurries. Additives were selected based on the curing conditions. Calcium chloride with a concentration of 1% by weight of cement was used for ambient pressure and temperature; whereas, D-013 was added in slurries cured at elevated temperatures and high pressures. The authors observed that the maximum and minimum compressive strengths and their time of occurrence vary with the combination of the curing pressure and temperature.

Pedam (2007) used acoustic techniques to determine Young's modulus, bulk modulus, and compressive strength. A slurry with a w/c of 0.38 was prepared using cement class H. ASA-301 was added as an additive to control the properties of cement. The sample was cured under an applied pressure of 6.89 MPa and at 65.5 ºC. The test was run for 120 hours. The values of Young's modulus and Bulk modulus at the end of the test were 19940 MPa and 12259 MPa respectively, while the compressive strength was noted to be 33.29 MPa. The value of Poisson's ratio was found to follow the same trend as the shear wave and transit time. It was observed that this value declined from 0.38 at the beginning to 0.23.

5.7 Experimental program

5.7.1 Materials and mixture preparation

The previously mentioned Class G non-thermal cement in Chapter 2 was used in this study. All slurries were prepared by mixing the cement with distilled water in accordance with API RP 10B specifications, with a w/c of 0.44. No admixture was used.

5.7.2 Ultrasonic pulse velocity measurements

In this research, the Mechanical Properties Analyzer apparatus, Model 6265 MPRO (Figure 5.2), was used to continuously determine the elastic mechanical properties of cement paste (shear modulus G, bulk modulus B, and Young's modulus E) from ultrasonic wave velocity measurements. The device consists of a steel pressure vessel with top and bottom caps. These caps have two US transducers (transmitter and receiver) that generate and receive compression and shear waves. The entire system is connected to a separate pressure control system, a Quizix pump, to apply confining pressure. The apparatus is equipped with a programmable temperature controller, which can be used to adjust the temperature profile to mimic the real conditions in the field. The temperature profile can be defined as ramp and soak segments. Up to 8 segments can be introduced. A thermocouple is placed horizontally in the middle of the sample through a hole in the top cap to measure the specimen temperature during the test. The ultrasonic velocity waves are

retrieved by the 5270 Data Acquisition and Control System (DACS). This data acquisition provides real-time measurements of the test parameters and the calculated mechanical properties; meanwhile, the data is stored and can be retrieved at any time.

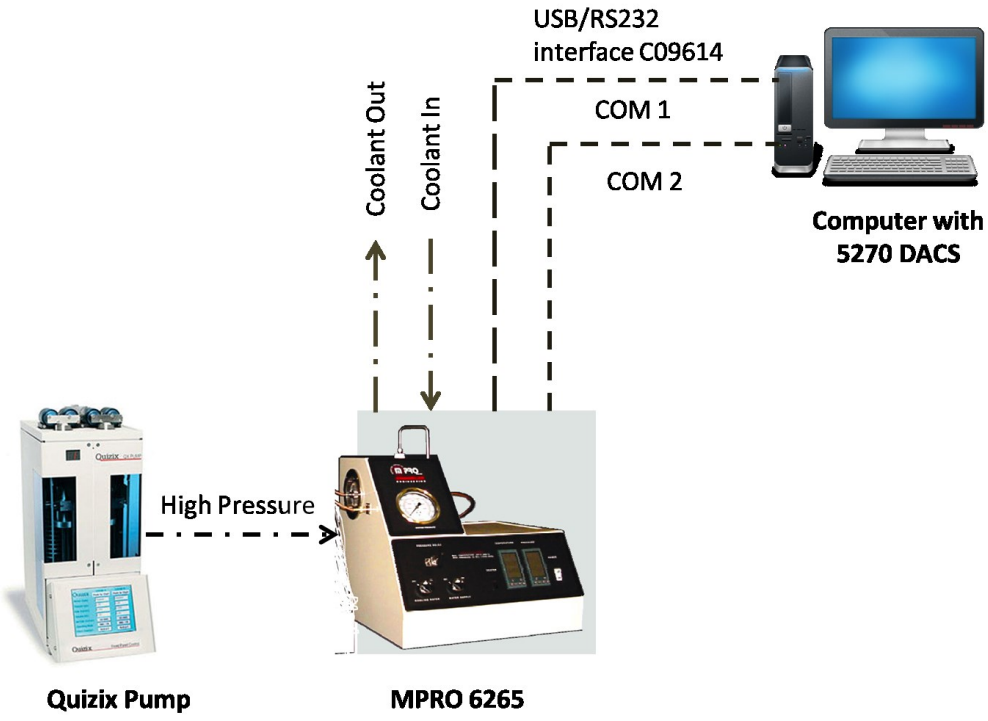

Figure 5.2 Schematic diagram of the Mechanical Properties Analyzer

5.7.3 Test procedures

After preparing the cement mixture, the pressurized fluid density scale was used to determine the density of the cement slurry; then the cement slurry was poured into the cell on a vibrating table. The mixture was allowed to vibrate for about 5 mins to eliminate air bubbles present in the slurry. After the cell was filled with cement up to the slurry level gauge, the top cap was attached to the cell. The thermocouple was inserted into the top cap. Thereafter, the cell was placed horizontally in the MPro apparatus. The entire system was connected to the Quizix

pump to apply the confining pressure. Distilled water was used as a confining fluid. A temperature bath was attached to the apparatus in order to cool down the system after the test. The pressure was increased to the target pressure in 10 mins. Meanwhile, the temperature was ramped up to the required value with a heating rate of 1.1 ºC /min. Both pressure and temperature were held constant for 24 hours. Then, the ultrasonic wave signals were monitored and recorded continuously for 24 hours.

The ultrasonic wave velocity was determined by measuring the travel time of the pulse through the sample. The first peak in each wave was taken as a reference point, and then the velocity was calculated from the following equation:

$$V = L/t \tag{5.14}$$

where V is the ultrasonic velocity; L is the distance between the two transducers; and t is the travel time of the pulse through the sample.

Then elastic moduli can be calculated as follows:

$$G = V_s^2 \rho \tag{5.15}$$

$$B = V_p^2 \rho - 4/3\ G \tag{5.16}$$

$$\nu = \frac{1}{2}\left[\frac{\left(V_p/V_s\right)^2 - 2}{\left(V_p/V_s\right)^2 - 1}\right] \tag{5.17}$$

$$E = V_s^2 \rho\ (1+\nu) \tag{5.18}$$

where G is the shear modulus; B is the bulk modulus; E is Young's modulus; ρ is slurry density; and ν is Poisson's ratio.

The basic experimental configuration for measuring the elastic properties of cement paste specimens, using the Mechanical Properties Analyzer, is presented graphically in Figure 5.3.

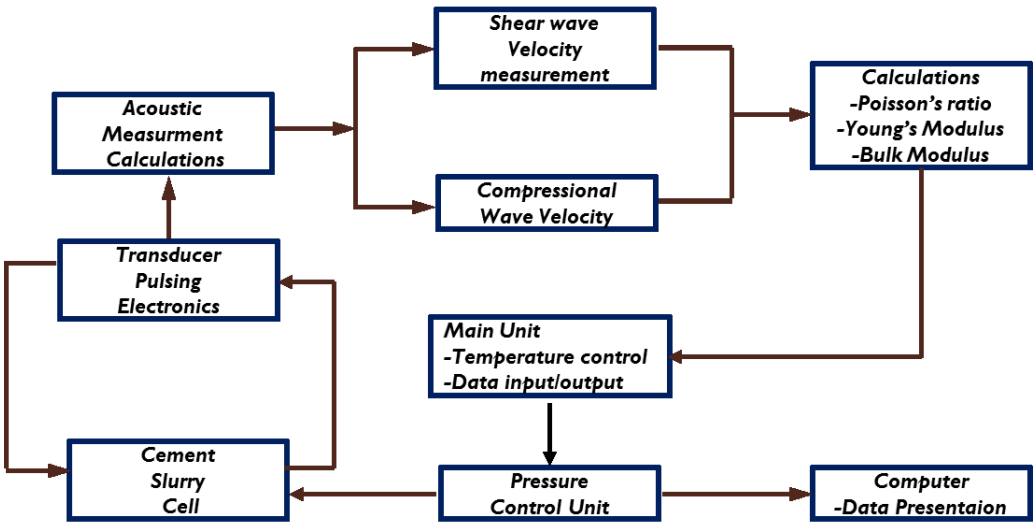

Figure 5.3 Schematic Diagram of Mechanical Properties Analyzer

5.8 Results and discussion

5.8.1 Test plan and repeatability of the tests

Pressures and temperatures during the tests were selected to span a wide variety of curing conditions. Nine mixtures were tested at different combinations of pressure and temperature. The pressure ranged from 0.1 kPa to 40 MPa while The temperature varied from 20 ºC to 120 ºC. In order to examine the reproducibility of the tests, each experiment was performed twice to determine the elastic moduli of the cement paste from ultrasonic wave measurements at a specific pressure and selected temperature. The results presented here for each curing condition provide the average value of the two tests.

5.8.2 Evolution of ultrasonic wave propagation

The microstructural evolution that occurs during the solidification process was observed to dominate the ultrasonic pulse velocity development through the cement slurry. Therefore, it was important to explore this process. To better understand the evolution of compression and shear wave velocities in cement paste, one test was performed for an extended period (8 days). Figure 5.4 shows the measured compression and shear wave velocities during this test. Unlike the shear

wave, the compression wave was transmitted through the slurry at the beginning with a speed of about 1450 m/sec. The initial ultrasonic pulse velocity right after mixing was low due to the presence of some air bubbles trapped in the cement slurry (Bentz, 2007). After the dormant period, the P-wave velocity started to increase because of the formation of ettringite and the consumption of water, filling the capillary space. The ultrasonic pulse velocity continued to increase rapidly during the acceleration period of the hydration process due to the formation of calcium silicate hydrate (C-S-H) and calcium hydroxide (CH). This led to the pore spaces being filled with hydration products, resulting in a higher volume fraction of the total and connected solid, which improved the connectivity of the cement matrix. Then, the rate of the increasing P-wave velocity declined until it reached a relatively plateaued zone, and the velocity stayed almost constant until the test was terminated. The time required to achieve the plateau value, was found to be largely dependent on the curing conditions, as discussed in the next section. As shown in Figure 5.4, the P-wave velocity curve can be divided into four different stages.

At the beginning, while the specimen was a fluid-like suspension, almost no shear wave was recorded. The first detection of shear wave signals was observed when the solid particles became more connected. The time at which the shear waves started to propagate through the medium was sensitive to the curing conditions. Lowering the curing pressure and temperature delayed the appearance of the shear wave. In general, the shear wave was found to be slower than the P-wave. This is because cement paste is almost incompressible; therefore, P-waves transmit quickly through cement samples.

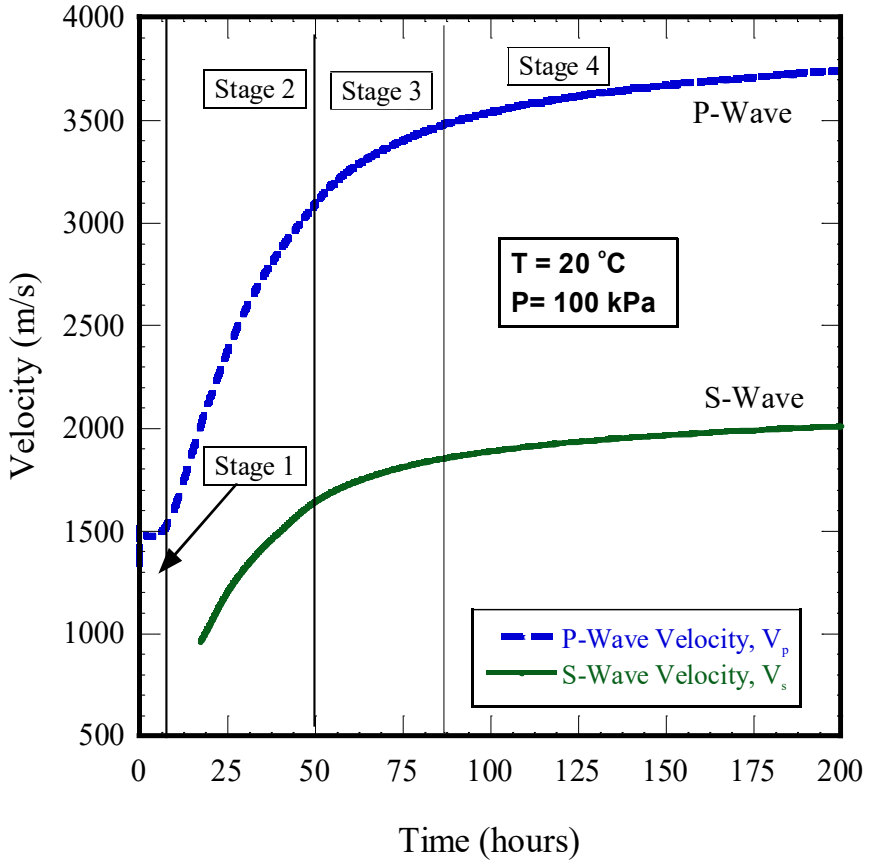

Figure 5.4 Evolution of ultrasonic velocities in cement paste during the first 8 days of hydration

5.8.3 Influence of curing conditions on ultrasonic wave propagation

The impact of curing conditions on the evolution of the P-wave is presented in Figure 5.5. The data shown in Figure 5.5 revealed that the curing temperature has a significant impact on the P-wave during the first few hours of hydration. Samples tested at elevated temperatures exhibited higher values of ultrasonic wave velocity. However, this influence decreased with time and became slightly insignificant when the P-wave curve reached the plateau zone. For example, after 24 hours, specimens tested at 60 ºC with no applied confining stress had a P-wave velocity almost similar to the samples tested at 90 ºC. Moreover, the difference between the wave speeds of samples tested at 20 ºC and those of samples cured at elevated temperatures started to decrease with time at the later age. In addition, it can be seen that when a sample was tested at elevated temperatures, the P-wave

velocity curve reached the plateau value faster than other samples. This can be attributed to the sensitivity of hydration product formation to temperature. Higher temperatures lead to an increase in the rate of the transformation from liquid to solid state, resulting in greater connectivity within the cement matrix.

The influence of the curing pressure on the P-wave velocity was found to be similar to the curing temperature. The higher the curing pressure, the greater the value of the P-wave velocity and the shorter the time required to achieve the plateau value.

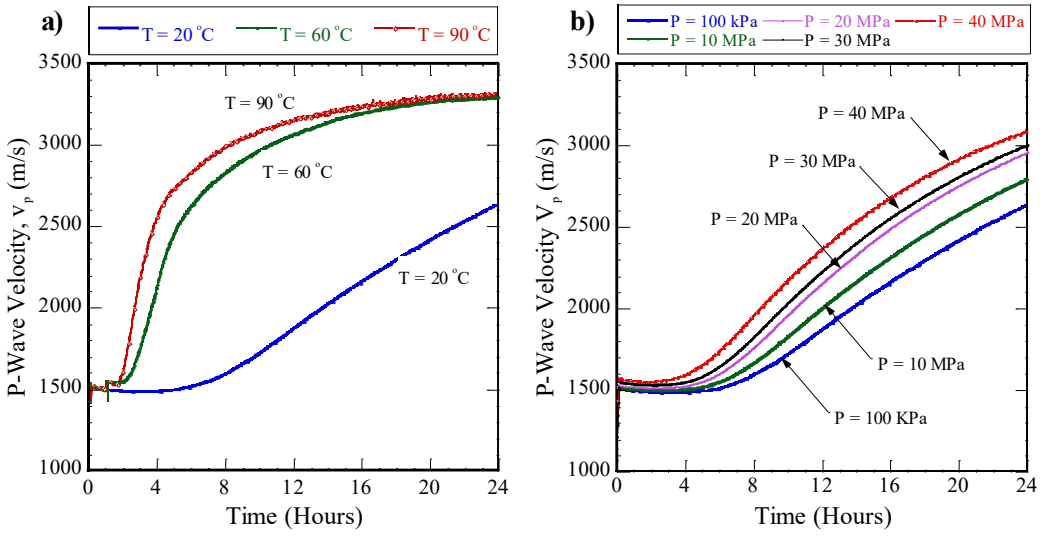

Figure 5.5 Evolution of P-wave in cement paste: a) at different temperatures; b) at various pressures

The impacts of the curing conditions on the S-wave are summarized in Figure 5.6. It can be seen that an elevated temperature and high pressure accelerate the occurrence of the shear wave. Shear wave velocity curves of cement paste cured at 60 ºC and 90 ºC were almost parallel to each other. However, the first shear wave signal was detected earlier at 90 ºC. On the other hand, the curve obtained at 20 ºC crossed over the curve of the sample tested at 60 ºC, although the detection of the shear wave signal at 20 °C was delayed a couple of hours. This means that shear wave velocity, obtained at 20 °C, increased rapidly with a higher rate than the rate observed at 60 °C.

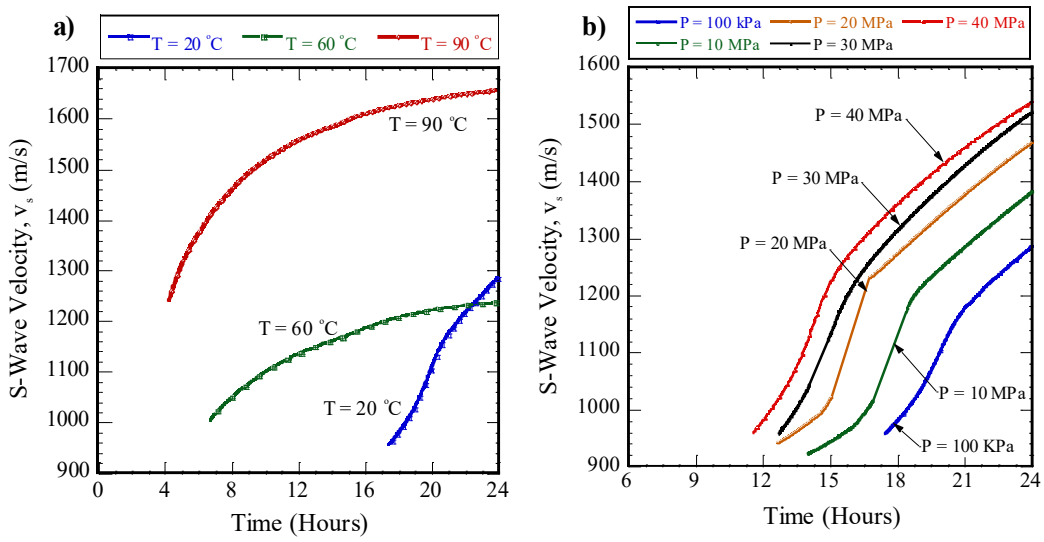

Figure 5.6 Evolution of S-wave in cement paste: a) at different temperatures; b) at various pressures

5.8.4 Development of compressive strength of cement paste

Theoretically, there is no direct correlation between ultrasonic wave velocities and compressive strength. However, both are dependent on density. Thus, an indirect relationship can be established between them, and the w/c significantly affects this relationship (Gabrijel et al., 2010). Curves, shown in Figure 5.7, present the influence of the curing conditions on the compressive strength. The development of mechanical properties can be divided into three stages. These stages are closely related to the evolution of the microstructure. The first stage starts after the mixing, where the compressive strength increases very slightly. During the second stage, which starts approximately 4 hours after mixing, the compressive strength increases rapidly due to the formation of calcium silicate hydrate (C-S-H) and increases the degree of connectivity within the solid network of the cement matrix. In the last stage, the compressive strength continues to increase at a slow rate.

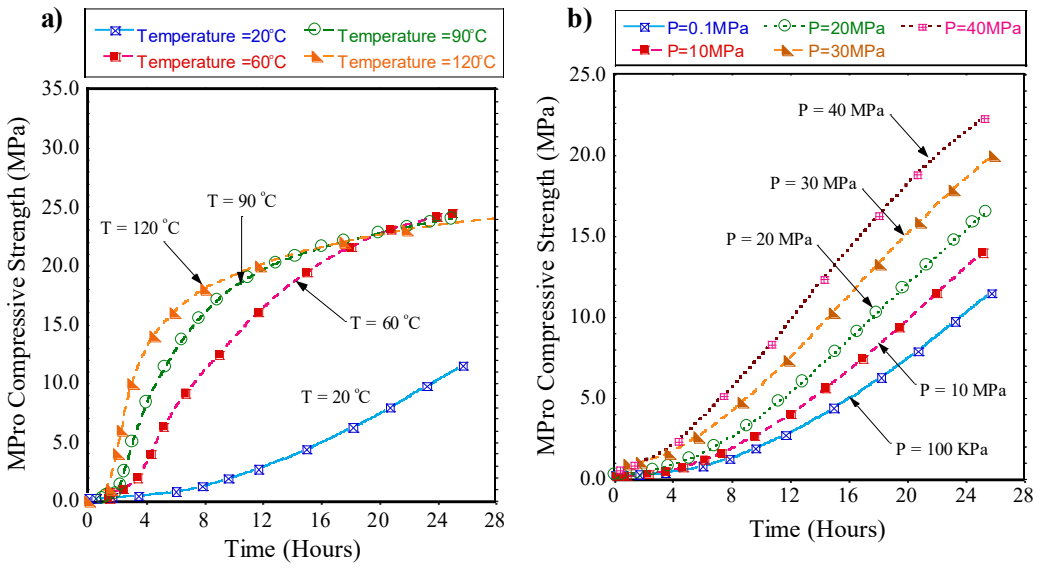

Figure 5.7 MPRO compressive strength versus curing time: a) at atmospheric pressure and different temperatures; b) at room temperature and different pressures

The impact of the curing temperature on the compressive strength is clearly demonstrated in Figure 5.7(a**)**. In general, higher curing temperatures led to a greater early compressive strength. However, after 12 hours of hydration, the rate of increase in strength declines with time, for specimens cured at 120 ºC and 180 ºC, due to temperature effects on the cement matrix. This resulted in a higher strength after 24 hours for samples cured at a moderate temperature (60 ºC) than for samples cured at high temperatures (120 ºC and 180 ºC). At 20 hours, all samples cured at 60 ºC, 120 ºC, and 180 ºC were observed to have the same compressive strength. This can be explained by the formation of non-uniform distributed hydrated product within the cement matrix and by the presence of larger pores from exposing the cement slurry to high temperatures, which consequently affects the strength of cement paste in later stages.

Unsurprisingly, the compressive strength was found to be not only affected by the curing temperature of the specimens, but also by the applied pressure. However, the test results showed that applied pressure has a less pronounced impact on cement's mechanical properties than on temperature. When the test temperature

changed from 20 ºC to 60 ºC, the 24-hour compressive strength increased from 12.5 MPa to 24 MPa. However, curing cement at 10 MPa caused only a 10% change in the compressive strength. Moreover, when the temperature was increased, the shape of the compressive strength curve itself changed from concave upward (slope increases) to concave downward (slope decreases). On the other hand, the compressive strength development curve was observed to have the same general trend; when applied pressure increased, the values only shifted up. This can be attributed to the fact that the reaction rate is more sensitive to temperature than pressure. In addition, the curing pressure has an insignificant impact on the C-S-H chain length and morphology, and it affects the hydration kinetics only.

5.8.5 Evolution of elastic moduli at early age

The evolution of the elastic moduli of cement paste at early age is complicated due to its viscoelastic behaviour at this stage. Figure 5.8 shows the development of elastic moduli with time at various temperatures and different pressures. It is clear that, at elevated temperatures, Young's modulus increased rapidly at the beginning. Afterwards, the rate of the increase declined as the reaction rate decreased. In addition, it can be seen that curves started to become closer to each other as the test temperature increased. This observation indicates a reduction in the dependency of Young's modulus on temperature changes once reaching an elevated temperature.

On the other hand, curing cement paste under high pressure enhances its elastic moduli at early age. The higher the applied pressure, the greater the elastic moduli achieved at 24 hours. Figure 5.8(b) revealed that regardless of the applied pressure, Young's modulus continued to increase at the same rate. All the curves of Young's modulus development were mostly parallel to each other. However, once again, curves started to become closer to each other as the applied pressure increased.

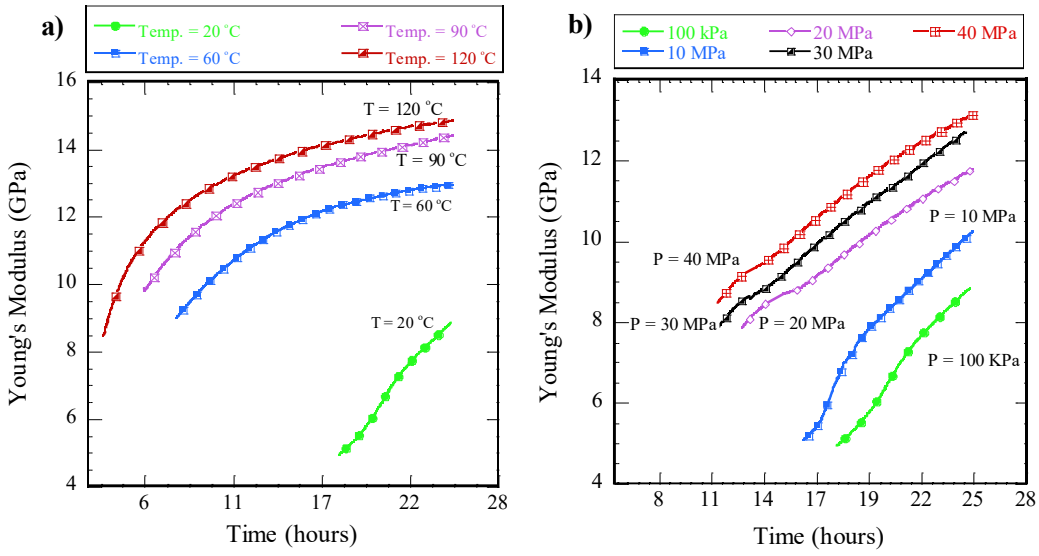

Figure 5.8 Young's Modulus versus curing time: a) at atmospheric pressure and different temperatures; b) at room temperature and different pressures

5.8.6 Impact of heating rate on compressive strength

To gain more insight into the influence of the heating rate on the compressive strength of cement paste, in a separate set of experiments, two tests were performed at 60 ºC and 90 ºC with a heating rate of 2.2 ºC/min. These experiments were compared with other tests conducted with a heating rate of 1.1 ºC/min, and the corresponding results are depicted in Figure 5.9 and Figure 5.10. It can be seen that initially the two curves were congruent. However, after about 7 hours, the two curves started to deviate from each other, resulting in a higher value of compressive strength for the sample cured at a heating rate of 2.2 ºC/min. In general, the impact of the heating rate does not rely on the test temperature, as the same trend was noted for samples cured at 60 ºC and 90 ºC.

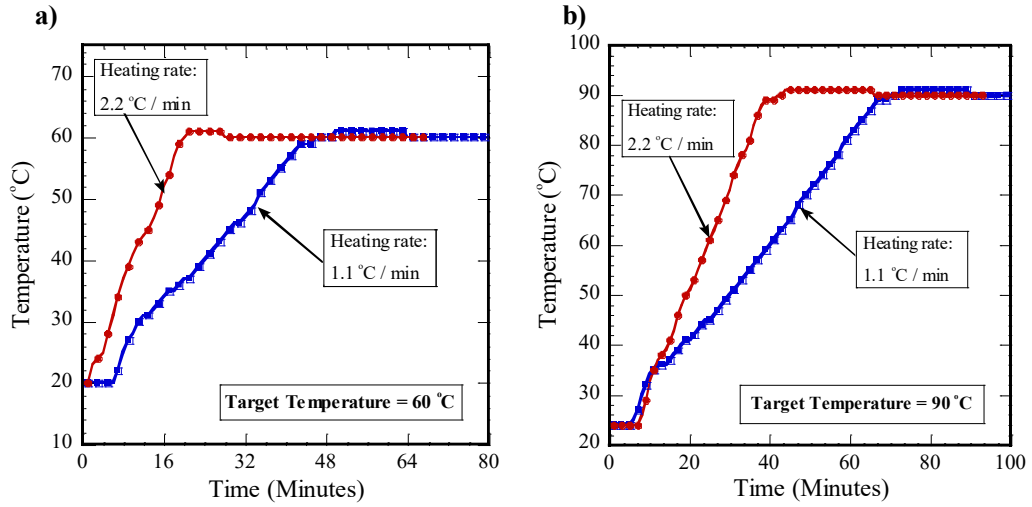

Figure 5.9 Heating profile: a) target temperature 60 ºC; b) target temperature 90 ºC

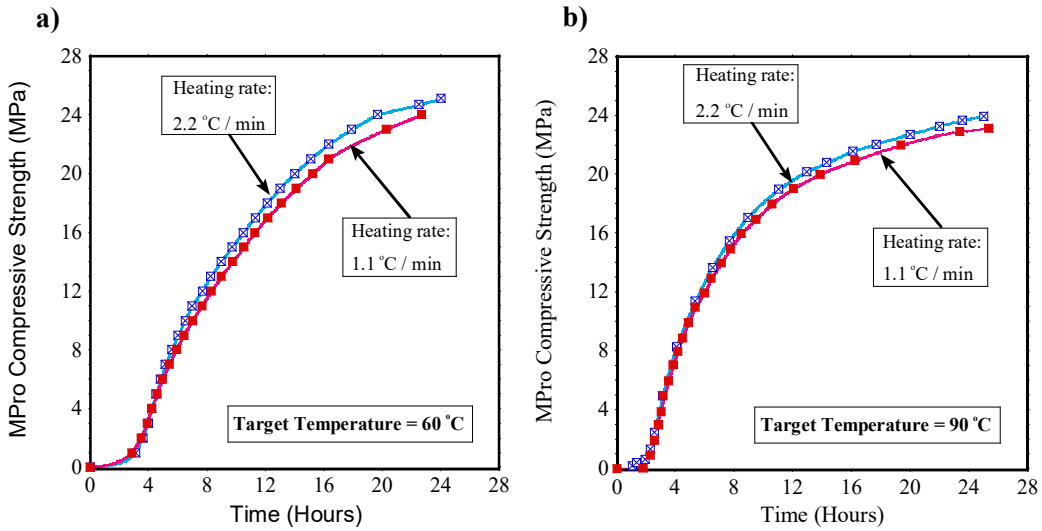

Figure 5.10 Impact of heating rate on compressive strength: a) target temperature is 60 ºC; b) target temperature is 90 ºC

5.9 Summary and conclusions

In this chapter, the acoustic method was used to assess the influence of elevated temperatures and high pressures on the development of the mechanical properties of cement paste at early age. Both compression and shear waves were monitored in cement paste during the solidification process. Several tests were performed on samples with a w/c of 0.44. Specimens were cured at different

pressures (10 MPa, 20 MPa, 30 MPa, 40 MPa) and various temperatures (20 °C, 60 °C, 90 °C, 120 °C). Experiments were conducted inside the MPRO apparatus. The main advantage of this machine lies in its capability to continuously monitor and record the elastic properties of cement paste in real time. The properties examined in this chapter included the bulk modulus, Young's modulus, and compressive strength. The following conclusions can be drawn based on the results:

1- The results of this preliminary experimental work showed that wave propagation measurements have proven to be a highly effective method to continuously monitor and measure the elastic mechanical properties of cement under downhole conditions, especially at early age and during hardening processes when the cement is still a slurry and no static tests can be conducted.
2- The accuracy of the results obtained from acoustic approaches is largely dependent on the quality of the cement slurry. The existence of air bubbles should be prevented by applying a good compaction on the slurry.
3- The mechanical properties of the cement slurry are strongly affected by pressure. Any increase in the applied pressure would enhance the compressive strength, Young's modulus, and the bulk modulus.
4- The influence of elevated temperatures on cement paste was more complicated than the effect of high pressure. The rate of increase of early-age compressive strength is more sensitive to changes in the curing temperature than pressure. This is logical, as temperature has a greater impact on the kinematic reaction rate of cement hydration, which leads to gaining strength rapidly. The results revealed a 20% increase in the compressive strength of the sample after 24 hours due to the increase in pressure from atmospheric pressure to 30 MPa. On the other hand, the compressive strength dropped from 24.1 MPa to 10.5 MPa when the curing temperature declined from 60 °C to room temperature.
5- Poisson's ratio does not depend heavily on the curing conditions. An insignificant change in Poisson's ratio was observed due to elevated temperatures and high pressure.
6- New correlations between the curing conditions (pressure and temperature) and the elastic moduli (Young's modulus and bulk modulus) were proposed.

However, further research should be conducted to fully understand the combined effect of both pressure and temperature changes on the elastic moduli.

7- Due to the discrepancy between the values of static and dynamic moduli, more effort should be exerted to establish reliable correlations between static properties and ultrasonic velocity measurements. In general, static tests are still required to obtain some properties that cannot be predicted from ultrasonic wave measurements, such as friction angle.

Chapter 6 : Modeling of Cement Hydration and Microstructure Evolution at Early Age

6.1 Hydration process of cement

Cement hydration is a complex exothermic process. During hydration, cement reacts with water, and the heat evolution resulting from this process can be measured using an isothermal calorimeter. As shown in Figure 6.1, the heat evolution curve can be divided into four stages:

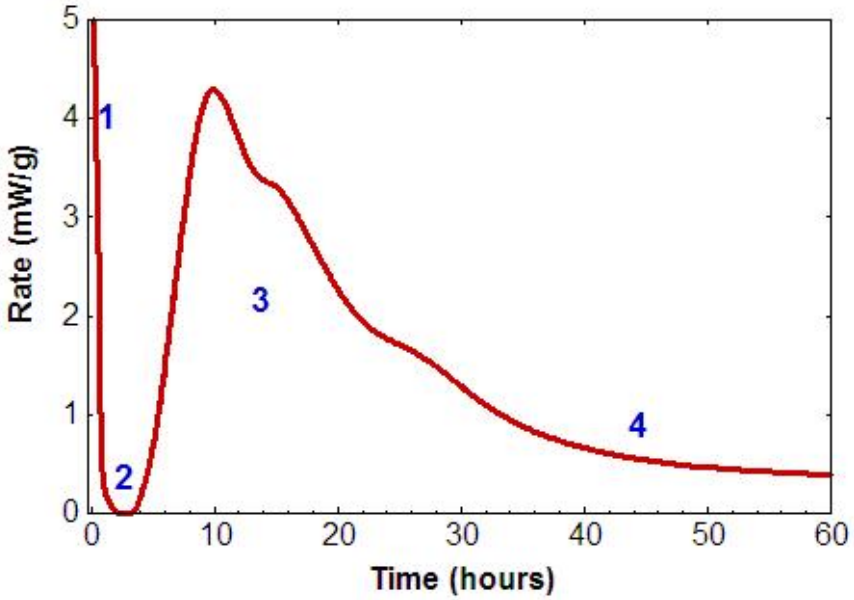

Figure 6.1 Typical heat evolution curve of Portland cement

1- **Dissolution period:** includes initial rapid dissolution of cement particles associated with a large evolution of heat. This heat mainly depends on the particle size distribution and crystalline structure of C_3S.
2- **Induction period:** reaction continues, but at a slow rate with a lower heat evolution. This reduction in reaction rate is due to the formation of protective layers of hydrates around the anhydrous particles.
3- **Acceleration period:** the reaction rate increases until it reaches the peak. Nucleation and growth mechanism controls the reaction in this period. In

this process, grains of the products grow at a rate proportional to the available surface area on these products. The nuclei continue to grow as long as there are available surface areas on these products.

4- **Deceleration period:** diffusion of ions controls the reaction rate during this stage. The thickness of hydrate deposits over the reactant particles increases with hydration, reducing the reaction rate to half the peak value. Afterwards, a steady state is achieved with a constant rate of reaction until most of the reactants are consumed. During this period, temperature has an insignificant effect on the hydration process.

During cement hydration, the products of this process form at different locations. Some hydrates grow on the surface of the reacting particles. Others grow in the pore spaces. The density of hydrates varies with time and the rate of hydrates formation depends on the available surface area existing on the particles.

6.2 Factors affecting the hydration process of Portland cement

The hydration of cementitious materials involves several processes, such as heat release, microstructure evolution, and strength development. The hydration kinetics are dominated by many factors. The following sections discuss these factors in detail.

6.2.1 The chemical composition of cement

The chemical composition of cement is one of the key parameters that controls the reaction rate. The chemical composition of cement can be described by Bogue equations, which assume that cement clinker consists of four phases, namely, Alite (tricalcium silicate), Belite (dicalcium silicate), Aluminate (tricalcium aluminate), and Ferrite (tetracalcium aluminoferrite). Bogue calculations define the proportions of the four phases in Portland cement clinker (Bogue, 1942). The reaction rate of each phase is different from the other phases, as each phase hydrates independently. For instance, Alite hydrates faster than the other phases (Lea, 1971). As a consequence, the rate of hydration and the generated heat at the beginning are mainly dependent on the amount of Alite and Belite

compounds (Mindess & Young, 1981). On the other hand, the impact of chemical composition on the initial porosity was found to be more significant than the influence of curing time. The ratio between C_2S and C_3S was observed to control the capillary porosity of the cement paste. The lower the C_2S to C_3S ratio (C_2S/ C_3S), the higher the cement paste capillary porosity (Berger et al., 1979). The capillary porosity tends to decrease with the degree of hydration.

6.2.2 The fineness of clinker particles

The fineness of clinker particles has a significant impact on the reaction mechanism, and the development of early strength can be enhanced by utilizing finer particles. This can be attributed to more surface area being in contact with water, which leads to an increase in the rate of reaction. However, the impact of fineness on hydration rate becomes insignificant at a low w/c (Bentz & Haecker, 1999). Many studies were conducted to investigate the effect of particle size distribution on the development of cement-based material properties (Frigione & Marra, 1976; Osbaeck & Johansen, 1989; and van Breugel, 1991). The particle size of Portland cement varies from 1 to 150 μm. The particle size distribution can be determined using different techniques, such as laser diffraction (Beuselinck et al., 1998), optical microscopy (Hutchinson, 1974), and sedimentation-based methods (Wagner, 1933). It was observed that cement with a lower granulometric range yields a higher compressive strength due to the increase in volume of the hydrated product (Frigione & Marra, 1976). Normally, the hydration rate increases with the reduction of median particle size. Bentz et al. (1999) investigated the influence of particle size distribution on the hydration kinetics and on the other performance properties. They pointed out that the setting times for finer cements are lower than those for coarser cements. However, the setting of coarser cement occurs at a smaller degree of hydration. The hydration of finer cement was found to generate higher hydration heat. In addition, utilizing coarser cements led to greater diffusion coefficients and lower chemical shrinkage.

6.2.3 Water to cement ratio (w/c)

The impact of the w/c on the solidification process has been discussed by many authors (Kirby & Biernacki, 2012). The effect of the w/c on the reaction rate is dependent on the hydration stage. This impact was observed to be significant at the middle stages of the hydration process, where the reaction rate increases with w/c. However, at the beginning of hydration, the influence of w/c was found to be trivial (Danielson, 1962; Taplin, 1969). In addition, w/c controls the ultimate degree of hydration (α_u). The relationship between these two variables can be written as follows (Mills, 1966):

$$\alpha_u = \frac{1.031\frac{w}{c}}{d0.194 + \frac{w}{c}} \leq 1.0 \tag{6.1}$$

In general, the higher the water-to-cement ratio, the more ettringite is formed from 5 mins to 2 hours, where the amount of C-S-H produced is insignificant. This can be attributed to an increase in the aqueous medium, which facilitates the dissolving process of calcium and sulphate ions and conveys ions to the surfaces of aluminate and ferrite, resulting in escalating the formation of the ettringite (Bensted, 1983).

6.2.4 Temperature

Temperature is an important factor that governs the chemistry of cement hydration. The hydration rate is more sensitive to temperature at early age rather than later age (Kjellsen & Detwiler, 1992). Not only does a higher temperature lead to a higher reaction rate, but it also increases the density of hydration products (Bentur et al., 1979). Verbeck and Helmuth (1968) pointed out that a high temperature decreases the ultimate degree of hydration because hydration products with a high density form around clinker particles, limiting the ability of sulfate ions to diffuse. On the other hand, temperature was found to have a negligible effect on the apparent activation energy up to 60% of hydration (Kjellsen, & Detwiler, 1992). Van Breugel (1991) suggested the following relationship between hydration products and the reacted cement at any temperature (T)

$$v(T) = \frac{Volume\ of\ Hydration\ Products\ at\ T}{Volume\ of\ Reacted\ Cement\ at\ T} \quad (6.2)$$

where

$$v(T) = v_{293}\, exp[-28\ x\ 10^{-6}\ (t - 293)^2] \quad (6.3)$$

where $v_{293} = 2.2$.

6.2.5 Pressure

Less attention has been given to the dependence of hydration kinetics on pressure. On the one hand, the applied pressure was observed to increase the degree of hydration and the density of the microstructure. On the other hand, it decreased the nitrogen surface area of cement paste. Bresson et al. (2002) pointed out that the hydration rate of C_3S increases with an increase in applied hydrostatic pressure. The same conclusion has been drawn regarding the hydration of Portland cement (Zhou & Beaudoin, 2003). The extent to which pressure affects hydration is mainly determined by the time of the pressure application. The earlier the specimen is exposed to pressure, the greater the influence of pressure on the hydration mechanism. The applied pressure was observed to have an insignificant impact on the pore structure of cement paste (Zhou & Beaudoin, 2003).

6.2.6 Admixture

It is common practice to employ chemical additives to improve the properties of cement paste or even to alter its behaviour. Consequently, it is important to understand how those chemical additions affect the hydration process. Cheung et al. (2011) addressed this issue in their literature review paper. They focused on the impact of various chemical additives, such as accelerators, setting retarders, and water-reducing dispersants, on the solidification mechanism. They pointed out that the utilization of retarders leads to an increase in induction period and a reduction in reaction rate. However, the addition of accelerators such as calcium chloride ($CaCl_2$) decreases the induction period due to the difference in diffusivity between Cl- and OH- (Singh & Ojha, 1981). The presence of calcium chloride was also observed to reduce the density of the cement paste (Ramachandran & Feldman, 1978).

6.3 Experimental approaches to investigating microstructure formation in cement-based materials at early age

6.3.1 Scanning electron microscopy image (SEM)

The scanning electron microscope (SEM) technique was first used by Scrivener and Pratt (1984) to study cement paste and concrete. Since then, it has become a popular method to study cement based-materials. Lachowsky and Diamond (1983) described the composition and morphology of cement paste particles using a SEM and analytical electron microscopy (AEM). Delgado et al. (1993) studied the possible reasons for the strength retrogression of cement mortar at high temperatures using SEM and X-ray diffraction (XRD). Gaël et al. (2016) used SEM to quantify the proportion of anhydrous cement.

Three types of signals are involved in the SEM image, namely secondary electrons (SE), backscattered electrons (BE), and X-rays. Backscattered electrons are mainly useful to distinguish between different compositions, especially on polished surfaces due to the variations in contrast to different phases. For example, phases with a higher weighted average atomic number (z) will have brighter colors (Goldstein et al., 1981). On the other hand, secondary electrons provide detailed information about surface topography, while an X-ray signal is used to investigate the element spatial distribution and relative concentrations.

6.3.2 Small-angle X-ray scattering

X-ray is a powerful tool to investigate the structure and surface characterization of solids, and it provides detailed microstructural information for particles ranging 1-100 nm in size. In this method, the microstructural property of a material is obtained by studying the changes in intensity of scattered X-ray beams, which are due to the variation in the scattering angle. To do so, the sample is exposed to X-ray beams with a wavelength (λ) of 0.05-0.2 nm. Meanwhile, the scattered X-ray intensities (I) are recorded as a function of the scattered angle (2θ). The latter is usually between 0º and 5º (Li, 2005) and can be written as a function of the scattering vector q (1/nm), as follows (Kriechbaum et al., 1994):

$$q = (4\pi/\lambda) \sin \theta \quad (6.4)$$

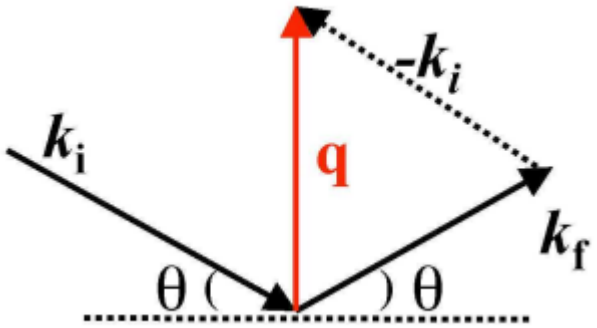

Figure 6.2 Scattering vector

Kriechbaum et al. (1994) used this method to investigate samples made of different types of cement and several values of w/c (0.3 to 0.8). The tests were performed on wet and dry specimens. The impact of dryness on the results was significant in the case of samples with a high w/c, as the mass fractal dimension (D_m) increased. This can be explained by the formation of a more compacted inner structure due to the drying process. The authors concluded that this method can provide additional structural information on the microstructure of cementitious materials.

6.3.3 Mercury intrusion porosimetry (MIP) measurements

Edel'man et al. (1961) were the first researchers who utilized mercury intrusion porosimetry (MIP) measurements to study the pore size distribution in cement. Since then, this technique has been used extensively to investigate the capillary porosity and pore structure of cement-based materials. In this method, pressure is applied incrementally to force mercury to intrude into the pore spaces of a dry sample of cementitious material, which is placed inside an evacuated chamber. The volume of the intruded mercury is monitored and recorded at each pressure incremental step; then the relationship between pore size (d) and pressure (P) can be written as follows:

$$d = \frac{-4\gamma_{Hg}\cos(\theta)}{P} \quad (6.5)$$

where θ is the contact angle of mercury on the solid and γ_{Hg} is the mercury surface tension.

In his review paper, Diamond (2000) assessed this technique to be a proper method for providing accurate estimates of the pore size distribution of cementitious materials. He mentioned that MIP measurements provide imprecise air void sizes because the mercury is unable to reach most of the pores in the specimen. He concluded that MIP can be used only to provide a general idea of the threshold diameter of the pores. Any estimation of the size distribution using this method would be inaccurate.

6.4 Numerical approaches for modeling cement microstructure

The application of computational materials science became a key topic in the field of cement and concrete. In the past several years, many models of the hydration and microstructure evolution of cementitious materials have been developed. Among those are studies have been conducted by Jennings and Johnson (1986), Bentz and Garboczi (1991), van Breugel (1991), Navi and Pignat (1996), Maekawa et al. (1999), and Bentz (1997).

6.4.1 The Jennings + Johnson microstructure simulation model

Jennings and Johnson (1986) were among those who realized the importance of mathematically modeling cement hydration to have a better understanding of cement paste behavior. In the Jennings + Johnson microstructure simulation model, cement particles were assumed to be spheres, which are placed inside a cubic volume randomly. If overlapping occurs between two particles, one of the particles is moved to the closest available place, or relocated to another random location. Various inputs and parameters have to be provided to the simulator, such as the number and size distribution of particles, the density of reactants and products, the thickness of the anhydrous layer available for reaction in each step, and the reaction rate at each stage. Afterwards, the final positions and sizes of the particles are stored in a data file.

6.4.2 The HYMOSTRUC model

The HYMOSTRUC model, which is a continuum model, was developed by van Breugel (1995). In this model, a vector approach is used to simulate microstructural evolution during the cement hydration. The HYMOSTRUC model considers hydration that occurs at the particle-water interface and the reaction rate of a particle is dependent on the particle size distribution, the chemical composition of the cement, the w/c, and the temperature. Particles with diameters smaller than 3μm are assumed to dissolve immediately after adding water. In the HYMOSTRUC model, the pore size distribution is assumed to follow a Rosin–Rammler model, shown in the following equation:

$$V_{por} = a.\ln\left(\frac{\Phi}{\Phi_0}\right) \tag{6.6}$$

where V_{por} is the pore-volume; ϕ is the size of the pore; ϕ_0 is the size of the smallest pore fixed at 0.002 μm, representing the boundary between gel pores and capillary pores; and a is the pore-structure constant that depends on the microstructure and is obtained experimentally.

6.4.3 Integrated Particle Kinetics model

The Integrated Particle Kinetics model was developed by Navi and Pignat (1996). This model is also based on a vector approach. However, the main difference between HYMOSTRUC and this model is that the Integrated Particle Kinetics model simulates the hydration of every individual particle, using kinetics laws and taking into account both the size of the particle and its neighbourhood. In addition, it allows the new nuclei to grow in the pore space, and not only on the surface of cement particles.

6.4.4 The CEMHYD3D model

The CEMHYD3D model is considered one of the most widely used models in studying cementitious materials. In this model, Bentz and Garboczi (1991) employed the Cellular-Automata (CA) approach to predict the microstructure evolution of cement paste. In this technique, user-specified particle size distribution

(PSD) is placed as digitized spherical particles into a three-dimensional computational volume. The computational volume is examined in terms of voxels. Each voxel represents a specific material, such as an anhydrous, hydrate phase, or pore space filled with water. The state of any voxel depends on the voxel's own value and the values of its neighbours. The evolution of the microstructure is predicted based on some written local rules, animating cells on a lattice. These rules are mainly dictated by the chemical composition of clinker, the temperature of the reaction, the w/c, and the phase volume fraction.

The model can reproduce the degree of hydration, heat release, chemical shrinkage, percolation, diffusivity, phase volume fractions, and setting of cementitious materials. The CEMHYD3D model has been used by many authors to examine various properties of cement-based materials, such as liquid permeability (Snyder & Bullard, 2005), and elastic moduli (Haecker et al., 2005).

6.4.5 The HydratiCA model

In 2007, Bullard developed a stochastic three-dimensional model, called the HydratiCA, to overcome the limitations of CEMHYD3D. This model was established based on the fundamentals of thermodynamics and has the capability of capturing the chemical and physical mechanisms that take place in aqueous systems, such as the kinetics of nucleation and the growth of particles, the diffusion of phases in the solution, and the impact of temperature on the reaction rate. The different phases of cement are discretized on a cubic lattice. Each lattice site consists of cells that represent a specific phase (solid, liquid, and solute). The lattice sites are defined by their position relative to a selective reference point. Local rules are utilized to describe the diffusion mechanism and reaction kinetics that take place at lattice sites over short time intervals.

Diffusion is represented by assuming that each cell has the ability to adjust its location to any place of one of its six closest neighbours. On the other hand, the temperature influence was incorporated by taking into consideration the dependency of rate constants on the reaction temperature. To deal with heterogeneous reactions that happen due to the presence of different phases in the

adjacent lattice site, a smoothing technique was used to eliminate the discontinuity between surfaces.

The input parameters, such as rate constants and activation enthalpy, are totally independent of the chemical compositions, or the w/c, as the effects of these factors are taken into account by properly defining all cell types and numbers at different lattice sites. This model was employed to study the solidification process of tricalcium silicate (Bullard, 2008) and to investigate the early hydration of Alite (Juilland et al., 2010).

From the discussion above, it should be pointed out that most models have some limitations. To improve the performance, most of these models neglect some properties of cement, such as its multi-scale nature. Also, it is clear that most of the currently available models have some assumptions and simplifications, which may render those models invalid in some cases, especially when cement paste hardens under downhole conditions. Moreover, in all previously discussed models, the microstructural evolution is based on specific mechanisms, which do not match the mechanisms occurring when cement slurry is subjected to downhole conditions.

6.5 Microstructural evolution in µic

Mic, a microstructural modelling framework developed by Bishnoi in 2008, was selected to be employed in this study to overcome the limitations of other models stated in §6.4.5. In this platform, the vector approach method is used to model the geometry of the clinker particles and the different phases of cement paste. Hydrating cement particles are assumed to be spheres, which have radii and initial positions inside a cubic computational volume. The assumption of cement particles being a sphere has been made for simplification purposes and to reduce the time required to determine the overlap between spheres. The main disadvantage of this approximation is that it affects the shapes of the pores and the boundaries between particles, resulting in angular contacts developing between phases (Bishnoi, 2008). This occurs because the sphere has a small surface area to volume ratio, compared to any other geometrical shape. However, this assumption is still deemed acceptable and has been assumed by different authors (Navi & Pignat 1996; Breugel, 1995).

6.6 Defining the model in µic

Figure 6.3 represents a schematic diagram of the workflow used during the course of this study to predict the microstructure evolution of cement paste in µic. It can be seen that modelling cement paste hydration in µic includes several stages, such as defining the different materials inside the cubic computational volume, describing particle models, determining the reactions that govern the hydration process, and setting up the required plug-ins to control the microstructure development. The following section describes how the model is built in µic to simulate the microstructural evolution of hydrating cement paste.

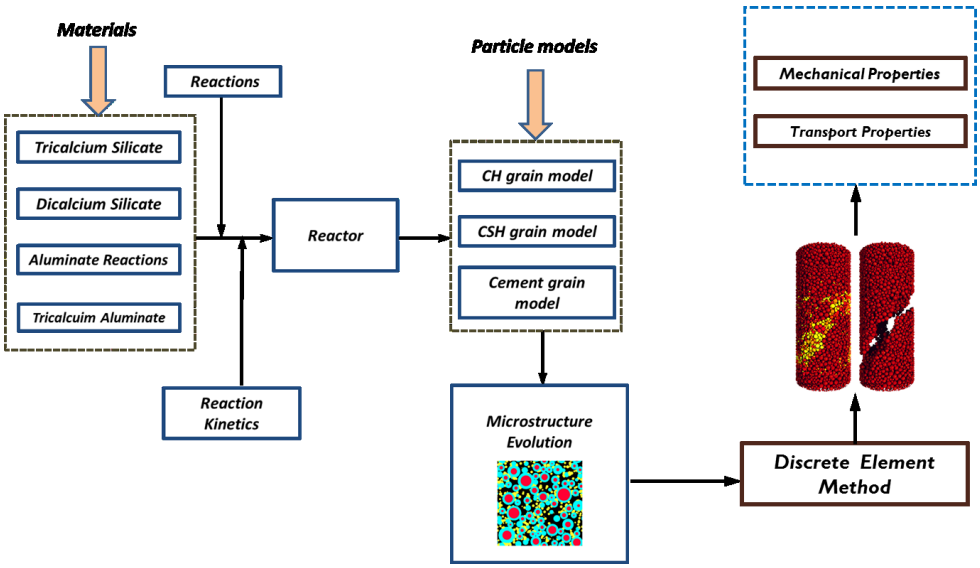

Figure 6.3 Schematic diagram of the workflow for µic

6.6.1 Materials

Portland cement is a mixture of limestone and clay. Clinker consists of four major phases called Alite, Belite, Aluminate, and Ferrite. Alite (tricalcium silicate, Ca_3SiO_5) is the most important phase in Portland cement, and it is a major factor in strength development during the first 28 days. The maximum crystal sizes of Alite can be up to 150 µm. Alite constitutes 50% to 70% of Portland cement. Belite (dicalcium silicate, Ca_2SiO_4) forms 15% to 30% of Portland cement clinkers and contributes to later-age strength (beyond 7 days). The sizes of Belite crystals

range from 5 μm to 40 μm and its reactivity is lower than Alite. Aluminate (tricalcium aluminate, $Ca_3Al_2O_6$) makes up 5% to 10% of Portland cement with crystal sizes of 1 μm to 60 μm and contributes slightly to early strength development. Aluminate crystals have irregular shapes and occupy the spaces between ferrite crystals. The reactivity of Aluminate with water is considered high compared to other phases. Finally, Ferrite (tetracalcium aluminoferrite, $Ca_2(Al,Fe)O_5$) makes up 5% to 15% of Portland cement and it may contain up to 10% of minor oxide with dendritic shape. It hydrates rapidly, but contributes little to strength.

When water is added to cement, a chemical combination of cement and water occurs. After a few hours of mixing with water, the strength starts to develop and the cement slurry transforms from a viscous fluid to a plastic solid to a stiff solid (Powers, 1958). Calcium hydroxide (CH) and calcium silicate hydrates (C-S-H) are the main hydration products. Calcium hydroxide, or portlandite, is the product of silicate hydration, and it forms 20% to 25% of the total product volume of well-hydrated cement (Laugesen, 2005). On the other hand, calcium silicate hydrates (C-S-H) are labeled as an inner and outer product. The inner product grows in the space between particles, while the outer product fills out the space formed due to the dissolution of Alite.

As C-S-H grows in different locations, it should be classified into different variants as follows:

- Variant 1 represents the inner product that replaces the reacting C_3S.
- Variant 2 represents particles that grow on the C_3S particles outside the original bounds of the particles.
- Variant 3 represents particles that grow on nuclei forming in the pores.
- Variant 4 represents a temporary material that helps the redistribution of the product. In this case, variant 4 does not take place in the microstructure and is defined as a universal material.

In this study, 13 materials were defined to describe anhydrous cement particles and hydration products, namely, Alite (C_3S), Belite (C_2S), Tricalcium Aluminate (C_3A), Tetracalcium Aluminoferrite (C4AF), gypsum (C S H_2), water, calcium silicate hydrate (C-S-H), calcium hydroxide (CH), grain CSH, pore C-S-H, outer C-S-H, inner ettringite, and outer ettringite. The physical properties of these materials are shown in Table 6.1.

Table 6.1 Physical Properties of Cementitious Materials

Compound Name	**Compound Formula**	**Density (kg/m^3)**	**Molar volume (cm^3/mole)**	**Heat of formation (kJ/mole)**
Tricalcium silicate	C3S	3210	71	-2927.82
Dicalcium silicate	C2S	3280	52	-2311.6
Tricalcium aluminate	C3A	3030	89.1	-3587.8
Tetracalcium aluminoferrite	C4AF	3730	128	-5090.3
Gypsum	C S H2	2320	74.2	-2022.6
Calcium silicate hydrate, C-S-H	C1.7SH4	2120	108	-3283
Calcium hydroxide	CH	2240	33.1	-986.1
Ettringite	C6 AS3 H32	1700	735	-17539

6.6.2 Grain model

Besides the different phases present in cement clinker, the hydration process involves the formation of new particles, either over the unhydrous cement particles, or in the pore space. In order to simulate cement paste microstructure accurately, each layer of the reacting particles and the hydration products should be defined through particle models. Three different particle models were employed to describe

the different compounds that existed, or developed, during the solidification process, as listed below.

1- The Cement Grain Model represents cement particles with C_3S and C-S-H phases. Kondo (1968) classified C-S-H into two categories: inner and outer C-S-H. Inner C-S-H replaces the C_3S, while the outer one grows in the space between the hydrating particles. These two types can be distinguished with a high-definition electron microscope as each type has a different morphology. This morphology is affected by the C/S ratio. C-S-H crystallites change from fibrous to corrugated foils with the reduction of the C/S ratio (Richardson, 2004). This can be attributed to the transition from propagating in one direction to two directions. Various opinions have been drawn on the size of C-S-H crystallites. Nonat (2004) pointed out that the layers of C-S-H, which coat the surface of cement particles, have a dimension of 30 x 60 nm and 5 nm thick. On the other hand, Richardson (2004) mentioned that the shape of inner C-S-H is a sphere and its size is dependent on the temperature as its diameter decreases from 4 nm to 8 nm at 20 °C to about 3 nm to 4 nm at higher temperatures.
2- The CH Grain Model represents calcium hydroxide (CH) particles that grow in the pores. CH constitutes about 20% to 26% by weight of cement paste and is present in different forms, such as crystalline, amorphous, and porous (Boyer & Berger, 2006). The size of the CH crystal is in the range of a few μm to hundreds of μm. The amount of CH present in the cement paste material can be obtained using different methods, such as calorimeter, X-ray, conductometric titration, chemical extraction, and thermal techniques. The CH amount formed during hydration is affected by both temperature and the degree of hydration, and it increases with the w/c due to a higher degree of hydration. The greatest rate of CH formation was found to take place in the first 24 hours (Ramachandran, 1979). Knowledge of the mechanism of CH growth and the morphology of these crystals is essential to understanding the behavior of cementitious materials. Some studies have pointed out that the crack propagations were mainly observed around and through CH crystals. In addition, the reactivity of pozzolanic materials can be estimated based on the free CH presents in the cement paste after hydration (Ramachandran, 1979).

3- The C-S-H Grain Model represents the calcium silicate hydrate (C-S-H) gel phase that grows in the pores. The solid density value of C-S-H found in the literature varies between 2500 Kg/m^3 to 2800 Kg/m^3 (Thomas & Jennings, 2006; Allen et al., 2007). On the other hand, the porosity of C-S-H has been determined to be between 28% and 48% (Powers, 1958; Thomas et al., 2006). Most cement paste properties are related directly to the formation of C-S-H.

6.6.3 Chemical reaction

As cement mixes with water, it hydrates and the microstructure forms. During hydration, a series of exothermic reactions occur, accompanied by heat release. Each phase of cement clinker has a specific reaction rate and generates a different type of hydrates. The following equations, adopted form Tazawa et al. (1995) and Mounanga et al. (2004) are used to represent the chemical reactions that occur during cement hydration:

Silicate Reactions

$$2C_3S + 10.6H \rightarrow C_{34}S_2H + 2.6CH_8 \quad (6.7)$$

$$2C_2S + 8.6H \rightarrow C_{34}S_2H + 0.6CH \quad (6.8)$$

Equations (6.7) and (6.8) show that both Alite (C_3S) and Belite (C_2S) form the same solid phase after hydration. However, Alite produces a large amount of CH. Alite reacts with water quickly after it is added and continues reacting for a short time. Most early age strength is mainly due to an Alite reaction.

Aluminate and Ferrite Reactions

An aluminate reaction consists of two stages. At early age, tricalcium aluminate (C_3A) reacts with water to form ettringite. Afterward, ettringite is converted into monosulfoaluminate, as shown in equations (6.9) to (6.13).

A ferrite reaction starts after mixing clinker with water. The rate of reaction decreases with time; this can be attributed to the development of iron hydroxide gel, which forms a barrier and stops the reaction.

$$C_3A + 6H \rightarrow C_3AH_6 \quad (6.9)$$

$$C_3A + 3C_2H_2 + 26H \rightarrow C_6AS_3H_{32} \quad (6.10)$$

$$2C_3A + C_6AS_3H_{32} + 4H \rightarrow 3C_4ASH_{12} \quad (6.11)$$

$$C_4AF + 3CSH_2 + 30H \rightarrow C_6AS_3H_{32} + CH + FH_3 \quad (6.12)$$

$$2C_4AF + C_6AS_3H_{32} + 12H \rightarrow 3C_4ASH_{12} + 2CH + 2FH_3 \quad (6.13)$$

$$C_4AF + 10H \rightarrow C_3AH_6 + CH + FH_3 \quad (6.14)$$

6.6.4 Reaction kinetics

Despite the tremendous amount of research that has been conducted during the last few decades on the cement solidification process, the hydration kinetics of cement reaction is still not fully understood. This is mainly due to the complex interaction between the different parameters that influence the hydration process and the formation of the cement matrix, resulting in an increase in the difficulty of this process. The term, reaction kinetics, is traditionally used to describe the impact of various experimental conditions on the chemical reaction mechanism and on its speed. Therefore, reaction kinetics controls the rate of reactions. As each of the four main phases present in clinker has a specific reaction rate, the kinetic rule should be defined for each compound separately. This is considered a critical step in the simulation process because reaction kinetics should take into account the effect of both high temperature and high pressure on the reaction.

To define the kinetics plug-in for each reaction occurring during cement hydration, the thermodynamics of multiphase porous media is used to develop a hydration kinetics model for Portland cement hydration at high temperature. Nucleation and growth kinetic laws are normally utilized to predict the cement hydration during different hydration steps. This kinetic law can be written in the following form:

$$\tau_x \frac{d\alpha}{dt} = A'(\alpha_x) \tag{6.15}$$

where α is the degree of hydration; τ_x is the characteristic time of the reaction; and $A'(\alpha_x)$ is the normalized affinity.

As the kinetic reaction of the solidification process is mainly dominated by the mechanism of water diffusion through the reaction products (i.e., the diffusion-controlled process), the degree of hydration can be expressed by the term of diffusion rate and the affinity $A'(\alpha_x)$; the latter can be written using the following Arrhenius equation:

$$A'(\alpha_x) = \frac{\alpha'}{\eta_\alpha} exp\left[\frac{Ea}{RT}\right] \tag{6.16}$$

where η_α is the permeability of the hydrates around the anhydrous cement; Ea is the apparent activation energy (J/mol); R is the universal gas constant (8.3145 J/mol K); and T is the absolute temperature (K).

The apparent activation energy Ea can be obtained experimentally (Glasstone et al., 1941) and it is the net result of the impact of temperature on numerous processes (van Breugel, 1991).

To take into account the effect of temperature and fineness on the reaction rate, the Arrhenius equation can be rearranged as (Pichler et al., 2006):

$$\tau(T, \varphi) = \tau(To) \frac{\varphi o}{\varphi} exp\left[\frac{Ea}{R}\left(\frac{1}{To} - \frac{1}{T}\right)\right] \tag{6.17}$$

where T_o is the reference temperature of a reaction (293 °K); T is the arbitrary temperature of the reaction; φ_o is the reference fineness (3602 $cm^2. g^{-1}$); and φ is the fineness of the cement.

According to Bernard et al. (2003), cement hydration can be divided into three processes. The normalized affinity and characteristic time depend on these processes. The first process is the dissolution of particles that occurs after adding

water to clinker. In this process, the normalized affinity is considered to be constant and equal to 1 (A' = 1), and is written as follows:

$$\tau = \frac{\alpha_o}{t_o} \tag{6.18}$$

where t_o is the duration of the initial induction period, and α_o is the critical degree of hydration at the end of the induction period.

At the second stage (nucleation process), the rate of reaction increases rapidly, where the nucleation and growth mechanism is affected by the shape and the dispersion of the phase (Bishnoi, 2008). Avrami's model was found to be a good way to describe the reaction rate during this stage (Avrami, 1939). Avrami's equation governs the process of nucleation and growth, and defines the mechanism of the transformation of solids from one state to another. It assumes that the material will follow a characteristic S-shape during the phase change.

According to Avrami (1939), phase transformation would be mainly dependent on the availability of germ nuclei in the cement clinker and in the cement slurry at early age. The amount of growth nuclei is proportional to the reaction time. However, the rate of growth decreases when germ nuclei reach a certain critical size and a steady state distribution is achieved, which is defined as the induction period. In the next stage, the phase transformation increases rapidly, accompanied by a rise in the surface area available for reaction and consumption of the initial phases, supporting increased production of new particles. In the final step, the rate of formation of new germ nuclei declines, due to a reduction in the amount of untransformed particles, until the transformation completely stops.

The normalized affinity and the characteristic time can be written as follows:

$$A'(\alpha_x) = \frac{1 - (\alpha_x - \alpha_{x,o})}{\left[\left(-\ln\left(1 - (\alpha_x - \alpha_{x,o})\right)\right)\right]^{\frac{1}{k}-1}} \tag{6.19}$$

$$\tau_x(T, \varphi) = \frac{1}{\acute{\kappa} K} \frac{\varphi_o}{\varphi} exp\left[\frac{Ea}{R}\left(\frac{1}{T} - \frac{1}{To}\right)\right] \tag{6.20}$$

where $\alpha_{x,o}$ is the degree of the hydration threshold of clinker X at the end of the induction period; *K* is the rate constant; and ќ is the reaction order

For T = constant, i.e., isothermal conditions, the following equation can be used to calculate α_x:

$$\alpha_x = \alpha_{x,o} + 1 - exp\left\{-\left[k\frac{\varphi_o}{\varphi}exp\left[\frac{Ea}{R}\left(\frac{1}{T}-\frac{1}{To}\right)\right](t-t_{xo})\right]^k\right\} \quad (6.21)$$

After reaching a critical degree of hydration, the diffusion of dissolved ions through the hydrates layers to clinker grain controls the kinetics of the hydration. The diffusion-controlled regime occurs when thick and continuous layers of hydrates are formed over the surface of reactant particles, allowing the free exchange of ions (Bishnoi, 2008). In this case, the reaction rate is dominated by the thickness of the C-S-H layer. Based on work by Fuji and Kondo (1974), the normalized affinity and the characteristic time can be written as follows:

$$A'(\alpha_x) = \frac{(1-\alpha_x)^{2/3}}{(1-\alpha_x^*)^{1/3}-(1-\alpha_x)^{1/3}} \quad (6.22)$$

$$\tau_x(T,\varphi) = \frac{R^2}{3D}\frac{\varphi_o}{\varphi}exp\left[\frac{Ea}{R}\left(\frac{1}{T}-\frac{1}{To}\right)\right] \quad (6.23)$$

where α_x^* is the critical hydration degree; *R* is the average initial radius of clinker grains; and *D* is a diffusion coefficient.

For T = constant, i.e. isothermal conditions, the following equation can be used to calculate α_x:

$$\alpha_x = \left\{1-\left[-\frac{(2D)^{\frac{1}{2}}(t-t_x')^{\frac{1}{2}}}{R\left\{exp\left[\frac{Ea}{R}\left(\frac{1}{T}-\frac{1}{To}\right)\right]\right\}^{\frac{1}{2}}\left(\frac{\varphi_o}{\varphi}\right)^{\frac{1}{2}}}+(1-\alpha_x')^{\frac{1}{3}}\right]^3\right\} \quad (6.24)$$

Then the overall hydration degree $\alpha(t)$ can be calculated from the following relationship:

$$\alpha(t) = \frac{\sum M_x \alpha_x(t)}{\sum M_x} \tag{6.25}$$

where M_x is the mass fraction of the clinker phases in the cement (M_{C3S}, M_{C2S}, M_{C3A} and M_{C4AF}).

Table 6.2 summarizes the parameters of Avrami's model.

Table 6.2 Parameters for affinity model of clinker hydration reactions (Berliner et al., 1998; Bernard et al, 2003)

Clinker	w/c	$T(T_o)$ [h]	κ	α_o	D [mm^2/h]	E_a [kJ/mol]
C_3S	0.3	13.5	1.86	0.02	$0.42x10^{-8}$	4500
	0.5	11.9	1.72		$2.64x10^{-8}$	
	0.7	10.5	1.66		$15.6x10^{-8}$	
C_2S	0.3	71.2	1.10	0.00	$6.64x10^{-8}$	2500
	0.5	60.9	0.96			
	0.7	58.6	0.84			
C_3A	0.3	57.7	1.14	0.04	$2.64x10^{-8}$	5500
	0.5	49.2	1.00			
	0.7	35.9	0.86			
C_4AF	0.3	27.0	2.44	0.40	$0.42x10^{-8}$	4200
	0.5	21.4	2.30		$2.64x10^{-8}$	
	0.7	14.3	2.16		$15.6x10^{-8}$	

6.6.5 Plug-in controlling microstructural formation

A plug-in is a short program that is compiled separately to modify the simulation process and to adjust the governing mechanism. In this study, two plug-ins are defined to control the evolution of the microstructure:

1. The surface distribution profile plug-in was used to control the formation rate of new C-S-H nuclei grown in the pores. In this plug-in, the numbers of new nuclei are calculated and new spaces are assigned to these nuclei.

The distribution of materials is proportional to the available surface area of each grain.

2. The nuclei generator type plug-in was used to control the number and location of new particles, and generators created new nuclei growing in the pores. In this model, a dependent exponential nuclei generator plug-in is used to generate a number of nuclei that exponentially decay.

6.7 Determining Young's modulus of early age cement paste

The evolution of elastic moduli at early age follows a complex mechanism and is affected by the hydration process. Many methods can be used to estimate the elastic modulus of cement-based material, such as the maturity approach (Byfors, 1980), degree of hydration (Van Breugel, 1991), and degree of solidification concept (Bazant et al., 1989). The finite element method (FEM) is also considered one of the most widely used numerical schemes in predicting effective properties of different materials. This technique was developed in the 1960s and was applied initially to study composites with a periodic microstructure. The discretization of the model can be performed using structured and non-structured meshing approaches. The discrepancy in the elastic properties, obtained by analytical approaches and the FEM, depends on the size of the pores at a particular degree of hydration. The difference in the results would increase if the capillary porosity is greater than 35%, while at higher degrees of hydration, both techniques would yield similar results (Stora et al., 2006). The main disadvantage of the FEM is that it requires an additional computational cost.

In contrast, research has been conducted on utilizing homogenization modeling approaches to study the elastic behavior of concrete, and proved that this technique has a high capability to predict the macroscopic elastic properties of cement paste with a low computational cost (Bernard et al., 2003; Smilauer, 2005; Le et al., 2008). Consequently, the same approach used by Bernard et al. (2003), was adopted here to predict the elastic modulus of cement paste at early age. In general, estimating effective properties of heterogenous material involves dividing the material into two scales of microscopic and macroscopic scales. The accuracy

of the results is largely dependent on the size of these scales. The microscopic scale should be sufficiently small to capture the heterogeneities of the material. Meanwhile, the macroscopic scale should be large enough so that all the phases exist in the material (Chamrova, 2010). To fulfill that, the multi-scale microstructure of cement paste has been divided into two levels: Level I, which contains the two types of C-S-H with different elastic properties, and Level II, which represents cement paste (homogeneous C-S-H with CH crystals, unhydrated products, water, and capillary porosity).

The Mori Tanaka scheme (1973) was chosen to determine the homogenized bulk and shear moduli for Level I. In this scheme, the matrix phase is selected to be a reference medium. Then, the homogenized bulk modulus and shear modulus can be written as follows:

$$\frac{k_{hom}}{k_m} = 1 + f_I \frac{{k_I}/{k_m} - 1}{1 + \beta_m(1 - f_I)\left({k_I}/{k_m} - 1\right)} \tag{6.26}$$

$$\frac{\mu_{hom}}{\mu_m} = 1 + f_I \frac{\mu_I - \mu_m}{1 + \beta_m(1 - f_I)\left({\mu_I}/{\mu_m} - 1\right)} \tag{6.27}$$

and

$$\alpha_{\mathrm{m}}^{\mathrm{est}} = \frac{3\mathrm{k_m}}{3\mathrm{k_m} + 4\mu_{\mathrm{m}}} \tag{6.28}$$

$$\beta_{\mathrm{m}}^{\mathrm{est}} = \frac{6\mathrm{k_m} + 12\mu_{\mathrm{m}}}{15\mathrm{k_m} + 20\mu_{\mathrm{m}}} \tag{6.29}$$

Where k_{hom}; μ_{hom}; k_m; and μ_m are the bulk moduli and the shear moduli of the homogenized and of the reference medium respectively

On the contrary, the self-consistent scheme was found to be appropriate for Level II. In this scheme, the reference medium is represented by the homogenized medium itself. Then, the following equations are used to calculate the homogenized Young's modulus and Poisson's ratio:

$$E_{hom}^{est} = \frac{9k_{hom}^{est}\mu_{hom}^{est}}{3k_{hom}^{est}+\mu_{hom}^{est}} \tag{6.30}$$

$$\nu_{hom}^{est} = \frac{3k_{hom}^{est} - 2\mu_{hom}^{est}}{6k_{hom}^{est}+2\mu_{hom}^{est}} \tag{6.31}$$

Where E_{hom}^{est} ; and ν_{hom}^{est} aree homogenized Young's modulus and Poisson's ratio respectively.

A detailed explanation about the derivation of these equations can be found in Bernard et al. (2003).

Determining the elastic properties of different phases that exist in cement is a crucial step in predicting the effective properties of cement-based materials. Many studies have been conducted to investigate the intrinsic elastic properties of cement paste constituents. Beaudoin (1983) compared the intrinsic value of Young's modulus (E) of CH with that of Portland cement paste. He performed the tests on disc and rectangular beams at different pressures. The modulus of elasticity was calculated from the load and deflection measurement. The value of Young's modulus for CH was found to be lower than that of Portland cement, but was in the same order of magnitude. They concluded that Young's modulus of CH is dependent on the contact between particles and porosity. Velez et al. (2001) measured the elastic modulus of the main four phases of Portland cement (C_3S, C_2S, C_3A, and C_4AF) at the microscopic and macroscopic levels by employing nano-indentation and resonance frequencies methods, respectively. The elastic moduli of those compounds were found to be porosity dependent, increasing as the porosity decreased. The values, calculated at the microscopic scale, were found to be consistent with the values estimated at the macroscopic scale by the means of extrapolation at zero porosity.

In their study, Constantinides and Ulm (2004) focused on two types of hydration products called high and low density C-S-H. They carried out nano-indentation tests on non-degraded and calcium-leached cement paste samples of 10 mm to 15 mm. The authors mentioned that the elastic properties obtained for C-S-

H are independent of mix proportion and they can be considered as intrinsic properties.

Table 6.3 presents the intrinsic elastic properties of cement paste constituents measured using different techniques. These measurements were used to predict the elastic modulus of cement paste. The bulk modulus and shear modulus of the aqueous phase, k_w, are estimated to be 2.2 GPa and zero, respectively.

Table 6.3 Intrinsic elastic properties of different phases of cement paste

	Phase	E (Gpa)	ν	References
Anhydrous Components	C_3S	135±7	0.3	Velez et al. (2001)
	C_2S	140±10	0.3	Acker (2002)
	C_3A	145±10	0.3	Velez et al. (2001)
	C_4AF	125±25	0.3	Velez et al. (2001)
Hydrates Components	CH	39.77	0.305	Monteiro & Chang (1995)
	C-S-H_{LD}	21.7	0.24	Constantinides & Ulm (2004)
	C-S-H_{HD}	29.4	0.24	Constantinides & Ulm (2004)
	$C_6AS_3H_{32}$	22.4	0.25	Constantinides & Ulm (2004)
	C_4ASH_{12}	42.3	0.324	Constantinides & Ulm (2004)
	C_3AH_6	22.4	0.25	Constantinides & Ulm (2004)
	FH_3	22.4	0.25	Constantinides & Ulm (2004)
	Al	24	0.24	Bernard et al. (2003)

6.8 Results and discussion

6.8.1 Microstructure evolution of cement paste at early age

The simulation of hydration of a 100 x 100 x 100 μm^3 cubic sample of Class G cement with a w/c of 0.44 cured at 60 ºC was carried out using μic. Figure 6.4 shows the graphic representation of 2D section images of microstructure evolution. The microstructure of cement paste mainly contained three phases (anhydrous material, reaction product, and aqueous phase). As shown in Figure 6.4 the two morphological types of C-S-H can be recognized easily in the cement matrix. The inner products of C-S-H particles grow over the cement particles and the outer products grow in the space between the cement particles. As the hydration process progresses, the outer layers of C-S-H increase, and the products become thicker until the small grains reach the point at which C-S-H particles have no cores of the Alite phase. However, some of the Alite grains were observed to be surrounded by C-S-H layers, which were more consolidated than the one formed at early age. CH particles were found to form new nuclei in the available pore space. The rate of formation for the CH phase was lower than that of C-S-H at early age. All microstructural characteristics can be obtained from the simulation results at each step, including the location and the size of both anhydrous and product particles, the volume fraction of each phase, pore volume, the contact surface, and the thickness of C-S-H and CH particles. This information is used later to calculate the elastic modulus of cement paste by applying the homogenization theory. It is apparent that the μic proved its ability to display the three-dimensional microstructure as two-dimensional slices in the middle plane and along the three directions.

During the solidification process, the internal volume of the anhydrous cement and aqueous phase decreases with time as the clinker particles dissolve in the pore solution and the free water is consumed to produce the hydrates. On the other hand, the volume of the solid in the cement matrix increases while gaining more strength. The rate of the reduction in the radius of C_3S particles and of the water consumption during the reaction is greatly dependent on several factors, such

as the w/c, temperature, pressure, and the hydration time. The total volume of the reactant materials (cement clinker, water, and any other additives) is higher than the volume of the hydrates (C-S-H and CH phases), resulting in what is called the shrinkage phenomenon.

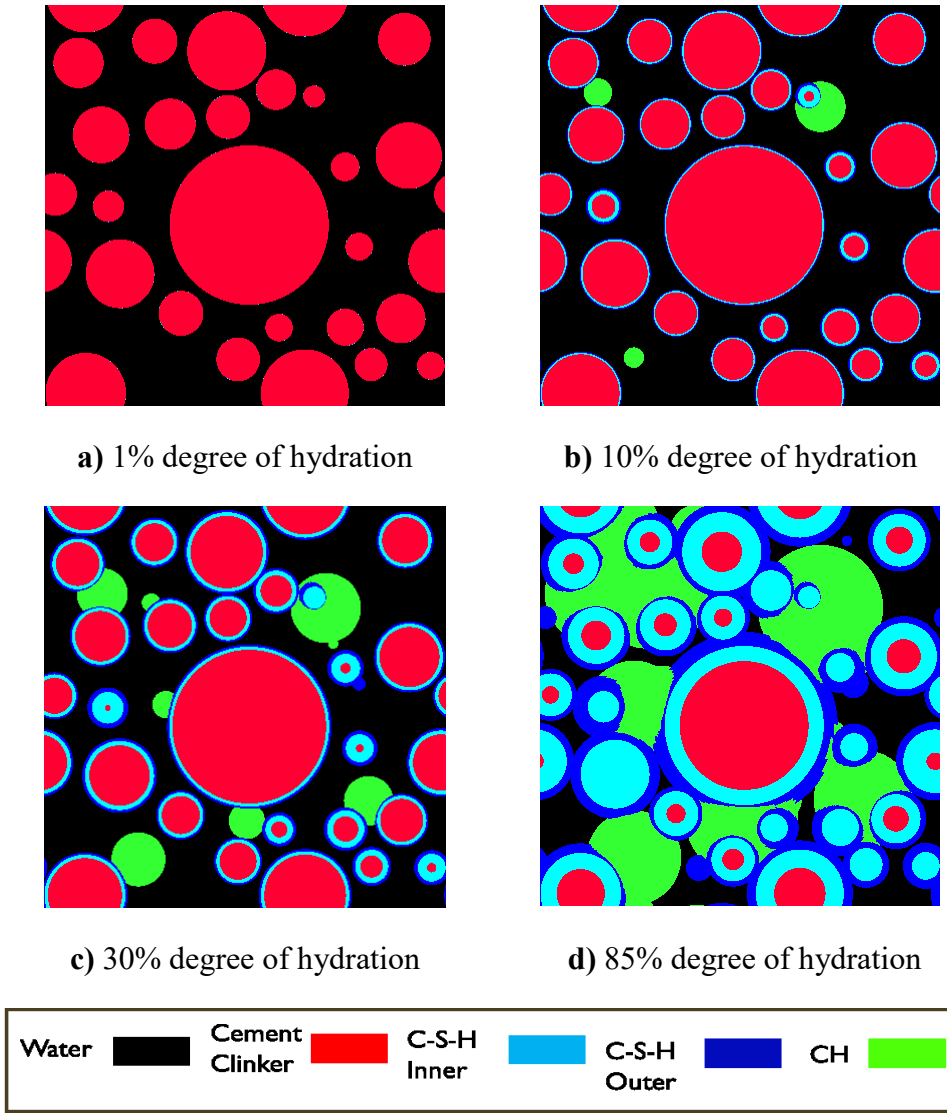

a) 1% degree of hydration

b) 10% degree of hydration

c) 30% degree of hydration

d) 85% degree of hydration

Figure 6.4 Microstructure evolution at different degrees of hydration: a) 1% degree of hydration; b) 10% degree of hydration; c) 30% degree of hydration; d) 85% degree of hydration

The evolution of the volume fractions of reactants and hydrates, as a function of the degree of hydration, is depicted in Figure 6.5. This method of illustrating the hydration results is very useful because it provides us with an

estimated volume fraction of the different material phases in the cement paste. It also gives us a clear idea about the distribution of different phases within the cement matrix. As shown in Figure 6.5, the amount of unhydrated cement particles and free water in the mix decrease with time due to the dissolution of anhydrous particles, which is accompanied by the production of hydrated particles. With the progress of the solidification process, the pore volume filled with water continues to decrease while the pore space occupied by air increases gradually. However, the total volume of the aqueous phase drops. CH products started to form in the pores between cement grains earlier than C-S-H. However, after some time, the rate of the formation of C-S-H became greater than that of CH, resulting in a higher total volume of C-S-H than CH. The outer product of C-S-H appeared earlier than the inner phase. In addition, the rate of consumption of both water and anhydrous grains was found to be similar. Test results revealed that at a degree of hydration of 50%, the pores had a volume fraction of approximately 1.5%, and the volume of clinkers that remained without hydration was 18%, while reaction products occupied around 49% of the total volume.

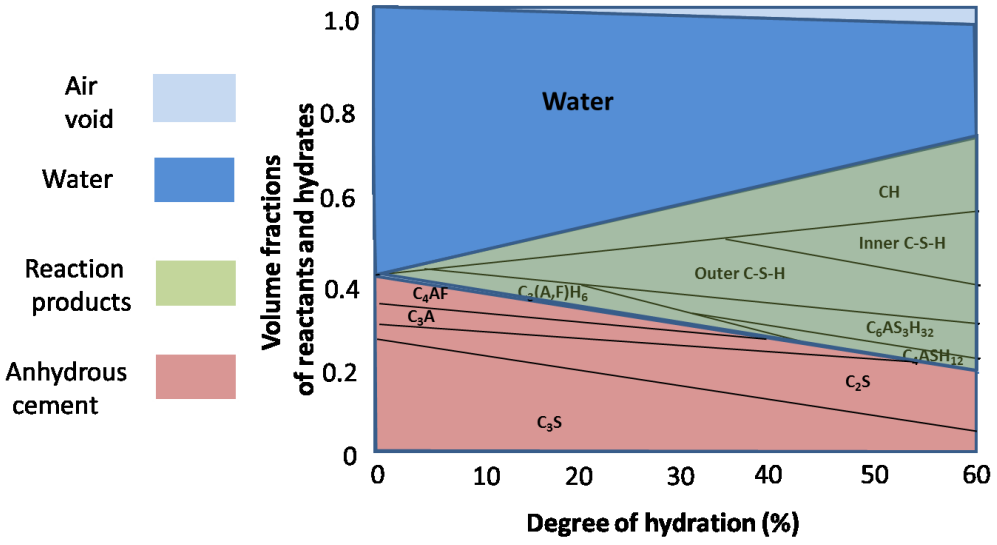

Figure 6.5 Evolution of the volume fractions of reactants and hydration products calculated using simulation output

In order to verify the model results, the outputs from µic were compared to the experimental results obtained from the literature. The input data to the model, such as cement type and curing conditions, were selected to represent the experimental conditions. In Figure 6.6, the degree of hydration obtained at different temperatures from the model as well as the experimental results are plotted in the same graphs. These graphs demonstrate the dependency of hydration kinetics on the curing temperature. It is clear that the total degree of hydration increased significantly with the rise in temperature with no crossover between curves, which means that the impact of temperature on the hydration rate continues even at later stages. The graphs reveal a good consistency between experimental and modelling results. It can be concluded that the model proved its capability to properly predict the degree of hydration of cement paste.

It is worth mentioning that the anhydrous cement grain packing is controlled mainly by the particle size distribution of the clinker. This initial packing is found to have a considerable impact on the microstructure evolution as it affects the thickness of the hydrate layers and the location of newly formed phases.

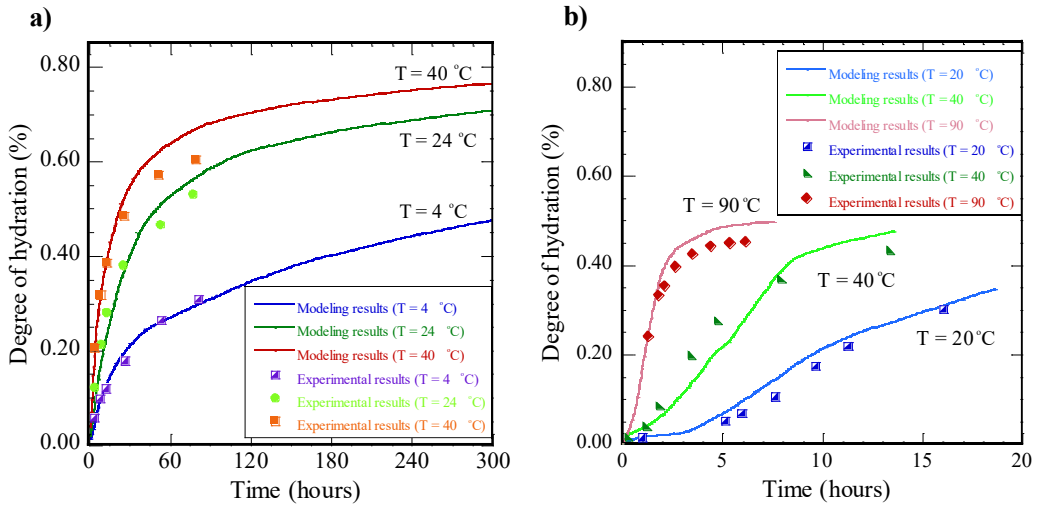

Figure 6.6 Comparison between modeling and experimental results a) Experimental data from W. Lerch, C.L. (1948). b) Experimental data from Hill et al. (2002).

6.8.2 Development of elastic modulus of cement paste

The results obtained from the homogenization technique is presented in Figure 6.7. As expected, the higher the curing temperature, the faster the development of Young's modulus. For further verification of the modeling output, the results of the latter were compared to the experimental results obtained in Chapter 5 of this thesis. As shown in Figure 6.7, both results have the same general trend; however, a small difference in the elastic properties was observed when the two results were compared. This outcome is expected since the experimental results represent dynamic elastic properties obtained from ultrasonic measurements. Generally, the elastic properties derived from dynamic techniques are greater than those obtained from static tests, as explained in Chapter 5.

It should be mentioned that the effective properties obtained by the homogenization method or any other techniques are sensitive to several parameters that may affect the precision of the results. One of these factors is the accuracy of the microstructural model, and whether or not it correctly represents the different phases of the reactants and hydration products along with capillary porosity. In addition, the results are largely dependent on the proposed values of the elastic properties for the different compounds and phases. Of course, the geometry of inclusion is another important factor. Most of the research that has been done on cement assumed various microstructural components to be spherical for simplicity. However, in reality, none of it is a sphere. For example, the shape of the CH crystals is affected by the confinement status. In general, the shape resembles platelets or flakes and becomes more like massive hexagonal plates in a non-confined environment (Richardson, 2000). The impact of assuming spherical inclusion approximation on the results is observed to be insignificant when the homogenization scheme is used in the case of sound cement paste (Stora et al., 2006).

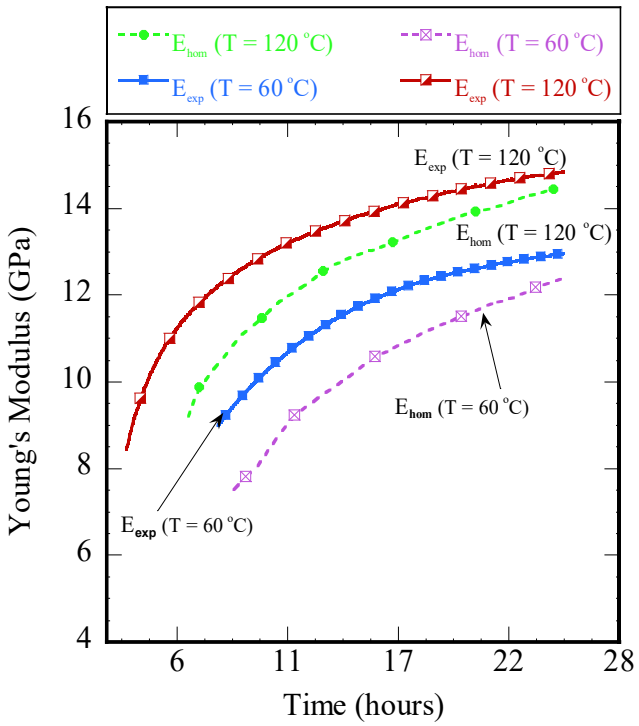

Figure 6.7 Comparison between modeling and experimental results of cement paste Young's modulus evolution

6.9 Summary and conclusion

The mechanical properties of cement paste, such as compressive, tensile, and shear strength, are largely dependent on the microstructure. Also, microstructure plays an important role in durability, as most durability problems are related to pore properties, and microstructure modeling can be used to study the transport properties of cementitious systems. On the other hand, permeability and shrinkage behavior are controlled by the solid matrix of cement paste.

In this study, μic (a platform developed by Bishnoi (2008) for modeling the hydration process of cement) was used to investigate the hydration kinetics of cement and to model the microstructural evolution of hydrating cement paste under elevated temperatures. The representation of the geometry of the cement matrix was based on a vector approach in which all anhydrous cement particles and hydration products were denoted as spheres and stored inside a cubic computational volume

according to their centroids and radii. Utilizing this approach not only gives μic the ability to represent the multi-scale nature of cement particles, which is important in covering the wide range of particle size distribution that exists in cement-based material, but it also allows each grain to react individually based on the properties of the grain and its neighboring particle. Clinker grains are placed inside the computational volume on a random basis where there is no overlapping between any particles.

The model incorporates many essential modifications that allow us to mimic the realistic behavior of the hydration process by including the impact of temperature on the hydration kinetics. A nucleation and growth mechanism was employed to describe the reaction rate while the deceleration stage was defined through the diffusion mechanism.

The simulation results revealed that many factors may affect the microstructure evolution, such as the chemical composition, particle size distribution, and degree of hydration. The impact of temperature on the formation of hydrates was clear as well. The higher the temperature, the greater the degree of hydration that can be attributed to the increase of reaction rates due to temperature. In addition, high temperatures led to the presence of a non-uniform distribution of hydrates and coarse pore structure within the cement matrix. These observations align with what has been found in the literature (Verbeck & Helmuth, 1968; Kjelsen et al., 1990).

In general, μic was found to be a valuable tool, as it gives a descriptive information about the formation of hydrates and provides us with a clear picture of the microstructure evolution that occurs with time due to the solidification process. The output from the model is a three-dimensional representation of the microstructure evolution at each step of the hydration. This representation describes the location and the size of all particles. The thicknesses of C-S-H that coat the original anhydrous particles are also defined. The microstructural information obtained from the simulation can later be used to investigate the mechanical and transport properties of the cement paste.

The second part of this chapter is devoted to estimating the effective elastic properties of cement at early age. To achieve this, the data of the microstructure evolution obtained from μic, along with homogenization modeling approaches, were used to predict the development of Young's modulus for cement paste during solidification. To effectively simulate the multi-scale nature of cement paste, the latter was assumed to consist of two levels, called the macro and micro levels. The macro level describes the cement matrix itself, while the micro level represents unhydrated clinker grains, hydrates, and pore spaces. Therefore, the results obtained using this approach are very sensitive to the accuracy of the output of the microstructural model. Any misrepresentation in hydration products and/or capillary pores will greatly affect the results.

The results obtained in both parts of this study were verified by experimental data. μic and homogenization modeling approaches demonstrated their capability to produce results that are in close agreement with experimental methods.

In conclusion, since microstructure can provide us with valuable information about pore spaces, more focus should be put towards studying the variations of capillary porosity with the degree of hydration. This would help us to better predict the strength of hydrated cement paste, as there is a close relationship between the total porosity and the strength of cement matrix. In addition, more studies should be carried out to investigate the impact of other variables, such as initial particle size distributions, pressure, and packing, on the characteristics of microstructure. Last but not least, attention has to be paid to the connection between the microstructure characteristics and the overall performance of cement, as this relationship has not been established yet.

Chapter 7 : Characterization of Steam Chamber Impact on the Integrity of Stratigraphic Wells Abandoned with Non-Thermal Cement

7.1 Introduction

The application of Steam Assisted Gravity Drainage (SAGD) technology to produce heavy oil was first proposed by Butler and his co-workers (Butler, 1980; Butler et al., 1981; Butler and Stephens, 1981) and first used in 1980 in Cold Lake. The fundamental concept of SAGD is to heat oil sand by steam in order to reduce the viscosity of oil. SAGD consists of two boreholes that are drilled horizontally, one on top of the other. Both boreholes are drilled close to each other, approximately 5 metres apart and close to the bottom of the oil sand layer. Steam is injected through the top injector. It takes a while (several months) until clear communication between two boreholes is identified. This is at the start of the project when the collector borehole begins producing oil. While steam is injected into the formation, a zone all around the injector will be affected by steam and heat transfer is established.

The affected zone is called the steam chamber (SC). Growth of the steam chamber is an indicator of progress both in production and injection. The steam chamber has two directional growths. At the very beginning of the project, it has the tendency to go upward. Once the steam chamber reaches a lower permeability barrier, lateral growth follows.

As mentioned before, in a SAGD operation, saturated steam is continuously injected into the injector. This process leads to an increase in the pore pressure and the temperature of the surrounding formation. Pore pressure and temperature decrease quickly with distance away from the well pair until it reaches the reservoir initial conditions. Consequently, delineation wells are exposed to different variations in pressure and temperature based on their relative position to SAGD well pair, resulting in more deformation of these wells, especially when these wells were abandoned with non-thermal cement.

This study investigates the geomechanical behavior of delineation wells abandoned with non-thermal cement, which are subjected to SAGD steam chamber evolution while taking into account reservoir heterogeneity. A sequentially coupled approach was utilized to define the permeability changes resulting from geomechanical effects. The methodology used in this chapter enables the response of the stratigraphic well to be evaluated, regardless of its location. The shared boundary modeling concept was employed in the simulation framework to make the calculation computationally feasible. To interpret the complex effects of elevated temperature and high pressure on the non-thermal cement behavior, two failure regimes were identified based on the deterioration of cement properties and permeability due to high temperature.

7.2 Geomechanical aspect in SAGD operation

Geomechanical effects are considered one of the major issues in the SAGD process. Besides the possibility of failure occurring, temperature changes due to heating lead to alteration in in-situ stresses and petro-physical properties (Farouq Ali, 1997). During SAGD operations, the total stress increases as a result of the thermal expansion of reservoir grains and pore fluids, due to the temperature. On the other hand, the effective stress of the reservoir decreases because steam injection causes a change in pore pressure. Consequently, several geomechanical behaviors may occur, including isotropic unloading, shear dilation, and compaction. These processes greatly affect oil recovery due to the impacts on reservoir petro-physical properties, such as absolute and relative permeability, porosity, and gas evolution. The permeability changes during isotropic unloading were observed to be dependent on the degree of unloading and the stress path (Scott et al., 1994).

In addition, SAGD operating conditions are highly affected by stress-strain changes that occur in the reservoir, especially changes in steam injection pressure. For instance, when the geotechnical response is ignored, a high recovery rate can be obtained by using low injection pressure, while high injection pressure is

preferable when a geomechanical feature is considered because of shear failure, improving the SAGD performance (Ito et al., 1996).

In the past, multiphase flow models, based on porous media behavior, were employed to describe the recovery process (Coats, 1978; Rubin, et al., 1985) until the significance of the geomechanical impacts on this mechanism was realized. Since then, the role of the geomechanical response in SAGD has been investigated numerically and experimentally. In their attempt to describe the thermal processes in oil sands, Settari et al. (1989) developed a model based on coupling the fluid flow mechanism and mechanical behavior. The model took into account the nonlinearity of soil behavior, assuming that the minimum effective stress controls the soil performance. The authors concluded that nonlinear mechanics should be employed to capture the real behavior of fracture zones.

In general, the behavior of soil has a sort of nonlinearity under a wide range of applied stresses. Therefore, selecting the appropriate mechanical constitutive model is essential to capturing the real performance. The mechanical properties of oil sands have been extensively investigated. The experimental results that were obtained by many authors revealed that oil sands material can be defined by the strain-softening constitutive model (Oldakowski, 1994; Samieh & Wong, 1997; Touhidi-Baghini, 1998).

Changes in pressure due to flow or thermal expansion of the fluid may lead to shear failure in oil sands. It was observed that the oil sands material tends to dilate during failure. This behavior increases the permeability and alters the stress distribution to reach to a new equilibrium state (Settari, 1989). Chalaturnyk and Li (2004) mentioned that shear failure might occur when the steam injection pressure is similar to the initial mean effective confining stress in the reservoir.

Permeability changes during SAGD have been discussed by several authors; Scott et al. (1994) noticed that permeability increased by 70% due to unloading from initial effective stresses of 4360 kPa. Chalaturnyk (1996) reported a 30% increase in the absolute permeability between the well pairs of A1 and A2 at UTF Phase A site. The corresponding maximum shear strain and volumetric strain

between the well pairs of A1 and A2 were 3% and 2.6%, respectively. Touhidi-Baghini (1998) observed an increase of 40% in vertical permeability (k_v) and 20% in horizontal permeability (k_h) as a result of increasing a dilative volumetric strain by 2%. He concluded that this behavior should be taken into account in a reservoir simulation, as it significantly affects the in-situ recovery process. It should be noted that Touhidi-Baghini conducted his experiments on the McMurray oil sands formation.

Usually, permeability changes occur during isotropic unloading and anisotropic loading or due to temperature variations. In the isotropic unloading stage, both the initial porosity and stress path control permeability variation. Having a formation with a high porosity leads to more permeability change. In addition, increasing pore pressure has a greater impact on permeability than reducing the total isotropic stress. On the other hand, mean effective stress, shear strength, and grain compressibility are the main factors that affect the permeability during the anisotropic loading stage. Unlike low-strength materials, formations of higher strength experience a reduction in permeability during shear at high effective stresses. The influence of elevated temperature on the permeability is dominated by the isotropic effective stress. Unlike high isotropic effective stress, permeability increases with temperature at low isotropic effective stress levels. The dependence of permeability on temperature was observed to be higher in the case of unconsolidated sand rather than sandstone (Scott et al., 1994).

7.3 Geomechanical zones around steam chamber

Three zones can be identified at the edge of the steam chamber based on the drainage conditions: drained, partially drained, and undrained zone (Li et. al, 2004). In the drained zone, geomechanical processes have an insignificant effect on the pore pressure development. The change in effective stress is mainly controlled by both steam injection pressure and thermal expansion. The fluid mobility in this zone is high enough to prevent pore pressure from building up and exceeding the injection pressure value. The partially drained zone is considered a transition region between drained and undrained zones. The area of this zone is largely dependent

on both pore pressure and temperature variations. For instance, the higher the injection pressure, the larger the size of the partially drained zone. The undrained zone exists next to the partially drained zone and covers the entire far-field area. This region is characterized by low fluid mobility that decreases the ability of pore pressure to dissipate. Undrained conditions can be adopted within this area. Therefore, shearing results in pore pressure variation with no volume change. The total stress variation dominates the effective stress behavior.

Li et al. (2004) employed the value of bitumen viscosity to define the boundaries between the three zones. They suggested that the boundary of the drained zone lies adjacent to the steam chamber surface and extends to areas where bitumen viscosity is less than 1000 cP. On the other hand, they defined a range of 1000 cP to 20000 cP for the partially drained zone.

Irani and Gates (2015) examined the validity of Li et al.'s (2004) assumption that in the undrained zone, shearing occurs under undrained conditions without any volumetric change, resulting in an increase in pore pressure. They mentioned that the drained zone includes a sheared zone as injection pressure dominates the pore pressure inside the shear zone. They concluded that SAGD system involves only drained and partially drained zones.

7.4 Comparison of coupling approaches

Coupling of reservoir flow and geomechanics has been an interest for a long time in the petroleum engineering industry. The importance of including geomechanical responses appears clearly, when the nonlinearity of the material behavior is considered. In such cases, a significant difference between the results obtained using a conventional simulator and coupled solution is observed. This is because, unlike a coupled approach, the impact of stress-strain variation on the flow calculation is completely ignored in an uncoupled solution (Dean et al., 2006). A coupled model may include more than two variables based on the type of analysis. For instance, in thermo-hydro-mechanical cases, three variables are involved, namely displacement, pore pressure, and temperature.

Several coupling techniques can be employed to investigate the interaction between reservoir fluid and geomechanical deformation, such as non-coupled, one-way coupled, sequentially coupled, and fully coupled methods. The numerical cost of solving a non-coupled problem is considered reasonable; however, it is not accurate, as it neglects the impact of geomechanics on the reservoir. In this approach, pore compressibility is defined through the relationship between porosity and pressure. Both flow and geomechanics are solved separately. The pore volume variation in the reservoir is calculated only based on the pore pressure change, which is not correct. In reality, stress changes in the reservoir affect volume variation as well. Consequently, both temperature variations and the thermo-hydro-mechanical properties of the reservoir have to be taken into account in the simulation process as these factors strongly dominate the stress variations.

In one-way coupling, the reservoir simulator results are fed back to the geomechanical module to calculate the mechanical equilibrium state. However, nothing is transferred back to the reservoir simulator. This means that geomechanical calculations are affected by the variation in reservoir flow parameters, but the geomechanical response has no impact on fluid flow calculations. This approach provides a good tool to estimate stress and strain changes in the reservoir and surrounding formations. The accuracy of one-way coupling approach is mainly dependent on the rule of geomechanical effects in the reservoir calculation.

In the sequentially coupled approach, flow and geomechanical calculations are performed separately. Deformation calculations are executed one step after solving the flow equations. However, the information is transferred back and forth between the flow simulator and geomechanical module after each time step. Consequently, this technique takes into consideration the impact of the geomechanical response on the reservoir flow.

The fully coupled approach represents the most accurate coupling technique, as it simultaneously solves the equations that govern the thermo-hydro-mechanical behavior in the same linear system. As a result, the running speed of

this simulation decreases dramatically, especially when the elastoplastic constitutive model is used. Fully coupled problems can be important when the dependence of flow properties on the nonlinear mechanical behavior of formation should be addressed.

7.5 Build SGrid for SAGD and geomechanical model

In this study, a Reservoir Simulation Grid model (SGrid) with dimensions of 3000 m x 2000 m x 170 m was built inside the SKUA software. The study area located 60 km northwest of Fort McMurray, Alberta. As indicated in Figure 7.1, the geological profile for the study area consists of five major layers. These layers, from the top of the model to the bottom, are Quaternary, Clearwater, Wabiskaw, McMurray, and Devonian.

SGrid was populated with flow and mechanical properties. The flow properties mainly include all the essential parameters needed to perform flow calculation inside STARS^{TM} (Steam Thermal and Advanced Processes Reservoir Simulator), such as permeability, porosity, and thermal rock types, while the mechanical properties contain the parameters used by the stress simulator (FLAC3D from Itasca) to compute stresses and deformations. These parameters include density, in-situ stresses, and constitutive properties such as friction angle and cohesion. The ground water table was set at 21 m below the ground surface. Pore pressure was computed based on water density and the degree of saturation. The ground surface initial temperature was set to 8 °C. Temperature was assumed to increase linearly with depth, with a gradient of 0.027 °C/m. The initial in-situ pore pressure and temperature at a depth of 102 m were 794 kPa and 10.7 ºC, respectively. The initial vertical stress was computed based on the density of the blocks. The initial maximum and minimum horizontal stresses were assumed to be 1.1 and 0.6 of the vertical stress.

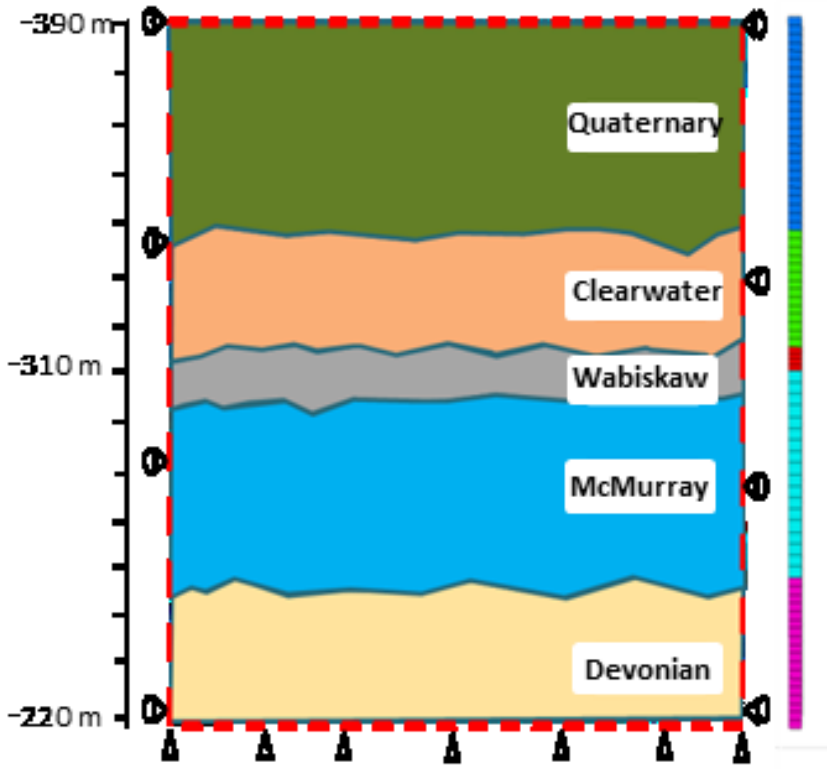

Figure 7.1 Geological profile used to build grid models

7.6 Simulation set up of SAGD process

Flow simulation was performed using a commercial reservoir simulator, STARS™, developed by Computer Modelling Group (CMG, 2015). The 3D reservoir simulation model contains five well pairs. The depth of the reservoir is 83 m while the thickness of the pay zone is 39 m. The production well was located 3 m above the bottom of the pay. The fluid is comprised of two phases; i.e., water and oil. The initial oil saturation and water saturation in the reservoir were 0.78 and 0.22, respectively. Neither a thermal boundary nor a flow boundary were defined at the faces of the grid. At the beginning, 150 days of preheating period was considered. Thereafter, a maximum injection pressure BHP of 1283 kPa, with a steam quality of 95% and temperature of 193 °C, was injected at the injector well. Table 7.1 summarizes the reservoir properties. A short review of some of these properties and how it may affect the SAGD process is presented in the next sections.

Table 7.1 Reservoir rock and fluid properties

Properties	**Value**
Depth to top of reservoir (m)	83
Reservoir thickness (m)	39
Reference depth (m)	77
Initial reservoir pressure (kPa)	794.61
Initial reservoir temperature (ºC)	10.75
Initial oil saturation, So	0.22
Initial water saturation, Sw	0.78
Rock heat capacity (kJ/m^3 ºC)	2390
Average horizontal permeability (mD)	3000
Average vertical permeability (mD)	1500
Oil density (kg/m^3)	980
Oil viscosity	17000 cps
Oil thermal conductivity (kJ/m day ºC)	9.27
Porosity	0.33
Horizontal well length, m	700
Spacing between injector and producer (m)	5
Well pairs pacing, m	100
Steam temperature (°C)	193
Steam quality (%)	95

7.6.1 Grid system size

Discretization of the model is a crucial step in any simulation. The pattern and the size of the grid system must be chosen judiciously as the accuracy of the numerical simulation results is highly affected by the grid system. Using a very coarse grid leads to unrealistic numerical results. On the other hand, using a very fine grid is computationally expensive. In other words, the number of grid blocks should be optimized in order to minimize the computing time without losing the desirable accuracy.

Two different types of grid systems can be distinguished, namely single and dual-grid systems. In a single grid system, the geomechanics grid is dependent on the reservoir grid. Both the fluid flow and geomechanics simulators use identical grid resolutions. This eventually increases the number of grid blocks and decreases the running speed.

The concept of a dual-grid system was presented by Tran et al. (1994) and Link et al. (1995). Firstly, this method was used in computational fluid dynamics to describe the movement of an object inside a fluid. The link between two grids was established by transferring the information between boundaries. Later on, Tran et al. (2010) utilized a dual-grid technique along with an iterative coupling approach to improve the computational efficiency of the hydrocarbon reservoir simulation.

In a dual-grid system, different grid arrangements are defined for geomechanics and reservoir simulators. This allows for flexibility to include overburden and underburden in the geomechanics simulator only. In these areas, no fluid or heat flow variations take place. Moreover, grid refinement can be performed on geomechanical grids or reservoir grids separately. For instance, finer grids are required around the well in the fluid flow simulator, which is not essential in geomechanical calculations. On the other hand, coarser grids can be used in the geomechanical simulator where the local deformations are small.

In this study, the grid block sizes were selected to be 10 m x 10 m in the xy plane. The size of the grid in the z direction was chosen based on refinement of the grids in the reservoir and cap rock regions. The grid system contains 200 grid blocks

in the x-direction and 300 grid blocks in the y-direction with a total of 2,000,000 grid blocks. In general, the grid block sizes were selected to respect the cell aspect ratio (5:1), which is required by FLAC3D.

7.6.2 Horizontal well length

In their study, Ong and Butler (1990) found that the maximum growth in the gravity head was achieved when the well length increased to 2000 m; however, the impact of reducing the well length on the gravity head was insignificant due to the linear inverse relationship between the flow rate along the well and its length. In general, the gravity head was found to be more sensitive to well size than the well length. Kamath et al. (1993) observed, from a two-dimensional numerical model, that the longer the horizontal well, the higher the production rate. The impact of well length on the oil-steam ratio (OSR) and oil recovery was noted to be trivial. Normally, horizontal well length varies from 500 m to 1000 m. In this study, the horizontal well length was chosen to be 700 m.

7.6.3 Spacing

Usually, multiple well pairs are drilled to improve the oil production with bitumen recovery from large areas, which is called a SAGD well pad. However, some difficulties still exist when producing oil from the areas between adjacent well pairs. In this configuration, each single well pair system is affected by nearby steam chambers.

The optimal spacing between well pairs is determined based on the geology. Generally, wider spacing can be used in the case of a high-quality, thick pay interval. This leads to an increase in not only the drainage volume per well pair but also the project life. In contrast, reducing lateral well pair spacing results in lower drainage volume, which explains why the oil recovery rate levels off early (Kamath et al., 1993). Singhal et al. (1998) stated that a horizontal distance of 100 m between well pairs is feasible in many cases. This is because the steam chamber is unlikely to spread more than 50 m horizontally away from the well.

On the other hand, the vertical spacing between the injector and producer (I/P spacing) is a key factor in SAGD operation. Both the oil production rate and circulation period are basically controlled by this distance. A higher vertical distance requires a longer preheating time; however, it increases the oil recovery rate. Based on the experiments performed by Sasaki et al. (2001), earlier generation of the steam chamber and higher oil production can be achieved by increasing the spacing between the injector and producer.

Kamath et al. (1993) mentioned that the greatest oil recovery can be achieved by placing the injector at the midpoint of the reservoir. The same conclusion was drawn by Sasaki et al. (2001). However, they pointed out that the magnitude of increasing oil production is linked to time. The maximum production rate was observed to happen close to the breakthrough time.

In brief, selecting the optimum injector-to-producer spacing is largely dependent on several factors, such as pay-zone thickness, oil mobility, permeability, and reservoir heterogeneity. In this study, 5 well pairs are used with a total length of 700 m, oriented in the J direction at a depth of 118m within the reservoir. A horizontal spacing of 100 m between consecutive well pairs was chosen. The injector well was placed 5 m above the producer. Figure 7.2 shows the grid system and the well locations.

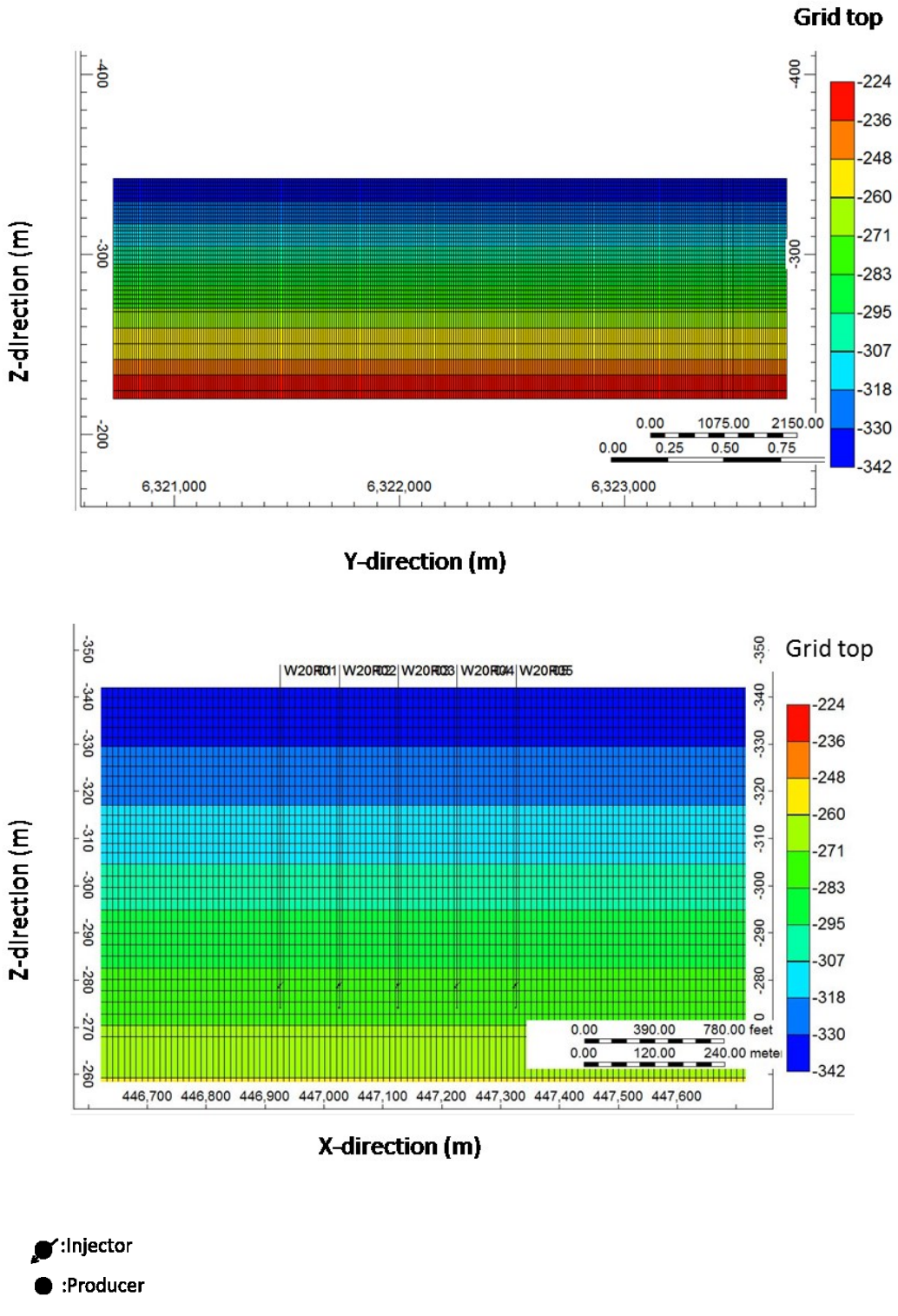

Figure 7.2 Grid system and well pair locations in the reservoir

7.6.4 Start-up

Start-up is a critical step in SAGD operation, especially in reservoirs with high oil viscosity. In this process, the steam is initially circulated in both injector and producer wells to initiate communication and enhance oil mobility between the well pairs.

The steam circulation period differs from one project to another based on several factors, such as reservoir properties and operation conditions. It is common practice to use the temperature of the midpoint between the producer and the injector as a reference to move from steam circulation mode to production phase. Typically, this reference temperature is taken in the range of 70 °C to 90 °C. The dependence of start-up on the tubing size and insulation was discussed by Tan et al. (2002). The authors mentioned that utilizing insulation improves the distribution of the heat in the well pair. The temperature of injection liner and tubing was found to be the same as the steam temperature. Steam breakthrough takes place close to the toe. The movement of steam through the slotted injection tubing is more uniform; thus, it enhances the production rate.

Unlike insulated cases, the heat loss effect in non-insulated cases on SAGD operation is evident. About a 3 °C to 4 °C difference in temperature between the injection tubing and liner was recorded (Tan et al, 2002). The potential for steam trap phenomenon to occur early increases due to the uneven distribution of the heat. This may cause a reduction in the efficiency of oil recovery, as the steam may not reach the regions close to the toe.

In addition, the preheating period is affected by the steam circulation rate, oil viscosity, and injection pressure. The more the steam circulation rate and the larger the injection pressure, the shorter the circulation period (Tan et al, 2002). In our simulation, electrical heating was conducted for 150 days at injector and producer wells to reduce the oil viscosity and to establish hydraulic communication between wells before steam injection started.

7.6.5 Pressure difference

The impact of pressure difference (ΔP), between the producer and the injector during steam circulation, on the temperature profile of the two horizontal wells is highly affected by steam quality. Utilizing steam with a quality of 100% and no pressure difference will improve the uniformity of temperature and enhance the growth of the steam chamber above the injector. In addition, it decreases the probability of early steam breakthrough occurring at the heel. The influence of ΔP on initialization time was found to be trivial when ΔP is close to the hydraulic head, regardless of the circulation rate and steam quality. On the other hand, when ΔP is higher than the natural hydraulic head then, the time needed to achieve the communication is less (Yuan & McFarlane, 2011). The influence of ΔP on the shape of the steam chamber near the breakthrough of both the injector and the producer was clearly observed. The higher the pressure difference, the narrower the steam chamber width. At the same time, the breakthrough time decreased (Sasaki et al., 2000).

7.6.6 Circulation rate

The selection of a proper steam injection rate is essential to improving the performance of a SAGD operation. The steam injection rate has an impact not only on bitumen production, but also on the cumulative steam-oil ratio (CSOR). Both production rate and CSOR increase when the steam injection rate rises (Nguyen et al., 2012).

The greater the circulation rate, accompanied with high steam quality, the higher the heat transfer occurring close to the heel. The latter leads to an increase in the non-uniformity of the heat transferred to the reservoir. Meanwhile, the heat transfer localization at the heel can be avoided by decreasing steam quality and utilizing a lower circulation rate (Yuan & McFarlane, 2011).

7.6.7 Steam chamber operation pressure

Steam generation is one of the most expensive processes in SAGD operations. Usually the cumulative steam-oil ratio (CSOR) is used to determine the

efficiency of bitumen production. This term refers to the ratio of the unit of steam needed to produce one unit of oil. Therefore, lower CSOR leads to a more economic process.

Using low injection pressure has some advantages such as enhancing the steam-oil ratio (SOR), reducing emissions, increasing the cumulative oil rate, and decreasing water usage. In addition, lower injection pressure allows the growth of the steam chamber under the top water zone when thief zones exist. Bao et al. (2010) noticed that increasing the injection pressure from 1,500 kPa to 3,000 kPa led to a 100% increase in SOR. Additionally, breakthrough occurred more quickly and the steam chamber rapidly penetrated the upper region of the thief zones. A similar conclusion was drawn by Sasaki et al. (2000). They pointed out that a higher expansion rate of the steam chamber and a lower breakthrough time can be achieved by increasing the injection pressure.

Regardless of the absence or the presence of thief zones, many factors have to be taken into account when choosing the ideal pressure, such as risk factors, operational difficulties, and lift difficulties. Economically, the operation pressure can be taken in the range of 300 to 900 kPa for most oil sands reservoirs in northeast Alberta (Edmunds, 2001). Gates and Chakrabarty (2006) developed a technique to optimize SAGD operations by employing a genetic algorithm. They found that CSOR can be decreased by using a variable steam injection pressure profile instead of a constant one. They suggested an optimized profile with an initial high injection pressure. Once the chamber hits the top of the formation, the injection pressure can be reduced to decrease the heat losses to the overburden. In all cases, the injection pressure has to be higher than the reservoir pressure. In brief, injection pressure should be determined judiciously in order to improve the efficiency of SAGD operation. It should be noted that reservoir heterogeneities make the selection of the optimum SAGD operating pressure a multifaceted process.

7.6.8 Steam quality

Utilizing a high quality steam is desirable in SAGD because the condensate fluids move by gravity towards the producer. The latter phenomenon decreases the

efficiency of heat transfer process to bitumen, resulting in a reduction in the production rate.

7.6.9 Heterogeneity

In reality, reservoirs are heterogeneous formations. Physical properties, mineralogy, natural fractures, hydraulically induced fractures, faults, permeability barriers, and porosity distribution vary from one location to another within the reservoir. These differences are mainly due to the lithological variations that occur during sedimentary deposition.

Many studies have focused on the impact of reservoir heterogeneity on SAGD operations. In general, the vertical variations in reservoir stratigraphy significantly affect steam chamber growth (Birrell et al., 2000). A mudstone baffle will lead the steam chamber to grow more in the horizontal direction because the mudstone baffle acts as a barrier and stops the penetration of steam into the top water zone (Bao et al., 2010). The presence of mudstone interbeds with thickness of a millimeter may lead to prevention of upwards steam chamber growth (Birrell et al., 2000).

Yang and Butler (1992) studied experimentally the impact of the presence of thin shale layers and the existence of horizontal layers with different permeabilities within the reservoir. They pointed out that having the higher permeability layer on top of the lower permeability layer increases the initial production rate. The effect of the shale layers was found to be dependent on the size of this barrier and either a top or bottom injection mode can be used. The existence of a short horizontal barrier has a minor influence on the SAGD performance. This impact increases in the case of a long barrier, where a reduction in the production rate was observed with the top steam injection mode. An increase in the bitumen temperature above the long barrier was recorded in the bottom injection mode. However, this heated bitumen is non-producible because steam pressure prevents the oil from flowing. In this situation, the authors recommended adding nitrogen to steam to improve the oil production from the top layer. The reservoir dip effect was also studied; the results revealed that the production rate can be improved by the

reservoir dipping upward because a higher total drainage height is achieved when the producer is located at the lowest point of a dipping reservoir.

Chen et al. (2008) emphasized in their study the role of reservoir heterogeneities on SAGD from a modeling perspective. The reservoir heterogeneity was represented by a random distribution of thin shale lenses. To take into account the effect of the shale lenses on permeability, the vertical permeability of shale-sand blocks was reduced by a factor of 10 to 5. No reduction factor was applied for the horizontal permeability, as it is insignificantly affected by the presence of shale lenses. Two flow regions were considered; the near-well region (NWR) and the above-well region (AWR). In addition, the presence of a hydraulic fracture was studied. A permeability of 106 mD and aperture of 0.01 m were used to represent the fracture. The permeability in the direction perpendicular to the fracture plane remained constant. The distribution of the shale was found to have a great effect on the flow of hot fluid within the NWR. In the case of AWR, SAGD performance was sensitive to shale percentage and continuity. Only a shale barrier length of 12 m or larger can affect steam chamber growth. The authors mentioned that hydraulic fracturing enhances steam injectivity and improves the production rate. Usually, the nature of the SAGD project, whether it is shallow or deep, controls the orientation of the hydraulic fracture. A vertical hydraulic fracture along the well direction is preferable for deep SAGD projects.

A clear picture of reservoir vertical heterogeneity can be obtained from well logs. On the other hand, surface seismic data can be used to investigate reservoir horizontal variability. However, these two methods have some drawbacks due to differences in the vertical spatial resolution of well logs and surface seismic data. Furthermore, spatial sampling of surface seismic data is normally located every 10 m to 30 m. These distances are much smaller than the space between well logs. To avoid that, Bonnell and Hurich (2008) employed cross-well seismic data to study the characterization of the horizontal heterogeneity. A detailed mapping of lateral stratigraphic variations was obtained using this tool. In addition, quantitative statistical information that can be used as constraints for reservoir simulations, was acquired.

7.6.10 Porosity

Research related to the impact of porosity on SAGD performance remains limited. However, the concept of increasing cumulative oil production with porosity is well known. Llaguno et al. (2002) used a sensitivity analysis to prove that cumulative oil production is more dependent on accumulation properties, including thickness, porosity, and oil saturation, than flow properties (viscosity, permeability, and reservoir pressure).

7.6.11 Time step

Selecting a feasible time step is a challenging task since simulation results are very sensitive to the time step. For instance, utilizing a very large time step leads to rapid variations in saturation and pressure, leading to unrealistic results (Odeh, 1969). On the other hand, the time required to perform reservoir simulation on a specific computer is mainly dependent on the number of cells and the number of time steps. The computing time of each time step increases, as the number of grid points increases. The number of time steps is determined based on the allowable length of the time step Δt. The latter can be represented as a function of the volume and the shape of the cell. Smaller cell size allows the use of a larger time step Δt. On the other hand, Δt decreases as the term $\left|\frac{\Delta x}{\Delta y} - 1\right|$ increases, where Δx and Δy are the horizontal dimensions of the cell (Odeh, 1969). The sensitivity of the results to Δx, Δy, and Δt can be investigated by reducing the time step and comparing the results. The optimum time step can be obtained once changing the time step does not affect the results significantly.

In a coupled multiphysics problem, different time step scales can be utilized to keep the simulation computationally feasible. Usually, a larger time step can be chosen for the mechanical part than for flow calculation, in order to have the same impact on the global error from flow and mechanics (Dureisseix et al., 2003).

In this study, a varying time step scale scheme (Table 7.2) was selected to reduce the computational cost of the problem and to obtain accurate results at the same time. At early times in the simulation, shorter time steps were applied to

capture the rapid variations in pressure and temperature and to obtain reliable results at the reservoir boundaries. The input data file for reservoir simulation model can be found in Appendix D.

Table 7.2 Time step scheme

Step No.	1	2	3	4	5	6	7	8	9
Days	1	5	15	31	45	59	73	88	90
Step No.	10	11	12	13	14	15	16	17	18
Days	100	150	160	200	250	300	365	485	608
Step No.	19	20	21	22	23	24	25	26	27
Days	730	912	1096	1277	1461	1642	1826	2007	2191
Step No.	28	29	30	31	32	33	34		
Days	2373	2738	2922	3103	3287	3468	3652		

7.7 Coupled reservoir geomechanics numerical simulation

The same reservoir grid system, mentioned previously in section §7.6.1, was used to build the 3D geomechanical model inside FLAC3D. Therefore, the grid contains 200 grid blocks in the x-direction and 300 grid blocks in the y-direction; the cells are 10 m long and 10 m wide. This grid system was selected to be fine enough to capture the real stress-strain behavior of the formations and to reduce the running time. The boundary conditions of the model were selected with no vertical displacement at the bottom and no tangential stresses at the faces of the grid. The top of the model was allowed to deform freely without any constrains. The strain-softening constitutive model was adopted for Clearwater, Wabiskaw, and McMurray. However, the Mohr-Coulomb model was chosen to represent both Quaternary and Devonian strata.

The RGRG coupled simulation platform, developed at University of Alberta, was utilized to conduct a coupled reservoir geomechanics (CMG-STARS and FLAC3D) numerical simulation. At each time step, the updated pore pressure and temperature (P & T) were transferred to FLAC3D. No interpolation was required because these parameters are stored in the centre of each grid block in both STARS and FLAC3D. Based on the updated values of pressure and temperature, FLAC3D

computes the new strain field, including both elastic and plastic deformations. Thereafter, the reservoir permeabilities are updated based on volumetric strain calculated from the stress simulator and sent back to STARS at the beginning of the next step. This procedure was repeated until the final step was achieved. The simulation runs were terminated after 10 years. Figure 7.3 summarizes the coupled reservoir geomechanics (CMG-STARS and FLAC3D) numerical simulation system architecture. The following equation, developed by Touhidi-Baghini (1998), was used to estimate the changes in absolute permeability due to volumetric strain:

$$\ln\frac{k_2}{k_1} = \frac{c}{\emptyset_1}\varepsilon_v \tag{7.1}$$

where k_1 is the initial value of absolute permeability; k_2 is the updated value of absolute permeability; and ε_v is the volumetric strain.

According to Touhidi-Baghini, c is equal to 5 and 2 for vertical and horizontal permeabilities, respectively.

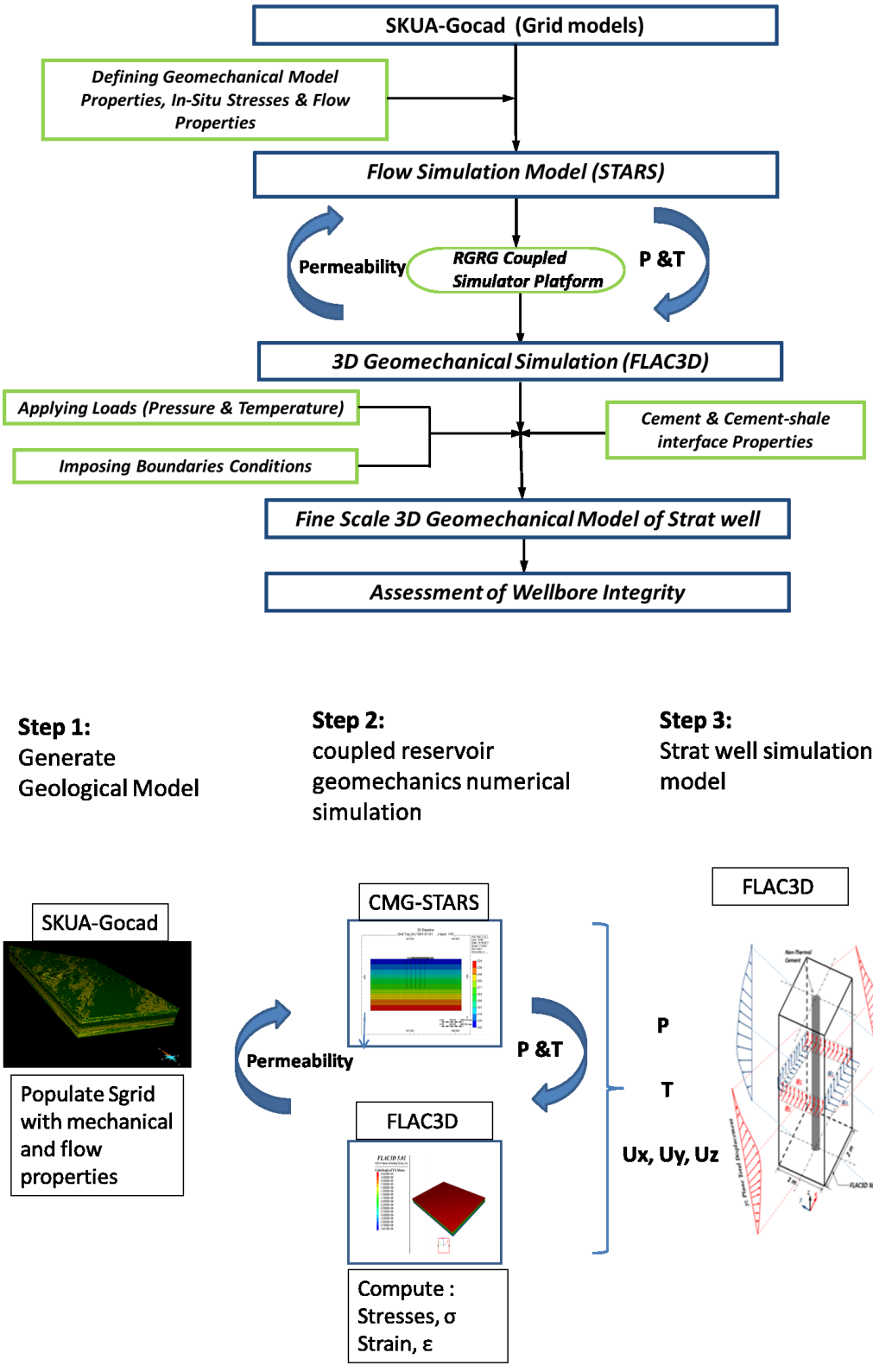

Figure 7.3 Schematic diagram of coupled reservoir geomechanics (CMG-STARS and FLAC3D) numerical simulation system architecture

7.8 Stratigraphic well simulation

Due to the efficiency and limitations of computational power, the stratigraphic well should be simulated separately from the large domain in a high resolution model. However, the impact of the SAGD process should be taken into account in the smaller model. Therefore, the small wellbore was modeled with the impact of the large SAGD process, using the concept of shared boundary modeling. This concept is used to investigate the effect of a large process on a small region. Accordingly, displacements, pressures, and temperatures are extracted from the larger model and applied into a refined, detailed wellbore model.

A generic 3D wellbore model was constructed within FLAC3D to simulate the stratigraphic well. The geometries of the stratigraphic well, formations, and the interface element are shown in Figure 7.4. The formations were extended horizontally 2 m away from the stratigraphic well axis. A stratigraphic well of 160 mm diameter was extended from the ground surface to the bottom of the pay zone. An artificial cement-formation interface element of 10 mm thickness was placed between the cement and formation to capture the bonding between the cement and the formation.

The Mohr–Coulomb criterion was adopted to describe the behavior of cement. Results obtained from the experimental work, presented previously in Chapters 2, 3, and 4 were used to define the thermo-mechanical properties of cement and the cement-shale interface, and to describe how these properties degraded with temperature.

Strain-softening behavior was adopted to represent other formations. The model was surrounded by a perimeter of elastic elements. The latter acts as a dampening effect to steadily transfer the displacement to the model and prevent the occurrence of boundary progressive failure. The boundary condition at the base of the model was chosen to be fixed in a vertical direction. However, the top of the model was assumed to have a free boundary to allow the surface to deform without restrictions.

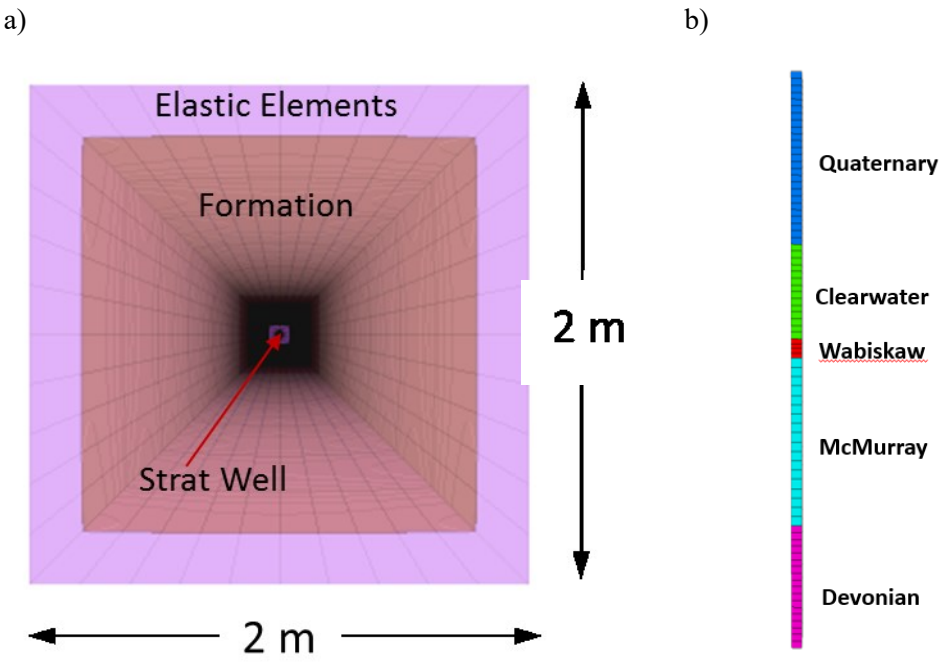

Figure 7.4 Stratigraphic well model geometry: a) top view; b) front view

Firstly, the model was initialized by in-situ stress, pore pressure, and initial temperature. Thereafter, pore pressure, temperature, and displacement, obtained from the FLAC3D and SAGD models, were extracted at the location of the stratigraphic well under investigation and then imposed at the boundaries of the 3D wellbore model. Displacements (ux, uy, uz) were introduced as boundary conditions by calculating the equivalent velocities (u_x^o, u_y^o , u_z^o) and imposing them incrementally at boundaries. Then, FLAC3D was run until an equilibrium between the applied boundary conditions (pressure, temperature, and displacement) and the initial state of stress in the model, was achieved. Subsequently, stress and strain were calculated. This procedure was repeated at each time step until the final time step was reached. The procedure is conceptually illustrated in Figure 7.5.

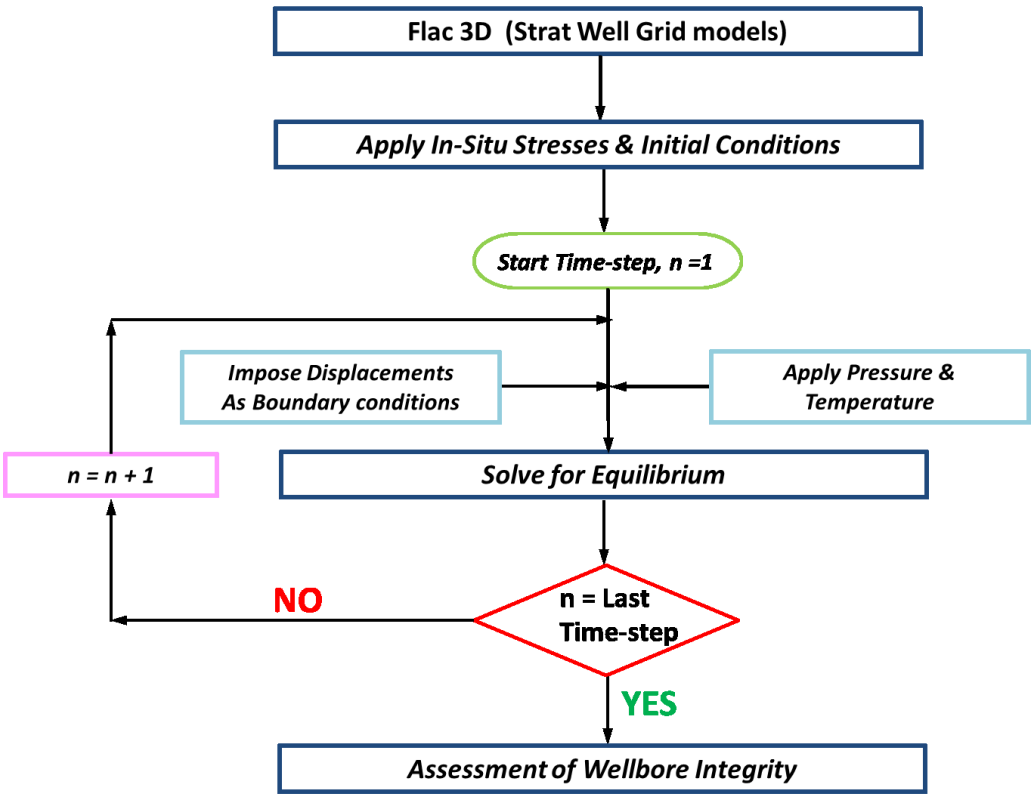

Figure 7.5 Workflow for utilizing the shared boundary concept to assess stratigraphic well integrity

7.9 Results and discussion

7.9.1 Reservoir heterogeneity

Log data of 100 observation wells were used to predict the formation profiles and each layer's content based on the ɣ-ray logs. High-resolution ɣ-ray values were employed to obtain sand and shale facies where API 65 was utilized as a cutoff for sand and shale. The facies distribution of the reservoir is shown in Figure 7.6. In addition, the heterogeneous nature of the reservoir was taken into account by considering the variations of the reservoir properties, such as density, permeability and porosity. Figure 7.7 illustrates the histogram of those properties.

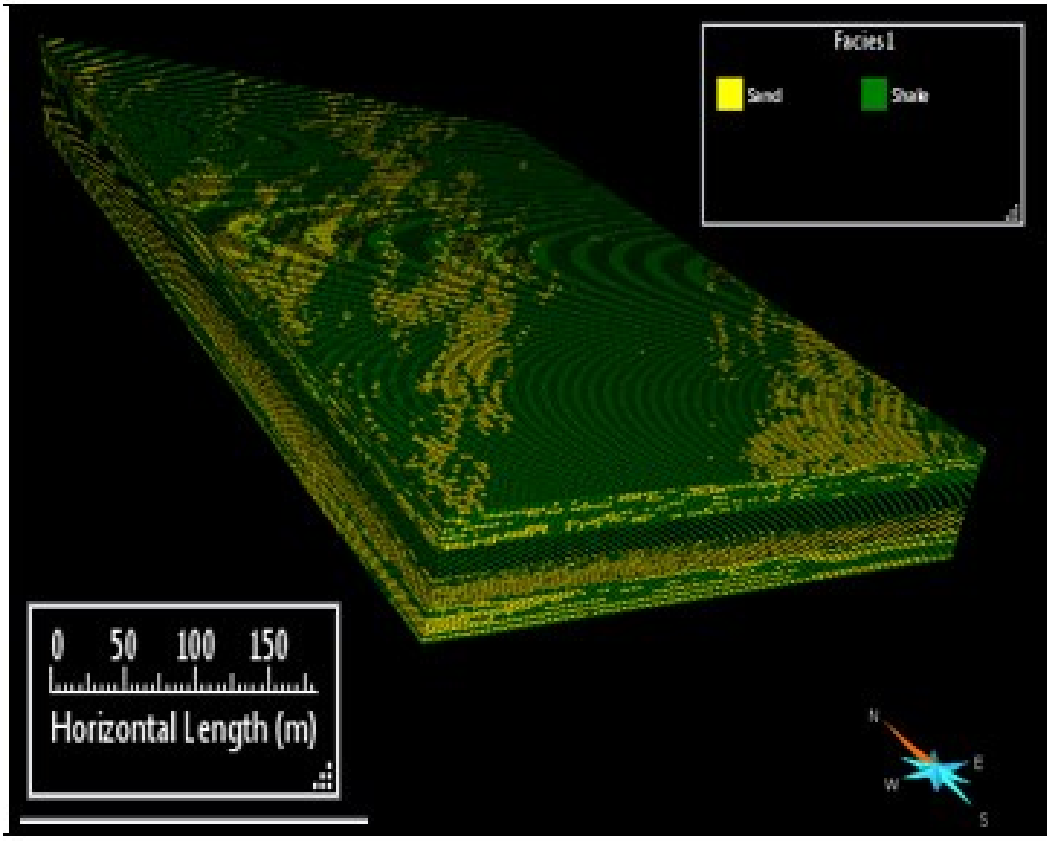

Figure 7.6 Facies distribution in the reservoir

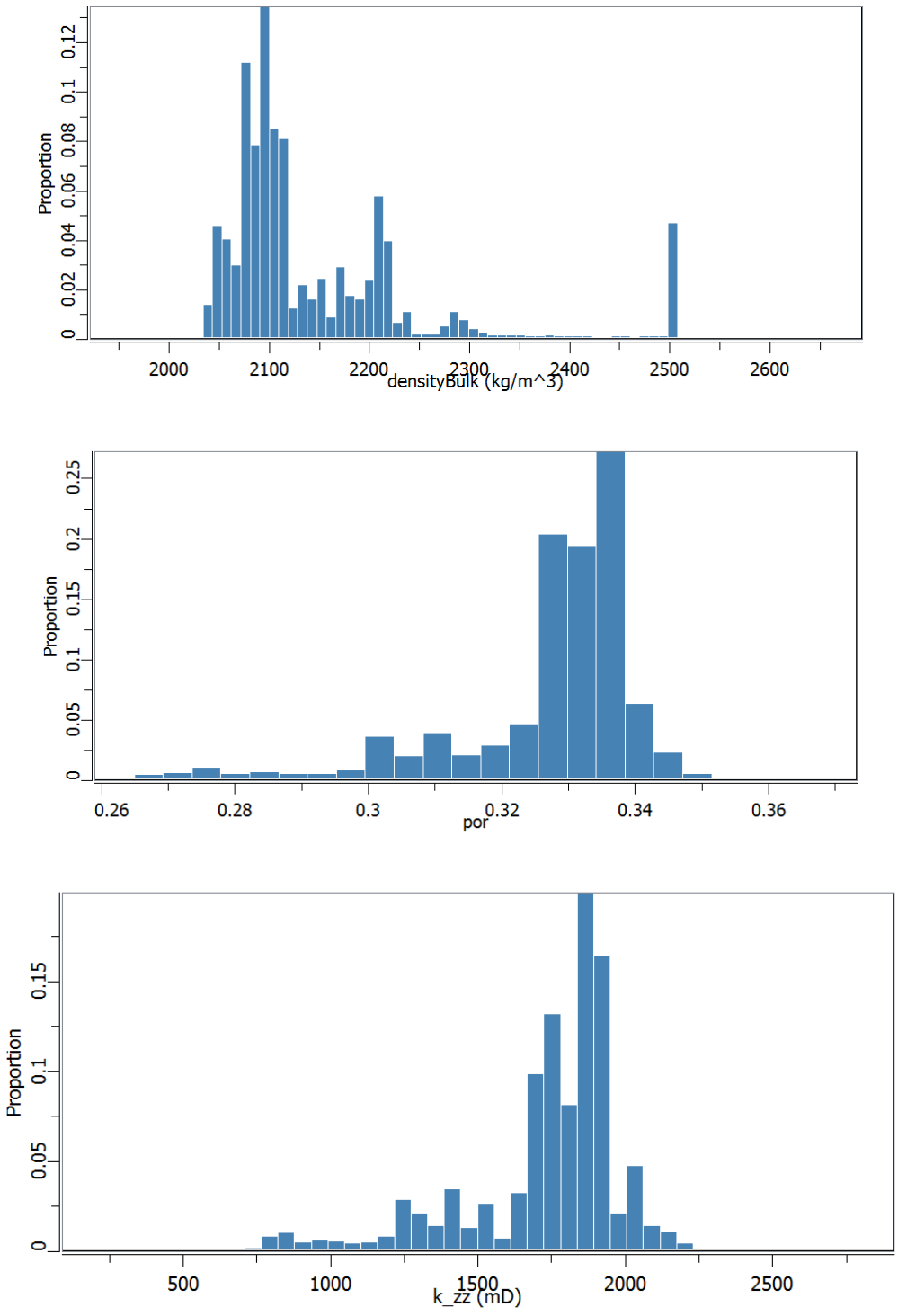

Figure 7.7 Histogram of reservoir properties variations due to reservoir heterogeneity: a) density); b) porosity; c) vertical permeability

7.9.2 Pressure and temperature distributions

Figure 7.8 depicts steam chamber growth after 2373 and 3653 days. It can be seen that reservoir temperature increased from its initial temperature to 193 ºC. Temperature first expanded vertically above the injection well until it hit the top of the reservoir. During this period, the maximum rate of production was achieved. Thereafter, lateral growth started to take place at a slower rate. Once the lateral expansion reached a distance similar to the formation thickness, the depletion stage dominated the process where steam chamber growth decays. The progressions of temperature distributions can be found in Appendix F.

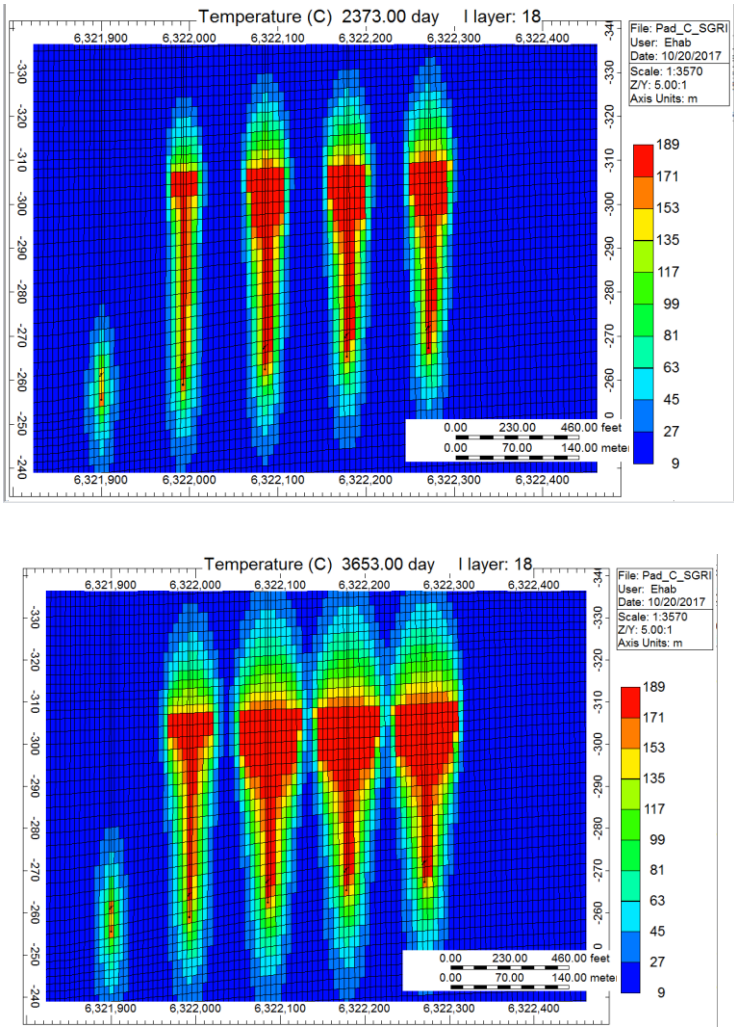

Figure 7.8 Temperature distribution at: a) 2373 days; b) 3653 days

It is apparent that steam chamber development has a complex mechanism. In general, several processes are involved in SAGD and affect steam chamber growth, such as counter-current flow, co-current flow, and water imbibition.

On the other hand, the reservoir pore pressure increased as a result of steam injection. However, it decreased gradually when moving away from the steam chamber. This process causes not only a reduction in effective confining stress of the reservoir but also leads to an increase in horizontal stress. In general, at a low confining stress level, failure is more likely to occur. Despite the reduction in confining pressure due to pore pressure increases, the simulation results showed that the shear strength of caprock is still higher than the shear stress developed in this zone. Hence, the caprock most likely will not fail in shear under the chosen operating pressure.

7.9.3 Displacement distributions

Figure 7.9 and Figure 7.10 provide detailed information about the upward vertical displacement profile (heave) and horizontal displacement obtained at the end of each time step. Heave was observed to occur at the beginning, directly above the well pairs. This can be attributed to the steam chamber growth mechanism. Initially, steam moved up and the temperature of the zone above the injector increased rapidly. Thereafter, it extended laterally with time due to steam chamber growth.

Simulation results revealed that the shape and the magnitude of the displacements are mainly affected by formation properties, pressure and temperature changes, and the chosen boundary conditions. Changing time steps does not have a significant impact on the displacement profile. In general, deformation profiles between the well pairs showed a complex pattern due to the interaction between the adjacent steam chambers.

While the steam chamber was growing, shear stress was observed to increase in the regions around and above injector wells. This occurred mainly due to an arching effect resulting in a higher vertical stress in the zones near to the steam

chamber, compared to stress levels observed in the areas between well pairs. The impact of this stress localization decreased, with the growth of steam chamber, due to stress relaxation

The magnitudes and directions of the deformation profile vary not only with the formation properties and SAGD process conditions, but also the relative position between the stratigraphic well and SAGD well pair. Wells located at the centre of the well pad showed much less horizontal displacement than wells existing at the corner. In general, at centre locations, the change in horizontal stresses becomes greater than the increase in vertical stresses, especially in the zones between the well pairs where temperature variations become more complex due to the interaction between adjacent steam chambers. On the other hand, the greatest heave was recorded above injection wells and tends to decrease by moving towards the edge of the pad.

Accordingly, several locations were investigated to cover different scenarios. Two main stratigraphic well locations were selected for the simulation based on the extreme displacement profile. The centre and corner locations of the well pad represent the largest vertical and horizontal displacement, respectively. Other locations were also chosen to cover the variability of the displacement profile resulting from the heterogeneity of the reservoir properties. These locations are conceptually illustrated in Figure 7.11. It is worth mentioning that other factors such as reservoir depth and thickness may affect the magnitude of surface heave.

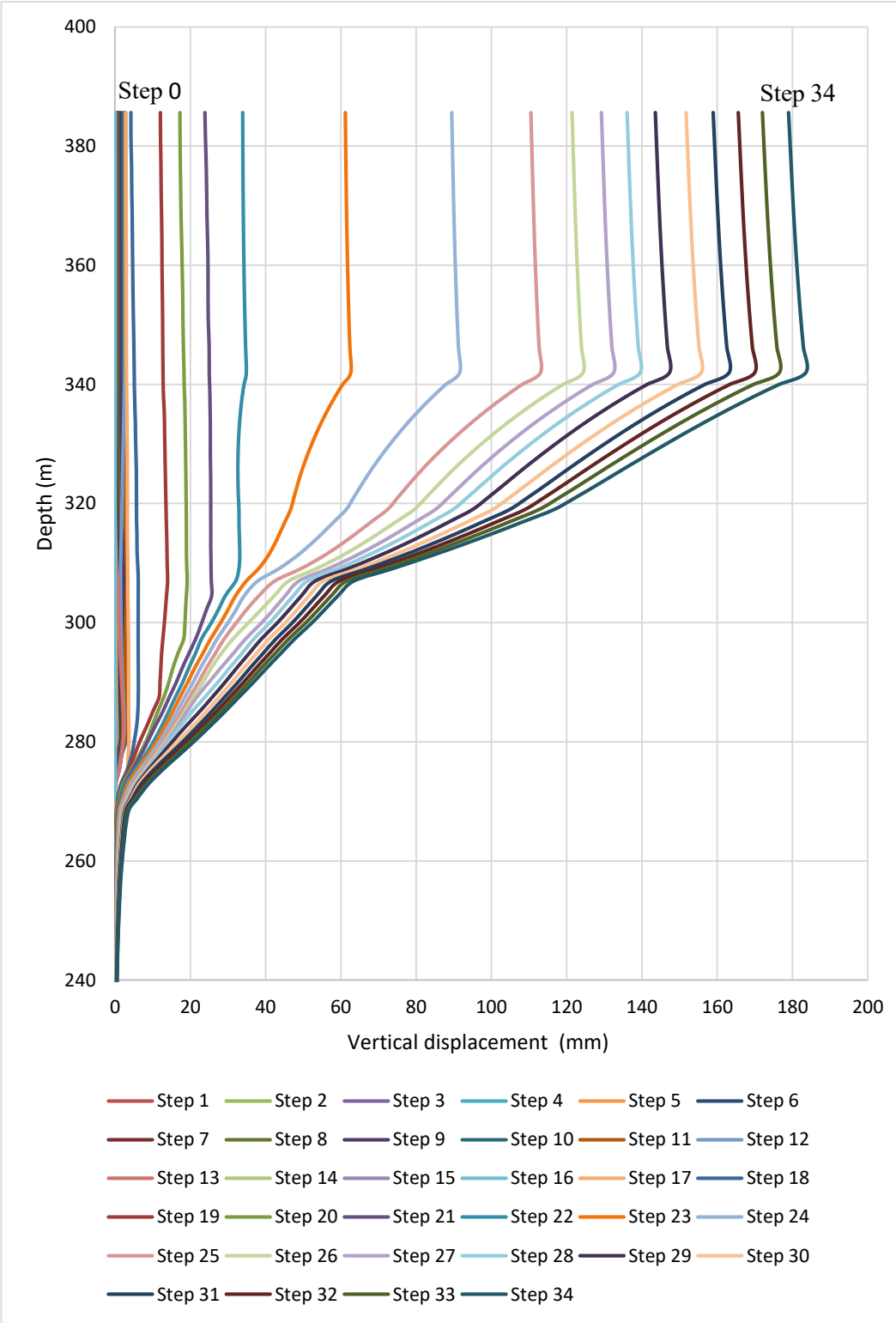

Figure 7.9 Progression of vertical displacement

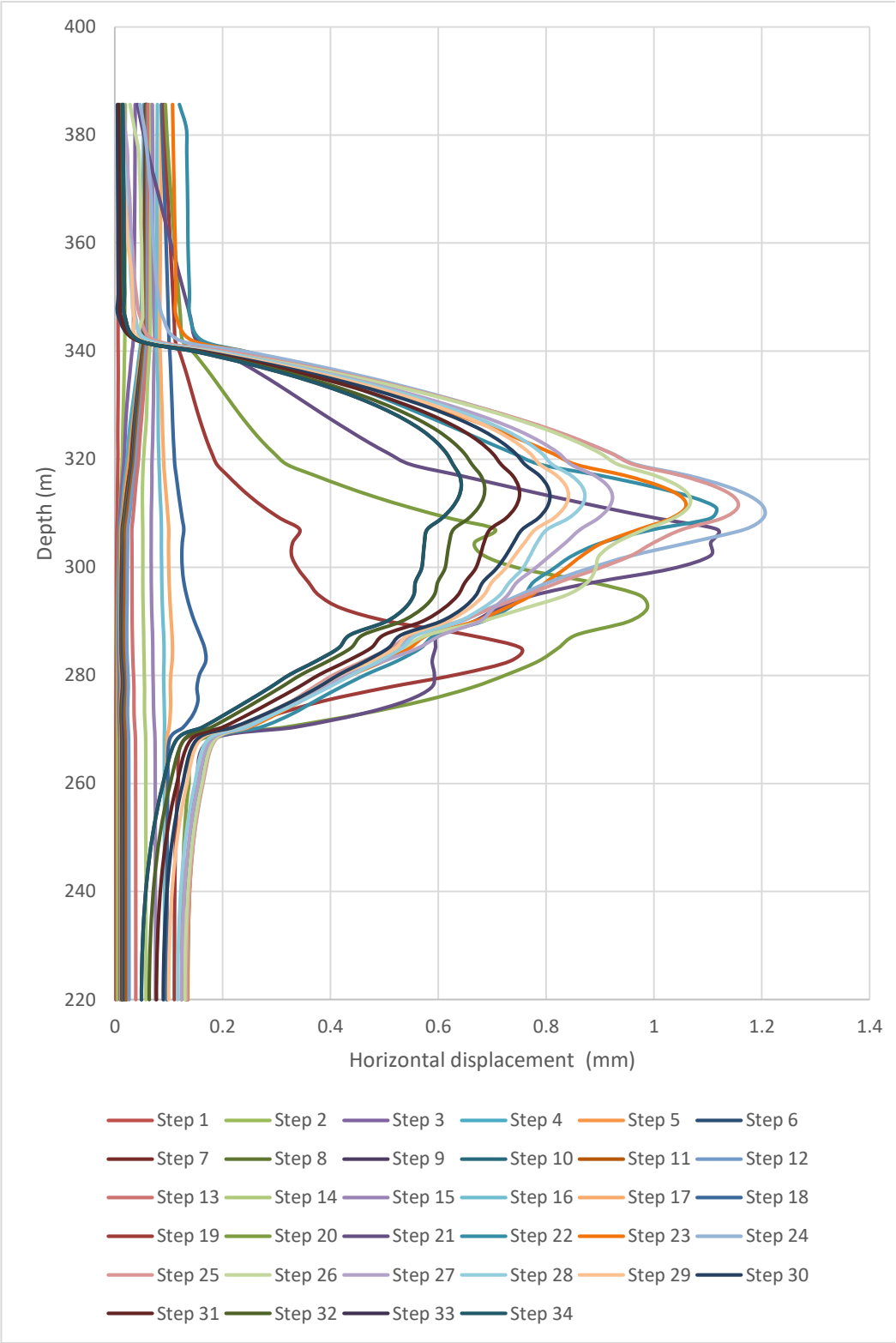

Figure 7.10 Progression of horizontal displacement

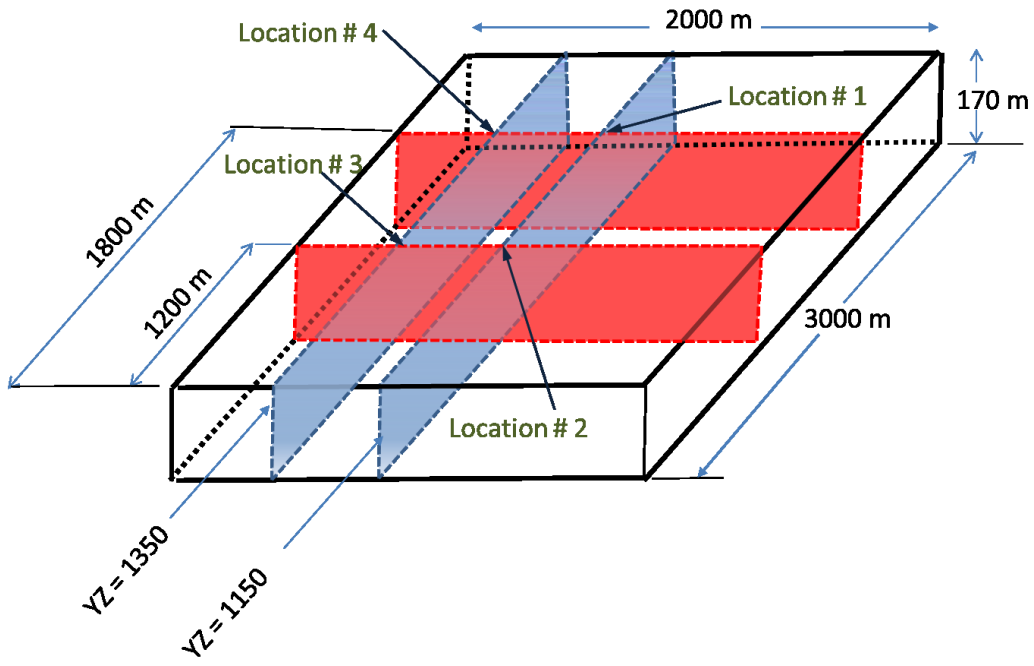

Figure 7.11 locations of stratigraphic wells selected for geomechanical simulation

7.9.4 Stratigraphic well integrity assessment

Both temperature and mechanical deformation act as triggers to alter cement permeability. The combination of these two factors, when non-thermal cement is used, may lead to a huge increase in the permeability of cement paste. In general, the variation in permeability with heat is highly affected by the temperature range. The higher the temperature, the greater the impact on permeability. This change in permeability occurs mainly due to the change in the internal pore space structure, resulting in an increase in the total porosity. Moreover, if the temperature is high enough, it may cause undesirable changes in the cement matrix due to chemical degradation, causing a further increase in permeability. On the other hand, the alteration in permeability due to mechanical deformation will vary with the stress/strain level and the extent of damage. Usually, at a low stress level, the permeability does not change significantly. However, once micro-cracks start to propagate, the permeability increases rapidly.

In general, the impact of mechanical deformation on the permeability increases with temperature due to the interaction between the two mechanisms. Therefore, in this work, the permeability is assumed to increase with temperature and due to failure as well. In order to accommodate the uncertainty of the variation in permeability that would occur when cement paste is exposed to the steam chamber, the following equations, based on the experimental results obtained by Choinska et al. (2007), were used to define the combined influence of temperature and damage on the permeability:

$$k / k_o = (1.25E\text{-}3)T + 1.0 \quad (7.2)$$

$$k / k_o = 1000; \text{ after failure} \quad (7.3)$$

where k_o is the initial permeability, and T is temperature (ºC).

The change in permeability (permeability map) resulting from the deterioration of both cement and cement-shale interface, due to elevated temperature and shear failure, was used to predict the probability of the occurrence of flow paths through the delineation well. To do so, interface and cement elements were unwrapped and plotted in the x-y direction, where the x-axis represents the radial location of the element (0 - 360º) and the y-axis defines the elevation of the element. Then, the permeability multiplier is shown on the same graph as color-coded. As illustrated in Figure 7.12, the stratigraphic well consists of six elements; however, the interface is modeled as one zone.

Figure 7.13 to Figure 7.16 illustrate the permeability multiplier maps of stratigraphic wells existing at four different locations. The results for cement elements are shown on unwrapped sections. These results represent the cement conditions at the final simulation step (at 3650 days). The blue zones depict the areas where cement can resist both the elevated temperature and shear stress resulting from steam chamber development. However, the red zones represent the regions where cement tends to fail due to the increase in permeability.

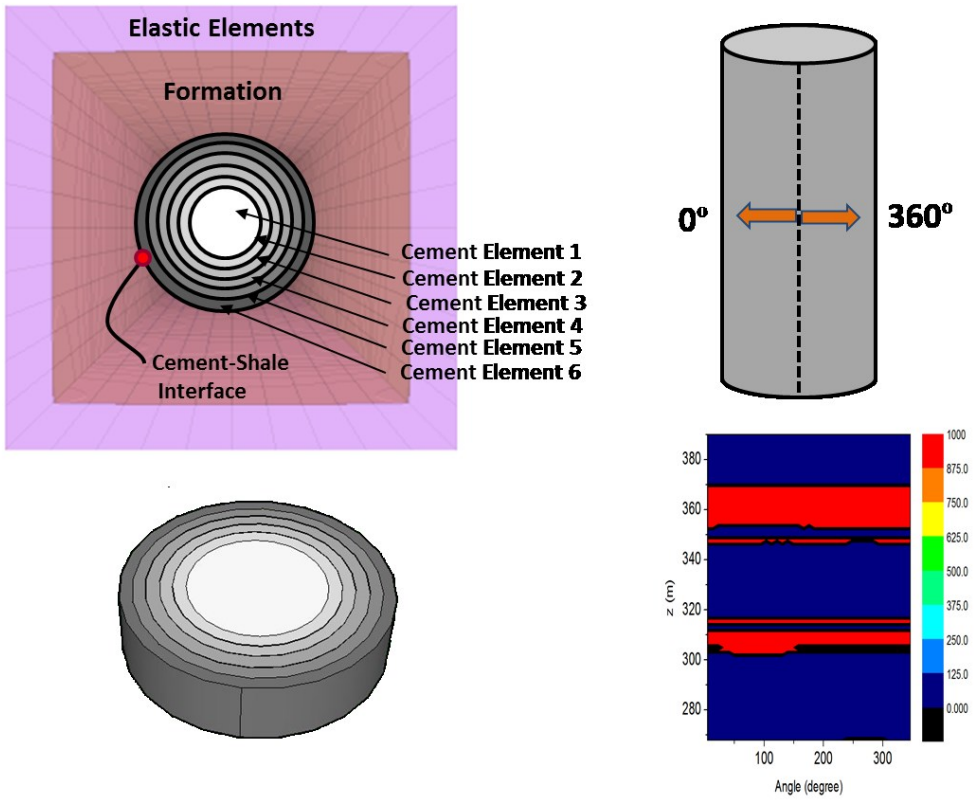

Figure 7.12 Schematic diagram illustrates unwrapped cement elements for permeability multiplier maps representation

As shown in Figure 7.13, within the reservoir, more red zones were observed in the outer cement elements. This means there is a substantial increase in permeability in the outer rings and the potential of failure occurrence is higher than the inner regions. Extensive zones of failure were observed in the portion of the stratigraphic well existing within caprock region. It can be seen that there are considerable amounts of red zones in the upper part of the stratigraphic well; however, these zones are much lower compared to caprock regions. In addition, the failure patterns were observed to be simple, which is possibly due to the reduction in the impact of steam chamber on this area. In most cases, within the upper 20 m, almost no failure was found.

It is apparent that failure occurs in the stratigraphic well at the top of Clearwater and extends to the surface between this layer and the Quaternary

formation. This is particularly true for all stratigraphic wells, regardless of their relative locations to the steam chamber.

The comparison between the results of stratigraphic wells existing at different locations showed that the performance of a stratigraphic well is related directly to its relative location to the steam chamber. As mentioned before, corner locations are exposed to complex combinations of horizontal and vertical displacements. These variations in displacement profiles develop a considerable amount of shear stress at these locations, resulting in inducing more loads on the stratigraphic well. On the other hand, the main direction of the displacement field acting on stratigraphic wells, existing horizontally on the midway of the well pairs, is vertical. Therefore, these locations will experience less shear stress than corner locations. In general, during the steam chamber growth, shear stress was observed to increase in the regions around and above injector wells. This occurred mainly due to arching effect, resulting in a higher vertical stress in the zones near the steam chamber compared to stress levels observed in the areas between well pair. The impact of this stress localization decreases with the growth of the steam chamber, due to stress relaxation.

The failure zones in the Quaternary tend to develop closer to the ground surface and become thicker. In addition, more failure zones were observed within the reservoir. It can be seen that most of regions in the outer cement element within the reservoir and caprock become red.

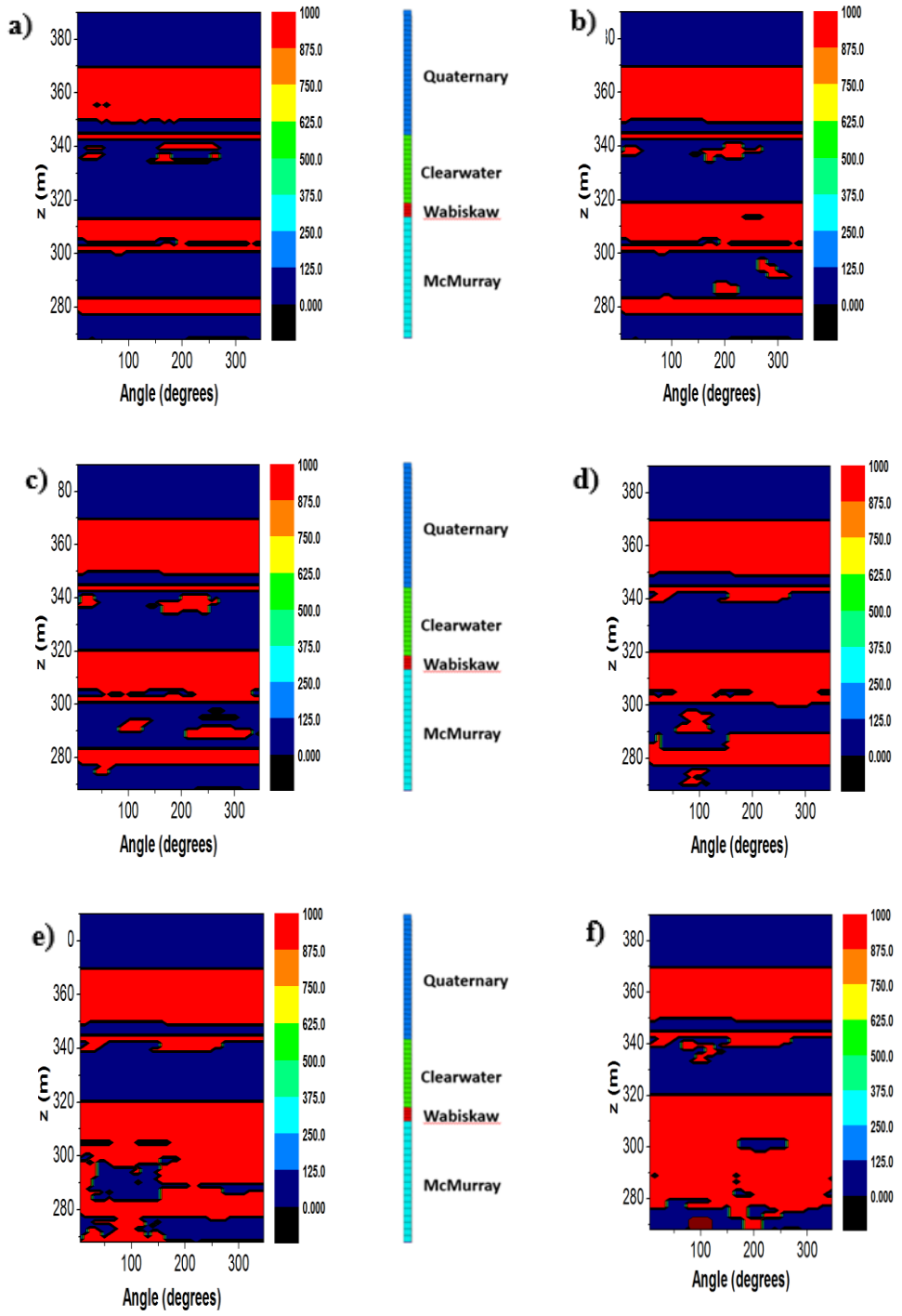

Figure 7.13 Cement permeability multiplier map for stratigraphic well location #1: a) element 1; b) element 2; c) element 3; d) element 4; e) element 5; f) element 6

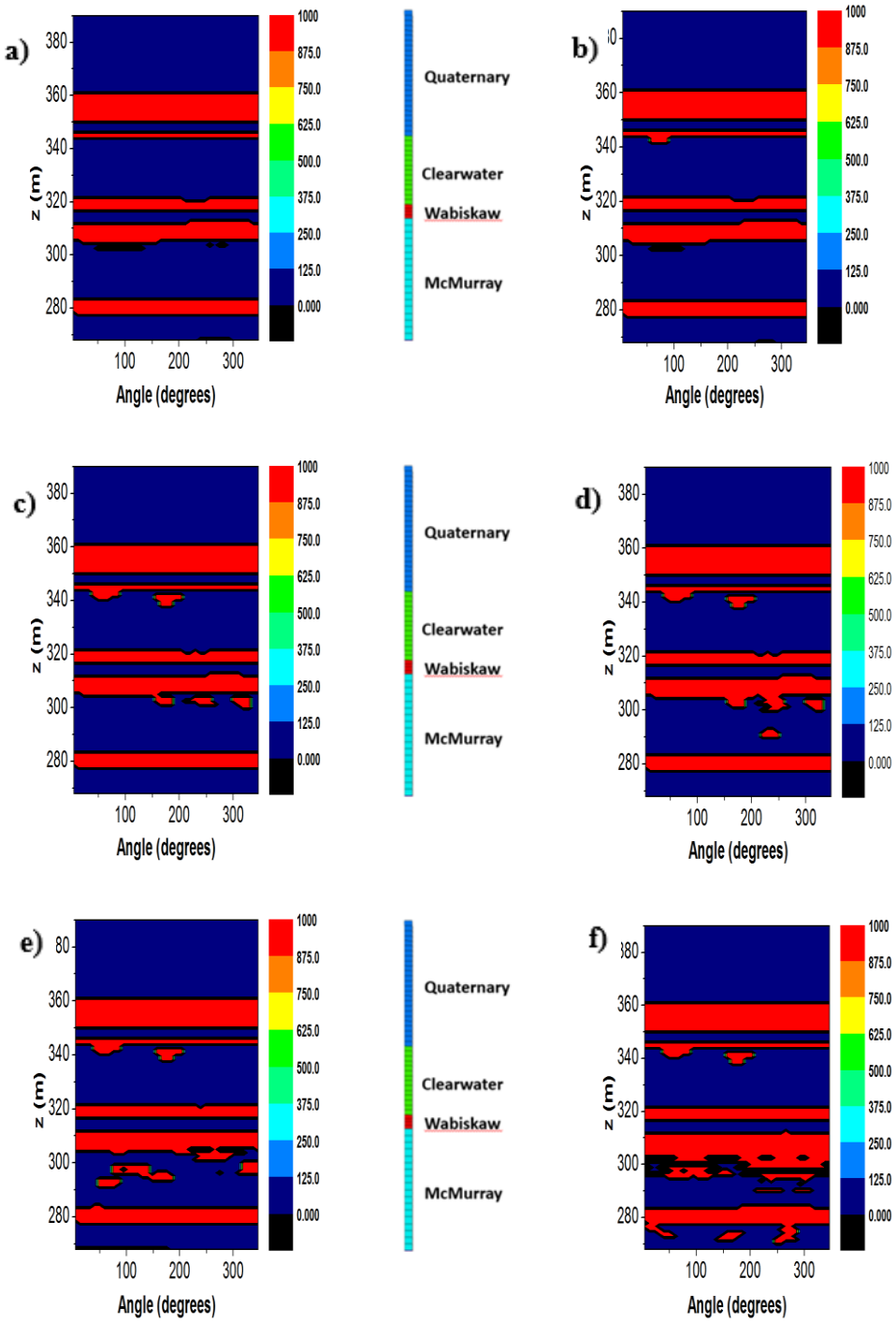

Figure 7.14 Cement permeability multiplier map for stratigraphic well location #2: a) element 1; b) element 2; c) element 3; d) element 4; e) element 5; f) element 6

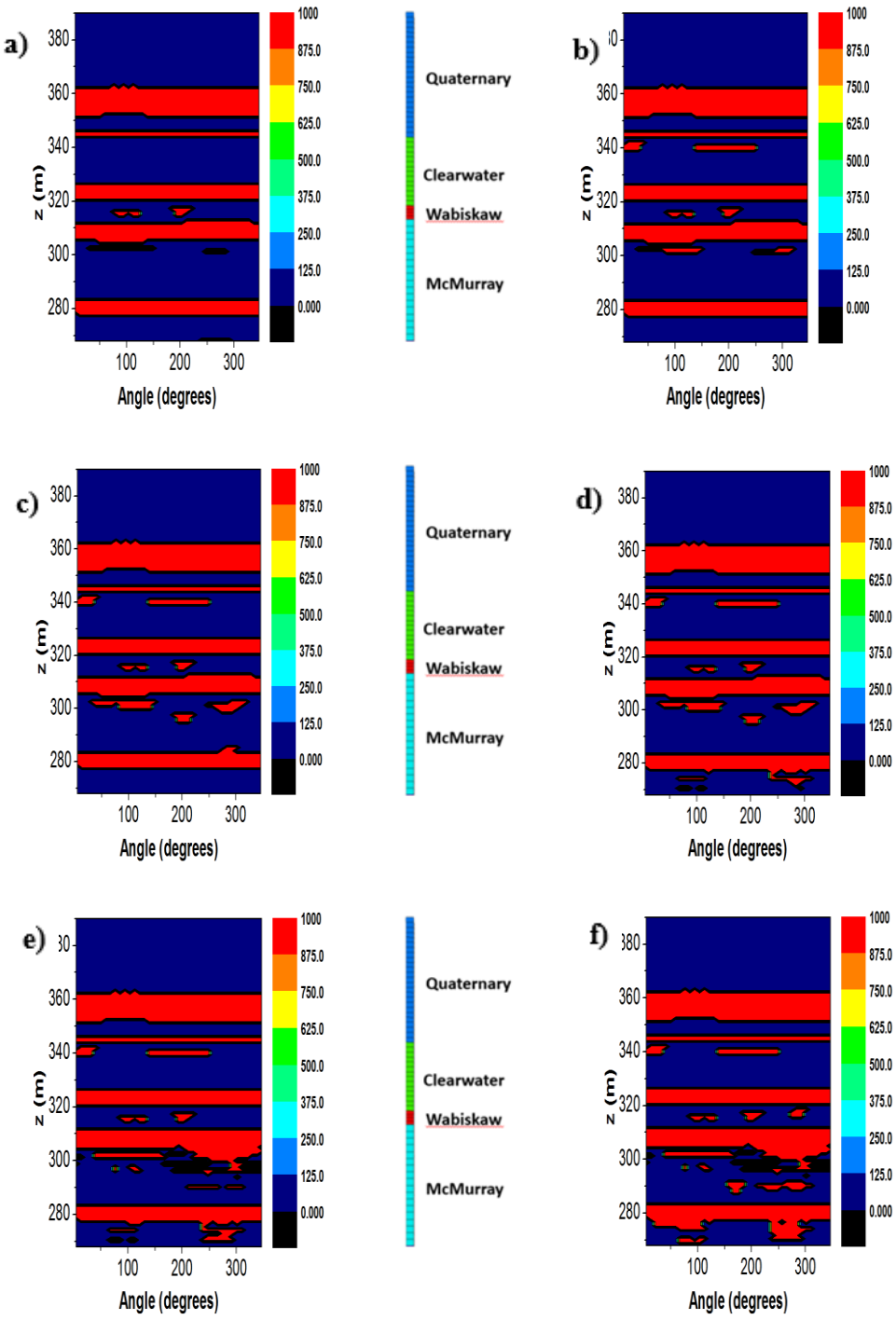

Figure 7.15 Cement permeability multiplier map for stratigraphic well location #3: a) element 1; b) element 2; c) element 3; d) element 4; e) element 5; f) element 6

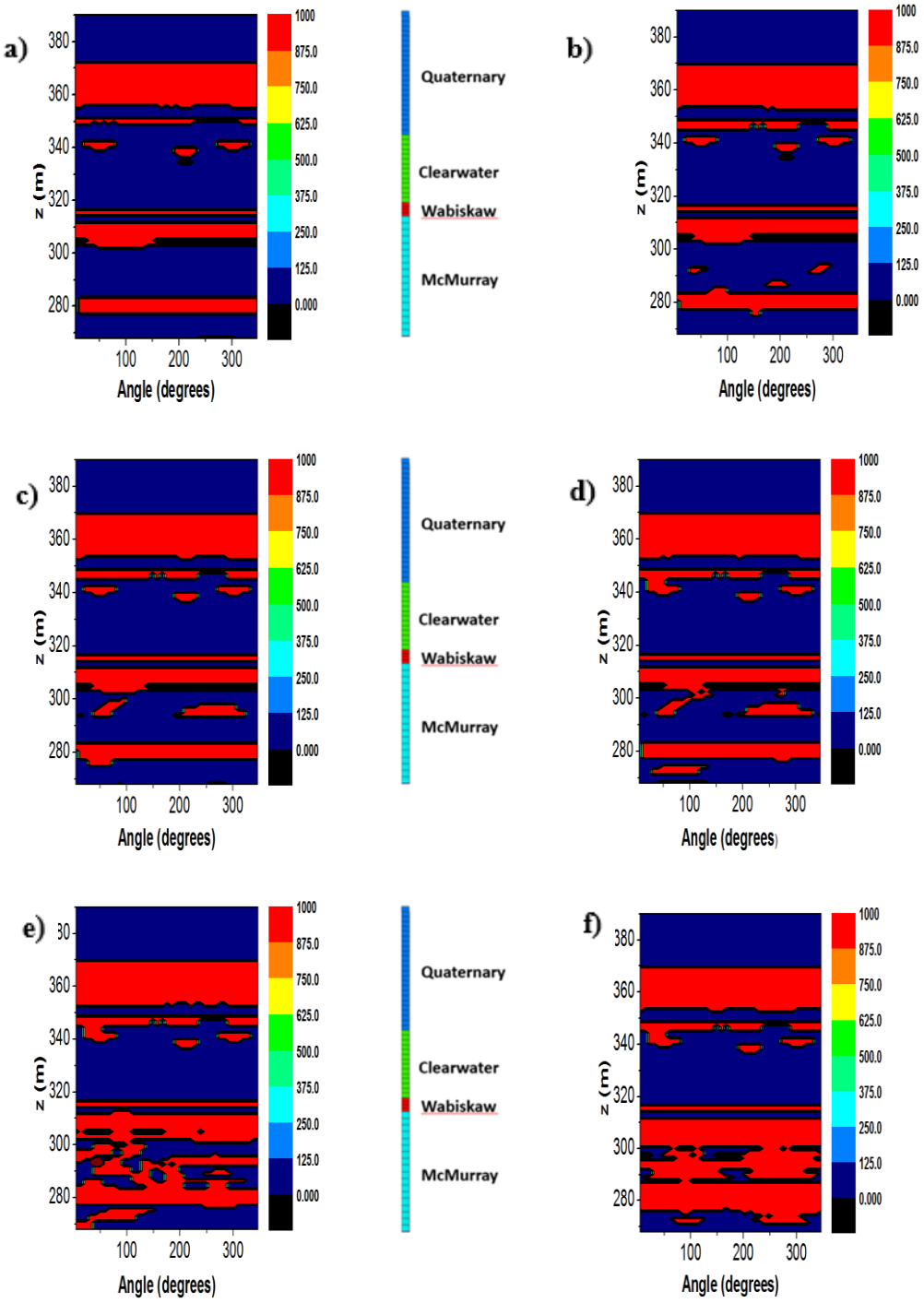

Figure 7.16 Cement permeability multiplier map for stratigraphic well location #4: a) element 1; b) element 2; c) element 3; d) element 4; e) element 5; f) element 6

7.10 Summary and conclusion

Studying the performance of a stratigraphic well when subjected to SAGD conditions was the main objective of this chapter. The concept of the sequentially coupled reservoir geomechanical simulation technique was utilized to model the SAGD process and to evaluate its influence on stratigraphic wells, which may be abandoned with non-thermally compatible cements. This method allowed for considering the impact of geomechanical effects on the flow calculations. Therefore, realistic forecasts for the flow and deformation calculations can be obtained.

For the SAGD simulation, a reservoir simulation model with dimensions of 3000 m in I direction, 1000 m in J direction, and 170 m in k direction was used. The complex effect of the interaction between adjacent steam chambers on the stratigraphic well was introduced by considering that the 3D reservoir contains five well pairs. Each well pair consists of two parallel horizontal wells. Production wells of 800 m length were placed at 5 m from the base of the reservoir, and the vertical distance between the injection and production well was 5 m. Reservoir heterogeneity was imposed by considering the variations in density, permeability, and porosity within the reservoir.

The concept of shared boundary modeling was used to capture the influence of the SAGD system on a small stratigraphic well and to keep the simulation computationally feasible at the same time. Therefore, the stratigraphic well was simulated separately from the larger domain using a high resolution model, and the impact of the large SAGD process was imposed as a boundary condition. The simulation runs were terminated after 10 years. Based on the analysis of the simulation results, the following conclusions can be drawn:

The integrity of the stratigraphic well is very sensitive to the cement type. Utilizing thermally compatible cements in a stratigraphic well is crucial to maintaining the integrity of these wells by minimizing the possibility of uncontrolled leakage occurring.

The accuracy of the simulation results is greatly affected by the properties assigned to each element, particularly cement and interfacial cement-shale properties. The deboning between the cement and formation that may occur depends on the values assigned to these properties, resulting in the development of leakage paths. Therefore, the performance of cement must be precisely predicted and the uncertainty in both cement and cement-shale interface properties has to be addressed. Accordingly, a sensitivity analysis should be carried out to take into account variability that may occur in those properties, resulting from having cement paste with average quality.

The magnitudes of vertical and horizontal displacements that developed due to SAGD operations depend not only on pressure and temperature changes but also on the proximity of the steam chamber.

The performance of a stratigraphic well and its failure mechanism are strongly affected by the temperature profile, relative distance between the well and steam chamber, and cement and formation properties. In general, low shrinkage cement with a low Young's Modulus is preferable. Utilizing flexible cement, with an elastic modulus close to those of formations, would minimize the probability of debonding between the two materials.

Stratigraphic wells constructed of non-thermal cement most likely will fail due to strength retrogression, which occurs as a result of exposing the cement to elevated temperature and the displacement field developed during steam injection. Failure occurred mainly within the part of the stratigraphic well that exists in the caprock region.

Chapter 8 : Summary, Conclusions, and Recommendations

8.1 Thesis overview

Based on an extensive experimental program accompanied by simulation work, this research intends to investigate the influence of high pressure and elevated temperature on the performance of cement, that would help the oil and gas industry to adopt the best technology to accomplish cementing job. Moreover, this study will assist in utilizing the most appropriate cement type and mix.

The testing program has been designed specifically to examine the alterations that might occur in the thermo-mechanical behavior of cement paste at high temperatures. The shrinkage process of cement during hydration was closely explored as well. A series of empirical correlations between temperature and the mechanical properties of cement paste was derived.

All laboratory experiments were conducted on specimens made of class G thermal and non-thermal cements. All slurries used in this study were prepared in accordance with API specifications. Afterwards, samples were cured at a temperature of 9 °C and a pressure of 3 MPa. These pressure and temperature were selected to simulate in-situ conditions. The following paragraphs describe the exerted effort to attain the goals of this thesis.

In the first part of this research, the concept of conventional triaxial test was employed to estimate the range of volumetric shrinkage that might occur to cement slurries with different water to cement ratio (w/c) under the placement conditions in SAGD operations. The arrangement proposed in this study enables specimens to be hydrated under high pressures, similar to field conditions, and to monitor the volume changes taking place during the solidification process at the same time. The proposed technique has proven to be a satisfactory and reliable method to measure the cement shrinkage that occurs while curing the samples at field conditions.

In the current study, the impact of high temperatures on determining the mechanical properties of cement paste was investigated in terms of compressive, tensile, and shear strength parameters. In order to achieve this objective, a series of

UCS tests, Brazilian, and drained triaxial tests were conducted at different temperatures (5 °C, 60 °C, 120 °C and 180 °C). Triaxial tests were conducted under a various range of confining pressures from 2 MPa to 10 MPa. Meanwhile, the pore pressure was kept constant at 2 MPa. In addition, a direct shear apparatus was employed to study the shear behavior of cement paste under varying normal stress levels. Test results were analyzed to explore the influence of cement content, cement type, and the normal stress level on the shear strength of cement paste. A comparison of the results obtained from tests performed on thermal and non-thermal cements was used to identify the dependency of the results upon cement chemical compositions.

As cement-formation interface is considered one of the potential leakage paths, it is of utmost importance to accurately predict the interface strength and bonding in order to guarantee having a leak-free well. Hence, it was a critical step in this research to give more attention to this zone. Accordingly, the cement-shale interface was characterized by performing a series of direct shear tests in order to obtain the shear strength parameter at the interface between cement and rock. Three mixes of non-thermal cement specimens were used with w/c of 0.4, 0.5, and 0.6. The tests were performed by applying normal loads of 0.158 kN, 0.79 kN, and 3.16 kN, corresponding to normal stresses of 50 kPa, 250 kPa, and 1000 kPa, respectively.

Ultrasonic techniques have shown their effectiveness in studying the mechanical properties evolution at early age. Moreover, they have proven their ability to monitor the setting and hardening of cementitious material. However, the majority of previous research was performed at ambient conditions, which may limit the feasibility of its use in the oil and gas industry, where cement solidifies under downhole conditions. Therefore, one objective of this research was to examine the impact of the curing conditions on the early-age behavior of cement paste by means of acoustic emission. The study employed both compression and shear waves to monitor the setting process of oilwell cement and to continuously measure the elastic mechanical properties (Young's modulus, E; and Bulk modulus, B) of cement paste, cured under high pressures and at elevated temperatures

(HP/HT). Moreover, the dependence of the compressive strength of cement paste on pressure and temperature was investigated.

In the last few decades, the microstructure evolution of cement-based materials has been an interest for many researchers, especially since the great advances that have been achieved in the computing technology field. Nowadays, it is very convenient to simulate the hydration process with more accurate information about the growth of cement particles in a reasonable time. One chapter of this thesis focused on this topic, where a microstructural modelling framework, called μic, has been used to investigate the microstructure evolution of cement paste and to determine the influence of temperature on the solidification process. The output of the simulation work enabled monitoring the mechanical properties development over time.

In brief, based on the test findings, the parameters required to describe the complete behavior of cement paste under loading conditions, such as stress-strain behavior, were determined. In addition, thermal and shrinkage properties were determined. The results will allow obtaining the mechanical properties of cement paste, taking into account the influence of SAGD placement and operation conditions. The results will help with understanding the impact of temperature on the performance of cement. Finally, the experimental results could be used as input parameters in simulation work.

The last part of this thesis introduced the numerical modeling approach developed to investigate the performance of stratigraphic wells abandoned with non-thermally compatible cements when exposed to a steam chamber. Shared boundary modeling concept was utilized to improve the computational efficiency of the simulation work by dividing the numerical model workflow into two stages. In the first stage, a coupled reservoir geomechanics (CMG-STARS and FLAC3D) numerical simulation was used to analyze the SAGD operation by constructing a large-scale 3D model, which represented the reservoir and included both overburden and underburden.

In the second stage of this study, a generic 3D wellbore model was constructed inside FLAC3D to simulate the stratigraphic well. Afterwards, pressure, temperature, and displacement were extracted from the large-scale model at the proposed locations of the stratigraphic well and were imposed at the boundary of the small-scale model of the stratigraphic well. As the deformation profile within the reservoir is mainly dependent on the relative position to the SAGD well pair, stratigraphic wells at different locations have been analyzed in order to clearly understand the impact of the relative location of the stratigraphic well to the steam chamber on the performance of these wells.

8.2 Conclusions

The main conclusions drawn from this research, based on the experiment results and numerical simulation outputs, are as follows:

1. The range of the chemical shrinkage of non-thermal cement was 5.46% to 4.45%. The highest value was reported for a sample of w/c equal to 0.4. This value decreased due to the reduction of cement content. On the other hand, thermal cement experienced less chemical shrinkage during hydration than non-thermal cement at the same w/c. The chemical shrinkage of thermal and non-thermal cement samples with a w/c of 0.5 were determined to be 4.13% and 4.83%, respectively.
2. With respect to thermal behaviour, the present study showed that the coefficient of linear thermal expansion (α) of non-thermal cement varied from 12.4 x 10^{-6} $°C^{-1}$ to 10.3 x 10^{-6} $°C^{-1}$ based on the w/c of the samples. A higher value of coefficient of linear thermal expansion was obtained for thermal cement compared to non-thermal cement at the same w/c. The reported value of the coefficient of linear thermal expansion (α) for thermal cement with a w/c of 0.5 was 12.1 x 10^{-6} $°C^{-1}$.
3. A significant difference between the compressive strengths, obtained from thermal and non-thermal cement specimens with a

w/c of 0.5, was observed. The compressive strength of non-thermal cement was higher than that of thermal cement. This difference in results depends on the test temperature. Overall, thermal cement showed a lower value of Young's Modulus.

4. For all non-thermal cement specimens, the compressive strength of cement paste decreased with an increase in the test temperature, regardless of the value of w/c. However, the effect of temperature on thermal cement was the opposite, as an improvement in compressive strength was noticed at high temperature.
5. As expected, specimens made of non-thermal cement showed higher values of shear strength parameters than samples made of thermal cement, regardless of test temperature. This indicates that the presence of silica flour obviously affects the shear behavior of cement paste.
6. The impact of confining pressure on the mode of failure in triaxial test was obvious for both thermal and non-thermal cements, regardless of test temperature. Whether the samples exhibited ductile or brittle behavior at failure was mainly dependent on temperature and confining pressure.
7. Increasing cement content clearly enhanced the shear strength of the cement paste. Both friction angle and cohesion increased due to using samples with lower w/c.
8. The direct shear test results of non-thermal cement samples showed that the stress-displacement behavior of cement paste is strongly affected by w/c and applied normal stress as well. The shear strength of cement increased linearly with the applied normal stress. Therefore, a linear relationship between normal stress and ultimate shear stress can be used to define the failure envelope of cement paste.
9. Based on the direct shear test results, the shear strength of non-thermal cement is generally higher than that of thermal cement.

Moreover, the dependency of non-thermal cement shear strength on normal stress is more significant than thermal cement, especially at high normal stress levels.

10. The maximum horizontal displacement achieved at failure in the case of non-thermal cement was observed to be greater than for thermal cement.
11. Direct shear test gives higher shear strength parameters for cement paste compared to those obtained from triaxial compression test. This can be attributed to the difference in failure mechanisms.
12. Direct shear test provides a valuable way to investigate cement-shale interface and to obtain reliable values for the interfacial shear strength parameters.
13. The impact of the variations of w/c on interfacial cement-shale shear behaviour was insignificant. The shear strength parameters of the cement-shale interface changed slightly with the increase of w/c. On the other hand, the interfacial cement-shale shear strength was more sensitive to cement type. Thermal cement showed a higher interface friction angle than non-thermal cement. However, the greater values of cohesion were recorded during tests conducted on non-thermal cement.
14. Based on test results, the recorded values for cohesion and friction angle of thermal cement-shale interface were 13 kPa and 29º, respectively. These values were observed to be 81 kPa and 24.5º for non-thermal cement.
15. The experimental results proved that the stress-displacement curve of the cement-shale interface is much more dependent on the level of applied normal stress than on the cement content or cement type.
16. The accuracy of the results obtained from ultrasonic techniques is highly affected by the quality of the cement slurry. The existence of air bubbles in the slurry leads to poor results. Therefore, the presence

of these air bubbles should be minimized by applying good compaction of the slurry.

17. Both curing pressure and temperature had similar impacts on the development of the early-age compressive strength of cement paste. The higher the curing pressure and/or temperature, the greater the early-age compressive strength that is achieved after 24 hours. The increase in compressive strength with pressure and temperature can be explained by the significant influence of these two parameters on the hydration kinetics of cement, where the reaction rate increases with any increase in curing pressure and temperature.
18. The development of the elastic moduli of cement was observed to be strongly dependent upon curing conditions. Both elevated temperatures and high pressures were able to accelerate the hydration process and increase the rate of change of the elastic moduli during early age.
19. New relationships were established between curing pressure and temperature and the elastic moduli of cement paste, which highlights the dependency of the microstructure evolution of cement slurry on the curing conditions. The proposed correlations are helpful in predicting the impact of curing conditions on cement paste performance.
20. Microstructural observation of cement paste at an early age confirmed the formation of inner C-S-H and outer C-S-H during the solidification process. The inner products of C-S-H particles grow over the cement particles, and the outer products grow in the space between the cement particles.
21. The modeling results showed that the microstructural evolution of cement paste during hydration is mainly temperature-dependent. The density of the hydration product increases due to temperature as the shells formed around the anhydrous material become denser. On the other hand, elevated temperatures lead to achieve a higher degree

of hydration, especially in the first stage, due to the significant increase in the rate of hydration.

22. Homogenization theory was proven to be a valuable tool to estimate the elastic modulus of cement paste based on microstructure information.
23. The performance of a stratigraphic well was found to be strongly dependent upon its location relative to the steam chamber.
24. According to the simulation results, stratigraphic wells constructed of non-thermal cement most likely will fail under displacements and stress imposed due to increases in both pressure and temperature resulting from steam injection.

8.3 Recommendations and future work

Based on the results of the experimental and modeling works performed in this study, and according to the findings obtained in this research, the following recommendations can be proposed for further research:

- It must be mentioned that these conclusions have been drawn based on the experimental results obtained from particular cement paste slurries, which were cured at 9 ºC and 3 MPa. Further research should be carried out on different types of cement at different conditions to identify the dependency of the results on the cement chemical composition and other curing conditions. This will allow us to employ a more precise constitutive model for numerical analysis to accurately reflect the real performance of cement, leading to more confident predications of the long-term integrity.
- Although the focus of this research was to evaluate the performance of stratigraphic wells, abandoned with non-thermal cement exposed to the SAGD steam chamber, the study provided useful information related to hydration kinetics that would further help to understand the mechanisms of the solidification process and its influence on the long-term behavior of cement paste. To fully understand the impact of this process on well

integrity, the microstructure evolution of cement paste under the placement conditions in SAGD operations needs to be further examined.

- Further investigation is required to obtain the optimum cement mix by adding different additives to a cement slurry and testing their influence on the mechanical properties of cement, as well as examining their thermal effects on the cement paste. In addition, efforts should be directed to studying the effect of high pressures and elevated temperatures on the behaviour of these additives.
- As the permeability of cement is a key factor in the leakage process, more effort should be exerted to explore the impact of high temperature on the permeability of cement paste and to monitor the permeability evolution of the specimen during the shearing stage.
- It is recommended to employ P-wave and S-wave measurements during the loading stage in order to have a better understanding of the effect of high temperature on the mode of failures during triaxial test.
- Further research should be conducted to explore the dependency of direct shear test results on the sample size by performing more tests on specimens with different diameters and determining the variations in shear strength parameters.
- Cement-formation interface experiments were conducted on a specific type of shale with certain properties. Additionally, these tests were performed parallel to the bedding plane in order to mimic the real situation in the field. Further studies, using several formations with different properties, are required to eventually obtain the shear parameters at the interface between the well and other formations.
- The cement-shale interface test can be repeated at different times with several different curing conditions, to identify the impact of the curing period and conditions on the interfacial shear strength parameters.
- Due to the discrepancy between the values of static and dynamic moduli of cement paste, additional laboratory testing should be carried out to establish solid correlations between the two moduli. Also, further research should be

directed towards understanding the impact of curing cement at high pressures and elevated temperatures on these correlations.

- More attention should be paid to the importance of the role of microstructure evolution during cement hydration in the late-age performance of cement. This could include studying the development of the cement matrix under different curing conditions, along with the impact of curing pressure and temperature on the early-age and later-age mechanical properties of cement paste.
- Further research should be performed to identify and model all-important SAGD operation parameters and to specify their influence on the long-term integrity of the oilwell and production rate as well. This will lead to future enhancement for SAGD operations, resulting a more efficient system. Also, simulation results should be compared with field measurements, such as displacements, for more verification. These measurements were not available during the course of this study.

BIBLIOGRAPHY

Al-Chalabi, M., & Huang, C. L. (1974). Stress distribution within circular cylinders in compression. *International Journal of Rock Mechanics and Mining Sciences & Geomechanics*, (11), 45-56.

Ali, S. M. F. (1997). Is there life after SAGD?. *Petroleum Society of Canada*. doi:10.2118/97-06-DAS

Al-Sahawneh, E. I. (2013). Size effect and strength correction factors for normal weight concrete specimens under uniaxial compression stress. *Contemporary Engineering Sciences*, 6(2), 57-68.

Al-Suwaidi, A. S., Soliman, A. A., Jammeli, K., Arif, M. B., Elatrache, B., Fattah, T., & Voon, E. W. (2008, January 1). A new cement sealant system for long-term zonal isolation for gas wells in Abu Dhabi. *Society of Petroleum Engineers*. doi:10.2118/117116-MS.

Al-Yami, A. S., Nasr-El-Din, H. A., Al-Humaidi, A. S., Al-Saleh, S. H., & Al-Arfaj, M. K. (2010, March 1). Evaluation and optimization of low-density cement: laboratory studies and field application. *Society of Petroleum Engineers*. doi:10.2118/113090-PA.

Ament, W. S. (1953). Sound propagation in gross mixtures. *Journal of the Acoustical Society of America*, (25), 638-641. https://doi.org/10.1121/1.1907156.

Amšiejus, J. (2000). Determination of the design values of soil shear strength parameters. *PhD Thesis*, Vilnius Gediminas Technical University, Lithuanian, p.141.

Amšiejus, J., Dirgėlienė, N., Norkus, A., & Skuodis, Š. (2014). Comparison of sandy soil shear strength parameters obtained by various construction direct shear apparatuses. *Archives of Civil and Mechanical Engineering*, 14(2), 327-334. https://doi.org/10.1016/j.acme.2013.11.004.

API RP 10B, Recommended practice for testing cements. *American Petroleum Institute*, April 2013.

ASTM C190-85, Standard test method for tensile strength of hydraulic cement mortars. *American Society for Testing and Materials*, West Conshohocken, PA, USA, 1985.

ASTM C215-14, Standard test method for fundamental transverse, longitudinal, and torsional resonant frequencies of concrete specimens. *American Society for Testing and Materials*, West Conshohocken, PA, USA, 2014.

ASTM D3967-08, Standard Test Method for Splitting Tensile Strength of Intact Rock Core Specimens. *American Society for Testing and Materials,* West Conshohocken, PA, USA, 2008.

ASTM D5607-16, Standard Test Method for Performing Laboratory Direct Shear Strength Tests of Rock Specimens Under Constant Normal Force. *American Society for Testing and Materials*, West Conshohocken, PA, USA, 2016.

ASTM D7012-14, Standard test methods for compressive strength and elastic moduli of intact rock core specimens under varying states of stress and temperatures. *American Society for Testing and Materials*, West Conshohocken, PA, USA, 2014.

Avrami, M. (1939). Kinetics of phase change I. *Journal of Chemical Physics*, 1103–1108.

Backe, K. R. (1994). Gas migration in oil well cement slurries. Report 1/94, Department of petroleum Engineering and Applied Geophysics, The Norwegian Institute of Technology at the University of Trondheim.

Backe, K. R., Lile, O. B., Lyomov, S. K., Elvebakk, H., & Skalle, P. (1999). Characterizing curing-cement slurries by permeability, tensile strength, and shrinkage. *SPE Drilling and Completion*, 14(3), 162-167.

Balonis, M., & Glasser, F. P. (2009). The density of cement phases. *Cement and Concrete Research*, (39)9, 733–9.

Bao, X., Chen, Z. J., Wei, Y., Dong, C. C., Sun, J., Deng, H., & Yu, S. (2010, January 1). Geostatistical modeling and numerical simulation of the SAGD process: Case study of an Athabasca reservoir with top water and gas thief zones. *Society of Petroleum Engineers*. doi:10.2118/137435-MS.

Barcelo, L., Boivin, S., Rigaud, S., Acker, P., Clavaud, B., & Boulay, C. (1999). Linear vs. volumetric autogenous shrinkage measurement: Material behavior or experimental artefact?. Proc. *2nd International Research Symposium on Self-desiccation and its Importance in Concrete Technology*, Lund, Sweden, 109-125.

Bažant, Z. P. (1970). Delayed thermal dilatations of cement paste and concrete due to mass transport. *Nuclear Engineering and Design*, 14(2), 308-318, doi:/10.1016/0029-5493(70)90108-1.

Beltzung, F., & Wittmann, F. H. (2000). Dissolution of cement and early chemical shrinkage of cement paste. *Proceedings RILEM Symposium on Shrinkage of Concrete*, Paris, (91–97).

Beltzung, F., & Wittmann, F. H. (2005). Role of disjoining pressure in cement based materials. *Cement and Concrete Research*, 35(12), 2364-2370. https://doi.org/10.1016/j.cemconres.2005.04.004

Beltzung, F., Wittmann, F. H., & Holzer, L. (2001). Influence of composition of pore solution on drying shrinkage. creep, shrinkage and durability mechanics of concrete and other quasi-brittle materials. Cambridge, MA, August 2001, Edited by F.-J. Ulm, Z.P. Bažant and F.H. Wittmann, Elsevier Science Publishers B.V., Amsterdam The Netherlands, 39-48.

Bensted, J. (1983). Early hydration of Portland cement — effects of water/cement ratio. *Cement and Concrete Research*, 13(4), 493-498. https://doi.org/10.1016/0008-8846(83)90007-8

Bentur, A., Berger, R. L., Kung, J. H., Milestone, N. B., & Young, J. F. (1979). Structural properties of calcium silicate pastes: II, effect of the curing temperature. *Journal of the American Ceramic Society*, 62 (7–8), 362–366.

Bentz, D. P. (1997). Three-dimensional computer simulation of Portland cement hydration and microstructure development. *Journal of the American Ceramic Society*, (80)1, 3-21.

Bentz, D. P. (2007). Transient plane source measurements of the thermal properties of hydrating cement pastes. *Materials and Structures*, 40, 1073–1080. https://link.springer.com/article/10.1617/s11527-006-9206-9

Bentz, D. P., Garboczi, E. J., Haecker, C. J., & Jensen, O. M. (1999). Effects of cement particle size distribution on performance properties of Portland cement-based materials. *Cement and Concrete Research*, 29(10), 1663-1671. https://doi.org/10.1016/S0008-8846(99)00163-5

Bentz, D. P., & Garboczi, E. J. (1991). A digitized simulation model for microstructural development. *Ceramic Transactions*, 16, 211-226.

Bentz, D. P., (1999). Modelling cement microstructure: Pixels, particles, and property prediction. *Materials and Structures*, 32, 187-195.

Bentz, D. P., Haecker, C. J. (1999). An argument for using coarse cements in high performance concretes. *Cement and Concrete Research*, 29(2) 615–618.

Bentz, D. P., Lura, P., & Roberts, J. W. (2005). Mixture proportioning for internal curing. *Concrete International*, 27, 35-40.

Berger, R. L., Bentur, A., Milestone, N. B., & Kung, J. H. (1979). Structural properties of Calcium Silicate pastes: I, effect of the hydrating compound. *Journal of the American Ceramic Society*, 62(7-8), 358-362. doi:10.1111/j.1151-2916.1979.tb19078.x.

Berliner, R., Popovici, M., Herwig, K. W., Berliner, M., Jennings, H. M., & Thomas, J. J. (1998). Quasielastic neutron scattering study of the effect of water-to-cement ratio on the hydration kinetics of Tricalcium Silicate. *Cement and Concrete Research*, 28(2), 231–243. https://doi.org/10.1016/S0008-8846(97)00260-3

Bernard, O., Ulm, F.-J., & Lemarchand, E. (2003). A multiscale micromechanics-hydration model for the early-age elastic properties of cement-based materials. *Cement and Concrete Research*, 33(9), 1293-1309. https://doi.org/10.1016/S0008-8846(03)00039-5

Beuselinck, L., Govers, G., Poesen, J., Degraer, G., & Froyen, L. (1998). Grain-size analysis by laser diffractometry: comparison with the sieve-pipette method. *CATENA*, 32(3–4), 193-208

Biot, M. A. (1956). Theory of propagation of elastic waves in a fluid-saturated porous solid. *Journal of Acoustical Society of America*, (28), 168-178. https://doi.org/10.1121/1.1908241.

Birrell, G. E., & Putnam, P. E. (2000, January 1). A Study of the influence of reservoir architecture on SAGD steam chamber development at the underground test facility, Northeastern Alberta, Canada, using a graphical analysis of temperature profiles. *Petroleum Society of Canada*. doi:10.2118/2000-104.

Bogue, R. H. (1942). The chemistry of Portland cement. *Reinhold Publishing Corp.*, NewYork, USA.

Bonnell, B. & Hurich, C. (2008). Characterization of reservoir heterogeneity: An investigation of the role of cross-well reflection data. *CSEG Recorder*, 33(2), 31-37

Bosma, M., Ravi, K., Van Driel, W., & Schreppers, G. J. (1999). Design approach to sealant selection for the life of the well. *Society of Petroleum Engineers*. doi:10.2118/56536-MS

Bouasker, M., Mounanga, P., Turcry, P., Loukili, A., & Khelidj, A. (2008). Chemical shrinkage of cement pastes and mortars at very early age: Effect

of limestone filler and granular inclusions. *Cement and Concrete Composites*, 30(1), 13-22. doi.org/10.1016/j.cemconcomp.2007.06.004.

Boulay, C., Determination of coefficient of thermal expansion, in: A. Bentur (Ed.), Early Age Cracking in Cementitious Systems, State-of-the-Art Report Number 25, RILEM TC 181, RILEM, 217–224.

Boumiz, A., Vernet, C., & Cohen-Tenoudji, F. (1996). Mechanical properties of cement pastes and mortars at early ages: Evolution with time and degree of hydration. *Advanced Cement Based Materials*, 3(3-4), 94–106. https://doi.org/10.1016/S1065-7355(96)90042-5.

Brace, W. F. (1965). Relation of elastic properties of rocks to fabric. *Journal of Geophysical Research*, 70(22), 5657-5667. https://doi.org/10.1029/JZ070i022p05657.

Brady, B. T. (1971). An exact solution to the radially end-constrained circular cylinder under triaxial loading. *International Journal of Rock Mechanics and Mining Sciences & Geomechanics*, 8(2), 165-178. doi:10.1016/0148-9062(71)90007-6.

Bresson, B., Meducin, F., & Zanni, H. (2002). Hydration of tricalcium silicates (C_3S) at high temperature and high pressure. *Journal of Materials Science*, 37(24), 5355–5365.

Brown, T. D., & Javaid, M.Y. (1970). The thermal conductivity of fresh concrete. *Matériaux de Construction*, 3(6), 411-416.

Buil, M. (1979). Studies of the shrinkage of hardening cement paste (in French).D.Eng. Thesis. Rapport de recherche LPC No. 92, Laboratoire Central des Ponts et Chaussées, Paris.

Butler, R. M., & Stephens, D. J. (1981). The Gravity drainage of steam-heated heavy oil to parallel horizontal wells. *JCPT*, 90-96, April-June.

Butler, R. M., McNab, G. S., & Lo, H. Y. (1981). Theoretical studies on the gravity drainage of heavy oil during steam heating. *Canadian Journal of Chemical Engineering*, 59, 455-460.

Carneiro, F. L. L., & Aguinaldo Barcellos. (1953). Strength of concrete., *RILEM bulletin No. 13, Union of testing and Research laboratories for Materials and Structures*, Paris, France, 97 - 123.

Carpinteri, A., Cardone, F., & Lacidogna, G. (2009). Energy emissions from failure phenomena: medical, electromagnetic, nuclear. *Proceedings of the SEM Annual Conference*, Albuquerque, New Mexico, USA.

Cerato, A. B., & Lutenegger, A. J. (2006). Specimen size and scale effects of direct shear box tests of sands. *Geotechnical Testing Journal,* 29(6), 507-516.

Chalaturnyk, R. J. (1996). Geomechanics of the Steam Assisted Gravity Drainage Process in Heavy Oil Reservoirs. *Ph.D. Thesis*, Department of Civil Engineering, University of Alberta.

Chalaturnyk, R. J., & Li, P. (2004, April 1). When is it important to consider geomechanics in sagd operations? *Petroleum Society of Canada*. doi:10.2118/04-04-05.

Charron, J., Marchand, J., Bissonnette, B. P. M., & Zuber, B. (2002). Comparative study of the effects of water/binder ratio and silica fume on the volume instability of hydrating cement pastes at early-age. *Proceedings of the 3rd International Research Seminar on self-desiccation and its importance in concrete technology*. Lund: Lund University, 39–50.

Chen, Q. (2009). Assessing and improving steam-assisted gravity drainage: reservoir heterogeneities, hydraulic fractures, and mobility control foams. *PhD Thesis*, Stanford University, USA.

Chen, Q., Gerritsen, M. G., & Kovscek, A. R. (2008, October 1). Effects of reservoir heterogeneities on the steam-assisted gravity-drainage process. *Society of Petroleum Engineers*. doi:10.2118/109873-PA.

Chen, R., & Stimpson, B. (1993). Indirect tension test on rock - Analytical/Numerical correction for material bimodularity. *Geotechnical Testing Journal*, (16) 2, 238-245.

Chenevert, M. E., & Shrestha, B. K. (1991, March 1). Chemical Shrinkage Properties of Oilfield Cements (includes associated paper 23477). *Society of Petroleum Engineers*. doi:10.2118/16654-PA

Cheng, C. H., Johnston, D. H. (1981). Dynamic and static moduli. *Geophysical Research Letters*, 8(1), 39-42.

Cheung, J., Jeknavorian, A., Roberts, L., & Silva, D. (2011). Impact of admixtures on the hydration kinetics of Portland cement. *Cement and Concrete Research*, 41(12), 1289–1309.

Cheung, P.R., & Beirute, R.M. (1985). Gas flow in cements. *Journal of Petroleum Technology*, 37(06), 1041-1048.

Choinska, M., Khelidj, A., Dufour, F., Pijaudier-Cabot, G. (2007). Effects of temperature, mechanical state and their interactions on permeability of

concrete. *5th International Conference on Concrete under Severe Conditions of Environment and Loading*, Tours, France.

Coats, K. H. (1978, October 1). A highly implicit steamflood model. *Society of Petroleum Engineers*. doi:10.2118/6105-PA.

Collins, P. M. (2007, August 1). Geomechanical effects on the SAGD process. *Society of Petroleum Engineers*. doi:10.2118/97905-PA

Combs, J., Quiett, S., and Axtell, L.H., 1977, Thermal conductivity measurement techniques for geothermal exploration heat flow surveys. *Transactions, Geothermal Resources Council*, (1), 49-51.

Constantinides, G., & Ulm, F. J. (2004). The effect of two types of C-S-H on the elasticity of cement-based materials: results from nanoindentation and micromechanical modeling. *Cement and Concrete Research*, 34(1), 67-80. doi:10.1016/S0008-8846(03)00230-8

Costoya, M. (2008). Kinetics and microstructural investigation on the hydration oftricalcium silicate. *Ph.D. Thesis*, École Polytechnique Fédérale de Lausanne, Switzerland.

Cowan, K. M., & Eoff, L. (1993, January 1). Surfactants: additives to improve the performance properties of cements. *Society of Petroleum Engineers*. doi:10.2118/25181-MS

Danielson, U. (1962). Heat of hydration of cement as affected bywater–cement ratio. Paper IV-S7, *Proceedings of the 4th International Symposium on the Chemistry of Cement,* Washington DC, USA, 519–526.

Das, B. M. (1985). Principles of geotechnical engineering. *PWS Engineering*, Boston.

Day, R. L., Thermal deformation of cement paste. *MSc Thesis*, University of Calgary, Canada.

De Schutter, G., & Taerwe, L. (1995). Specific heat and thermal diffusivity of hardening concrete. *Magazine of Concrete Research*, (47)172, 203-208. doi:/10.1680/macr.1995.47.172.203.

Dean, R. H., Gai, X., Stone, C. M., & Minkoff, S. E. (2006, March 1). A comparison of techniques for coupling porous flow and geomechanics. *Society of Petroleum Engineers*. doi:10.2118/79709-PA.

Delgado, D., Specht, M. I., Rodriguez, W., Blanco, A., Soto, J. & Velez, M. (1993). Strength retrogression study of Venezuelan Portland class H Oilwell cement at high temperatures by electron microscopy and XRD.

Proceedings of the 15th International Conference on Cement Microscopy, USA, 218-232.

Derjaguin, B. V., & Churaev, N. V. (1974). Structural component of disjoining pressure. *Journal of Colloid and Interface Science*, 49, 249-255. doi:10.1016/0021-9797(74)90358-0

Dettling , H., The thermal expansion of hardened cement paste, Aggregates, and Concrete. Bulletin No. 164, Berlin. A vailable from SLA Translation Center, John Crerar Library, Chicago.

Di Lullo, G., & Rae, P. (2000, January 1). Cements for long term isolation - design optimization by computer modelling and prediction. *Society of Petroleum Engineers*. doi:10.2118/62745-MS.

Diamond, S. (2000). Mercury porosimetry; an inappropriate method for themeasurement of pore size distributions in cement-based materials. *Cement and Concrete Research*, (30)10, 1517– 1525.

Dixon, N. (2010). Soil-geosynthetic interaction: interface behaviour. Palmeira, E.M. ... et al (eds.). *Proceedings, 9th International Conference on Geosynthetics,* Guaruja Brazil, May 23rd-27th, 563-582.

Dureisseix. D., L. P., Neron. D. & Schrefler. A. (2003). A multi-time-scale strategy for multiphysics problems: application to poroelasticity. *International Journal for Multiscale Computational Engineering*, 1(4), 387-400.

Edel'man, L. I., Sominskii, D. S., & Kopchikova, N. V. (1961). Pore size distribution in cement rocks. *Colloid Journal*, 23, 192–196.

Edmunds, N., & Chhina, H. (2001, December 1). Economic optimum operating pressure for SAGD projects in Alberta. *Petroleum Society of Canada*. doi:10.2118/01-12-DAS.

Emanuel, J. H. & Hulsey, J. L. (1977). Prediction of the thermal coefficient of expansion of concrete. *Journal of the American Concrete Institute*, 74 (4), 149–155. .DOI: 10.14359/10996.

Emborg, G. M. (1989). Thermal stresses in concrete structures at early ages. *PhD Thesis*, Lulea University of Technology, Sweden.

Escalante-Garcia, J. I. (2003). Nonevaporable water from neat OPC and replacement materials in composite cements hydrated at different temperatures. *Cement and Concrete Research*, 33(11), 1883–1888.

Eshelby, J. D. (1957). The determination of the elastic field in an ellipsoidal inclusion. *Proceedings of the Royal Society of London* A 241 376– 392.

Ferraris, C., & Wittmann, F .H. (1987). Shrinkage mechanisms of hardened cement paste, *Cement and Concrete Research*, 17(3) 453-464. doi:10.1016/0008-8846(87)90009-3.

Feylessoufi, A., Cohen-Tenoudji, F., Morin, V., & Richard, P. (2001). Early ages shrinkage mechanisms of ultra-high-performance cement-based materials. *Cement and Concrete Research*, 31(11), 1573–1579. https://doi.org/10.1016/S0008-8846(01)00602-0.

Frigione, G., & Marra, S. (1976). Relationship between particle size distribution and compressive strength in Portland cement. *Cement and Concrete Research*, 6(1), 113–127.

Fuji, K., & Kondo, W. (1974). Kinetics of the hydration of tricalcium silicate. *Journal of American Ceramics Society*, 57, 492– 502.

Fulton, F. S. (1963). The early dilation of Portland cement paste. *Laboratory report of the Portland cement institute of Johannesburg*, SF-7.

Gabrijel, I., Mikulić, D., & Bijelić, N. (2010). Ultrasonic characterization of cement composite during hydration. *Technical Gazette*, (17)4, 493-497.

Gaël, B., Christelle, T., Gilles, E., Sandrine, G., & Tristan, S. (2016). Determination of the proportion of anhydrous cement using SEM image analysis. *Construction and Building Materials*, 126, 157-164. doi:org/10.1016/j.conbuildmat.2016.09.037.

Garnier, A., Fraboulet, B., Saint-Marc, J., & Bois, A.-. (2007 January 1). Characterization of Cement Systems to Ensure Cement Sheath Integrity. *Offshore Technology Conference*. doi:10.4043/18754-MS.

Gates, I. D., & Chakrabarty, N. (2006, September 1). Optimization of steam assisted gravity drainage in McMurray reservoir. *Petroleum Society of Canada*. doi:10.2118/06-09-05.

Gaunaurd, G. C., & Uberall, H. (1981). Resonance theory of bubbly liquids. *Journal of Acoustical Society of America*, 69(2), 362-370. https://doi.org/10.1121/1.385462.

Geiker, M. & Knudsen, T. (1982). Chemical shrinkage of Cement Pastes. *Cement and Concrete Research*, 12, 603-610.

Geiker, M. (1983). Studies of Portland cement hydration: measurements of chemical shrinkage and a systematic evaluation of hydration curves by means of the dispersion model. *PhD thesis*, Institute of Mineral Industry, Technical University of Denmark.

Ghabezloo, S., Sulem, J., & Saint-Marc, J. (2009). The effect of undrained heating on a fluid-saturated hardened cement paste. *Cement and Concrete Research,* 39(1), 54-64. doi.org/10.1016/j.cemconres.2008.09.004.

Goldstein, J. I., Newbury, D. E., Echlin, P., Joy, D. C.; Fiori, C., & Lifshin, E. (1981). Scanning Electron Microscopy and X-Ray Microanalysis. Plenum Press, New York.

Gonnerman, H. F. (1925). Effect of size and shape of test specimen on compressive strength of concrete. *Proc. ASTM,* 25, 237–250

Griggs, D. (1936). Deformation of rocks under high confining pressures: i. experiments at room temperature. *The Journal of Geology,* 44 (5), 541-577. http://www.jstor.org/stable/30067365.

Grosse, C. U., & Ohtsu, M. (2008). Acoustic Emission testing. Heidelberg. Springer.

Grosse, C. U., Reinhardt, H. W., & Beutel, R. (2004). Impact-echo measurements on fresh and hardening concrete. In Kovler, K., J. Marchand, S. Mindess, J. Weiss (Eds.), Proceedings of the International RILEM Symposium on Concrete Science and Engineering: A Tribute to Arnon Bentur. RILEM Publications s.a.r.l., Bagneux, France, RILEM Proceedings PRO 36, 95–104.

Grosse; C. U., & Reinhardt, H.-W. (1994). Continuous ultrasound measurements during setting and hardening of concrete. *Otto-Graf-Journal,* 5, 76-98.

Guang, Y., van Breugel, K., & Fraaij, A. L. A. (2001). Experimental study on ultrasonic pulse velocity evaluation of the microstructure of cementitious material at early age. HERON, 46(3). http://resolver.tudelft.nl/uuid:593dd877-763b-4355-a9ae-dcdffb6066aa.

Han, S. H., & Kim, J. K. (2004). Effect of temperature and age on the relationship between dynamic and static elastic modulus of concrete. *Cement and Concrete Research,* (34)7, 1219–1227. https://doi.org/10.1016/j.cemconres.2003.12.011.

Handin, J. (1965, December 1). Strength of oil well cements at downhole pressure-temperature conditions. *Society of Petroleum Engineers.* doi:10.2118/1300-PA

Hansen, W. (1987). Drying shrinkage mechanisms in Portland cement paste. *Journal of the American Ceramic Society,* 70(5), 323-328.

Harker, A. H., & Temple, J. A. G. (1988). Velocity and attenuation of ultrasound in suspensions of particles in fluids. *Journal of Physics D: Applied Physics,* 21(11), 1576–1588. https://iopscience.iop.org/article/10.1088/00223727/21/11/006/meta.

Hass, G.D. (1975). The chemical shrinkage of hardening cement paste and mortar. *Cement and Concrete Research,* 5(4), 295-320.

Herdan, G. (1953). Small particle statistics, Elsevier, London, P.413

Hewlett, P. C. (2003). Lea's Chemistry of Cement and Concrete, 4th Edition, Elsevier, Butterworth-Heinemann, New York, P.1092

Hill, J., Whittle, B., Sharp, J., & Hayes, M. (2002). Effect of elevated curing temperature on early hydration and microstructure of composites. *MRS Proceedings,* 757, II10.3. doi:10.1557/PROC-757-II10.3

Holt, E. E. (2001). Early age autogenous shrinkage of concrete. VTT Publication No. 446, Espoo: Technical Research Center of Finland.

Holt, E. E. (2005). Contribution of mixture design to chemical and autogenous shrinkage of concrete at early ages. *Cement and Concrete Research,* 35(3), 464-472. doi:10.1016/j.cemconres.2004.05.009.

Holtz, R. D., & Kovacs, W. D. (1981). An introduction to geotechnical engineering. Prentice-Hall, Inc., Englewood Cliffs, New Jersey.

Hua, C., Acker, P. & Erlacher, A. (1995). Analyses and models of the autogenous shrinkage of hardening cement paste: I. Modelling at macroscopic scale. *Cement and Concrete Research,* 25(7) 1457-1468. https://doi.org/10.1016/0008-8846(95)00140-8

Hutchinson, C. S. (1974). Laboratory handbook of petrographic techniques. Wiley & Sons, New York, London, Sydney, Toronto.

Ide, J. M. (1936). Comparison of statically and dynamically determined Young's Modulus of rocks. *Proceedings of the National Academy of Sciences of the United States of America,* 22(2), 81-92.

Irani, M., & Gates, I. (2016, October 1). Drained/undrained-zones boundary in steam-assisted-gravity-drainage process. *Society of Petroleum Engineers.* doi:10.2118/174417-PA

Ito, Y., & Suzuki, S. (1996). Numerical simulation of the SAGD process in the hangingstone oil sands reservoir. *Petroleum Society of Canada.* doi:10.2118/96-57.

James, S. G., & Boukhelifa, L. (2006, January 1). Zonal isolation modelling and measurements-Past myths and todays realities. *Society of Petroleum Engineers.* doi:10.2118/101310-MS.

Jennings, H. M., & Johnson, S. K. (1986). Simulation of microstructure development during the hydration of a cement compound. *Journal of American Ceramic Society,* 69, 790–795.

Jennings, S. S. (2005, January 1). Long-term high-temperature laboratory cement data aid in the selection of optimized cements. *Society of Petroleum Engineers.* doi:10.2118/95816-MS

Jensen, O. M. (1993). Autogenous deformation and rh-change –self-desiccationand self-desiccation shrinkage. *PhD Thesis,* Building Materials Laboratory, The Technical University of Denmark, TR 285/93.

Jensen, O. M., & Hansen, P. F. (1995). A dilatometer for measuring autogenous deformation in hardening Portland cement paste. *Materials and Structures,* 28(181), 406-409.

Jensen, O. M., & Hansen, P. F. (2001). Autogenous deformation and RH-change in perspective. *Cement and Concrete Research,* 31(12), 1859-1865. https://doi.org/10.1016/S0008-8846(01)00501-4

Jones, R. (1949). A non-destructive method of testing concrete during hardening. *Concrete and Constructional Engineering,* 44(4), 127–128.

Joshi, S. D. (1986). A laboratory study of thermal oil recovery using horizontal wells. *Society of Petroleum Engineers.* doi:10.2118/14916-MS

Justnes, H., Reyniers, B., Van Loo, D., & Sellevold, E. J. (1994). An evaluation of methods for measuring chemical shrinkage of cementitious paste. *Nordic Concrete Research,* 14, 45–61.

Justnes, H., Sellevold, E. J., Reyniers, B., Van Loo, D., Van Gemert, A., Verboven, F., et al. (2000). Chemical shrinkage of cement pastes with plasticizing admixtures. *Nordic Concrete Research,* 24, 39–54.

Justnes, H., Skalle, P., Sveen, J., & Øye, B. A. (1995). Porosity of oil well cement slurries during setting. *Advances in Cement Research,* 7(25), 9-12.

Justnes, H., Van Loo, D., Reyniers, B., Skalle, P., Sveen, J., & Sellevold, E. J. (1995). Chemical shrinkage of oil well cement slurries. *Advance in Cement Research,* 7 (26), 85-90.

Kamath, V. A., Sinha, S., & Hatzignatiou, D. G. (1993, January 1). Simulation Study of Steam-Assisted Gravity Drainage Process in Ugnu Tar Sand Reservoir. *Society of Petroleum Engineers.* doi:10.2118/26075-MS.

Karim, G. A., & Hanafi, A. (1981). The thermal conductivity of oils sands. *The Canadian Journal of Chemical Engineering,* 59, 461-464.

Keating, J., Hannant, D. J., & Hibbert, A. P. (1989a). Comparison of shear modulus and pulse velocity techniques to measure the buildup of structure in fresh cement pastes used in oil-well cementing. *Cement and Concrete Research,* 19(4), 554–566. https://doi.org/10.1016/0008-8846(89)90007-0.

Kersten, M. S. (1949). Thermal properties of soil. Bulletin 28. University of Minnesota, Mineapolis: Institute of Technology Engineering Experiment Station.

Kim, J. K. & Yi, S. T. (2002). Application of size effect to compressive strength of concrete members. *Sadhana,* 27(4), 467-484 doi:10.1007/BF02706995.

Kim, K. H., Jeon, S. E., Kim, J. K., & Yang, S. (2003). An experimental study on thermal conductivity of concrete. *Cement and Concrete Research,* 33(3), 363–371. doi.org/10.1016/S0008-8846(02)00965-1.

King, M. S. (1969). Static and dynamic elastic moduli of rocks under pressure. Paper ARMA-69-0329 presented at the 11th U.S *Symposium on Rock Mechanics (USRMS),* Berkeley, California.

Kirby, D. M., & Biernacki, J. J. (2012). The effect of water-to-cement ratio on the hydration kinetics of tricalcium silicate cements: Testing the two-step hydration hypothesis. *Cement and Concrete Research,* 42(8), 1147-1156.

Kjellsen, K. O., & Detwiler, R. J. (1992). Reaction kinetics of Portland cement mortars hydrated at different temperatures. *Cement and Concrete Research,* 22(1), 112–120.

Kmack, R. M. (2008). Characterization of air voids in fresh cement paste through ultrasonic nondestructive testing. Master's thesis, Georgia Institute of Technology.

Knudsen, T., & Geiker, M. (1982). Chemical shrinkage as an indicator of the stage of hardening. Proceedings of the International RILEM Conference

on Concrete of Early Ages, I, Session V: Methods of indicating the stage of hardening. Ecole National des Pouts et Chaussees, 163-167.

Kriechbaum, M., Degovics, G., Laggner, P., & Tritthart, J. (1994). Investigation on cement pastes by small-angle X-ray scattering and BET: the relevance of fractal geometry. *Advanced Cement Research,* (6)23, 93– 101.

Kuhlmann, K., Ellerbrock, H. G., & Sprung, S. (1985). Particle size distribution and properties of Portland cement. *Zement.-Kalk-Gips,* 38, 136-144.

Kuster, G. T. & Toksoz, M. N. (1974). Velocity and attenuation of seismic waves in two-phase media: part I. theoretical formulations. *Geophysics,* 39(5), 587-606. https://doi.org/10.1190/1.1440450.

Kutchko, B. G., Strazisar, B. R., Dzombak, D. A., Lowry, G. V., & Thaulow, N. (2007). Degradation of well cement by CO2 under geologic sequestration conditions. *Environmental Science and Technology,* 41(13), 4787-4792.

Labibzadeh, M., Zahabizadeh, B., & Khajehdezfuly, A. (2010). Early-age compressive strength assessment of oil well class G cement due to borehole pressure and temperature changes. *Journal of American Science,* 6(7), 38-46.

Lachowsky, E. E. & Diamond, S. (1983). Investigation of the composition and morphology of individual particles of Portland cement paste: 1. C-H-S gel and calcium hydroxide particles. *Cement and Concrete Research,* (13)2, 177-85.

Ladva, H. K. J., Craster, B., Jones, T. G. J., Goldsmith, G., & Scott, D. (2005, September 1). The cement-to-formation interface in zonal isolation. *Society of Petroleum Engineers*. doi:10.2118/88016-PA.

Lasič, D. D., & Stepišnik, J. (1984). An investigation of the osmotic model of cement curing by ultrasonics. *Cement and Concrete Research,* 14(3), 345–348. https://doi.org/10.1016/0008-8846(84)90052-8.

Laugesen, J. L. (2005). Density functional calculations of elastic properties of portlandite, CaOH2. *Cement and Concrete Research,* 35(2), 199-203. https://doi.org/10.1016/j.cemconres.2004.07.036

Le Chatelier (1900). Bulles de la Société d'Encouragement pour l'Industrie Nationale.

Le Roy-Delage, S., Baumgarte, C., Thiercelin, M., & Vidick, B. (2000, January 1). New Cement Systems for Durable Zonal Isolation. *Society of Petroleum Engineers*. doi:10.2118/59132-MS.

Le, Q. V., Meftah, F., He, Q. C., & Le-Pape, Y. (2008). Creep and relaxation functions of a heterogeneous viscoelastic porous medium using the Mori-Tanaka homogenization scheme and a discrete microscopic retardation spectrum. *Mechanics of Time Dependent Materials,* 11(3-4), 309-331.

Lea, F. M., Chemistry of Cement and Concrete, 3rd Ed. Chemical Publishing Company, Inc., USA.

Lee, H. K., Lee, K. M., Kim, Y. H., Yim, H. & Bae, D. B. (2004). Ultrasonic in-situ monitoring of setting process of high-performance concrete. *Cement and Concrete Research,* 34(4), 631–640. https://doi.org/10.1016/j.cemconres.2003.10.012.

Lerch, W., & Ford, C. L. (1948). Long-term study of cement performance in concrete: chapter 3. Chemical and physical tests of the cements, *ACI Materials Journal,* 19 (8), 745–795.

Leslie, J. R. & Cheesman, W. J. (1949). An ultrasonic method of studying deterioration and cracking in concrete structures. *Journal of the American Concrete Institute,* 46(9), 17-36.

Li, L. (2005). Structural analysis of cylindrical particles by small angle X-ray scattering. PhD Thesis, University of Bayreuth.

Li, P., Chalaturnyk, R. J., & Polikar, M. (2004, May 1). Issues with reservoir geomechanical simulations of the SAGD process. *Petroleum Society of Canada*. doi:10.2118/04-05-02

Link, R., Tran, D., Chen, L., Thibault, P.A., Noewood, M., & Slater, J. (1995). Solution of 2D and 3D fully coupled FSI problems for compressible flows. proc., *Third Annual Conference of the CFD Society of Canada,* Banff, Aberta, Canada, 25 -27 June, 2, 71-78.

Liu, X., Nair, S. D., Cowan, M., & van Oort, E. (2015). A novel method to evaluate cement-shale bond strength. *Society of Petroleum Engineers.* doi:10.2118/173802-MS.

Llaguno, P. E., Moreno, F., Garcia, R., Mendez, Z., & Escobar, E. (2002, January 1). A reservoir screening methodology for SAGD applications. *Petroleum Society of Canada*. doi:10.2118/2002-124.

Loser, R., Münch, B., & Lura, P. (2010), A volumetric technique for measuring the coefficient of thermal expansion of hardening cement paste and mortar. *Cement and Concrete Research,* 40(7) 1138-1147. https://doi.org/10.1016/j.cemconres.2010.03.021

Lura, P. (2003). Autogenous deformation and Internal curing of concrete. PhD Thesis, Delft University, Delft, The Netherlands.

Lura, P., Couch, J., Jensen, O. M., & Weiss, J. (2009). Early-age acoustic emission measurements in hydrating cement paste: Evidence for cavitation during solidification due to self-desiccation. *Cement and Concrete Research,* 39(10), 861-867. https://doi.org/10.1016/j.cemconres.2009.06.015.

Lura, P., Jensen, O.M. & van Breugel, K. (2003). Autogenous shrinkage in high-performance cement paste: An evaluation of basic mechanisms. *Cement and Concrete Research,* 33(2), 223-232. https://doi.org/10.1016/S0008-8846(02)00890-6

Mack, D. J., & Dillenbeck, R. L. (2002). Cement: how tough is tough enough? A laboratory and field study. *Society of Petroleum Engineers.* doi:10.2118/78712-MS.

Maekawa, K., Ishida, T., & Kishi, T. (2003). Multi-scale modeling of concrete performance integrated material and structural mechanics. *Journal of Advanced Concrete Technology,* 1(2), 91-126.

Mehta, P. K., & Monteiro, P. J. M. (1993). Concrete: microstructure, properties, and materials. 2nd Edition, The McGraw- Hill Companies, Inc., 548 p.

Meyers, S. L. (1940). Thermal coefficient of expansion of Portland cement - long-time tests. *Industrial and Engineering Chemistry,* 32(8), 1107 -112.

Meyers, S. L. (1951). Thermal expansion characteristics of hardened cement paste and of concrete. *Highway Research Board Proceedings,* 30, 193-203.

Mills, R. H. (1966). Factors influencing cessation of hydration in water cured cement pastes. Special Report No. 90, Proceedings of the Symposium on the Structure of Portland Cement Paste and Concrete, Highway Research Board, Washington DC, USA, 406 – 424.

Mindess, S., & Young, J. F. (1981). Concrete, Prentice-Hall Inc., N.J., 671 pp.

Mirza, S. A., Hatzinikolas, M., & MacGregor, J. G. (1979). Statistical descriptions of the strength of concrete. *Journal of the Structural Division,* 105(6), 1021-1037.

Mitchell, L. J. (1953). Thermal expansion tests on aggregates, neat cements and concretes. Proceedings of the ASTM, 963–977.

Monteiro, P. J. M., & Chang, C. T. (1995). The elastic moduli of calcium hydroxide. *Cement and Concrete Research,* 25(8), 1605-1609. doi:10.1016/0008-8846(95)00154-9.

Morabito, P. (2001). Thermal properties of concrete: variations with the temperature and during the hydration phase. BE96–3843/2001:18–4.

Mori, T., & Tanaka, K. (1973). Average stress in matrix and average elastic energy of materials with misfitting inclusions. *Acta Metallurgica,* 21(5), 1605– 1609.

Moritis, G. (1990). Horizontal drilling scores more successes. *Oil and Gas Journal,* 53-64.

Mounanga, P., Khelidj, A., Loukili, A., & Baroghel-Bouny, V. (2004). Predicting $Ca(OH)_2$ content and chemical shrinkage of hydrating cement pastes using analytical approach. *Cement and Concrete Research,* 25(2), 255–265. https://doi.org/10.1016/j.cemconres.2003.07.006

Mushkelishvili, N. I., Some basic problems of the mathematical theory of elasticity. The Netherlands: Kluwer Aca.

Navi, P., & Pignat, C. (1996). Simulation of cement hydration and the connectivity of the capillary pore space. *Advanced Cement Based Materials,* 4(2), 58-67. https://doi.org/10.1016/S1065-7355(96)90052-8

Nelson, E.B. & Guillot, D. (2006). Well cementing, second edition, Sugar Land: Schlumberger.

Neville, A. M. (1996). Properties of concrete. 4th ed.; John Wiley & Sons Inc: New York.

Neville, A. M. & Brooks, J.J. (1987). Concrete Technology, Longman Scientific and Technical, New York.

Nguyen, H. X., Wisup, B., Tran, X., Ta, D. Q., & Nguyen, H. D. (2012, January 1). Effects of reservoir parameters and operational design on the prediction of SAGD performance in Athabasca oilsands. *Society of Petroleum Engineers.* doi:10.2118/154778-MS.

Noik, C., & Rivereau, A. (1999, January 1). Oilwell cement durability. *Society of Petroleum Engineers.* doi:10.2118/56538-MS.

Odeh, A. S. (November 1969). Reservoir simulation ...What is it. *Society of Petroleum Engineers.* doi:10.2118/2790-PA.

Ong, T. S., & Butler, R. M. (1990, November 1). Wellbore flow resistance in steam-assisted gravity drainage. *Petroleum Society of Canada.* doi:10.2118/90-06-04.

Opedal, N., Todorovic, J., Torsaeter, M., Vralstad, T., & Mushtaq, W. (2014, February 26). Experimental study on the cement-formation bonding. *Society of Petroleum Engineers.* doi:10.2118/168138-MS.

Osbaeck, B., & Johansen, V. (1989). Particle size distribution and rate of strength development of Portland cement. *Journal of the American Ceramic Society,* 72(2), 197–201.

Palmeira, E. M. (1988). Discussion on direct shear tests on reinforced sand. *Geotechnique,* 38(1), 146-148.

Pang, X., Meyer, C., Funkhouser, G. P., & Darbe, R. (2015). An innovative test apparatus for oil well cement: In-situ measurement of chemical shrinkage and tensile strength. *Construction and Building Materials,* 74, 93-101. doi.org/10.1016/j.conbuildmat.2014.10.025

Parcevaux, P. A., & Sault, P. H. (1984). Cement shrinkage and elasticity: A new approach for a good zonal isolation. *Society of Petroleum Engineers.* doi:10.2118/13176-MS

Pedam, S. K. (2007). Determining strength parameters of oil well Cement. M.Sc. Thesis, the University of Texas at Austin, U.S.A.

Peng, S. D. (1971). Stresses within elastic circular cylinders loaded uniaxially and triaxially. *International Journal of Rock Mechanics and Mining Science & Geomechanics,* 8(5), 399-432. https://doi.org/10.1016/1365-1609(71)90009-8

Pessiki, S. P., & Carino, N. J. (1988). Setting time and strength to concrete using the impact-echo method. *ACI Materials Journal,* 85(5), 389–399.

Pessiki, S., & Johnson, M. (1994). In-place determination of concrete strength by the impact-echo method. In Baker, N. C., Goodno, B. J. (Eds.), Proceedings of the Structures Congress XII. Lehigh University, Bethlehem, PA, USA, *American Society of Civil Engineers (ASCE),* 2, 1340–1345.

Peterson, B. (1963, January 1). Bond of cement compositions for cementing wells. World Petroleum Congress.

Pickett, G. (1945). Equations for computing elastic constants from flexural and torsional resonant frequencies of vibration of prisms and cylinders.

Proceedings of the American Society for Testing and Materials, 45, 846-865.

Pignat, C., Navi, P., & Scrivener, K. (2005). Simulation of cement paste microstructure hydration, pore space characterization and permeability determination. *Materials and Structures,* 38(4), 459-466.

Powers, T. C. (1958). Structure and physical properties of hardened Portland cement paste. *Journal of American Ceramic Society,* 41(1), 1-6. https://doi.org/10.1111/j.1151-2916.1958.tb13494.x

Powers, T. C. (1968). Section I The Thermodynamics of Volume Change and Creep. *Materials and Structures,* 1(6), 487-507.

Powers, T. C., & Brownyard, T. L. (1948). Studies of the physical properties of hardened Portland cement paste (9 parts). *Journal of American Concrete Institute 43,* Bulletin 22, Research Laboratories of the Portland Cement Association, Chicago.

Ramachandran, V. S., & Feldman R. F. (1978). Time-dependent and intrinsic characteristics of Portland cement hydrated in the presence of calcium chloride. *Cemento,* 75(3), 311–322.

Rebeiz, K. S., Fowler, D. W., & Paul, D. R. (1992). Polymer concrete and polymer mortar using resins based on recycled poly (ethylene terephthalate). *Journal of Applied Polymer Science,* 44(9), 1649-1655.

Rocco, C., Guinea, G. V., Planas, J., & Elices, M. (1999). Size effect and boundary conditions in the Brazilian test: Experimental verification. *Materials and Structures,* 32(3), 210-217.

Rubin, B., & Buchanan, W. L. (1985, April 1). A general-purpose thermal model. *Society of Petroleum Engineers.* doi:10.2118/11713-PA.

Sabins, F. L., & Sutton, D. L. (1991). Interrelationship between critical cement properties and volume changes during cement setting. *Society of Petroleum Engineers.* doi:10.2118/20451-PA .

Sabri, S., & Illston, J. M. (1982). Immediate and delayed thermal expansion of hardened cement paste. *Cement and Concrete Research,* 12(2), 199-208. doi.org/10.1016/0008-8846(82)90007-2.

Saint-Venant, B. (1864). Notes to Navier's Resume des Lecons de la Re'sistance des Corps Solides, 3rd ed., Paris, pp. 175.

Sant, G., Lura, P., & Weiss, J. (2006). Measurement of volume change in cementitious materials at early ages: review of testing protocols and

interpretation of results. *Journal Transportation Research Record,* (1979), 21–29. doi.org/10.1177/0361198106197900104

Sasaki, K., Akibayashi, S., Yazawa, N., Doan, Q. T., & Ali, S. M. F. (2001, March 1). Experimental modeling of the SAGD process - Enhancing SAGD performance with periodic stimulation of the horizontal producer. *Society of Petroleum Engineers.* doi:10.2118/69742-PA.

Sayers, C. M., & Dahlin, A. (1993). Propagation of ultrasound through hydrating cement pastes at early times. *Advanced Cement Based Materials,* 1(1), 12-21. https://doi.org/10.1016/1065-7355(93)90004-8.

Schwartz, L., & Plona, T. J. (1985). Ultrasonic propagation in close- packed disordered suspensions. *Journal of Applied Physics,* 55(11), 3971-3977. https://doi.org/10.1063/1.332983.

Scott, J. D., Proskin, S. A., & Adhikary, D. P. (1994, July 1). Volume and permeability changes associated with steam stimulation in an oil sands reservoir. *Petroleum Society of Canada.* doi:10.2118/94-07-06

Scrivener, K. L., & Pratt, P. B. (1984). Electron images of polished cement sections in the scanning electron microscope. In: Bayless J, editor. Proceedings 6th International Conference on Cement Microscopy, Albuquerque. Duncanville, TX: ICMA; pp.145–55.

Settari, A., & Mourits, F. M. (1998, September 1). A Coupled reservoir and geomechanical simulation system. *Society of Petroleum Engineers.* doi:10.2118/50939-PA.

Settari, A., Kry, P. R., & Yee, C. T. (1989, January 1). Coupling of fluid flow and soil behavior to model injection into uncemented oil sands. *Petroleum Society of Canada.* doi:10.2118/89-01-08

Shetty, M. S. (2006). Concrete Technology Theory and Practice, S. Chand & Company Ltd., New Delhi, (Chapter 7).

Shui, Z., Zhang, R., Chen, W., & Xuan, D. (2010). Effects of mineral admixtures on the thermal expansion properties of hardened cement paste. *Construction and Building Materials,* 24(9), 1761-1767. doi.org/10.1016/j.conbuildmat.2010.02.012.

Simmons, G. & Brace, W. F. (1965). Comparison of static and dynamic measurements of compressibility of rocks. *Journal of Geophysical Research,* 70(22), 5649-5656.

Singh, N. B., & Ojha, P. N. (1981). Effect of $CaCl_2$ on the hydration of tricalcium silicate. *Journal of Material Science,* 16(10), 2675–2681.

Singhal, A. K., Ito, Y., & Kasraie, M. (1998, January 1). Screening and design criteria for Steam Assisted Gravity Drainage (SAGD) Projects. *Society of Petroleum Engineers.* doi:10.2118/50410-MS.

Skalle, P., Backe, K. R., Lyomov, S. K., Lile, O. B., Justnes, H., & Sveen, J. (1997, January 1). Shrinkage of oil well cement slurries. *Petroleum Society of Canada.* doi:10.2118/97-77

Smilauer, V. (2005). Elastic properties of hydrating cement paste determined from hydration models. PhD Thesis, Technical University in Prague.

Snyder, K. A., & Bullard, J. W. (2005). Effect of continued hydration on the transport properties of cracks through Portland cement pastes in a saturated environment: A microstructural model study, NIST IR 7265, U.S. Department of Commerce, Washington, DC.

Soroka, I. (1979). Portland Cement Paste and Concrete, Macmillan, London, UK.

Spec. 10A, Specification for Cements and Materials for Well Cementing, twenty-fourth edition, American Petroleum Institute, December 2010.

Spinner, S., & Tefft, W. E. (1961). A method for determining mechanical resonance frequencies and for calculation elastic moduli from these frequencies. *Proceedings of the American Society for Testing and Materials,* 1221-1238.

Stepisnik, J., Lukac, M., & Kocuvan, I. (1981). Measurement of cement hydration by ultrasonic. *American Ceramic Society Bulletin,* 60(4), 481–483.

Stewart, R. B., & Schouten, F. C. (1988). Gas invasion and migration in cemented annuli: Causes and cures. *SPE Drilling Engineering,* 3(1), 77-82.

Stiles, D. A. (1997, January 1). Successful cementing in areas prone to shallow saltwater flows in deep-water Gulf of Mexico. *Offshore Technology Conference.* doi:10.4043/8305-MS.

Sumner, M. S., Hepher, N. M., & Moir, G. K. (1989). The influence of a narrow particle size distribution on cement paste and concrete water demand. *Ciments, Betons, Platr. Chaux,* 778(3), 164–168.

Sun, Z., Ye, G., & Shah, S. (2005). Microstructure and early-age properties of portland cement paste effects of connectivity of solid phases. *ACI Materials Journal,* (102)2, 122-129. https://www.concrete.org/publications/acimaterialsjournal.aspx.

Sutton, D. L., & Sabins, F. L. (1984). New evaluation for annular gas flow potential. *Oil and Gas Journal,* 65-70.

Swamy, N., & Rigby, G. (1971). Dynamic properties of hardened paste, mortar and concrete. *Materiaux et Constructions,* (4)1, 13-40. https://doi.org/10.1007/BF02473927.

Sykes, R. L., & Logan, J. L. (1987). New Technology in Gas Migration Control. *Society of Petroleum Engineers.* doi:10.2118/16653-MS

Tan, T. B., Butterworth, E., & Yang, P. (2002, January 1). Application of a thermal simulator with fully coupled discretized wellbore simulation to SAGD. *Petroleum Society of Canada.* doi:10.2118/02-01-01

Taplin, J. H. (1969). A method for following hydration reaction in Portland cement paste. *Australian Journal of Applied Sciences,* 10, 329–345.

Tavares, F., Rocha, J., & Calado, V. (2013). Study of the influence of cement slurry composition in the gas migration. *Offshore Technology Conference.*

Taylor, W. H. (1977). Concrete Technology and Practice. McGraw-Hill, New York, 4th edn.

Tazawa, E., Miyazawa, S., & Kasai, T. (1995). Chemical shrinkage and autogenous shrinkage of hydrating cement paste. *Cement and Concrete Research,* (25)2, 288-292. doi:10.1016/0008-8846(95)00011-9.

Terzaghi, K. (1945). Stress conditions for the Failure of Saturated Concrete and Rock. *American Society for Testing Materials Proceedings,* 45, 777-801

Thiercelin, M. J., Dargaud, B., Baret, J. F., & Rodriguez, W. J. (1997). Cement design based on cement mechanical response. *Society of Petroleum Engineers.* doi:10.2118/38598-MS.

Thiercelin, M., Baumgarte, C., & Guillot, D. (1998, January 1). A soil mechanics approach to predict cement sheath behavior. *Society of Petroleum Engineers.* doi:10.2118/47375-MS.

Touhidi-Baghini, A. (1998) Absolute permeability of McMurray Formation oil sands at low confining stresses, Ph.D. thesis, Dept. of Civil Eng., University of Alberta, Edmonton, Alberta 339 pp.

Tran, D., Buchanan, W. L., & Nghiem, L. X. (2010, March 1). Improved gridding technique for coupling geomechanics to reservoir flow. *Society of Petroleum Engineers.* doi:10.2118/115514-PA

Tran, D., Link, R., Penrose, J., & Thibault, P.A. (1994). CFD modelling of fluid-structure and liquid-gas interactions. proc., Second Annual Conference of the CFD Society of Canada (CFD 94), Toronto, Ontario, Canada, 1-3 June, 171-178.

Troxell, G. E., Daves, H. E., & Kelly, J. W. (1968). Composition and properties of concrete. McGraw-Hill Book Company, Second edition, New York, USA, 513p.

Trtnik, G., & Gams, M. (2014). Recent advances of ultrasonic testing of cement based materials at early ages. *Ultrasonics,* 54(1), 66-75. doi.org/10.1016/j.ultras.2013.07.010.

Trtnik, G., Turk, G., Kavcic, F., & Bosiljkov, V. B. (2008). Possibilities of using the ultrasonic wave transmission method to estimate initial setting time of cement paste. *Cement and Concrete Research,* 38(11), 1336–1342. https://doi.org/10.1016/j.cemconres.2008.08.003.

Urick, R. J. (1947). A sound velocity method for determining the compressibility of finely divided substances. *Journal of Applied Physics,* 18, 983-987. doi.org/10.1063/1.1697584.

Valiˇc, M. I., & Stepiˇsnik, J. (1999). Applications of pulsed USWR method for materials studies. *Kovine, Zlitine, Tehnologije,* 33(5), 341–344.

Valiˇc, M. I., & Vuk, T. (2000). A study of the influence of additives and admixtures on the hydration of cement with the pulsed USWR method. *Materiali in Tehnologije,* 34(5), 249–255.

Van Breugel, K. (1991). Simulation of hydration and formation of structure in hardening cement based materials. PhD Thesis, Delft University of Technology, The Netherlands.

Van Breugel, K. (1995a). Numerical simulation of hydration and microstructural development in hardening cement-based materials (I): Theory. *Cement and Concrete Research,* 25(2), 319-331. doi.org/10.1016/0008-8846(95)00017-8

Van Breugel, K. (1995b). Numerical simulation of hydration and microstructural development in hardening cement-paste (II): Applications. *Cement and Concrete Research,* 25(3), 522-530.

Verbeck, G. J. & Helmuth, R. H. (1968). Structures and physical properties of cement pastes. Proceedings of the 5th International Congress on the Chemistry of Cement, Tokyo.

Verbeck, G. J., & Helmuth, R. H. (1968). Structures and physical properties of cement pastes. Proceedings of the 5th International Congress on the Chemistry of Cement, Tokyo, Vol. III, pp.1.

Viviani, M., Glisic, B., & Smith, I. F. C. (2007), Separation of thermal and autogenous deformation at varying temperatures using optical fiber sensors. *Cement and Concrete Composites,* 29(6), 435-447.

Vutukuri, V. S., Lama, R. D., & Saluja, S. S. (1974). Handbook on mechanical properties of rocks, Trans Tech Publications, Vol. 1, 281.

Wagner, L. A. (1933). A rapid method for the determination of the specific surface of Portland cement. Proceedings, *American Society for Testing Materials,* 33(II), 553-570.

Walsh, J. B. (1965). The effect of cracks on the uniaxial elastic compression of rocks. *Journal of Geophysical Research,* 70(2), 399-411. doi.org/10.1029/JZ070i002p00399.

Wijk, G. (1978). Determination of the tensile strength of rock by a compression test of an irregular test piece. *International Journal of Rock Mechanics and Mining Sciences & Geomechanics Abstracts*, (15), 149-160.

Wittman, F. H., & Lukas, J. (1976). Experimental Study of thermal expansion of hardened cement paste. *Materiaux et Constructions,* 7(40), 247-252

Xu, Y., & Chung, D. D. L. (1999). Increasing the specific heat of cement paste by admixture surface treatments. *Cement and Concrete Research,* (29)7, 1117-1121. doi:/10.1016/S0008-8846(99)00080-0.

Yamakawa, H., Nakauchi, H., Kita, T., & Onuma, H. (1986). A study of the coefficient of thermal expansion of concrete. *Transactions of the Japan Concrete Institute,* 8, 111–118.

Yang, G., & Butler, R. M. (1992, August 1). Effects of reservoir heterogeneities on heavy oil recovery by Steam-Assisted Gravity Drainage. *Petroleum Society of Canada.* doi:10.2118/92-08-03

Ye, G. (2003). Experimental study and numerical simulation of the development of microstructure and permeability of cementitious materials. *PhD Thesis*, Delft.

Ye, G., Sun, Z., Voigt, T., van Breugel, K., & Shah, S. P. (2004). A micro-mechanical model for characterization of cement paste at early age validated with experiments. *International RILEM Symposium on Concrete Science and Engineering,* Evanston.

Ye, G., van Breugel, K., & Fraaij, A. L. A. (2003). Experimental study and numerical simulation on the formation of microstructure in cementitious materials at early age. *Cement and Concrete Research,* 33(2), 233–239. doi.org/10.1016/S0008-8846(02)00891-8.

Yodsudjai, W., & Wang, K. (2013). Chemical shrinkage behavior of pastes made with different types of cements. *Construction and Building Materials,* 40, 854-862. doi:10.1016/j.conbuildmat.2012.11.053.

Yoon, S., Macphee, D. E., & Imbabi, M. S. (2014). Estimation of the thermal properties of hardened cement paste on the basis of guarded heat flow meter measurements. *Thermochimica Acta,* 588, 1-10. doi:10.1016/j.tca.2014.04.015.

Yuan, J.-Y., & McFarlane, R. (2011, January 1). Evaluation of steam circulation strategies for SAGD startup. *Society of Petroleum Engineers.* doi:10.2118/143655-PA.

Zhang, L., & Thornton, C. (2007). A numerical examination of the direct shear test. *Géotechnique,* 57(4), 343-354. doi:10.1680/geot.2007.57.4.343

Zhang, T., Gao, P., Luo, R., Guo, Y., Wei, J., & Yu, Q. (2013). Measurement of chemical shrinkage of cement paste: Comparison study of ASTM C 1608 and an improved method. *Construction and Building Materials,* 48, 662-669. doi:10.1016/j.conbuildmat.2013.07.086.

Zhang, Y. M., & Napier-Munn, T. J. (1995). Effects of particle size distribution, surface composition on Portland cement. *Powder Technology*, 83, 245-252.

Zhou, Q., & Beaudoin, J. J. (2003). Effect of applied hydrostatic stress on the hydration of Portland cement and C_3S. *Advances in Cement Research,* 15(1), 9–16.

Zhu, J., Kee, S., Han, D., & Yi-Te Tsai. (2011). Effects of air voids on ultrasonic wave propagation in early age cement pastes. *Cement and Concrete Research,* 41(8), 872–881. doi.org/10.1016/j.cemconres.2011.04.005.

Zisman, W. A., Comparison of the statically and seismologically determined elastic constants of rocks. *Proceedings of the National Academy of Sciences of the United States of America,* 19(11), 989-990.

APPENDIX A. SLURRY AND SAMPLE PREPARATION

A-1 Preparation of slurry

This step is considered a very important step because the quality of cement slurry has a significant effect on cement paste performance. The following items describe the procedures that have been used to prepare cement slurries and samples.

1. The mix water is weighted (distilled water is used to prepare the slurries). The temperatures of the mix water is measured and documented. The temperature of the mix water is kept to 23 ºC ±1 ºC immediately before mixing.
2. The dry cement is weighted and blended uniformly. The temperatures of the dry cement is measured and documented. The temperature of the dry cement is kept to 23 ºC ±1 ºC immediately before mixing.
3. Water is poured in the mixing container and the motor is turned on and maintained at 4,000 r/min ±200 r/min.
4. The cement is added to the mixing container at a uniform rate during 15 s, after that the motor speed is adjusted to be 12,000 r/min ± 500 r/min for 35 ± 1 s.
5. The rotational speed under load is measured and documented.

Figure A1. Shows the mixing device

Figure A1. Mixing device

A-2 Preparation of Samples

1. Cylindrical moulds made of brass are used to prepare the samples. The base plate of the mould is made of metal and the cover plate has a thickness of 6 mm and has two grooves on it.
2. A thin layer of grease is applied to the interior faces of the mould, the base plate, and the cover plate as well.
3. Cement slurry is poured into the moulds to one-third of the mould depth.
4. Puddling rod made of corrosion- resistant material with a width of 6 mm is used to puddle the slurry 30 times.
5. This step is repeated until cement slurry fills the mould.
6. Thereafter, the molds are placed in a pressurized curing chamber (Figure A3) to be cured at 9 ^{o}C and 3 MPa.
7. After one day, specimens are demolded and taken to the moisture room where samples are kept inside water of 7±2 °C and relative humidity higher than 90% until the testing date.

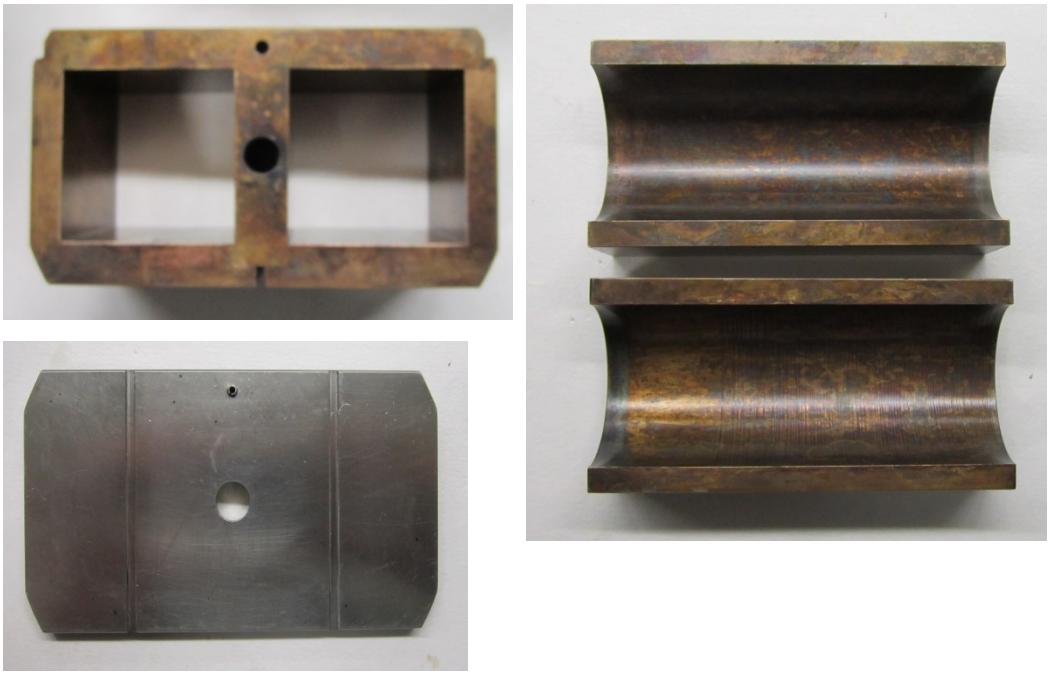

Figure A2. Brass mould and base plate

Figure A3. Pressurized curing chamber

APPENDIX B. STANDARD OPERATING PROCEDURES FOR DIFFERENT EXPERIMENTS (SOP)

B-1 Thermal expansion testing procedures

B-1.1 Sample Preparation

1. The sample is examined to make sure that there are no cracks in the sample.
2. The sample is trimmed to a 1.5” diameter and 3.0” length specimen in the moisture room using an electrical diamond cutter.
3. After trimming, both ends of the specimen should be flat and parallel and are perpendicular to the vertical axis.
4. The sample is weighed and all specimen’s dimensions should be measured.
5. Initial Vp and Vs measurements are conducted on the specimen.
6. Photos are taken for the sample.

B-1.2 Set up and testing

1. Fill the bottom section of the high temperature oedometer cell with brine fluid and place the specimen in the 1.5” diameter interchangeable stainless steel oedometer ring with the saturated sintered stainless steel porous stone and the stainless steel plate on top of the specimen.
2. Fill the top piston load section of the oedometer cell with white oil.
3. Saturate all drainage lines with the corresponding fluid.
4. A computer controlled positive displacement pump is used to apply the hydraulic pressure to the piston. Back pressure may be applied to the top or bottom of the specimen through ports located in the side of the cell.
5. An LVDT is mounted on the top of the cell to measure vertical displacement of the piston and specimen.
6. Apply balancing pressure for back pressure at 7000 kPa and piston load at the desired axial stress level.
7. Apply seating load with back pressure at 7000 kPa and piston load of $\sigma' = 50$ kPa. Hold for at least a 12 hour period to achieve back saturation.

8. Apply piston load of σ'= 500 kPa to make sure the piston touches the specimen. Unload the piston load back to the seating load. Let the system be stable.
9. Apply the piston loadings, simultaneously in several increments, to the in-situ desired axial stress level. Let the specimen stabilize.
10. Start thermal expansion test:
    i. Heat up the cell, simultaneously in a heating rate of 10 ºC per hour, to the desired temperature 180 ºC. At each temperature increment, let the specimen be heated and consolidated at a stable temperature until the vertical displacement is in stable steady state.
    ii. Cool down the cell, simultaneously in each decrement of 10 ºC, to ambient conditions of room temperature. At each temperature decrement, let the specimen be cooled and consolidated at a stable temperature until the vertical displacement is in stable steady state.

B-1.3 Post test step

1. Remove the specimen for full examination and take photo.

B-2 Unconfined compressive strength testing procedures (UCS)

B-2.1 Sample Preparation

1. The sample is examined to make sure that there are no cracks in the sample.
2. The sample is trimmed to a 1.5" diameter and 3.0" length specimen in the moisture room using an electrical diamond cutter.
3. After trimming, both ends of the specimen should be flat and parallel and are perpendicular to the vertical axis.
4. The sample is weighed and all specimen's dimensions are measured.
5. Initial Vp and Vs measurements are conducted on the specimen.
6. Photos are taken for the sample.
7. For samples tested at 120 ^{o}C and 180 ^{o}C, the sample is placed in water curing bath and slowly heated up to 95 ^{o}C.

B-2.2 Set up and testing

1. The specimen is placed in the INSTRON loading frame. The axial strain rate is adjusted at 0.050 mm/min. Then the loading frame is moved down to make the loading ram in contact with the specimen.
2. Loading test is started and the maximum compressive strength and strain are recorded.
3. For samples tested at 120 and 180 ^{o}C, the sample is removed from water curing bath and placed inside a triaxial cell. Cell pressure and back pressure are applied to allow increasing the temperature to the target temperature while keeping the sample wet. The triaxial cell is placed inside the environmental chamber and the temperature is increased slowly to heat the sample up to the desired temperature.

B-2.3 Post-test step

1. The specimen is removed for fully examination and photos.

B-3 Brazilian testing procedures

B-3.1 Sample Preparation

1. The sample is examined to make sure that there are no cracks in the sample.
2. The sample is trimmed to a 1.5” diameter and 1.0” length specimen in the moisture room using a diamond cutter.
3. After trimming, both ends of the specimen should be flat and parallel and are perpendicular to the vertical axis.
4. The sample is weighed and all specimen’s dimensions are measured.
5. Initial Vp and Vs measurements are conducted on the specimen.
6. Photos are taken for the sample.
7. For samples tested at 120 and 180 ^{o}C, the sample is placed in water curing bath and slowly heated up to 95 ^{o}C.

B-3.2 Set up and testing

1. The specimen is placed in between the curved surfaces of two aluminum sample holders (Figure A4).
2. The sample holders with specimen is placed under the INSTRON loading frame, and the loading ram is moved down to be in contact with the specimen.
3. For samples tested at 120 ºC and 180 ºC, the sample is removed from water curing bath and is placed inside the environmental chamber and the temperature is slowly increased to heat the sample up to the desired temperature.
4. Loading is started continuously and without shock at constant rate and axial load and strain values are recorded until sample ruptures.

B-3.3 Post-test step

1. The specimen is removed for full examination and photos.

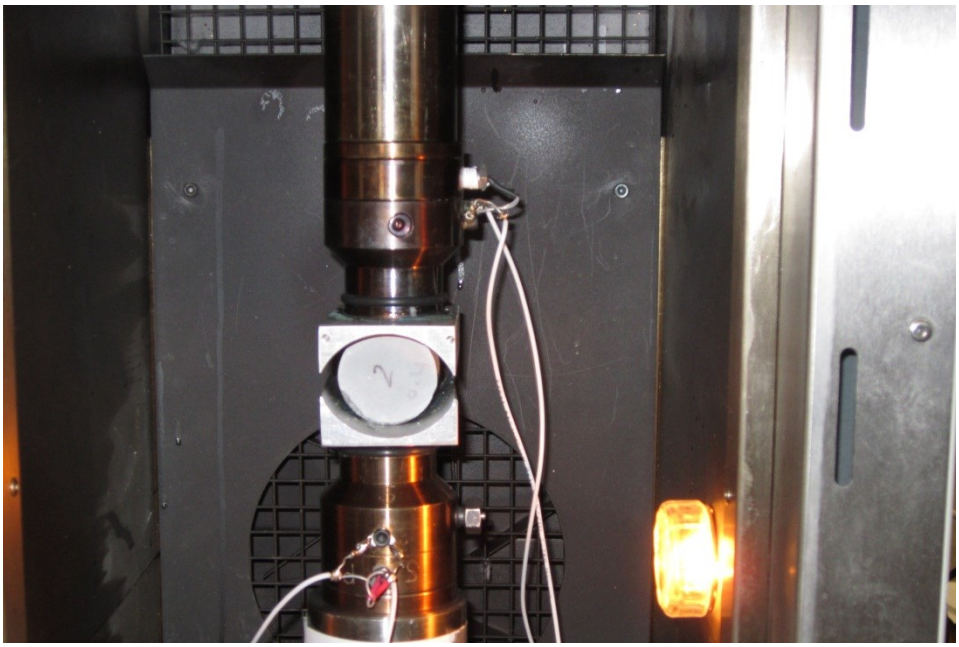

Figure B1. Brazilian test set-up

B-4 Isotopically consolidation drained triaxial testing procedures

B-4.1 Sample Preparation

1. The sample is examined to make sure that there are no cracks in the sample.
2. The sample is trimmed to a 1.5” diameter and 3.0” length specimen (H:D ratio is 2:1) using an electrical diamond cutter.
3. After trimming, both ends of the specimen should be flat and parallel and are perpendicular to the vertical axis.
4. The sample is weighted and all specimen’s dimensions are measured. Photos are taken.
5. Initial Vp and Vs measurements are conducted on the specimen.
6. For the samples which will be tested at 120 and 180 ºC, the samples are placed in water curing bath and slowly heated up to 95 ºC.

B-4.2 Triaxial cell set-up

1. Saturate all drainage lines of triaxial cell with brine fluid (3% NaCl) by injecting brine from one side until fluid is received from the other side.
2. Boil two porous stones in DI water and prepare two-pieces of filter paper.
3. Place the specimen on the bottom pedestal with two saturated sintered stainless steel porous stones and filter paper at both ends of specimen.
4. Use Viton membranes, and carefully place it over the specimen.
5. Pour some brine fluid on the sample.
6. Place the top pedestal on top of the specimen. Seal the specimen with two Viton O-rings on both the top and bottom pedestals. Then connect the top drainage line to the top pedestal.
7. Assemble the top triaxial cell body with a 38.1mm (1.5”) diameter loading ram.
8. Place the whole triaxial cell under a high pressure triaxial loading frame, and move the loading frame down to just above the loading ram.

9. Saturate the confining pressure line then connect it to the cell pressure port at the base of the triaxial cell. ISCO pump is used to apply the hydraulic confining pressure. Once the confining pressure system is connected, apply a desired confining pressure.

B-4.3 Back Saturation

1. Saturate the pore pressure lines with brine fluid and connect to a pore pressure ISCO syringe pump. Pore pressure line is also connected with Quizix Pump which is to be used during permeability test.
2. Incrementally increase confining pressure and pore pressure respectively to the desired effective confining stress, σ' with pore pressure at in-situ stress level.
3. Hold the system to achieve back saturation for the specimen.
4. For samples tested at 120 and 180 ºC, the triaxial cell is placed inside the environmental chamber which will be used to heat the sample up to the desired temperature.

B-4.4 Triaxial Test

1. Slowly increase axial stress, σ_1, at a very low axial strain rate by moving ram down.
2. After sample shears and reaches constant residual stress, stop ram moving down.

B-4.5 Post Test Step

1. Dis-assemble the Triaxial cell and remove the specimen for full examination.

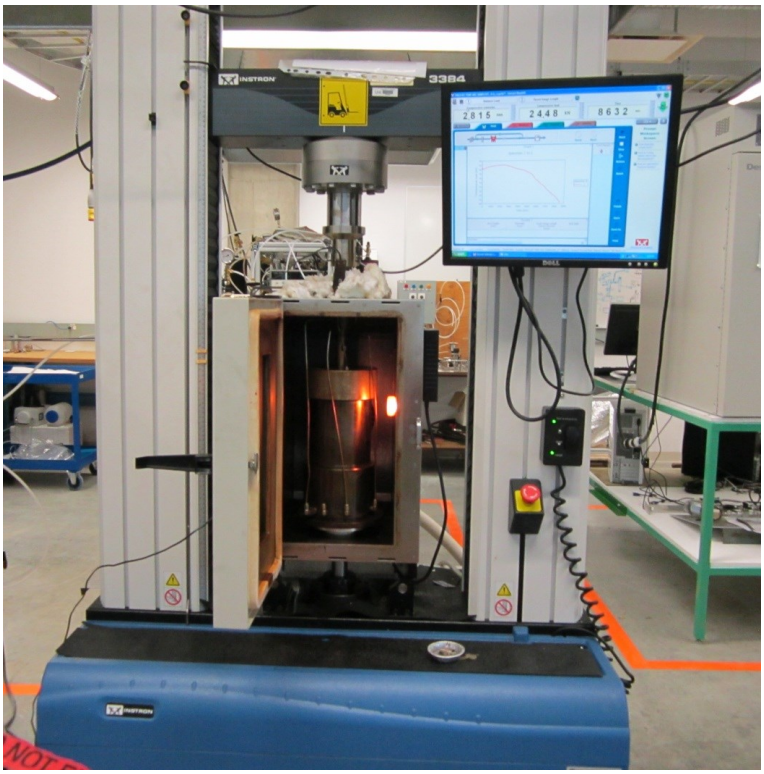

Figure B2. Triaxial test set-up

APPENDIX C. EXPERIMENTAL PROGRAM PLAN

Table C1. Chemical shrinkage test plan.

Cement Type	Test ID	w/c (bwoc)	Applied Pressure	Temp. (ºC)
Non-thermal cement	VS1-NT-0.4	0.4	3.0 MPa	9 ºC
	VS2-NT-0.4	0.4	3.0 MPa	9 ºC
Non-thermal cement	VS1-NT-0.5	0.5	3.0 MPa	9 ºC
	VS2-NT-0.5	0.5	3.0 MPa	9 ºC
Non-thermal cement	VS1-NT-0.6	0.6	3.0 MPa	9 ºC
	VS2-NT-0.6	0.6	3.0 MPa	9 ºC
Thermal cement	VS1-T-0.5	0.5	3.0 MPa	9 ºC
	VS2-T-0.5	0.5	3.0 MPa	9 ºC

Table C2. Thermal expansion test plan.

Cement Type	Test ID	w/c (bwoc)	Applied Pressure	Temp. Range (ºC)
Non-thermal cement	TEX1-NT-0.4	0.4	3 MPa	22 - 180 ºC
	TEX2-NT-0.4	0.4	3 MPa	22 - 180 ºC
Non-thermal cement	TEX 1-NT-0.5	0.5	3 MPa	22 - 180 ºC
	TEX 2-NT-0.5	0.5	3 MPa	22 - 180 ºC
Non-thermal cement	TEX 1-NT-0.6	0.6	3 MPa	22 - 180 ºC
	TEX 2-NT-0.6	0.6	3 MPa	22 - 180 ºC
Thermal cement	TEX 1-T-0.5	0.5	3 MPa	22 - 180 ºC
	TEX 2-T-0.5	0.5	3 MPa	22 - 180 ºC

Table C3. Unconfined Compressive Strength test plan.

Cement Type	Test ID	w/c (bwoc)	No. of Samples	Temp. (ºC)
Non-thermal cement	UCS5-NT-0.4	0.4	3	5 ºC
	UCS60-NT-0.4	0.4	3	60 ºC
	UCS120-NT-0.4	0.4	3	120 ºC
	UCS180-NT-0.4	0.4	3	180 ºC
Non-thermal cement	UCS5-NT-0.5	0.5	3	5 ºC
	UCS60-NT-0.5	0.5	3	60 ºC
	UCS120-NT-0.5	0.5	3	120 ºC
	UCS180-NT-0.5	0.5	3	180 ºC
Non-thermal cement	UCS5-NT-0.6	0.6	3	5 ºC
	UCS60-NT-0.6	0.6	3	60 ºC
	UCS120-NT-0.6	0.6	3	120 ºC
	UCS180-NT-0.6	0.6	3	180 ºC
Thermal cement	UCS5-T-0.5	0.5	3	5 ºC
	UCS60-T-0.5	0.5	3	60 ºC
	UCS120-T-0.5	0.5	3	120 ºC
	UCS180-T-0.5	0.5	3	180 ºC

Table C4. Triaxial test plan.

Cement Type	Test ID	w/c (bwoc)	Back pressure (kPa)	Cell pressure (kPa)	Confining Pressure (kPa)	Temp. (ºC)
Non-thermal cement	TRX2-NT-0.4-C	0.4	2000	3850	2000	20, 60, 120, 180
	TRX6-NT-0.4-C	0.4	2000	7850	6000	20, 60, 120, 180
	TRX10-NT-0.4-C	0.4	2000	11850	10000	20, 60, 120, 180
Non-thermal cement	TRX2-NT-0.5-C	0.5	2000	3850	2000	20, 60, 120, 180
	TRX6-NT-0.5-C	0.5	2000	7850	6000	20, 60, 120, 180
	TRX10-NT-0.5-C	0.5	2000	11850	10000	20, 60, 120, 180
Non-thermal cement	TRX2-NT-0.6-T	0.6	2000	3850	2000	20, 60, 120, 180
	TRX6-NT-0.6-C	0.6	2000	7850	6000	20, 60, 120, 180
	TRX10-NT-0.6-T	0.6	2000	11850	10000	20, 60, 120, 180
Thermal cement	TRX2-T-0.5-C	0.5	2000	3850	2000	20, 60, 120, 180
	TRX6-T-0.5-T	0.5	2000	7850	6000	20, 60, 120, 180
	TRX10-T-0.5-C	0.5	2000	11850	10000	20, 60, 120, 180

Table C5. Direct shear test plan

Formulation	Test Code	w/c (bwoc)	σ_n' (kPa)	Remarks
Non-Thermal Cement	DSN1-NT1	0.4	1,000	All samples were cured at 9 ºC and 3 MPa
	DSN1-NT2	0.4	2,500	
	DSN1-NT3	0.4	4,000	
	DSN1-NT4	0.4	8,000	
	DSN2-NT1	0.5	1,000	
	DSN2-NT2	0.5	2,500	
	DSN2-NT3	0.5	4,000	
	DSN2-NT4	0.5	8,000	
	DSN3-NT1	0.6	1,000	
	DSN3-NT2	0.6	2,500	
	DSN3-NT3	0.6	4,000	
	DSN3-NT4	0.6	8,000	
Thermal Cement	DSN4-T1	0.5	1,000	
	DSN4-T2	0.5	2,500	
	DSN4-T3	0.5	4,000	
	DSN4-T4	0.5	8,000	

Table C6. Cement-shale interface test plan.

Formulation	Test Code	w/c (bwoc)	σ_n' (kPa)	Remarks
Non-Thermal Cement	IDS1-NT1	0.4	1000	Shale bedding planes normal to surface of cement sample
	IDS1-NT2	0.4	250	
	IDS1-NT3	0.4	50	
	IDS2-NT1	0.5	1000	
	IDS2-NT2	0.5	250	
	IDS2-NT3	0.5	50	
	IDS3-NT1	0.6	1000	
	IDS3-NT2	0.6	250	
	IDS3-NT3	0.6	50	
Thermal Cement	IDS4-T1	0.5	1000	
	IDS4-T2	0.5	250	
	IDS4-T3	0.5	50	

APPENDIX D. COMPRESSIVE STRENGHT TEST RESULTS

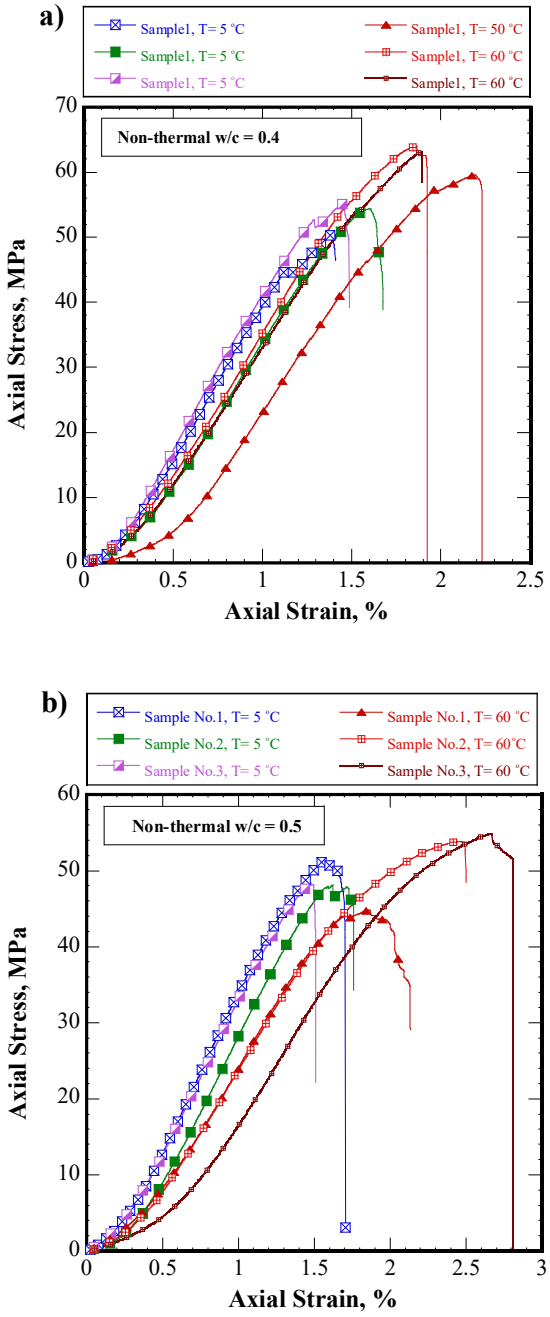

Figure D1. Unconfined compressive strength test results for: a) non-thermal cement of w/c = 0.4; b) non-thermal cement of w/c =0.5

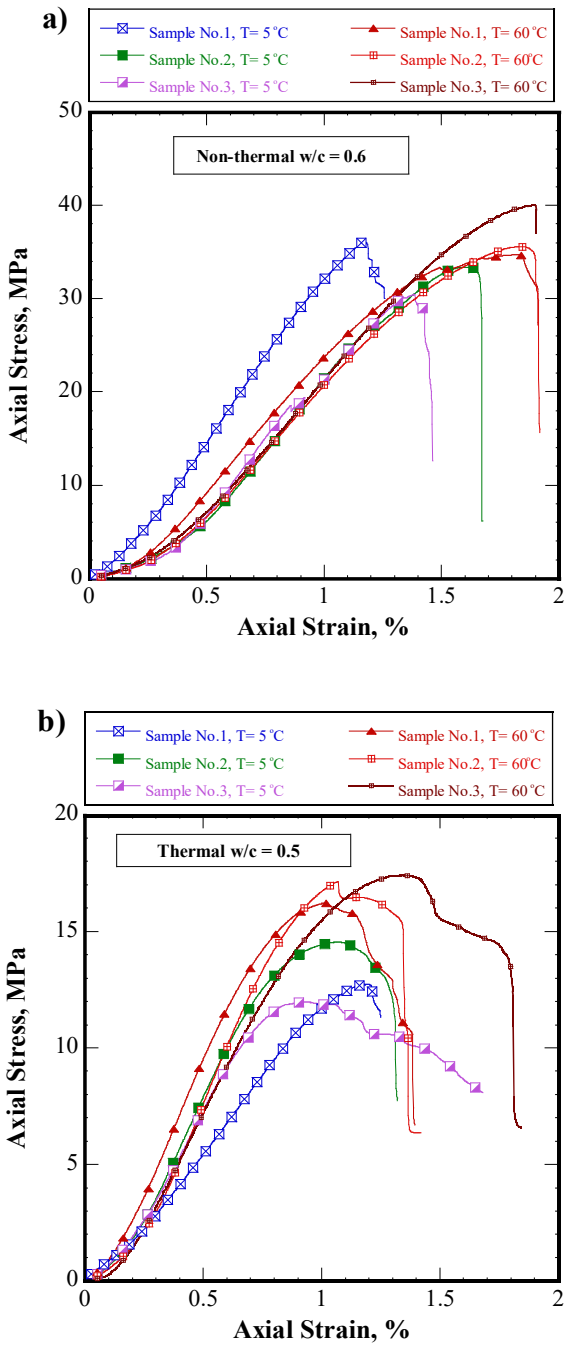

Figure D2. Unconfined compressive strength test results for: a) non-thermal cement of w/c = 0.6; b) thermal cement of w/c =0.5

APPENDIX E. INPUT DATA FILE FOR RESERVOIR SIMULATION MODEL

```
** ================== OVERVIEW =================
** 1) 3D - Model
** 2) Five well-pairs
** 3) Reservoir heterogeneities are considered
** ================== FLUID DEFINITIONS  =================
MODEL    2 2 2 1
COMPNAME 'WATER' 'OIL'
CMM      0.018   0.5                **molecular mass [ kg / gmol ]
PCRIT    2.206E+4  1.360E+3         **critical pressure [ kPa ]
TCRIT    3.742E+2 7.039E+2          ** critical temperature [ ºC ]
CPG1     0.0E+0 9.42E+2
AVG      0.0E+0 0.0E+0
BVG      0.0E+0 0.0E+0

PRSR 10000
TEMR 10
PSURF    1.013E+2
TSURF    2.0E+1

MOLDEN   5.5500E+4 2.200E+3
CP       4.463E-07 1.5E-6
CT1      1.563E-04 6.84E-4
CT2      0.0E+0 0.0E+0
```

```
VISCTABLE
**    TEMP   WATER      OIL
     5.0      0       4300000
     10.0     0       1700000
     20.0     0       3190000
     40.0     0       22300
     60.0     0       3073.0
     80.0     0       680.6
     100.0    0       212.63
     120.0    0       85.54
     140.0    0       41.57
     160.0    0       23.32
     200.0    0       9.96
     220.0    0       7.26
     240.0    0       5.59
     260.0    0       4.49
     280.0    0       3.73

** ==================  ROCK-FLUID PROPERTIES   ==================
ROCKFLUID
*RPT 1 *WATWET *STONE2
*SWT   ** Water-oil relative permeabilities
**Sw             Krw             Krow
**-------        ---------       ---------
0.195000      0.000000      0.994200
0.250000      0.001400      0.858200
0.300000      0.005200      0.721000
0.350000      0.012900      0.588000
0.400000      0.025500      0.463400
0.450000      0.044100      0.350900
```

0.500000 0.070000 0.252900

0.550000 0.104300 0.171300

0.600000 0.148400 0.106700

0.650000 0.203500 0.059000

0.700000 0.270800 0.027100

0.750000 0.351700 0.009100

0.800000 0.447300 0.000000

0.850000 0.558800 0.000000

0.900000 0.687400 0.000000

0.950000 0.834100 0.000000

1.000000 1.000000 0.000000

*SLT ** Liquid-gas relative permeabilities

** Sl Krg Krog

**------- --------- ---------

0.195000 0.956700 0.000000

0.250000 0.840000 0.001400

0.300000 0.714300 0.005500

0.350000 0.587200 0.013200

0.400000 0.465200 0.025700

0.450000 0.353100 0.044100

0.500000 0.254900 0.069700

0.550000 0.173100 0.103900

0.600000 0.109000 0.147900

0.650000 0.062600 0.203200

0.700000 0.033000 0.270800

0.750000 0.017600 0.352100

0.800000 0.013000 0.448100

0.850000 0.008700 0.559600

0.900000 0.004300 0.687300

0.950000 0.000000 0.831700

```
1.000000      0.000000      0.994200
**  ==================  INITIAL CONDITION   =================
*INITIAL
**VERTICAL DEPTH_AVE
*VERTICAL  *ON
INITREGION 1
*REFPRES 560.725
*REFDEPTH 313
*SW  *C0N 0.22
*S0    *C0N 0.78
** Compositions of the initial oil phase
MFRAC_OIL 'OIL' CON          1
**  ==================  NUMERICAL CONTROL   =================
NUMERICAL
CONVERGE TOTRES NORMAL
DTMAX 5
MATBALTOL 1E-3
UPSTREAM KLEVEL
ITERMAX 200
AIM STAB BACK 20
NORTH 100

**  ==================  RECURRENT DATA   ================
**  WELL LOCATIONS AND INITIAL OPERATIONAL CONSTRAINTS
DTWELL 0.01
********** WELL Pair 1 ********************************
WELL  'W20I01'  FRAC  1.0
INJECTOR MOBWEIGHT IMPLICIT 'W20I01'
INCOMP  WATER  1.0  0.0
TINJW  193.0
```

```
QUAL  0.9
OPERATE  MAX  BHP  1283.0  CONT REPEAT
XFLOW-MODEL 'W20I01' ZERO-FLOW
HEAD-METHOD 'W20I01' GRAV-FRIC-HLOS HEADRROUGH 0.0 DUKLER-BANKOFF
**        rad  geofac  wfrac  skin
GEOMETRY  J  0.11  0.249  1.0  0.0
    PERF      GEO  'W20I01'
** UBA             ff        Status  Connection
   80 110 29       1.0  OPEN    FLOW-FROM  'SURFACE'  REFLAYER
   80 111 29       1.0  OPEN    FLOW-FROM  1
   80 112 29       1.0  OPEN    FLOW-FROM  2
   80 113 29       1.0  OPEN    FLOW-FROM  3
   80 114 29       1.0  OPEN    FLOW-FROM  4
   80 115 29       1.0  OPEN    FLOW-FROM  5
   80 116 29       1.0  OPEN    FLOW-FROM  6
   80 117 29       1.0  OPEN    FLOW-FROM  7
   80 118 29       1.0  OPEN    FLOW-FROM  8
   80 119 29       1.0  OPEN    FLOW-FROM  9
   80 120 29       1.0  OPEN    FLOW-FROM  10
   80 121 29       1.0  OPEN    FLOW-FROM  11
   80 122 29       1.0  OPEN    FLOW-FROM  12
   80 123 29       1.0  OPEN    FLOW-FROM  13
   80 124 29       1.0  OPEN    FLOW-FROM  14
   80 125 29       1.0  OPEN    FLOW-FROM  15
   80 126 29       1.0  OPEN    FLOW-FROM  16
   80 127 29       1.0  OPEN    FLOW-FROM  17
   80 128 29       1.0  OPEN    FLOW-FROM  18
   80 129 29       1.0  OPEN    FLOW-FROM  19
   80 130 29       1.0  OPEN    FLOW-FROM  20
   80 131 29       1.0  OPEN    FLOW-FROM  21
```

80 132 29 1.0 OPEN FLOW-FROM 22

80 133 29 1.0 OPEN FLOW-FROM 23

80 134 29 1.0 OPEN FLOW-FROM 24

80 135 29 1.0 OPEN FLOW-FROM 25

80 136 29 1.0 OPEN FLOW-FROM 26

80 137 29 1.0 OPEN FLOW-FROM 27

80 138 29 1.0 OPEN FLOW-FROM 28

80 139 29 1.0 OPEN FLOW-FROM 29

80 140 29 1.0 OPEN FLOW-FROM 30

80 141 29 1.0 OPEN FLOW-FROM 31

80 142 29 1.0 OPEN FLOW-FROM 32

80 143 29 1.0 OPEN FLOW-FROM 33

80 144 29 1.0 OPEN FLOW-FROM 34

80 145 29 1.0 OPEN FLOW-FROM 35

80 146 29 1.0 OPEN FLOW-FROM 36

80 147 29 1.0 OPEN FLOW-FROM 37

80 148 29 1.0 OPEN FLOW-FROM 38

80 149 29 1.0 OPEN FLOW-FROM 39

80 150 29 1.0 OPEN FLOW-FROM 40

80 151 29 1.0 OPEN FLOW-FROM 41

80 152 29 1.0 OPEN FLOW-FROM 42

80 153 29 1.0 OPEN FLOW-FROM 43

80 154 29 1.0 OPEN FLOW-FROM 44

80 155 29 1.0 OPEN FLOW-FROM 45

80 156 29 1.0 OPEN FLOW-FROM 46

80 157 29 1.0 OPEN FLOW-FROM 47

80 158 29 1.0 OPEN FLOW-FROM 48

80 159 29 1.0 OPEN FLOW-FROM 49

80 160 29 1.0 OPEN FLOW-FROM 50

80 161 29 1.0 OPEN FLOW-FROM 51

80 162 29 1.0 OPEN FLOW-FROM 52

80 163 29 1.0 OPEN FLOW-FROM 53

80 164 29 1.0 OPEN FLOW-FROM 54

80 165 29 1.0 OPEN FLOW-FROM 55

80 166 29 1.0 OPEN FLOW-FROM 56

80 167 29 1.0 OPEN FLOW-FROM 57

80 168 29 1.0 OPEN FLOW-FROM 58

80 169 29 1.0 OPEN FLOW-FROM 59

80 170 29 1.0 OPEN FLOW-FROM 60

80 171 29 1.0 OPEN FLOW-FROM 61

80 172 29 1.0 OPEN FLOW-FROM 62

80 173 29 1.0 OPEN FLOW-FROM 63

80 174 29 1.0 OPEN FLOW-FROM 64

80 175 29 1.0 OPEN FLOW-FROM 65

80 176 29 1.0 OPEN FLOW-FROM 66

80 177 29 1.0 OPEN FLOW-FROM 67

80 178 29 1.0 OPEN FLOW-FROM 68

80 179 29 1.0 OPEN FLOW-FROM 69

80 180 29 1.0 OPEN FLOW-FROM 70

80 181 29 1.0 OPEN FLOW-FROM 71

80 182 29 1.0 OPEN FLOW-FROM 72

80 183 29 1.0 OPEN FLOW-FROM 73

80 184 29 1.0 OPEN FLOW-FROM 74

80 185 29 1.0 OPEN FLOW-FROM 75

80 186 29 1.0 OPEN FLOW-FROM 76

80 187 29 1.0 OPEN FLOW-FROM 77

80 188 29 1.0 OPEN FLOW-FROM 78

80 189 29 1.0 OPEN FLOW-FROM 79

80 190 29 1.0 OPEN FLOW-FROM 80

```
WELL  'W20P01'  FRAC  1.0
PRODUCER 'W20P01'
OPERATE  MIN  BHP  800.0  CONT REPEAT
OPERATE  MIN  STEAMTRAP  5.0  CONT REPEAT
**        rad  geofac  wfrac  skin
GEOMETRY  J  0.11  0.249  1.0  0.0
    PERF      GEO  'W20P01'
** UBA              ff        Status  Connection
   80 110 31       1.0  OPEN    FLOW-TO  'SURFACE'  REFLAYER
   80 111 31       1.0  OPEN    FLOW-TO  1
   80 112 31       1.0  OPEN    FLOW-TO  2
   80 113 31       1.0  OPEN    FLOW-TO  3
   80 114 31       1.0  OPEN    FLOW-TO  4
   80 115 31       1.0  OPEN    FLOW-TO  5
   ……..        ……..    ……
   ……..        ……..    ……
  ……..        ……..    ……
   80 189 31       1.0  OPEN    FLOW-TO  79
   80 190 31       1.0  OPEN    FLOW-TO  80



WELL  'W20H01'  FRAC  1.0
PRODUCER 'W20H01'
OPERATE  MIN  BHP  800.0  CONT
**        rad  geofac  wfrac  skin
GEOMETRY  J  0.11  0.249  1.0  0.0
    PERF      GEO  'W20H01'
** UBA              ff        Status  Connection
```

```
   80 110 31       1.0  OPEN    FLOW-TO  'SURFACE'  REFLAYER
   80 111 31       1.0  OPEN    FLOW-TO  1
   80 112 31       1.0  OPEN    FLOW-TO  2
   80 113 31       1.0  OPEN    FLOW-TO  3
   80 114 31       1.0  OPEN    FLOW-TO  4
   80 115 31       1.0  OPEN    FLOW-TO  5
   ……..        ……..    ……
   ……..        ……..    ……
  ……          ……..    ……
   80 189 31       1.0  OPEN    FLOW-TO  79
   80 190 31       1.0  OPEN    FLOW-TO  80


********** WELL Pair 2 ********************************
WELL  'W20I02'  FRAC  1.0
INJECTOR MOBWEIGHT IMPLICIT 'W20I02'
INCOMP  WATER  1.0  0.0
TINJW  193.0
QUAL  0.9
OPERATE  MAX  BHP  1283.0  CONT REPEAT
XFLOW-MODEL 'W20I02' ZERO-FLOW
HEAD-METHOD 'W20I02' GRAV-FRIC-HLOS HEADRROUGH 0.0 DUKLER-BANKOFF
**        rad  geofac  wfrac  skin
GEOMETRY  J  0.11  0.249  1.0  0.0
    PERF      GEO  'W20I02'
** UBA             ff        Status  Connection
   90 110 29       1.0  OPEN    FLOW-FROM  'SURFACE'  REFLAYER
   90 111 29       1.0  OPEN    FLOW-FROM  1
   90 112 29       1.0  OPEN    FLOW-FROM  2
   90 113 29       1.0  OPEN    FLOW-FROM  3
```

```
   90 114 29       1.0  OPEN    FLOW-FROM  4
   90 115 29       1.0  OPEN    FLOW-FROM  5
   ……..            ……..         ……
   ……..            ……..         ……
   ……..            ……..         ……
   90 189 29       1.0  OPEN    FLOW-FROM  79
   90 190 29       1.0  OPEN    FLOW-FROM  80


WELL  'W20P02'  FRAC  1.0
PRODUCER 'W20P02'
OPERATE  MIN  BHP  800.0  CONT REPEAT
OPERATE  MIN  STEAMTRAP  5.0  CONT REPEAT
**         rad  geofac  wfrac  skin
GEOMETRY  J  0.11  0.249  1.0  0.0
    PERF      GEO  'W20P02'
** UBA              ff        Status  Connection
   90 110 31       1.0  OPEN    FLOW-TO  'SURFACE'  REFLAYER
   90 111 31       1.0  OPEN    FLOW-TO  1
   90 112 31       1.0  OPEN    FLOW-TO  2
   90 113 31       1.0  OPEN    FLOW-TO  3
   90 114 31       1.0  OPEN    FLOW-TO  4
   90 115 31       1.0  OPEN    FLOW-TO  5
   ……..            ……..         ……
   ……..            ……..         ……
   ……..            ……..         ……
   90 189 31       1.0  OPEN    FLOW-TO  79
   90 190 31       1.0  OPEN    FLOW-TO  80
```

```
WELL  'W20H02'  FRAC  1.0
PRODUCER 'W20H02'
OPERATE  MIN  BHP  800.0  CONT
**        rad  geofac  wfrac  skin
GEOMETRY  J  0.11  0.249  1.0  0.0
    PERF      GEO  'W20H02'
** UBA              ff        Status  Connection
   90 110 31       1.0  OPEN    FLOW-TO  'SURFACE'  REFLAYER
   90 111 31       1.0  OPEN    FLOW-TO  1
   90 112 31       1.0  OPEN    FLOW-TO  2
   90 113 31       1.0  OPEN    FLOW-TO  3
   90 114 31       1.0  OPEN    FLOW-TO  4
   90 115 31       1.0  OPEN    FLOW-TO  5
   ……..        ……..    ……
   ……..        ……..    ……
   ……..        ……..    ……
   90 189 31       1.0  OPEN    FLOW-TO  79
   90 190 31       1.0  OPEN    FLOW-TO  80


********** WELL Pair 3 ********************************
WELL  'W20I03'  FRAC  1.0
INJECTOR MOBWEIGHT IMPLICIT 'W20I03'
INCOMP  WATER  1.0  0.0
TINJW  193.0
QUAL  0.9
OPERATE  MAX  BHP  1283.0  CONT REPEAT
XFLOW-MODEL 'W20I03' ZERO-FLOW
HEAD-METHOD 'W20I03' GRAV-FRIC-HLOS HEADRROUGH 0.0 DUKLER-BANKOFF
**        rad  geofac  wfrac  skin
```

```
GEOMETRY  J  0.11  0.249  1.0  0.0
    PERF      GEO  'W20I03'
** UBA              ff        Status  Connection
   100 110 29       1.0  OPEN    FLOW-FROM  'SURFACE'  REFLAYER
   100 111 29       1.0  OPEN    FLOW-FROM  1
   100 112 29       1.0  OPEN    FLOW-FROM  2
   100 113 29       1.0  OPEN    FLOW-FROM  3
   100 114 29       1.0  OPEN    FLOW-FROM  4
   100 115 29       1.0  OPEN    FLOW-FROM  5
   ……..        ……..    ……
   ……..        ……..    ……
   ……..        ……..    ……
   100 189 29       1.0  OPEN    FLOW-FROM  79
   100 190 29       1.0  OPEN    FLOW-FROM  80


WELL  'W20P03'  FRAC  1.0
PRODUCER 'W20P03'
OPERATE  MIN  BHP  800.0  CONT REPEAT
OPERATE  MIN  STEAMTRAP  5.0  CONT REPEAT
**        rad  geofac  wfrac  skin
GEOMETRY  J  0.11  0.249  1.0  0.0
    PERF      GEO  'W20P03'
** UBA              ff        Status  Connection
   100 110 31       1.0  OPEN    FLOW-TO  'SURFACE'  REFLAYER
   100 111 31       1.0  OPEN    FLOW-TO  1
   100 112 31       1.0  OPEN    FLOW-TO  2
   100 113 31       1.0  OPEN    FLOW-TO  3
   100 114 31       1.0  OPEN    FLOW-TO  4
   100 115 31       1.0  OPEN    FLOW-TO  5
```

```
   ……..        ……..    ……
   ……..        ……..    ……
   ……..        ……..    ……
   100 189 31       1.0  OPEN    FLOW-TO  79
   100 190 31       1.0  OPEN    FLOW-TO  80

WELL  'W20H03'  FRAC  1.0
PRODUCER 'W20H03'
OPERATE  MIN  BHP  800.0  CONT
**         rad  geofac  wfrac  skin
GEOMETRY  J  0.11  0.249  1.0  0.0
    PERF      GEO  'W20H03'
** UBA              ff        Status  Connection
   100 110 31       1.0  OPEN    FLOW-TO  'SURFACE'  REFLAYER
   100 111 31       1.0  OPEN    FLOW-TO  1
   100 112 31       1.0  OPEN    FLOW-TO  2
   100 113 31       1.0  OPEN    FLOW-TO  3
   100 114 31       1.0  OPEN    FLOW-TO  4
   100 115 31       1.0  OPEN    FLOW-TO  5
   ……..        ……..    ……
   ……..        ……..    ……
   ……..        ……..    ……
   100 189 31       1.0  OPEN    FLOW-TO  79
   100 190 31       1.0  OPEN    FLOW-TO  80


********** WELL Pair 4 ********************************
WELL  'W20I04'  FRAC  1.0
INJECTOR MOBWEIGHT IMPLICIT 'W20I04'
INCOMP  WATER  1.0  0.0
```

```
TINJW  193.0
QUAL  0.9
OPERATE  MAX  BHP  1283.0  CONT REPEAT
XFLOW-MODEL 'W20I04' ZERO-FLOW
HEAD-METHOD 'W20I04' GRAV-FRIC-HLOS HEADRROUGH 0.0 DUKLER-BANKOFF
**        rad  geofac  wfrac  skin
GEOMETRY  J  0.11  0.249  1.0  0.0
    PERF      GEO  'W20I04'
** UBA              ff        Status  Connection
   110 110 29       1.0  OPEN    FLOW-FROM  'SURFACE'  REFLAYER
   110 111 29       1.0  OPEN    FLOW-FROM  1
   110 112 29       1.0  OPEN    FLOW-FROM  2
   110 113 29       1.0  OPEN    FLOW-FROM  3
   110 114 29       1.0  OPEN    FLOW-FROM  4
   110 115 29       1.0  OPEN    FLOW-FROM  5
      ……..    ……..    ……
   ……..       ……..    ……
   ……..       ……..    ……
   110 189 29       1.0  OPEN    FLOW-FROM  79
   110 190 29       1.0  OPEN    FLOW-FROM  80

WELL  'W20P04'  FRAC  1.0
PRODUCER 'W20P04'
OPERATE  MIN  BHP  800.0  CONT REPEAT
OPERATE  MIN  STEAMTRAP  5.0  CONT REPEAT
**        rad  geofac  wfrac  skin
GEOMETRY  J  0.11  0.249  1.0  0.0
    PERF      GEO  'W20P04'
** UBA              ff        Status  Connection
   110 110 31       1.0  OPEN    FLOW-TO  'SURFACE'  REFLAYER
```

```
   110 111 31       1.0  OPEN    FLOW-TO  1
   110 112 31       1.0  OPEN    FLOW-TO  2
   110 113 31       1.0  OPEN    FLOW-TO  3
   110 114 31       1.0  OPEN    FLOW-TO  4
   110 115 31       1.0  OPEN    FLOW-TO  5
   ……..        ……..    ……
   ……..        ……..    ……
   110 189 31       1.0  OPEN    FLOW-TO  79
   110 190 31       1.0  OPEN    FLOW-TO  80

WELL  'W20H04'  FRAC  1.0
PRODUCER 'W20H04'
OPERATE  MIN  BHP  800.0  CONT
**        rad  geofac  wfrac  skin
GEOMETRY  J  0.11  0.249  1.0  0.0
    PERF      GEO  'W20H04'
** UBA              ff        Status  Connection
   110 110 31       1.0  OPEN    FLOW-TO  'SURFACE'  REFLAYER
   110 111 31       1.0  OPEN    FLOW-TO  1
   110 112 31       1.0  OPEN    FLOW-TO  2
   110 113 31       1.0  OPEN    FLOW-TO  3
   110 114 31       1.0  OPEN    FLOW-TO  4
   110 115 31       1.0  OPEN    FLOW-TO  5
   110 116 31       1.0  OPEN    FLOW-TO  6
   ……..        ……..    ……
   ……..        ……..    ……
   ……..        ……..    ……
   110 189 31       1.0  OPEN    FLOW-TO  79
   110 190 31       1.0  OPEN    FLOW-TO  80
********** WELL Pair 5 ********************************
```

```
WELL  'W20I05'  FRAC  1.0
INJECTOR MOBWEIGHT IMPLICIT 'W20I05'
INCOMP  WATER  1.0  0.0
TINJW  193.0
QUAL  0.9
OPERATE  MAX  BHP  1283.0  CONT REPEAT
XFLOW-MODEL 'W20I05' ZERO-FLOW
HEAD-METHOD 'W20I05' GRAV-FRIC-HLOS HEADRROUGH 0.0 DUKLER-BANKOFF
**        rad  geofac  wfrac  skin
GEOMETRY  J  0.11  0.249  1.0  0.0
    PERF      GEO  'W20I05'
** UBA              ff        Status  Connection
   120 110 29       1.0  OPEN    FLOW-FROM  'SURFACE'  REFLAYER
   120 111 29       1.0  OPEN    FLOW-FROM  1
   120 112 29       1.0  OPEN    FLOW-FROM  2
   120 113 29       1.0  OPEN    FLOW-FROM  3
   120 114 29       1.0  OPEN    FLOW-FROM  4
   120 115 29       1.0  OPEN    FLOW-FROM  5
   ……..        ……..    ……
   ……..        ……..    ……
   ……..        ……..    ……
   120 189 29       1.0  OPEN    FLOW-FROM  79
   120 190 29       1.0  OPEN    FLOW-FROM  80

WELL  'W20P05'  FRAC  1.0
PRODUCER 'W20P05'
OPERATE  MIN  BHP  800.0  CONT REPEAT
OPERATE  MIN  STEAMTRAP  5.0  CONT REPEAT
**        rad  geofac  wfrac  skin
GEOMETRY  J  0.11  0.249  1.0  0.0
```

```
    PERF      GEO  'W20P05'
** UBA             ff        Status  Connection
   120 110 31       1.0  OPEN    FLOW-TO  'SURFACE'  REFLAYER
   120 111 31       1.0  OPEN    FLOW-TO  1
   120 112 31       1.0  OPEN    FLOW-TO  2
   120 113 31       1.0  OPEN    FLOW-TO  3
   120 114 31       1.0  OPEN    FLOW-TO  4
   120 115 31       1.0  OPEN    FLOW-TO  5
   ……..        ……..    ……
   ……..        ……..    ……
   120 189 31       1.0  OPEN    FLOW-TO  79
   120 190 31       1.0  OPEN    FLOW-TO  80

WELL  'W20H05'  FRAC  1.0
PRODUCER 'W20H05'
OPERATE  MIN  BHP  800.0  CONT
**        rad  geofac  wfrac  skin
GEOMETRY  J  0.11  0.249  1.0  0.0
    PERF      GEO  'W20H05'
** UBA             ff        Status  Connection
   120 110 31       1.0  OPEN    FLOW-TO  'SURFACE'  REFLAYER
   120 111 31       1.0  OPEN    FLOW-TO  1
   120 112 31       1.0  OPEN    FLOW-TO  2
   120 113 31       1.0  OPEN    FLOW-TO  3
   120 114 31       1.0  OPEN    FLOW-TO  4
   120 115 31       1.0  OPEN    FLOW-TO  5
   ……..        ……..    ……
   ……..        ……..    ……
   120 189 31       1.0  OPEN    FLOW-TO  79
   120 190 31       1.0  OPEN    FLOW-TO  80
```

APPENDIX F. RESULTS OF SAGD RESERVOIR SIMULATION

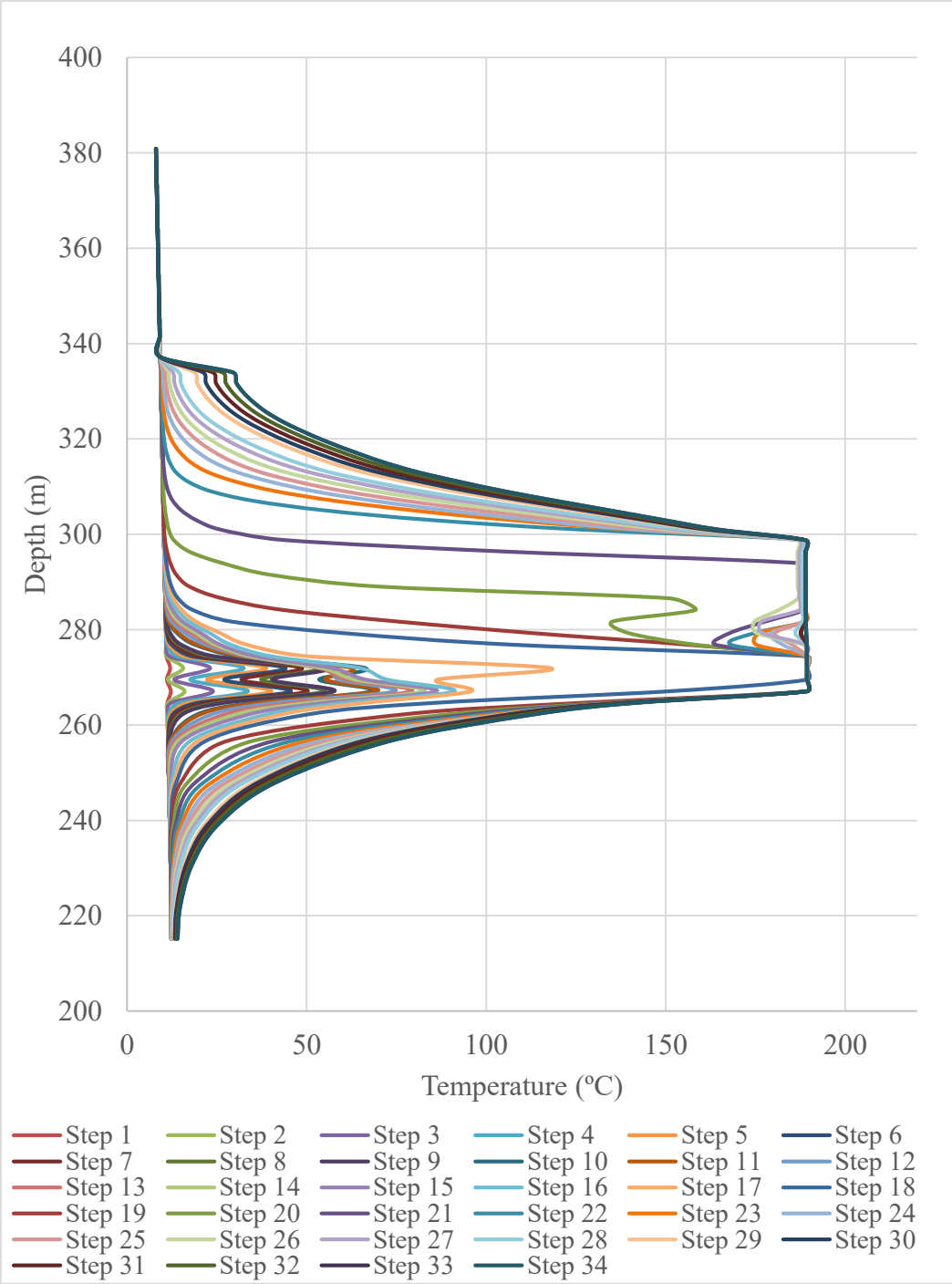

Figure F1. Progression of temperature distribution at location No.1

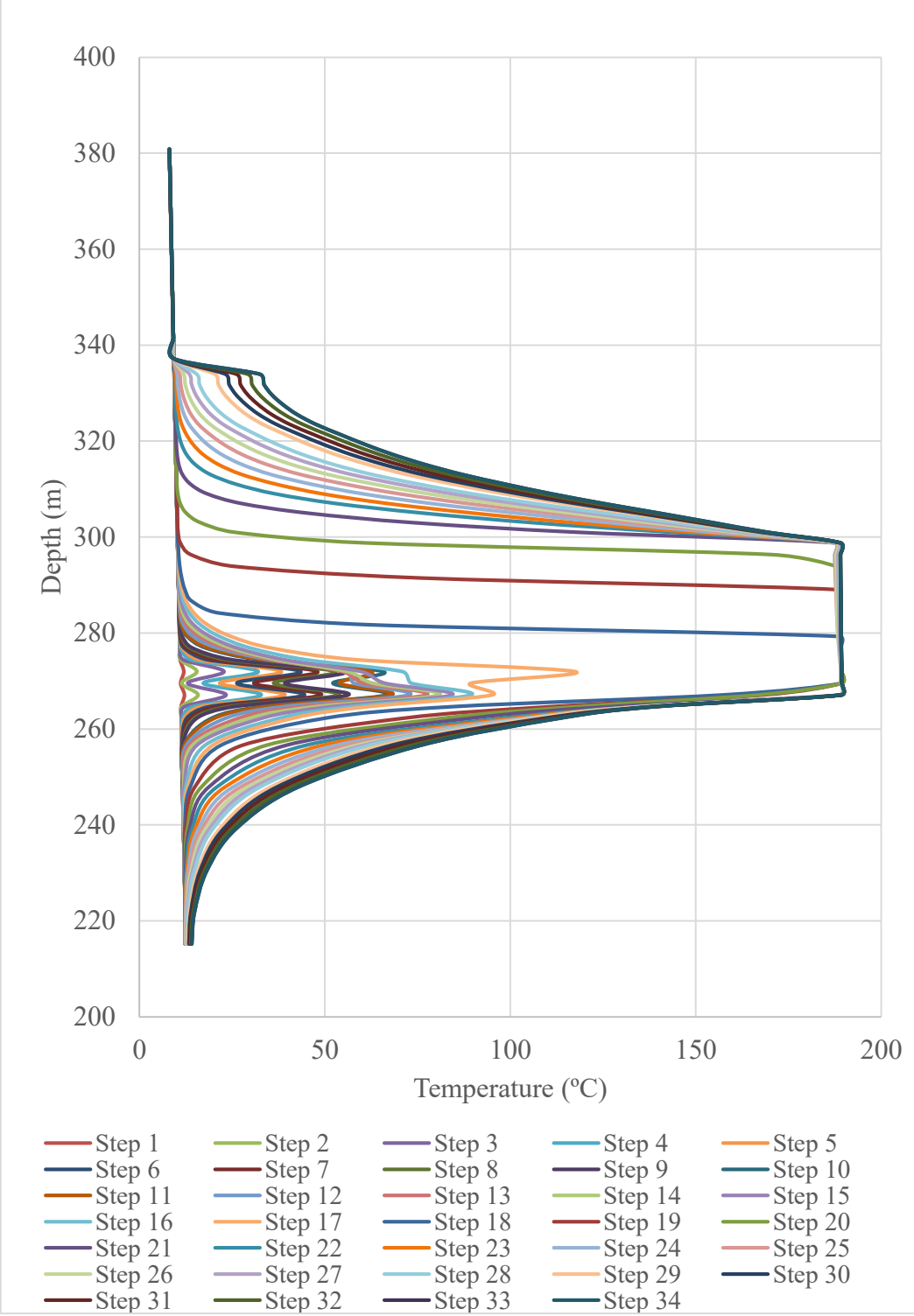

Figure F2. Progression of temperature distribution at location No.2

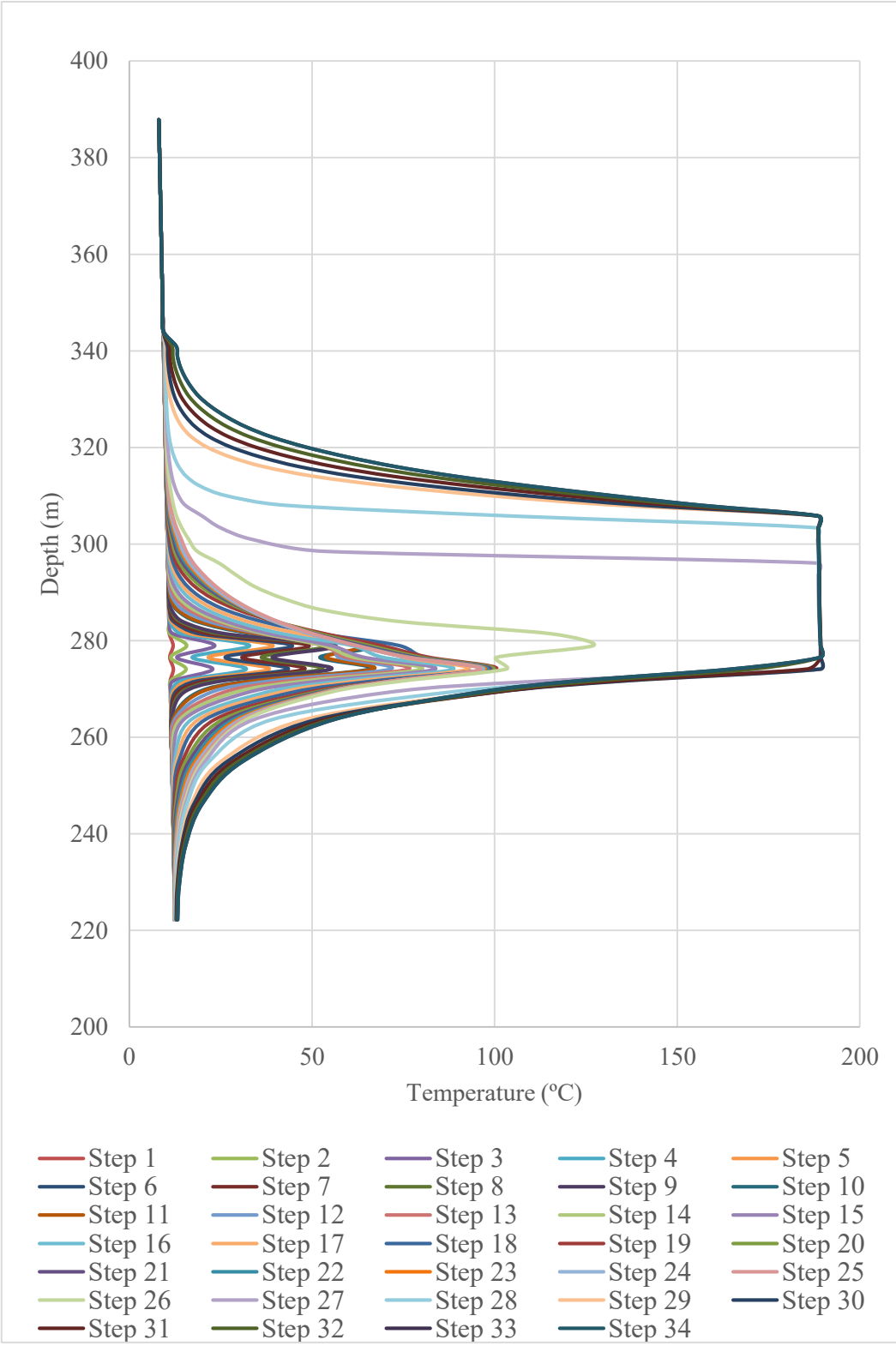

Figure F3. Progression of temperature distribution at location No.3

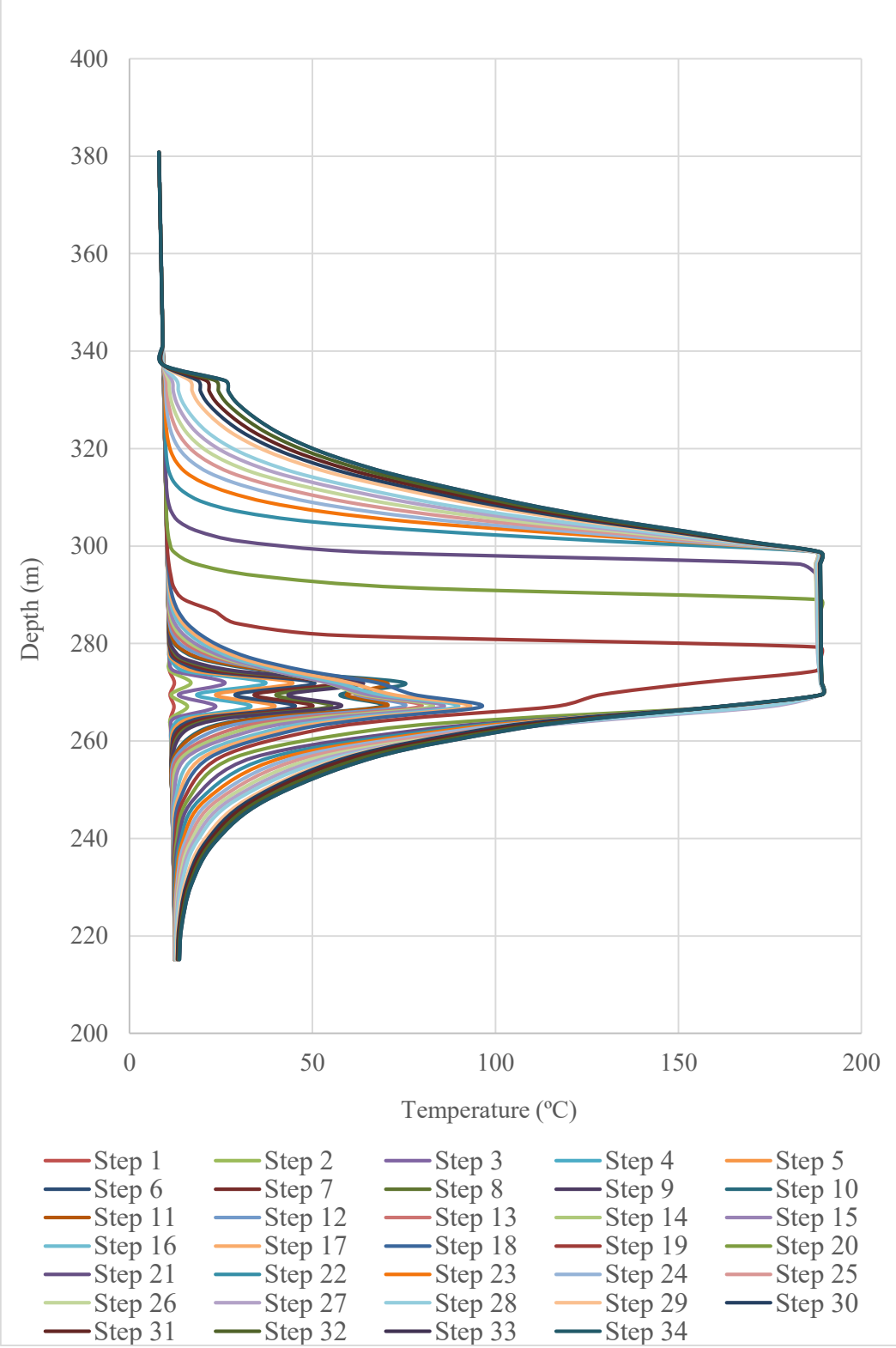

Figure F4. Progression of temperature distribution at location No.4